



**BERGISCHE
UNIVERSITÄT
WUPPERTAL**

Development and Characterization of capillary Atmospheric Pressure Electron Capture Ionization (cAPECI)

Dissertation

zur Erlangung des akademischen Grades
Doktor der Naturwissenschaften (Dr. rer. nat.)

vorgelegt von
Valerie Ann Christin Derpmann
geb. Funcke

Bergische Universität Wuppertal
Fachbereich C - Mathematik und Naturwissenschaften
Physikalische und Theoretische Chemie
unter der Anleitung von Prof. Dr. Thorsten Benter

Wuppertal, Oktober 2014

Die Dissertation kann wie folgt zitiert werden:

urn:nbn:de:hbz:468-20150410-102234-8

[<http://nbn-resolving.de/urn/resolver.pl?urn=urn%3Anbn%3Ade%3A468-20150410-102234-8>]

"There is a theory which states that if ever anybody discovers exactly what the Universe is for and why it is here, it will instantly disappear and be replaced by something even more bizarre and inexplicable... There is another theory which states that this has already happened."

"So long, and thanks for all the fish."

Douglas Adams, Hitchhikers Guide to the Galaxy

Danksagung

Ohne die Hilfe vieler Menschen wäre diese Arbeit nicht möglich gewesen. Ich möchte all diesen Menschen herzlichst danken, egal wie groß oder klein ihr Anteil daran war.

Erklärung

"Ich versichere, dass ich die von mir vorgelegte Arbeit selbständig angefertigt und andere als die angegebenen Hilfsmittel nicht benutzt, sowie jede wörtlich oder inhaltlich übernommene Stelle kenntlich gemacht habe."

Wuppertal, 10. Oktober 2014

Valerie Derpmann

Abstract

In this work a novel method for the generation of negatively charged ions is developed. Most analytes form stable positive ions and are thus easily accessible to mass spectrometric analysis, but there are a few compound classes that undergo fragmentation when they are positively charged, for example, nitro-aromatic compounds. For these compound classes negative ionization is desirable.

The novel method is based upon the photoelectric effect, which is the generation of electrons by the interaction of light, in particular *ultra violet* (UV) light, with metal surfaces. Thus, only negative ions are produced. This is in contrast to all other ionization methods operating in the gas phase where both positive and negative ions are generated, which may lead to adverse recombination reactions.

Within this work the ionization method is characterized, an optimized ionization source is developed and several applications are shown. The ion source exhibits short reaction times as the mixing of primary ions and the analyte containing gas stream takes place inside the channel of an inlet capillary. Therefore, the method has been termed *capillary Atmospheric Pressure Electron Capture Ionization* (cAPECI). The short reaction times lead to kinetically controlled reaction product distributions of the occurring ion-molecule/radical reactions and thus to mass spectra which resemble closely the ion distribution inside the ion source. With longer reaction times, as present in common ion sources, thermodynamically controlled product distributions are generally obtained.

The ionization method produces solely negative ions and only a small quantity of neutral radicals. Because of both, the short reaction times and the high selectivity of the method, ion-transformation processes are minimized. Mass spectra with low background signal levels and high signal-to-noise ratios are obtained.

For a deeper understanding of the processes occurring during and following ionization, investigations were carried out with respect to:

- the photoelectric effect at atmospheric pressure
- the reaction mechanism in the negative ion mode
- the ion transmission characteristics of (modified) inlet capillaries

Work functions reported in the literature have been determined at low pressures, thus, work functions at elevated pressures were measured during this work. At atmospheric pressure the surface is covered with molecular layers of water or even oxidation

of the surface occurs. This can alter the work function of the metals, whereby lower or higher values than for clean surfaces might occur.

Photoelectrons are quickly captured by oxygen in air at atmospheric pressure. For the ionization mechanism in the negative mode, depending on the electron affinity and gas-phase acidity of the analyte, two major pathways leading from the electron capture of oxygen to analyte ions were found. In atmospheric pressure ion sources water is always present in the upper ppmV to low percentage range. Clusters of the type $[\text{O}_2(\text{H}_2\text{O})_n]^-$ form, where n depends on the water mixing ratio. With increasing cluster size the gas-phase basicity decreases and the electron affinity increases. Thus, the water concentration inside the ion source is an important factor for the ionization efficiency.

The ion transmission properties of inlet capillaries were investigated in-depth, as ionization inside the capillary requires modifications of the capillary material. The transmission depends on the capillary materials and the composition of the ion containing bulk gas stream. While the presence of both ion polarities in the gas stream always leads to stable ion currents with time, gas streams containing ions with only one polarity can lead to charging effects if materials with different conductivities are used for the inlet capillary assembly.

Finally, several applications of the novel ionization method were examined:

- the hyphenation with gas-chromatographic separation prior to the ionization
- product analysis of photolysis studies in atmospheric chemistry
- the desorption of analytes from surfaces
- the determination of rate constants for reactions of neutral analyte with primary ions

In summary, with cAPECI a novel ionization method for analytes with high electron affinity (e.g., nitro-aromatics) or gas phase acidity (e.g., phenols) has been developed. Its high selectivity leads to good signal-to-noise ratios and thus to low detection limits. The method was successfully applied in various research areas.

Contents

1	Introduction	1
1.1	Ion Chemistry in Atmospheric Pressure Mass Spectrometry	1
1.1.1	Common Atmospheric Pressure Ion Sources	1
1.1.2	Collision Induced Dissociation	2
1.1.3	Ion-Molecule/Radical Reactions	3
1.1.4	Cluster Formation	4
1.2	Inlet Capillaries	5
1.3	Negative Ion Mass Spectrometry	8
1.3.1	Ionization Pathways	8
1.3.2	Ionization Methods	11
1.4	Photoelectric Effect	14
1.5	Ionization Methods based on the Photoelectric Effect	16
1.6	Proton Transfer Reaction Mass Spectrometry	18
1.7	Analytes accessible with Negative Ionization	18
2	Aim of this Work	21
3	Experimental	23
3.1	Chemicals	23
3.2	Computational Investigations	23
3.3	Ion Trap Mass Spectrometer	24
3.4	Ion Transmission Measurements	26
3.4.1	Setup	26
3.4.2	Capillaries	30
3.5	The Photoelectric Effect at Atmospheric Pressure	34
3.6	Reaction Mechanism in Negative Mode API-MS	36
3.6.1	Ionization Mechanism	36
3.6.2	Dinitrotoluenes	39
3.7	Ion Source Development	41
3.7.1	Sample Introduction	41
3.7.2	UV Lamp	42
3.7.3	Laminar Flow Ion Source	43
3.7.4	Silica Capillary	45
3.7.5	cAPECI Design 1	46

Contents

3.7.6	cAPECI Design 2	50
3.8	GC-cAPECI-MS Hyphenation	52
3.9	Atmospheric Chemistry Studies	54
3.10	Determination of Reaction Rate Constants	57
3.11	Desorption APECI	58
4	Ionization Mechanism in Negative Mode API-MS	59
4.1	Verification of Thermal Sampling	59
4.2	Reagent Ions	61
4.3	Formation of Molecular Anions	67
4.4	Formation of Deprotonated Anions	71
4.5	Dinitrotoluenes	77
4.6	Summary and Outlook	82
5	Ion Transmission Measurements	84
5.1	Ion Transmission of Different Materials	86
5.1.1	Intact Inlet Capillaries	86
5.1.2	Composite Capillaries	95
5.1.3	cAPECI Source Design 1	103
5.2	Dependence on Relative Humidity	112
5.3	Application of Voltages	113
5.4	Summary and Outlook	118
6	Ion Source Development	122
6.1	The Photoelectric Effect at Atmospheric Pressure	122
6.1.1	Tunable Laser System	124
6.1.2	Low Pressure Mercury Lamp	133
6.2	Light Source	134
6.2.1	Calculation of the Photolysis Rate	135
6.2.2	Lamp Stability	136
6.3	Laminar Flow Ion Source	139
6.3.1	Metal Coated Windows	141
6.4	Silica Capillary	142
6.4.1	Branched Capillary	145
6.5	cAPECI Design 1	146
6.6	cAPECI Design 2	150
6.7	Summary and Outlook	154
7	Applications	156
7.1	GC-cAPECI-MS Hyphenation	156
7.2	Atmospheric Chemistry	163
7.2.1	Comparison of cAPECI and PTR	164
7.2.2	Photo-Oxidation Study	164
7.3	Determination of Rate Constants	171

Contents

7.4	Description APECI	178
7.5	Summary and Outlook	181
8	Summary and Outlook	184
	Abbreviations	190
	List of Tables	191
	List of Figures	196
	References	197

1 Introduction

1.1 Ion Chemistry in Atmospheric Pressure Mass Spectrometry

In *atmospheric pressure ionization* (API) *mass spectrometry* (MS) ions can undergo several types of ion-transformation processes during their lifetime from generation inside the ion source until detection. These ion-transformation processes alter the ion distribution, so that the mass spectra do not necessarily reflect the analyte ion distribution in the ion source [1–3]. Possible ion-transformation processes are:

- fragmentation or declustering by *collision induced dissociation* (CID) [4–11]
- reactions with neutral radicals or molecules [3, 10, 12–16]
- recombination with oppositely charged ions [17–19]
- clustering with neutral molecules [20, 21]

Recombination of oppositely charged ions normally does not change the signal distribution in the mass spectrum, but leads to a decrease in sensitivity [17, 19]. When reagent and/or analyte ions cluster with polar bulk molecules as for example water, a concentration dependent cluster distribution is observed. CID processes further downstream of the mass spectrometer decluster the analyte ions [20], so that the initial cluster distribution cannot be deduced from the mass spectrum. These CID processes may also lead to fragmentation of the analyte ions and thus to smaller *mass-to-charge* (m/z) ratios than the precursor analyte ions. Reactions with neutral radicals or molecules mostly yield reaction products with higher m/z ratios. While chemical transformations by CID processes or recombination processes are often taken into account in mass spectra interpretation, ion-molecule/radical reactions are mostly ignored, which can lead to misinterpretation of mass spectra.

1.1.1 Common Atmospheric Pressure Ion Sources

Common ion sources for AP-MS are designed for liquid sample introduction [22]. They have large volumes in which the ionization takes place. Inside this volume electrical fields and fluid dynamical forces guide the ions towards the inlet of the low pressure part of the mass spectrometer. The fluid dynamical forces are not easily predictable for

1 Introduction

most ion sources because at least two heated gas streams are introduced orthogonally into the ion source [23]. If the analyte is introduced as a liquid sample it is delivered via a heated nebulizer. Inside the nebulizer a nitrogen flow is added, producing a spray of the liquid, which transfers the analyte to the gas phase. This procedure is slightly different if the widely used *electrospray ionization* (ESI) is used. However, details of ESI sources will not be dealt with in this work [14, 24, 25]. The other gas stream present in the ion source is a sheath gas of clean nitrogen, which envelops the inlet of the mass spectrometer. Ionic species are pulled to the entrance of the low pressure region of the mass spectrometer by electrical forces. The sheath gas stream ensures that only clean nitrogen and charged species enter the mass spectrometer, while all neutral impurities are flushed into the ion source drain. The combined volume flow of the nebulizer and sheath gas is higher than the inflow into the mass spectrometer. Due to the geometry of the ion source, complex gas flows form, resulting in a nearly isotropic neutral analyte distribution and long residence times of the neutral analyte within the ion source [23, 26, 27]. For gaseous samples, e.g., *gas chromatography* (GC) coupled to AP-MS [27–29] or direct sampling of air for applications in atmospheric chemistry [30–32], other designs are preferable, where the analyte gas stream is less diluted.

The transport of the ions from the inlet capillary (see section 1.2 for more details) or the sampling orifice of the mass spectrometer to the analyzer is controlled by ion optical devices, e.g., radio frequency driven multipoles and/or electrostatic lenses [22]. While ions are guided by electrical fields neutral gas is continuously pumped.

1.1.2 Collision Induced Dissociation

The transfer of ions from the atmospheric pressure region to the first vacuum stage ($p=1$ to 10 mbar) is accomplished via inlet capillaries or orifices with a hole with small *inner diameter* (ID) [22]. At background pressures of 1 mbar the mean free path of the ions in the first vacuum stage is approximately 1×10^{-4} m [33] and the collision frequency of each particle is around 4×10^6 s⁻¹ [33], which is still sufficient for chemical reactions to occur. However, the local pressure in the gas stream expanding from the capillary exit is higher. At around 1 mbar the particle density is low enough that applied electrical fields lead to high reduced field strengths (E/N , up to several hundred Townsend¹). Therefore, ions gain significant amounts of *kinetic energy* (E_{kin}) between two collisions. Ions can undergo collision induced dissociation processes when they collide with the bulk gas if they have gained sufficient energy exceeding the binding energy [4, 34]. Inside the ion source the reduced field strength seldom exceeds 10 Td (around 2500 V cm⁻¹ at AP), i.e., CID processes do not occur. In the second vacuum chamber, separated from the first vacuum stage by a skimmer or an aperture, the pressure is in the 1×10^{-2} mbar range [22]. In this pressure regime high reduced field strengths are achieved even with low voltages applied to the ion

¹ E/N : E =electrical field strength [V cm⁻¹], N =molecular number density [molecule m⁻³]; resulting in [V cm²]; 1×10^{-17} V cm² = 1 *Townsend* (Td).

1.1 Ion Chemistry in Atmospheric Pressure Mass Spectrometry

optical devices due to the low number density of molecules. The collision frequency of each particle is rather low with around $4 \times 10^4 \text{ s}^{-1}$ and the mean free path is increased to approximately 1 mm, but nonetheless CID processes and chemical reactions are possible [7]. During the transport of the ions to the high vacuum region of the analyzer the pressure decreases further and ion-transformation processes become essentially negligible. Most analyzers as for example *time-of-flight* (TOF) [35] or *Fourier transform ion cyclotron resonance* (FT-ICR) [36] instruments do not further alter the ion distribution. In contrast, in *quadrupole ion traps* (QIT) [37] it is virtually impossible to avoid significant amounts of CID processes occurring within the analyzer. In a QIT ions are stored in a quadrupolar field previous to their ejection on the detector [37]. The ions can only be trapped inside the quadrupolar field if they collide with a buffer gas, which is mostly helium, argon or nitrogen, to transfer their excess energy. To establish the quadrupolar field a *radio frequency* (RF) and a *direct current* (DC) electrical field are necessary, whereby the ions gain kinetic energy, potentially leading to extensive CID processes [38].

Although fragmentation of analyte ions due to collision induced dissociation is often an unwanted side effect, it can be an important tool for the structure determination of analyte ions [4–6] or the differentiation of molecular ions and clusters as shown by Kambara et al. [34].

1.1.3 Ion-Molecule/Radical Reactions

Most ionization methods do not ionize the analyte directly, instead ionization occurs by charge transfer or chemical reactions with reagent ions. The generation of reagent ions inside the ion source is initiated by different means, e.g., by corona discharges [14, 39] or by interaction of photons with molecules [14, 40–42]. During the generation of reagent ions most methods additionally produce large amounts of various other ions and neutral radicals [3, 43–45]. The residence times of the neutral analyte in common ion sources can be up to several seconds [23, 26, 27], a residence time of ions inside the ion source up to several hundred microseconds [46, 47] caused by the complex gas flow characteristics. During these long dwell times reactions between the neutral or ionized analyte and ions or neutral radicals may well occur. Gas phase ion-molecule/radical reactions are often collisionally controlled² and can be even faster than the calculated maximum rate constant, caused by polarizability effects [48–51]. Thus, within common ion sources thermodynamic equilibrium is reached before the ions arrive in the low pressure region of the mass spectrometer, leading to only a few signals of the thermodynamically most favored ions [3, 38, 52]. In the following the term "thermodynamically controlled" will be used to describe these reaction conditions. The thermodynamic equilibrium cannot be reached if the transfer times of the ions

²A collision controlled rate constant assumes that every collision of a particle leads to the specified chemical reaction. Thus, the collision controlled value for a bimolecular rate constant corresponds to the calculated collision frequency of a particle which is approximately $1 \times 10^9 \text{ s}^{-1}$ for standard conditions [33]

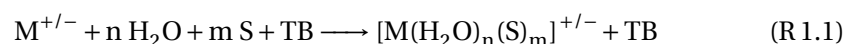
1 Introduction

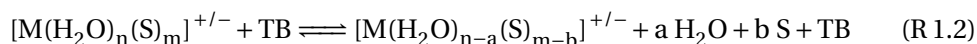
are less than a millisecond. Under such conditions the ion distribution reaching the analyzer of the mass spectrometer is "kinetically controlled" because the fastest rates of reaction within the ion-molecule/radical reaction scheme control which reaction products will be recorded in the mass spectrum [3, 38].

Even though ion-molecule/radical reactions cannot be suppressed, they are mostly neglected in the interpretation of mass spectra and additional signals are often attributed to "impurities". As early as 1983 oxygenated benzene was observed in a mass spectrum obtained with *atmospheric pressure chemical ionization* (APCI) [53]. The signals were ascribed to reactions initiated by OH radicals. In positive ion mode *atmospheric pressure photoionization* (APPI) Robb et al. [54] and Kauppila et al. [55] observed additional signals for the analyte, $[M+15/16/17]^+$, when toluene was used as a so called reagent gas dopant [54, 55]. Laser ionization with a 193 nm excimer laser resulted in the formation of the same signal distribution [3]. However, Kersten et al. [3] were able to identify the underlying ionization mechanisms, including reaction of neutral radicals.

1.1.4 Cluster Formation

In addition to chemical reactions where covalent bonds are broken and formed, clustering reactions of reagent or analyte ions with neutral molecules may occur. A main clustering agent is water, which is omnipresent in atmospheric pressure ion sources. Even with extensive experimental effort a water mixing ratio in the low ppmV range is rarely achievable inside the ion source, due to the water concentration present in most solvents and gas cylinders. Under normal conditions, where the ion source enclosure is exposed frequently to ambient air and nitrogen from a N_2 generator is used for nebulizer and sheath gas flow, the water mixing ratio is often in the low percentage range [56]. As a result of the polar character of the water molecule it clusters with both positive and negative ions. In addition to water most polar solvents used in *liquid chromatography* (LC) also cluster extensively with ionic species and are abundant with high mixing ratios in the ion source compared to the neutral and ionic analyte molecules. Song et al. [10] reported adducts with O^- , OH , O_2H^- , CN^- and CH_2CN^- when analyzing nitro compounds dissolved in acetonitrile with APCI. Ions that cluster with water and/or solvent molecules (S) show a cluster distribution, $[M(H_2O)_n(S)_m]^{+/-}$ with the numbers n and m depending on the water and solvent mixing ratios, in the mass spectra of thermally sampling mass spectrometers [7, 56–61]. In this context, thermally sampling means that the thermodynamically equilibrated cluster distribution, which is formed inside the ion source, is not significantly altered during the transport of the ions through the ion optics of the mass spectrometer. High reduced field strengths during the transfer of the clusters to the analyzer or in the analyzer itself cause CID processes, which decrease the cluster size [7, 8, 56, 62–64]. Cluster formation and declustering by CID processes is shown in the following reaction scheme.





where TB denotes a *third body* which takes the excess energy of the cluster reaction or delivers the necessary energy for declustering reactions. The cluster sizes can become so small that they fall below the m/z ratio range covered by common mass spectrometers. Even though cluster formation is extensively present, ionic-water/solvent clusters are normally not included in the ionization mechanisms of the common ionization methods. During the 1970s and '80s the important role of clusters in API or *chemical ionization* (CI) MS was common knowledge [52, 57]. In the *ion mobility spectrometry* (IMS) community [65–68] this is still the case. However, it is only recently that the impact of cluster systems on ionization mechanisms and the dependence of the ionization efficiency on the cluster sizes has been reconsidered and examined for AP-MS [7, 56].

On its passage from the ion source to the analyzer the ions have to traverse different ion optical devices and gas expansions. Most API mass spectrometers have at least two gas expansion required. The first occurs when the bulk gas stream exits the inlet capillary or the sampling orifice at the local speed of sound into the first vacuum stage. Another expansion forms between the first and the second vacuum stage when it is separated by a skimmer. Depending on the pressure difference and the distance to the next vacuum stage different types of expansions occur. When the pressure difference is high, adiabatic expansions or supersonic gas jets occur, which lead to cooling of the gas stream, by transforming internal degrees of freedom of the molecules into translational energy [69]. This cooling changes the cluster equilibrium, increasing the cluster size. If the gas stream has to pass through a region of higher gas density, e.g., a shock front (Mach disk) [62, 70], the collision frequency is greatly increased, the static temperature of the gas rises and thus the cluster distribution thermalizes again. Otherwise, a broad cluster distribution with cluster masses up to several thousand Dalton, is observed in the mass spectrum [56, 61, 62, 71, 72].

1.2 Inlet Capillaries

In many mass spectrometers ions traverse a glass or metal capillary to reach the first vacuum stage. The capillary is used to restrict the gas flow into the vacuum system and lead to a reduction of the pressure from atmospheric pressure at the entrance to some hundred millibars at its exit, while the background pressure in the first vacuum stage is around 1 to 10 mbar as stated previously. Common inner diameters of glass inlet capillaries used in Bruker Daltonik mass spectrometers are 0.5 or 0.6 mm. With a length of 18 cm gas flows of 0.8 to 1.5 Lmin⁻¹ are obtained. The gas flow through these capillaries can be described as a fully developed turbulent choked flow [73, 74], even though a laminar flow through the capillary is assumed in the literature. It is argued that only a laminar flow explains the good transfer efficiency for ions through capillaries [75–77], however, this appears to be incorrect (cf. chapter 5). A flow becomes choked if a critical pressure difference, depending on the inner diameter and

1 Introduction

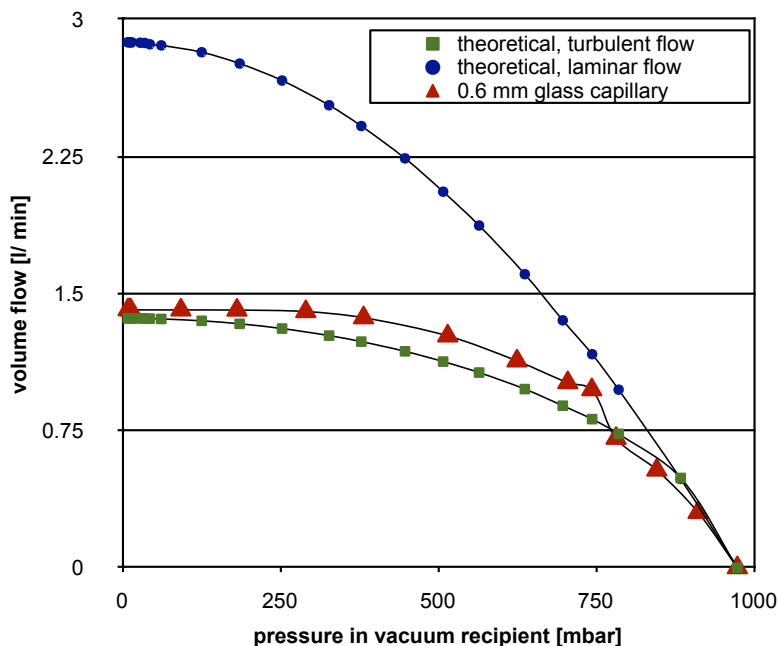


Figure 1.1: The measured flow dependence of a capillary with 0.6 mm ID on the pressure difference is compared with calculated values for ideal laminar and turbulent conditions. Figure taken from [73].

the length of the capillary, is reached. In this flow state, the mass flow through the capillary becomes independent of the downstream pressure. The equations to describe the fluid dynamic characteristics are found in e.g. [76, 78, 79]. In previous studies the flow through the capillary measured as a function of the pressure difference between inlet and outlet of the capillary was compared with calculated values for laminar and turbulent gas flows [73, 74] (see figure 1.1, equations for ideal laminar and turbulent flow were taken from [78, 80]). It is readily seen that the capillary flow existing in Bruker Daltonik mass spectrometers matches the curve calculated for a turbulent flow at room temperature.

The turbulent nature of the gas flow inside the capillary has been demonstrated by experiments [38, 81, 82]. For turbulent flows the static pressure³ and the velocity along the capillary channel have been calculated, as shown in figure 1.2 [78]. To measure the static pressure inside the capillary, holes were drilled into the channel. The measured values are in agreement with the theoretical values [38, 73]. Drilling holes into the capillary channel and forming edges inside the channel would lead to turbularization

³"To distinguish it from the total and dynamic pressures, the actual pressure of the fluid, which is associated not with its motion but with its state, is often referred to as the static pressure, [...]" [83]

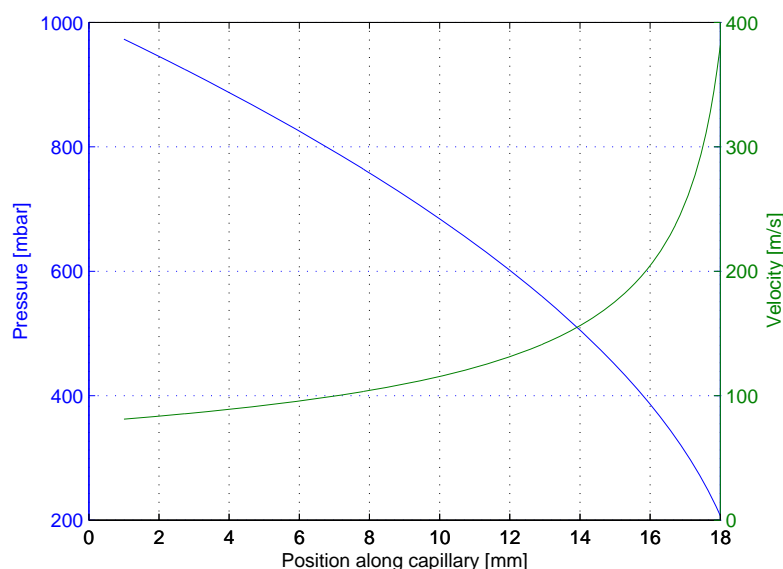


Figure 1.2: Calculated static pressure (blue, decreasing) and velocity (green, increasing) gradients along a capillary with 0.6 mm ID and 1000 mbar pressure difference for turbulent flow characteristics. Figure taken from [73].

of the gas flow if it was originally laminar. However, the mechanical modification of the capillary does not noticeably change the flow properties or ion transmission efficiency [38], which contradicts the assumption of a laminar flow. Measured ion transmission efficiencies were very high even though the flow is turbulent; the ion loss was smaller than one order of magnitude for gas streams containing ions of both polarities (denoted “bipolar ion gas stream” in the following) [73, 84]. Measurements of the transmission of unipolar ion gas streams have not been reported yet.

From data shown in figure 1.2 transfer times from a specific point inside the capillary to the capillary exit can be calculated. These values are in good agreement with measurements [38, 85]. Ions which are generated directly at the entrance of the capillary have transfer times of around 1.3 ms. Compared to transfer times from common large volume AP ion sources this is about two orders of magnitude lower [46, 47]. Replacing a common ion source with a *laminar flow ion source* (LFIS) [27, 38] results in transfer times of 5 ms. As stated in section 1.1.3, the occurrence of ion-molecule/radical reactions leading to a thermodynamically controlled product ion distribution is only suppressed if the reaction times of the ions are minimized. Shifting the ionization process into the inlet capillary is one method to obtain transfer times which are short enough to observe the kinetically controlled ion distribution in the mass spectrum [38].

As already mentioned, inlet capillaries are made of glass or metal, which does not

1 Introduction

allow the application of common ionization methods inside the capillary channel without further modifications. Modifications of the glass capillary by introducing other materials, e.g., ultra violet transparent windows or metallic sections, require that the capillary channel has to be interrupted. Even with extensive effort the introduction of edges is inevitable when mounting the capillary sections. Shifting the ionization process inside the inlet capillary is thus only possible when the gas flow through the capillary is already turbulent.

Several ionization methods have been realized as so-called "capillary" ionization techniques. They are denoted with the small letter "c" in front of the acronym, e.g., cAPPI for *capillary Atmospheric Pressure Photoionization* [74]. Other methods are laser ionization [85] or chemical ionization [29, 86]. An overview of the capillary ionization methods is given by Benter et al. [87]. For further investigations of the ion transmission of glass and modified glass capillaries see chapter 5.

1.3 Negative Ion Mass Spectrometry

Over the past decades negative ion mass spectrometry has received considerably less attention than positive ion MS. This is due to the much broader analyte range accessible with positive ionization. While most molecules are easily positively charged by removal of an electron, protonation or the attachment of positively charged ions, only a small number of molecules form stable negative ions. Thus, most ionization methods are optimized for positive ion generation. For the fast and mobile detection of explosives, ion mobility spectrometers are frequently used instead of mass spectrometers. However, the same ionization methods as for mass spectrometry are frequently used for IMS [88]. Because IMS is operated at atmospheric pressure in most cases, the fragmentation processes that may take place in the ion optics of API-MS cannot occur.

1.3.1 Ionization Pathways

Possible reaction channels leading to negative ions are: [89]

- electron capture (dissociative/non-dissociative)
- electron transfer
- proton abstraction
- attachment of negatively charged ions

For all of these negative ionization pathways thermal electrons⁴ are essential, which are then captured by the analyte or by reactant molecules, forming reagent ions. Practically all commonly used negative ionization methods produce thermal electrons as a

⁴"thermal" refers to a kinetic energy of the electron which is in the range of the kinetic energy of molecules at *room temperature* (RT), $E_{\text{kin}} = \frac{3}{2} \cdot k \cdot T$; $E_{\text{kin}}(\text{RT}) \approx 0.04 \text{ eV}$.

1.3 Negative Ion Mass Spectrometry

side product from positive ionization. For positive ionization an electron is removed from the molecule by supplying sufficient energy to overcome the ionization potential. These electrons possess thermal kinetic energy, which is necessary for efficient electron capture processes (see reaction R 1.3). Direct electron capture reactions can only occur if a molecule exhibits a positive *electron affinity* (EA).



$$\text{if } EA_M > 0$$

The electron affinity is defined as the electron binding energy of an electron in an anion ($A^- \rightarrow A + e^-$). For negative reaction enthalpies the anion is not thermodynamically stable, giving negative electron affinities. Only molecules with a positive electron affinity form stable negative ions via electron capture or electron transfer reactions [90].

For many molecules thermal electron capture is a non-dissociative reaction [91–95]. Exceptions are e.g., chloro- and bromobenzenes [96, 97] or ozone [98, 99], which show extensive dissociations when capturing thermal electrons (see reaction R 1.4).



Each molecule has a characteristic electron capture cross sections that depends on the kinetic energy of the electrons and on the electronic states of the molecule [97]. Molecules which undergo non-dissociative electron capture under certain conditions, also exhibit cross sections for dissociative electron capture reactions at higher kinetic energies of the electrons [97, 100].

The mixing ratio of free thermal electrons is normally relatively low compared to bulk gas and analyte molecules. From the bulk gases which are present in AP ion sources only some exhibit positive electron affinities such as molecular oxygen and some oxygen containing molecules and radicals, e.g., ozone, OH radicals, carbon dioxide and NO [101]. From all of these molecules oxygen has the highest mixing ratio in most cases. It has an electron affinity of 0.45 eV [101] and a collisionally limited termolecular electron capture reaction rate constant of $2 \times 10^{-30} \text{ cm}^6 \text{ molecule}^{-2} \text{ s}^{-1}$ [102] with oxygen as third body. It follows that in air (i.e., around 20%V oxygen) thermal electrons are quantitatively captured by oxygen after less than a hundred nanoseconds. Therefore, at atmospheric pressure the direct electron capture reaction of analytes can only be observed under very clean, oxygen-free conditions. Nevertheless, superoxide, O_2^- , is a widely used reactant ion for electron transfer or proton abstraction reactions [103–105]. The comparably low electron affinity which is exceeded by many other molecules makes electron transfer processes possible.



$$\text{if } EA_M > EA_{O_2}$$

1 Introduction

For electron transfer reactions dissociation of the analyte can occur as well, especially for halide containing analytes; see reaction R 1.6 for fluoride containing species [89] and R 1.7 for chloro- or bromo-containing analytes. Hydrogen or nitro-groups can be dissociated in some cases [106–109].

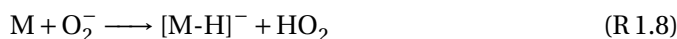


mainly for X=F



mainly for X=Cl,Br

The high *gas-phase basicity* (ΔG_{acid}) of 15.03 eV [101] makes superoxide a suitable reactant ion for proton abstraction reactions even with molecules with moderately acidic protons.

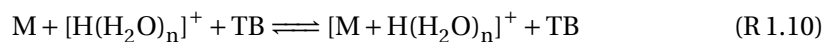


if $\Delta G_{\text{acid}}(M) > \Delta G_{\text{acid}}(HO_2)$

Anion attachment is used to form negative ions from polar compounds. As reactant ions mostly halide ions are used, produced by dissociative electron capture of reactant molecules, e.g., chlorobenzene, trichloromethane or bromomethane, as shown in reaction R 1.6 [110, 111].



However, the reaction mechanism leading from the reagent ions to analyte ions is not yet clear in the case of negative ionization. In contrast, the mechanism leading to protonated positive analyte ions starting from the toluene radical cation formed by photoionization has been recently resolved [56]. It includes proton bound water clusters formed by proton transfer to neutral water. Mixed solvent water clusters as described in section 1.1.3 in reaction R 1.2 can also be formed. These water/solvent clusters react with the analyte by a so-called "ligand-association/ligand-switching" mechanism (cf. R 1.10 and R 1.11 for pure water clusters) [112–115].



In thermally sampling MS it is possible to detect the resulting analyte-water/solvent cluster distributions, while the fragmentation processes in common mass spectrometers lead solely to $[M+H]^+$ ions of the analyte. It has also been shown that this mechanism is not only applicable to *dopant assisted atmospheric pressure photoionization* (DA-APPI) but to all methods which form proton bound water/solvent clusters

during the ionization cascade, e.g., ionization induced by radioactive decay of ^{63}Ni or corona discharge ionization [56].

McEwen et al. [116] stated that the ionization pathway is basically the same for APPI and *direct analysis in real time* (DART) in the negative mode at atmospheric pressure. Even though it is accepted that the ionization mechanism is independent of the way of generating thermal electrons, the ion-molecule/radical reaction cascade leading to analyte ions is not entirely known. In the literature the formation of superoxide in air via direct electron capture by oxygen is accepted as the first step [89, 116, 117] and the formation of superoxide water clusters, $[\text{O}_2(\text{H}_2\text{O})_n]^-$, is frequently observed. However, when discussing the reaction pathways leading to analyte ions, it appears as if clusters are not taken into account [103, 105, 116, 118, 119]. Most proposed ionization mechanisms proceed via the formation of $[\text{M}+\text{O}_2]^-$ adducts, which may be formed by neutral analyte molecules and superoxide or analyte anions and neutral oxygen. These clusters can dissociate to M^- or $[\text{M}-\text{H}]^-$ ions. Other reagent ions have been proposed, e.g., O_4^- , CO_3^- , CO_4^- , NO_2^- or $[\text{NO}_2(\text{H}_2\text{O})]^-$ [89, 119, 120], but these are generally not included in the ionization pathways.

Reactant molecules that are added to the sample or introduced into the ion source in relatively high mixing ratios to increase the ionization efficiency are often called dopants, as for example in dopant assisted atmospheric pressure photoionization [41, 42]. They directly interact with the primary source of ionization, e.g., highly energetic photons or electrons. These dopants increase the number of charge carrying species, which ionize the analyte by chemical reactions, thus increasing the ionization efficiency. Through the use of a dopant the ionization pathway after initial ion generation is changed to chemical ionization resulting in identical ionization mechanisms for a number of methods [56]. The disadvantage of a dopant is the increase of the density of reactive species inside the ion source, which may potentially lead to ion-transformation processes. Additional signals in the mass spectra arising from the dopant ion and its ion-molecule/radical reaction products are possible. When oxygen is present during negative ionization at elevated mixing ratios it potentially acts as a dopant.

1.3.2 Ionization Methods

A number of alternative ionization methods may be used for the generation of negative ions in AP-MS. In the following the most relevant methods, photoionization and chemical ionization at atmospheric pressure, are briefly introduced.

1.3.2.1 Atmospheric Pressure Photoionization

One method of thermal electron generation is the absorption of photons by molecules as in atmospheric pressure photoionization, a widely used method for LC-MS [121–125]. To overcome the ionization potential of most organic species by the absorption of a single photon energies above 7 eV are necessary [101], corresponding to wave-

1 Introduction

lengths (λ) below 180 nm. In most cases krypton-RF lamps are used to provide light in the *vacuum ultra violet* (VUV) range, with the main emission lines at 116.5 nm and 123.6 nm corresponding to 10.03 eV and 10.64 eV, respectively. This energy is sufficient for direct ionization of most organic molecules. Some bulk gases present in the ion source, such as oxygen and many solvents used for LC, e.g., acetonitrile or hexane, exhibit high absorption cross sections of around $1 \times 10^{-17} \text{ cm}^2 \text{ molecule}^{-1}$ at these wavelengths [126–132]. The absorption of photons by those substances does not lead to ionization since their ionization potentials are well above 10 eV. However, in many cases very efficient photolysis occurs and thus extensive formation of neutral radicals, increasing the probability that ion-transformation processes occur [3, 133]. The strong absorption of VUV light results in a penetration depth within the AP ion source of just some millimeters, which decreases the ionization efficiency. Dopants like toluene or anisole are prior added to the bulk gas flow to increase the ionization efficiency by several orders of magnitude by increasing the number of charge carrying species [41, 42, 54, 123]. As stated previously, the use of dopants changes the ionization mechanism in the positive ion mode from direct photoionization to chemical ionization. This effect is observed in the positive ion mode mass spectrum where the radical cation, M^+ , is the most abundant signal for most analytes with direct photoionization, and the protonated analyte molecules, $[M+H]^+$, with DA-APPI [134].

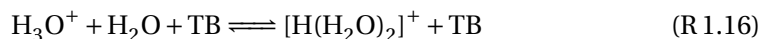
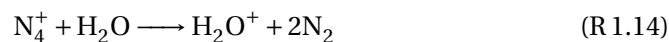
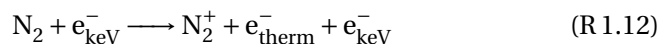
For the negative ion mode both ionization pathways, direct ionization or chemical ionization via a dopant, are feasible [89, 106]. To increase the number of thermal electrons toluene or anisole are typically used as dopants [133, 135]. Other substances such as chlorobenzene [133], CS_2 [136] or tetrahydrofuran [137] are used as dopants in the negative mode as well. For direct ionization thermal electrons are captured by the analyte. If the thermal electrons are mainly captured by oxygen or other reactant gases present in the sample stream negative DA-APPI is performed. Strictly speaking, the term negative DA-APPI means the use of one or two dopants. For thermal electron generation a dopant species is used to increase the yield of thermal electrons and/or another dopant is used to scavenge the electrons (e.g., molecular oxygen), resulting in reactant ions that ionize the analytes by the mechanisms discussed previously. One has to carefully ascertain which kind of "negative DA-APPI" is meant when different results are compared. If oxygen is used as an electron scavenger it initiates a similar ionization cascade in different negative ionization methods, which is explained in more detail in chapter 4. The generation of the oxygen-water cluster system by photoionization is accompanied by extensive formation of ions and neutral radicals inside the ion source. As mentioned previously, this potentially leads to ion-molecule/radical reactions and recombination reactions (cf. section 1.1).

1.3.2.2 Atmospheric Pressure Chemical Ionization

The term atmospheric pressure chemical ionization does not specify how the primary charges are produced. In the literature APCI often refers to ionization induced by a corona discharge. However, for all types of chemical ionization at atmospheric

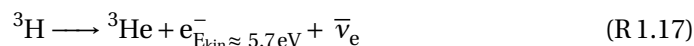
pressure (i.e., DA-APPI) in the positive ion mode, the ionization mechanism is basically the same [56], except for the primary charge generation and the types and amounts of neutral radicals and other primary ions generated as well.

Corona Discharge Ionization Corona discharge ionization is the most popular APCI method. The primary charges are produced in a point to plate discharge, leading to a plasma at the needle tip [14, 39]. The discharge induces not only primary ion generation but also leads to the generation of a considerable amount of neutral radicals. Positive ionization takes place by a reaction cascade beginning with nitrogen which is ionized by electrons with high kinetic energies produced in the plasma. Reactions of N_2^+ , via formation of N_4^+ and H_2O^+ , lead to a proton bound water cluster distribution as shown in Reactions R 1.12 to R 1.16.



The proton bound water clusters react with analytes in a “ligand-association/ligand-switching” mechanism as described in section 1.3.2.1 in reactions R 1.10 and R 1.11 [56]. Thermal electrons are produced in the discharge plasma and are captured by the analyte or by dopants like O_2 . Fragmentation, recombination and ion-molecule/radical reactions are likely to occur when the analyte enters the ionization region, due to the high density of primary ions and neutral radicals in the plasma.

Ionization induced by Radioactive Decay The production of primary ions by radioactive β decay is the most frequently used method in IMS [138–140]. Different radioactive isotopes are used, e.g., ^{63}Ni or tritium (^3H). During the decay of a β emitter a neutron decays to a proton, an electron and an antineutrino ($\bar{\nu}_e$)⁵, as described in reaction R 1.17 for tritium [141]. The free electrons exhibit kinetic energies in the keV range. Interaction of these electrons with molecules leads to excitation and fragmentation of the molecule or to ionization by the emission of a thermal electron (see reaction R 1.12). The interaction with molecules retards the electrons, but they continue to ionize or excite molecules until their kinetic energy is such that they are captured by molecules or until they reach the chamber wall.



⁵Antineutrinos are the antiparticles of neutrinos. Neutrinos are electrically neutral elementary particles that are only affected by the weak electromagnetic force, which means that they pass through normal matter almost without interaction. They belong to the leptons as e.g., quarks, photons or electrons [141].

1 Introduction

The fast electrons initiate the same reaction cascade as described for APCI in reactions R 1.12 to R 1.16 [56]. The excitation and fragmentation of molecules by the electrons emitted during the radioactive decay results again in the formation of a large number of neutral radicals in the ionization volume.

1.4 Photoelectric Effect

Generation of thermal electrons based on the photoelectric effect is a way to produce negative primary charges without producing positively charged species, thus preventing recombination reactions. The photoelectric effect was first described by Heinrich Hertz in 1887 [142], it was further investigated by Lenard and others [143, 144] until 1905 Einstein was able to explain the theoretical background of this effect [145]. He was awarded with the Nobel Prize in 1922 for his theory of light as quantized photons, marking the beginning of quantum physics [146].

The external photoelectric effect is the interaction of light with matter, where the energy of a photon is sufficient to overcome the work function (Φ) of the material so that an electron is emitted. On the contrary, the internal photoelectric effect describes the excitation of electrons to the conduction band of a material. In the following only the external photoelectric effect is considered. Photoelectric emission of an electron can be simply explained by a three step mechanism:

1. absorption of a photon, followed by excitation of an electron to an unoccupied state
2. transport of the electron to the surface of the bulk material
3. exeedance of the surface potential barrier and escape of the electron from the bulk metal

The kinetic energy of the emitted electron depends on the energy difference between the photon and the work function of the material [145, 147].

$$E_{\text{electron}} = \frac{R}{N_A} \cdot \beta \nu - \Phi \quad (1.1)$$

with: E_{electron} = kinetic energy of the emitted electron
 R = gas constant
 N_A = Avogadros constant
 β = constant (4.866×10^{-11})
 ν = frequency of light
 Φ = work function of the material

whereby $\frac{R}{N_A} \cdot \beta$ is equivalent to the Planck constant, h [148]. The kinetic energy of the emitted electron is only in the thermal range if the photon energy is near the work

function threshold. In vacuum, electrical fields are often applied to the photoemissive material to attract the electrons because back diffusion to the cathode would diminish the electron current [149]. These fields accelerate the electrons so that their kinetic energy exceeds the thermal energy range and can even become sufficient for *electron ionization* (EI) [150]. As mentioned previously, at atmospheric pressure electrons with higher kinetic energies can be captured by molecules via dissociative electron capture reactions or can lose their kinetic energy by collisions with bulk gases until they are scavenged by molecules with positive electron affinity.

The work function is material specific and dependent on the surface conditions, e.g., on the crystal face of a metal [101, 151] or the grade of oxidation/adsorption [152–156]. For metals work functions are in the range of 2.2 to 5.9 eV [101]. Alkali metals exhibit very low work functions of 2.2 to 2.8 eV, while metals as aluminum (4.20 eV), gold (5.47 eV) or platinum (5.9 eV, highest work function of all metals), that are stable at atmospheric conditions, exhibit significantly higher work functions [101]. To overcome these work functions light in the visible to VUV range is necessary. Metals as samarium (2.7 eV [101]) and materials such as lanthanhexaboride (LaB_6 , 2.16 eV [157]) are also used as photoemissive cathodes at low pressures [158, 159]. When oxygen is present, these materials cannot be used because the oxidation of the surface and reaction with water leads to changes of the work function or for alkali metals to the destruction of the photoelectrode [152, 155, 156, 160]. At atmospheric pressure only metals with high work functions are suitable photoemissive materials making the use of VUV light unavoidable. However, even for these metals the work function changes with time when its surface is exposed to oxygen or water. For aluminum the decrease in the work function from the literature value was up to 1 eV when only small amounts of oxygen were present at reduced total pressures [155]. In contrast, molybdenum showed a maximum increase in the work function of 1.8 eV in the presence of oxygen also at reduced total pressure [156]. Adsorption of organic molecules also alters the work function. Frankevitch et al. [161] showed that organic layers on metal surfaces decrease the work function of the metal by changing the electronic structure at the metal/organic layer interface.

There are only a few work function measurements at atmospheric pressure found in the literature [162–164]. Inumaru et al. [162] have investigated the influence of different organic solvents on the work function of gold at ambient air. While acetone increased the work function by 0.25 eV, other solvents, e.g., cyclohexene or ethanol, decreased the work function by less than -0.1 eV.

From equation 1.1 it follows that with increasing photon energy the kinetic energy of the emitted electron increases, but the amount of electrons emitted by the material will not be affected. To increase the electron yield the intensity of the light has to be increased. However, it is not entirely true that the electron current is independent of the photon energy. With shorter wavelengths the quantum yield increases due to the increasing difference between the photon energy and the work function of the material [165–167]. Quantum yields for the photoelectric effect generating nearly thermal electrons are in the range of 1×10^{-3} to 1×10^{-5} and increase by one or two

1 Introduction

orders of magnitude when the wavelength of the photons is further decreased into the VUV range [165, 166].

As light sources various lamps or lasers operating in the near UV up to far VUV are used. Due to the higher photon fluxes laser light can also cause electron generation via two or multi photon photo effects [168–172]. The interaction of two photons with an atom to overcome the work function or the ionization potential of the material was postulated in 1929 by Göppert-Mayer [173]. However, due to the lack of intense photon sources it was only in the 1960s, with the invention of the laser, that this postulate was experimentally verified.

The work function can not only be overcome by photons but also by thermal energy, this approach is called thermionic emission. It is not only used for the generation of large quantities of electrons but also for the determination of work functions [174, 175]. The most common application of thermionic emission is the use of hot metal filaments ($T > 1000$ K) in the vacuum to produce free electrons [174].

Applications of the photoelectric effect are photomultiplier tubes, which make low photocurrents measurable by converting a photon to a large amount of electrons and photoemission spectroscopy, which is used to gain information on electronic states of solid materials [175, 176]. A more detailed description of the photoelectric effect and its applications is beyond the scope of this work. It can be found in solid state physics and quantum physics text books and in the literature, for example, in [147, 175, 177, 178].

1.5 Ionization Methods based on the Photoelectric Effect

Several ionization methods based on the photoelectric effect are found in the literature. They are used to circumvent the presence of positively charged ions in the ion source enclosure and to minimize radical formation. They can be divided in two groups; i) those which work under vacuum conditions and ii) those which are operated at atmospheric pressure. Generating electrons by the photoelectric effect is easier under vacuum conditions, as stated previously, due to the stability of the photoemissive electrode and the optical path of the UV light. When photoelectrons are generated at low pressure the electrons are directly captured by analytes or they are used for positive ionization, which means that they are accelerated to high kinetic energies that allow EI [179–182, 182, 183]. Apart from ion sources for mass spectrometry or ion mobility spectrometry, photoelectron generation has also been described as an electron source for GC *electron capture detectors* (ECD) by Simmonds et al. [149]. Here, the electrons were generated using thin gold films that were directly deposited on a low pressure mercury UV lamp.

Most methods operating at low pressure use laser light for photoelectron generation. The laser light is directed through the analyte gas stream, to induce direct photoionization on a metallic surface or wire, where the photoelectrons are produced. These are accelerated by a counter electrode to kinetic energies typically used in EI (70 eV). An advantage of this procedure is the possibility to switch between a broadening of the ac-

1.5 Ionization Methods based on the Photoelectric Effect

cessible analyte range compared to laser ionization and an increase in selectivity by the introduction of single-/multi photon ionization by lasers and lamps [179, 180, 184, 185]. Furthermore, EI with laser generated photoelectrons enables the synchronization of pulsed analyzers such as TOF instruments with the ionization process by providing pulsed electron beams [179, 180]. Due to the higher electron current during the pulses increased sensitivities are obtained [180, 181, 184].

Low pressure electron capture ionization sources have been developed by the research groups of Boesl [183] for use in supersonic beams and Petrucci [182, 186] for the mass spectrometric analysis of organic compounds. The process of photoelectron generation is the same as for photoelectron induced EI mentioned before. The tunable kinetic energy of the electrons by tunable acceleration voltages enables efficient resonance electron capture processes. Increasing the electron energy initiates dissociative electron capture, giving further structural information on the compound. With this method several analytes ranging from sulfur hexafluoride [182] over fatty acids [186] to particle face organic compounds [182] were sensitively measured.

Ionization methods based on the photoelectric effect have been designed for atmospheric pressure applications as well. The first methods reported in the literature were designed for ion mobility spectrometry [19, 187–190], it is only recently that ion sources for coupling with AP-MS have been developed [119, 191]. Atmospheric pressure ion sources for IMS were built to replace the common ^{63}Ni APCI sources. Besides the advantage of getting rid of the safety precautions associated with the radioactive source, producing pulsed electron beams with lasers or pulsed lamps circumvent the use of a shutter grid at the entrance to the drift tube of the IMS [19, 188]. The first reported photoemissive ion source for IMS by Begley et al. [19] used a gold coated silica window, that is illuminated by a pulsed xenon UV lamp on the rear uncoated surface. This prevents the UV light from entering the drift region, which would lead to photolysis reactions and thus neutral radical production or cause a depletion of the neutral analyte concentration. Later UV lasers were used to generate photoelectrons, which increased the sensitivity of the instruments, but still relied on the presence of thin gold films with a thickness of around 20 to 100 nm on silica windows [187]. The laser light is directed on the window at an angle that causes total reflection, so that no light enters the ion source.

The ion source introduced by Chen et al. [191] uses VUV light of a common APPI lamp, which is also applied for direct photoionization. The light is directed onto a metallic grid, where photoelectrons are generated. Due to extensive ozone formation negatively charged ozone water clusters, $[\text{O}_3(\text{H}_2\text{O})_n]^-$, are the main reactant ions. For several explosives low limits of detection were reached with this approach [191].

Photoemissive ion sources for AP-MS are rarely described in the literature. Short et al. [119] introduced a photoemissive ion source using a UV *light emitting diode* (LED) ($\lambda = 280$ or 240 nm) as photon source in combination with several different metals in front of the orifice of a common AP mass spectrometer. Different ions were identified as reagent ions, e.g., superoxide, CO_3^- or NO_2^- , mostly as anion-water clusters. Due to the small difference between the photon energy and the work func-

1 Introduction

tions of most metals resulting in small quantum yields as well as to the relatively low photon fluxes of the UV LED this method lacks sensitivity. Furthermore, most analyzed molecules suffered from fragmentation or ion-transformation processes, so that additional signals were observed in the mass spectra, e.g., $[M-H+90]^-$ for 1,3,5-trinitro-1,3,5-triazacyclohexane (RDX, *royal demolition explosive*) [119].

The generation of photoelectrons may also be a cause for reduced sensitivities of positive ionization methods. They are inadvertently generated when VUV light falls on metallic parts of the ion source housing or when photons are produced in the plasma of corona discharges for APCI. This is further illustrated for *matrix assisted laser desorption/ionization* (MALDI), which shows an increase in sensitivity of two orders of magnitude when non-metallic targets were used [161].

1.6 Proton Transfer Reaction Mass Spectrometry

Even though some analytes are more easily accessible in negative ion mass spectrometry several positive chemical ionization methods are used for their detection as well. For example *proton transfer reaction* (PTR) mass spectrometry is widely used for applications in atmospheric chemistry [30, 31, 192, 193] and for the detection of explosives [32, 194]. Primary ions are generated in a hollow cathode discharge in the presence of a defined water mixing ratio, leading to proton bound water clusters. Water clusters are guided into a drift tube where the analyte gas stream is added. A pressure of approximately 3 mbar is maintained inside the drift tube. At this pressure DC voltages of some hundred volts across the entire drift tube are sufficient to reach reduced field strengths of some hundred Townsend. These high reduced field strengths lead to fragmentation of the water clusters to yield mainly H_3O^+ . Its acidity is sufficiently high so that proton transfer reactions with most organic molecules occur, which is not the case for larger proton bound water clusters [195]. The high reduced field strengths may lead to fragmentation of the protonated analyte ions as well, as these are also accelerated by the electrical field. With PTR limits of detection in the low pptV range have been achieved for many compounds, e.g., acetone, benzene and isoprene [31]. In summary, most analytes that are studied in atmospheric chemistry are ionizable with PTR-MS, but the fragmentation of analyte ions, due to the high reduced field strengths inside the drift tube, and the non-selective nature of the method can lead to complex mass spectra.

1.7 Analytes accessible with Negative Ionization

Analytes that are accessible with negative ion mass spectrometry or ion mobility spectrometry must exhibit positive electron affinities or relatively high gas-phase acidities. Aromatic compounds with high positive electron affinities are benzenes with electron accepting groups, e.g., halides, cyanide- or nitro-groups. Benzene itself exhibits a negative electron affinity of approximately -1.15 eV [101]. *Polycyclic aromatic hydro-*

1.7 Analytes accessible with Negative Ionization

carbons (PAH) have positive electron affinities, however, this compound class is also favorably accessible with positive ion mass spectrometry. With resonant two photon laser ionization (*atmospheric pressure laser ionization*, APLI [126, 196]) very low *limits of detection* (LOD) are obtained. Thus, negative ionization of these compounds is rarely described in the literature [197–199]. However, if the PAHs possess nitro- or hydroxyl-groups (*oxygenated polycyclic aromatic hydrocarbons*, OPAH), removing an electron from the highest occupied molecular orbital generally results thus in fragmentation [200–203]. For these compounds negative ionization is advantageous as they form stable anions [200, 202, 204, 205]. Molecules with an acidic proton, e.g., aromatic phenols, are accessible to negative ion mass spectrometry via proton abstraction by primary ions, e.g., superoxide or OH^- (cf. section 1.3.1 reaction R 1.8).

A main application field for negative ionization is the detection of explosives [206–209]. Explosives contain large numbers of oxygen and/or nitrogen atoms, often as nitro-groups, resulting in positive electron affinities. A major drawback for mass spectrometric detection is that many explosives are thermally unstable or tend to readily undergo fragmentation reactions. Fragmentation most often occurs at the C-NO₂ bond if present in the molecule, leading to NO_2^- , NO_3^- or HN_2O_6^- as charge carrying species [210–213]. The observation of these signals in the mass spectrum is not specific for a particular explosive so that compounds cannot be differentiated. The same ions are observed when sampling takes place in ambient air, as NO₂ is always present in low mixing ratios (up to 50 ppbV [214]). Their presence in the mass spectrum is thus not a specific indicator that explosives are present. Furthermore, ionization methods that use electrical discharges or plasmas for ionization, e.g., APCI initiated by corona discharge, produce large quantities of NO_3^- and HN_2O_6^- during reagent ion formation, so that the presence of explosives does not lead to significant differences in the mass spectrum [38, 45, 215]. The use of fragment ions for the detection of explosives is not reliable, especially not for the high security standards required at airports or other points of public interest, e.g., governmental buildings. Since most explosives have low vapor pressures low limits of detection are necessary for negative ionization methods.

Environmental chemistry is another important application field for negative ionization. For example aromatic phenols are intermediates in the atmospheric degradation of aromatic compounds [216, 217]. The analysis of these species gives valuable insights into the chemical mechanisms that are fundamental for the understanding of the degradation processes of the atmosphere. Chlorinated compounds are ubiquitous pollutants in water and air [214, 217]. The detection of nitro-aromatic compounds is the most important application of negative ionization mass spectrometry in environmental chemistry because of their phytotoxic and mutagenic properties. Furthermore, they are assumed to cause damage to plants and trees [218–220]. Nitro-aromatic compounds are directly emitted by combustion processes and by the production of goods, e.g., explosives, dyes or drugs [221]. Apart from direct emission nitro compounds are formed *in situ* in the atmosphere by the degradation of organic hydrocarbons [213, 216, 217]. During the day this degradation is initiated by OH and in

1 Introduction

the night by NO_3 radicals, respectively [210–213]. Nitro-aromatic compounds are found in clouds, soil, rain and snow [222–224]. Their atmospheric concentration is in the ngm^{-3} range [221, 225]. The importance of ortho-nitrophenols as source for nitrous acid (HONO) as precursor for OH radicals is currently discussed [226, 227]. To reveal the mechanism leading to the formation of HONO sensitive ionization methods for negative ionization are necessary that do not alter the structure of the ions by ion transformation reactions.

2 Aim of this Work

As pointed out in chapter 1 most ionization methods for the generation of negative ions have several disadvantages, such as a lack of selectivity or presence of extensive ion-transformation processes. Due to the long reaction times in common atmospheric pressure ion sources the analyzed product distribution is thermodynamically controlled. This decreases the sensitivity towards the analytes and renders the detection of the ion distribution present in the ion source difficult. It follows from the literature that nearly all methods, e.g. DA-APPI, APCI and DART, both in the negative and positive ionization mode, initiate the same reaction cascade and differ only in the extent of neutral radical generation and formation of additional ions [56, 89]. Thus, even when developing a novel ionization method the same reaction products are expected. A shift in the signal distribution is only achievable by reducing the reaction time, since this leads to the kinetically controlled product distribution and by i) reducing the amount of neutral radicals and ii) the variety of primary ions.

The aim of this work is the development of a selective and sensitive ionization method for the negative ion mode. The use of the photoelectric effect for the generation of electrons is a simple and elegant procedure; it ensures that only negative ions are produced and that the number of neutral radicals is minimized. Compared with other methods this reduces the occurrence of ion-transformation processes. For the detection of kinetically controlled product distributions the transfer times of the ions from their generation inside the ion source to the low pressure part of the mass spectrometer needs to be less than 1 ms. Thus, the novel method operates inside the inlet capillary of a mass spectrometer and is accordingly termed *capillary atmospheric pressure electron capture ionization (cAPECI)*.

In the available large body of literature, nearly all investigations on the photoelectric effect have been carried out at low pressure. A first step towards a cAPECI ion source is the investigation of the photoelectric effect at atmospheric pressure. Molecular layers of, e.g., water, oxygen and/or other molecules, which are unavoidable at AP conditions, potentially lead to changes of the work function. To be able to optimize the ion source and understand the occurrence of ion transformation reactions the ionization mechanism is determined. Water is an omnipresent species in atmospheric pressure ion sources and participates in the ionization mechanism. Thus, the influence of the water concentration inside the ion source is also examined. The proposed reaction schemes are verified by theoretical ab initio calculations and kinetic simulations. Since the photoelectric effect cannot be operated in a standard glass capillary modifications of the capillary are unavoidable for cAPECI. The influence of these modifications,

2 Aim of this Work

e.g., the combination of different materials with different conductivities on the ion transmission properties is investigated. Using the photoelectric effect for ionization inevitably leads to unipolar ion streams. Thus, a fundamental knowledge about the parameters affecting the ion transmission by e.g. charging effects is necessary to build an ion source with stable signal intensities.

Finally, applications for the new ionization method are investigated to assess the advantages and disadvantages of the novel method. The hyphenation of mass spectrometry with gas chromatography is a common analytical approach for the analysis of complex samples. Thus, cAPECI-GC hyphenation is one goal of the experimental work for this thesis. For application in atmospheric chemistry a photolysis study is carried out, which additionally provides a comparison with PTR-MS, a widespread used method in this field. The detection of explosives is often done by desorption from wipe tests. Thus, an ambient cAPECI method is developed and characterized.

3 Experimental

3.1 Chemicals

All chemicals were purchased from Sigma Aldrich GmbH (Seelze, Germany) in the highest purity grade available if not otherwise stated and were used without further treatment. All solvents were from Fisher Scientific (Waltham, MA, USA) and had analytical or chromatographic purity. Synthetic air (80 % nitrogen, 20 % oxygen), nitrogen and argon were purchased from Gase.de (Sulzbach, Germany) with a stated purity of 99.999 %vol. Sulfur hexafluoride was purchased from Messer Industriegase GmbH (Bad Soden, Germany) with a purity of 99.90 %vol.

3.2 Computational Investigations

For *ab initio* calculations Gaussian 03W [228] and Gaussian 09 [229] were used in combination with the graphical user interface GaussView 4.1 [230]. Gaussian 03W was run on a personal computer, calculations with Gaussian 09 were performed on a UNIX based computer cluster, with 4 x 16-Core CPUs (6282SE AMD Opteron™, Advanced Micro Devices GmbH, Dornach, Germany) and 32 x 16 GB memory. The system was obtained from Delta Computer Products GmbH (Reinbek, Germany). Energy calculations of molecules were carried out with the Gaussian software, to obtain the Gibbs free energy and enthalpy corrected total energy of the optimized geometry of a neutral or ionic molecule. Possible reaction pathways were examined, using the energies of the ions and neutrals that are involved in the reaction to calculate the *Gibbs free energy of a reaction* ($\Delta_R G$). If a reaction has a positive Gibbs free energy additional energy is necessary for the reaction to take place, whereas negative Gibbs free energies indicate thermodynamically favored reactions. However, these reactions may be kinetically hindered. The calculations reported in this work were carried out using *density functional theory* (DFT) with the *Becke-3-Parameter-Lee-Yang-Parr* (B3LYP) functional and the 6-31++G(d,p) doubly-diffuse and doubly-polarized split-valence basis set. This functional in combination with the used basis set has been successfully applied for many other comparable reaction systems [3, 231, 232] and provides an optimum cost-to-benefit ratio with respect to CPU time [233].

The software package Chemked-I/II version 3.3 [234] was used for kinetic simulations. It was run on a personal computer. All reactions and rate constants used for

3 Experimental

the kinetic simulations in this work are listed in table 3.1. Rate constants for electron attachment reactions refer to electrons with thermal kinetic energy (cf. section 1.3).

For the kinetic simulation that determines which ions are possibly present inside the ion source the conditions present inside the cAPECI source design 1 were used (cf. section 3.7.5). Inside the ion source, in the ion generation region a pressure in the range of 900 to 500 mbar is established. Thus, the kinetic simulations were carried out at 900 mbar to obtain an upper limit. Synthetic air with a mixing ratio of 1 % water was assumed as the main gas stream. The high water mixing ratio is realistic as the ion source and the tubing system are frequently open and exposed to ambient air. Thus, the starting mixing ratios for the simulation to calculate the temporal evolution of ozone and OH radicals were 79 % nitrogen, 20 % oxygen, 1 % water and zero for ozone and hydroxyl radicals. The starting mixing ratio for photoelectrons was set to 100 pptV. Reactions R3.5 to R3.14 were taken into account in the simulation.

3.3 Ion Trap Mass Spectrometer

The instrument used for most mass spectrometric experiments was an esquire6000 quadrupol ion trap (Bruker Daltonik GmbH, Bremen, Germany). It is equipped with a glass inlet capillary as first gas flow restriction stage from atmospheric pressure to approximately 4 mbar. The section in which the inlet capillary is mounted is called the "Desolvation Stage", as droplets coming from an ESI source should be vaporized inside this stage. A skimmer is placed several centimeters behind the capillary exit to separate the first and the second vacuum region, which has a pressure of approximately 1×10^{-4} mbar. Here, two octopoles and ion lenses guide the ions to the analyzer region, in which a pressure of 1×10^{-6} mbar is maintained. The ions reach the quadrupol ion trap where they are stored and ejected mass selective into the detector, which consists of a conversion dynode and an electron multiplier [235]. The signal is digitized, processed and displayed by the Bruker Daltonik GmbH software "Esquire control service" version 6.1 [236]. Data processing of the raw data was performed with Data Analysis 3.4 from Bruker Daltonik GmbH [237]. As the ion trap mass spectrometer was used as an analytical instrument without further modifications, detailed information on the operating principle of the ion trap analyzer is not given here and can be found elsewhere [37, 235].

Voltages are applied to all ion optical devices. The capillary end cap has a higher voltage than the skimmer to focus the ions to the skimmer orifice. This can easily lead to a reduced field strength well above 100 Td in this region, probably inducing CID processes. A RF voltage is applied to the octopoles to guide the ions through the second vacuum stage. The voltages needed for an efficient ion transfer through the octopoles are sufficiently high to induce CID processes. Depending on the RF voltage ions with a selected range of m/z ratios are transferred through the octopoles, while higher and lower m/z ratios are discriminated. However, even if these voltages are decreased to avoid CID processes inside the ion optics, CID free conditions cannot be

Table 3.1: Rate constants for neutral radical and electron capture reactions.

No.	Reaction	Rate constant ¹	Absorption cross section ²	Ref.
R 3.1	$O_2 + e^- + O_2 \longrightarrow O_2^- + O_2$	$2.3 \times 10^{-30} \text{ }^{+++}$		[102]
R 3.2	$O_2 + e^- + N_2 \longrightarrow O_2^- + N_2$	$9 \times 10^{-32} \text{ }^{+++}$		[102]
R 3.3	$OH + e^- + N_2 \longrightarrow OH^- + N_2$	$1 \times 10^{-29} \text{ }^{+++}$		estd. ³
R 3.4	$O_3 + e^- \longrightarrow O_2 + O^-$	$2 \times 10^{-10} \text{ }^{++}$		[98]
R 3.5	$O_2 + h\nu \longrightarrow 2 O(^3P)$	$1.8 \times 10^{-6} \text{ }^+$	$1.7 \times 10^{-20} / < 1 \times 10^{-24}$	[238]
R 3.6	$O_2 + O(^3P) + N_2 \longrightarrow O_3 + N_2$	$6.0 \times 10^{-34} \text{ }^{+++}$		[239]
R 3.7	$O_3 + h\nu \longrightarrow O(^1D) + O_2$	$6.8 \times 10^{-2} \text{ }^+$	$7 \times 10^{-19} / 1.1 \times 10^{-17}$	[238]
R 3.8	$O(^1D) + N_2 \longrightarrow O(^3P) + N_2$	$2.6 \times 10^{-11} \text{ }^{++}$		[239]
R 3.9	$O(^1D) + H_2O \longrightarrow 2 OH$	$2.2 \times 10^{-10} \text{ }^{++}$		[239]
R 3.10	$H_2O + h\nu \longrightarrow H + OH$	$1.2 \times 10^{-5} \text{ }^+$	$6.8 \times 10^{-20} / < 1 \times 10^{-24}$	[240]
R 3.11	$2 O(^3P) + N_2 \longrightarrow O_2 + N_2$	$1.0 \times 10^{-30} \text{ }^{+++}$		[239]
R 3.12	$O_3 + OH \longrightarrow HO_2 + O_2$	$6.7 \times 10^{-14} \text{ }^{++}$		[239]
R 3.13	$HO_2 + O_3 \longrightarrow 2 O_2 + OH$	$2.0 \times 10^{-15} \text{ }^{++}$		[239]
R 3.14	$O_2 + H + N_2 \longrightarrow HO_2 + N_2$	$1.4 \times 10^{-32} \text{ }^{+++}$		[239]

¹Rate constants are given in ⁺ [s^{-1}] (first order), ⁺⁺ [$cm^3 \text{ molecule}^{-1} s^{-1}$] (second order), ⁺⁺⁺ [$cm^6 \text{ molecule}^{-2} s^{-1}$] (third order), respectively; T = 298.15 K.

Photolysis rate constants are calculated, using photon fluxes of $6 \times 10^{15} \text{ photons cm}^{-2} s^{-1}$ ($\lambda = 254 \text{ nm}$) and $1.8 \times 10^{14} \text{ photons cm}^{-2} s^{-1}$ ($\lambda = 185 \text{ nm}$; 3% of the 254 nm photon flux).

²At 185 nm/254 nm; unit [$cm^2 \text{ molecule}^{-1}$]; taken from [241].

³No rate constant was found in the literature for the electron attachment to OH-radicals. The electron affinity of OH-radicals is much larger than that of oxygen (1.8 eV compared to 0.5 eV [101]), thus, a slightly higher reaction rate constant than for the electron attachment of oxygen was estimated.

3 Experimental

obtained with the QIT analyzer. In front of the analyzer an ion lens is used to focus the ions into the ion trap. The voltages applied to this lens are not crucial for CID processes as the pressure in this region is sufficiently low. To trap the ions inside the ion trap RF and DC fields are necessary, in combination with collisions with a buffer gas (approximately 1×10^{-6} mbar) to “cool” the ions. Without these collisions ions would not be trapped inside the analyzer. However, these collisions make CID processes always possible with this mass spectrometer, even with low trap voltages, i.e., low trapping efficiencies.

As mentioned in section 1.1.2, CID processes are used in ion trap mass spectrometers for structural identification. The ion trap used for most experiments during this work is capable of these so-called MS^n experiments, whereby n is the number of isolation and fragmentation steps. The selected ion is isolated inside the ion trap and the radio frequency that is in resonance with this mass is then increased. This leads to collisions with the buffer gas with higher kinetic energies, resulting in dissociation reactions. If it is required, a dissociation fragment is isolated, activated and then dissociated again.

With the mass spectrometer m/z ratios down to approximately 30 are accessible. However, discrimination of the lower mass-to-charge ratio range occurs, due to the storage characteristics of the ion trap analyzer [235]. Because of the low resolution, only nominal mass-to-charge ratios are obtained from the mass spectra. Ions are normally stored inside the ion trap for times between 0.01 ms and 1 s. With the normal scan speed of $8100 m/z s^{-1}$ [235], the cooling time between trapping and the start of the scan and the time in which remaining ions are cleared out of the trap, one measurement cycle, is in the range of 50 to 2000 ms.

3.4 Ion Transmission Measurements

3.4.1 Setup

Ion transmission measurements of inlet capillaries were performed with a custom built setup consisting of a vacuum recipient with ion current measurement facilities and an airtight ionization chamber. This setup has the advantage of simulating the inlet of a mass spectrometer without the influence of the ion optical devices and the discrimination against low mass-to-charge ratios downstream of the mass spectrometer. Figure 3.1 shows the setup of the ion transmission measurements for the ion current detection with two electrodes, figure 3.2 depicts an overview of the measurement setup, including data processing and gas introduction.

The ionization chamber was held at atmospheric pressure, volume flows of synthetic air were added via mass flow controllers with different ranges ($2 L min^{-1}$ and $1 mL min^{-1}$; El-Flow® select; Bronkhorst Mättig GmbH, Kamen, Germany). The generation of ions was carried out with two different ionization methods: APLI inside the ionization chamber and photoelectron production inside the cAPECI source (cf. section 3.7.5). For APLI a KrF* excimer laser (ATLEX300, ATL Lasertechnik, Wermelskirchen, Ger-

3.4 Ion Transmission Measurements

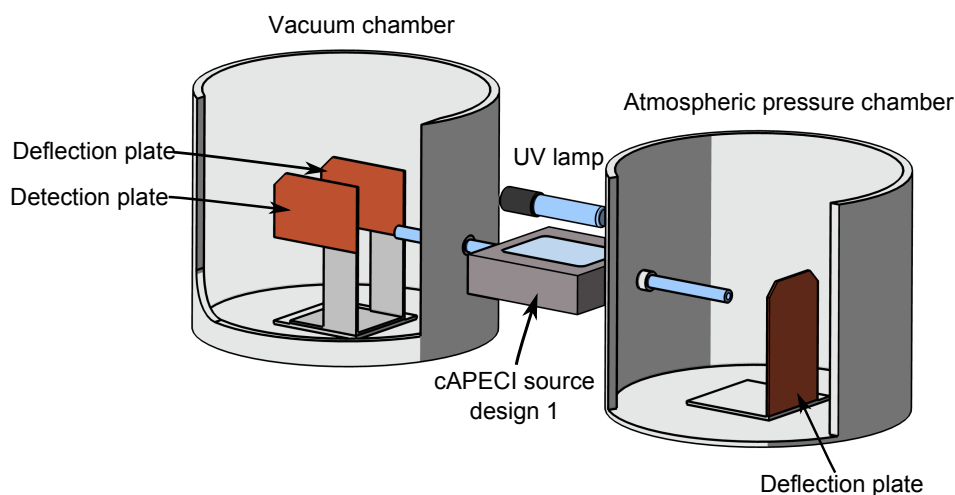


Figure 3.1: Schematic of the ion transmission measurement setup, consisting of a vacuum recipient, the inlet capillary with cAPECI ion source and an atmospheric pressure chamber.

many) with a wavelength of 248 nm and anisole as analyte was used. Typical laser pulse energies were around 2 mJ with repetition rates of 10 Hz, unless otherwise stated. The laser beam irradiated area was approximately 1×1 cm.

A constant mixing ratio of anisole was necessary to produce a constant density of ions during the ion current measurements. This was realized by flowing pure N_2 gas over liquid anisole at a fixed temperature and diluting this gas stream with the main gas flow, resulting in mixing ratios in the low ppmV range. The liquid anisole was held at 0°C by putting it into a dewar flask with a water-ice mixture, resulting in a vapor pressure of 1 mbar [101]. Most experiments were performed with a gas flow of 1 mL min^{-1} over anisole and a main gas flow of 1.4 L min^{-1} leading to a mixing ratio of 750 ppbV. To prevent pressure changes inside the ionization chamber if the mounted inlet capillary causes a lower gas flow than 1.4 L min^{-1} a 1 L min^{-1} flow controller (Mass-Flo-Controller; MKS Instruments, Andover, MA, USA) was used to monitor the required balance flow, as the difference between balance flow and adjusted gas flow is the volume flow through the capillary.

With APLI both ion polarities are produced. To investigate the transmission characteristics of unipolar ion currents the ions were separated by their polarity in the ionization volume. An electrode was mounted inside the ionization chamber opposite to the inlet of the capillary, which has a metalized end cap. A voltage of $\pm 80 \text{ V}$ was applied to the electrode to pull ions of the counter polarity to the electrode, ions of the same polarity were pushed towards the grounded capillary inlet, where they enter the

3 Experimental

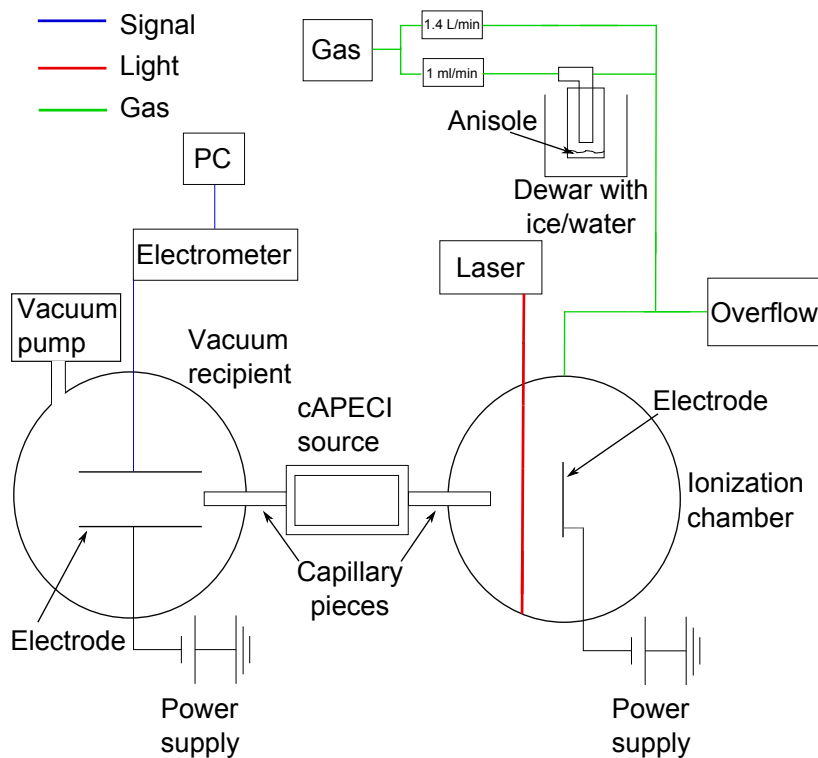


Figure 3.2: Scheme of the ion transmission measurement setup, including data processing and gas/sample introduction. Graphic reproduced after [81]

capillary by fluid dynamical forces. For some experiments, the laser beam was blanked out for different time periods. This was done by using a beam stop to hinder the laser beam from entering into the measurement chamber. The laser was not switched off during this time and all other parameters, e.g., the gas flows, were held constant.

The capillary connected the atmospheric pressure and the vacuum pressure chamber. The inlet capillary was easily exchanged to examine different material combinations (cf. section 3.4.2) or to mount the capillary photoelectron ion source (for detailed information on this ion source see section 6.5).

Ionization inside the capillary ion source was the second option for ion generation. Therefore, the inlet capillary was replaced by the cAPECI source. In this case the atmospheric pressure chamber was only used to introduce the gas flow. As window material served silica and LiF (both Korth Kristalle GmbH, Altenholz, Germany); silver was used as photoemissive material, which was also exchangeable. For most experiments anodized aluminum was used. The light source was a low pressure mercury lamp (Pen-Ray® lamp, LSP035, LOT-Oriel GmbH & Co. KG, Darmstadt, Germany), providing light with a wavelength of 185 nm for photoelectron generation (see section 3.7.2). The ion current generated with this ionization method is purely unipolar.

3.4 Ion Transmission Measurements

The vacuum recipient was equipped with a rotary vane pump ($80 \text{ m}^3 \text{ h}^{-1}$, Duo 060A, Pfeiffer Vacuum GmbH, Aslar, Germany) to establish a pressure of approximately 3 mbar inside the chamber. The pressure was monitored using a pressure transducer (Barocel 600A-1000T, Datametrics/Dresser, Wilmington, MA, USA) with a range of 1 to 1013 mbar. One or two electrodes were mounted inside the vacuum chamber to enable the measurement of the ion current by a sensitive electrometer (617 programmable electrometer or Keithley 6430 Sub-Femtoamp remote SourceMeter, both Keithley Instruments Inc., Cleveland, OH, USA). The output of the 617 programmable electrometer was digitized with a multimeter (VC820, Voltcraft, Conrad Electronic SE, Hirschau, Germany) and recorded on generic computer hardware with a custom data recording software. The output of the 6430 Sub-Femtoamp meter was directly recorded by generic computer hardware. In all measurements one data point per second was recorded.

Two different measurement assemblies were applied. The first utilizes a Faraday cup placed in front of the capillary outlet. A voltage of 100 V was applied to the metalized end cap of the capillary to accelerate the ions towards the Faraday cup. The use of a Faraday cup does not allow the entire separation of the ion polarities inside the gas stream, so that probably both ion polarities reach the Faraday cup, at least partly reducing the measured *total ion current* (TIC). This is not an issue if unipolar ion currents pass through the inlet capillary, as is the case for cAPECI and APLI when the ion polarities are separated inside the ionization chamber.

If bipolar ion streams pass through the capillary a different electrode assembly is more suitable. Two electrodes were placed parallel to the inlet capillary directly at the exit port of the capillary. On one electrode an adjustable deflection potential of ± 10 to 100 V was applied to direct one ion polarity towards the other electrode, while the oppositely charged ions were pulled to the deflection electrode where they are discharged. The other electrode is connected to the electrometer [26]. The deflection voltage was optimized before each measurement. This setup enables the detection of unipolar ion currents when bipolar ion streams pass through the capillary. It also allows verification that the ion current is purely unipolar.

To examine the influence of the water mixing ratio on the transmission characteristic, a capillary made of two glass segments was used. The setup was opened between the capillary segments for a certain time period in which the measurement chamber was constantly flushed with clean and dry air to hold the analyte mixing ratio constant. The inlet capillary piece that is connected with the detection chamber was flushed with air that is saturated with water. This was realized by directing synthetic air through a bubble counter filled with water. Before the measurement started, both capillary segments were connected again and the laser was switched on.

For all measurements shown here, normalized signals are shown. Different levels of noise are due to variable ranges with different sensitivities adjusted at the electrometer. The total intensities of the signals were not reproducible because the position of the laser beam varied considerably between two measurements.

3 Experimental



Figure 3.3: Different inlet capillaries (f.l.t.r.): Lead oxide coated lead silicate capillary; lead silicate capillary; completely nickel-plated borosilicate capillary; capillary with nickel-plated end caps; borosilicate glass capillary. Picture taken by David Müller [81].

3.4.2 Capillaries

With the setup described in the previous section ion transmission characteristics of different capillary types were examined. Standard glass capillaries made of borosilicate glass as used in Bruker Daltonik mass spectrometers have a length of 18 cm, with an outer diameter of 6.5 mm and an inner diameter of 0.5 mm or 0.6 mm. Due to the high cost of these capillaries (around 1000 Euro) and the need for capillaries of other lengths, home-built glass capillaries were made from bulk stock purchased from Hilgenberg GmbH (Malsfeld, Germany). These capillaries have identical inner and outer diameters as the Bruker capillaries, but can be made in any desired length. As the standard capillaries the home-built capillaries were electrochemically nickel plated at both ends (cf. section 3.5 for details of the nickel plating process), unless otherwise stated. The metallic end caps allow the application of acceleration voltages to the capillary inlet and outlet. Direct comparison of standard Bruker capillaries with home-built capillaries showed that both have identical flow and ion transmission characteristics [38].

Capillaries of identical dimensions but made of other materials were also available for the examination of their ion transmission properties. Figure 3.3 shows a picture of the different capillaries used in the experiments. Capillaries with nickel-plated end caps are the standard inlet capillaries. Home-made borosilicate glass capillaries without metalized end caps were often used when no acceleration potentials were required. A lead silicate capillary has a very low conductivity, even lower than that of normal glass capillaries. They are often used as inlet capillaries in modern mass spectrometers, since the long term stability of their ion transmission is considered better than that of standard glass capillaries. If the lead glass is reduced in a hydrogen

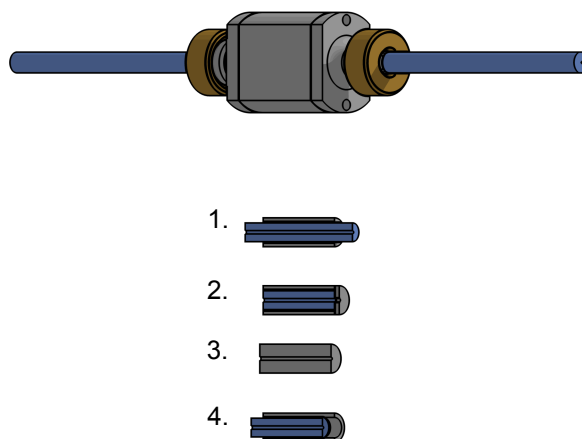


Figure 3.4: Schematic view of the adaptor to connect two capillary sections with of the different capillary inserts (silica/metal; metal) which are positioned between the two sections.

atmosphere, the resistance decreases by several orders of magnitude. As can be seen in figure 3.3 lead oxide coated lead silicate capillaries also have nickel-plated end caps. When a high voltage is applied to one or both end caps a potential gradient is established along the capillary. It was proposed, that this gradient would lead to a so-called "electrodynamical focusing" of the ions, which should increase the ion transmission through the capillary [242]. However, this was never observed in the experiments. Both capillaries were obtained from Bruker Daltonik. They may be purchased from Photonis Inc. (Lancaster, PA, USA). The entirely nickel-plated capillary was made in house (see section 3.7.5), the measured resistance between inlet and outlet of the capillary was nearly zero Ω at the outside.

To obtain an airtight connection between two or more capillary segments an adaptor as shown in figure 3.4 was used. Between the two capillary segments capillary pieces made of different materials, such as silica and/or metal, were added to examine the change in the ion transmission characteristics for different materials. The capillary pieces have a length of approximately 1 cm and an inner diameter similar to the standard capillaries. The different capillary inserts and the adaptor to join both ends of the insert to the two other capillary sections that make up the whole capillary assembly are shown in figure 3.4. For the investigations a combination of silica and metal in three variations has been used for the inserts, besides one section made of metal (no. 3 in figure 3.4). The first variant consisted of a 1 cm long silica capillary

3 Experimental

covered with a metal husk as illustrated in no. 1 in figure 3.4. In the second variant the metal husk was on the outlet end of the capillary, apart from a bore hole, completely closed. The other side of the husk was open. With this variant the ions passed through the silica capillary and then for approximately 1 mm through stainless steel (see no. 2 in figure 3.4). This variant did not allow the gas stream to be in contact with the metal surface and also established a conductive contact to the adaptor. The third insert variant was the same as the second except that the metal husk was longer than the silica capillary on the inlet side (no. 4 in figure 3.4). With this capillary insert variant both glass capillary sections were separated from the silica insert capillary by metal and the gas stream passes through 1 mm metal, 1 cm silica and then through an expanded volume surrounded by stainless steel before it entered the second capillary section.

The adaptor was not only used to assemble capillaries consisting of different segments, but was also used to apply voltages with a laboratory power supply (High Voltage power supply HNC3500; Heinzinger electronic GmbH, Rosenheim, Germany) to examine the influence of external fields on the ion transmission characteristics. The examination of the influence of voltages on the ion transmission was carried out by putting the adaptor on an intact glass capillary and applying a voltage to it. The same procedure was used for two capillary segments, where a voltage was also applied to the metallic adaptor. Inlet capillaries that consisted of two glass capillary sections and a short silica or metal segment were treated differently. The short segment was attached with adhesive tape to the glass capillary sections and the voltage was directly applied to the metal or the metallic husk of the segment. Instead of the adaptor a CAPECI source was inserted between two capillary sections for some experiments. The ion source is described in detail in section 6.5.

3.4.2.1 Numerical Simulations

Numerical simulations of the ion motion at the entrance and outlet of an inlet capillary were carried out with the SIMION 8.1.1 [243] charged particle simulation package in combination with the *statistical diffusion simulation* (SDS) algorithm [244] and with the particle tracing module of Comsol Multiphysics version 4.4 [245]. The basic simulation approach of both models was validated previously [246]. Both calculations used simplified two dimensional axial symmetric models of the geometry of the capillary inlet. The Comsol model used a profile cut through the main axis of the capillary channel, which had a diameter of 0.6 mm in both cases. The model is shown in figure 3.5. The end cap was approximated by a nearly spherical shape. For the Simion model a longitudinal cut was used and the end cap was simplified as a flat electrode with a thickness of 0.8 mm and a hole of 2 mm at the end of the capillary. The Simion model is shown in figures 5.1 and 5.2. In both models the gas flow consisted of nitrogen at standard conditions with an uniform velocity parallel to the capillary axis.

The ion mobility in the SIMION/SDS model was estimated by the SDS algorithm for ions with m/z 60. The capillary wall and the end cap were approximated as electrodes

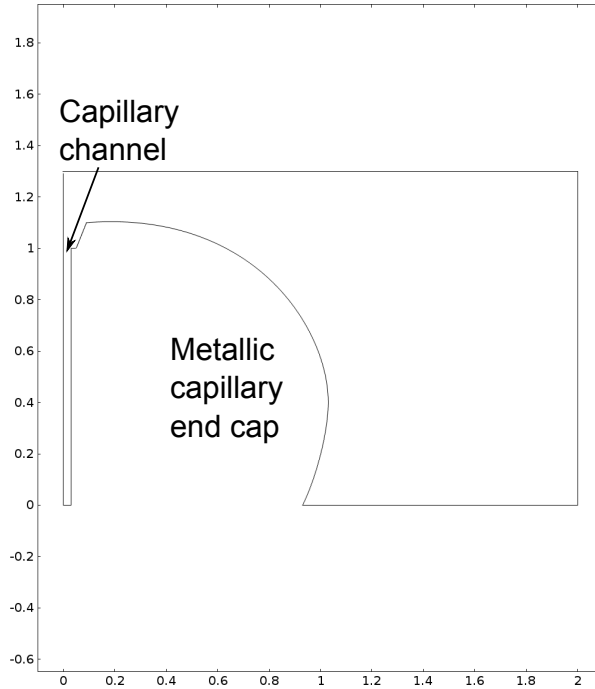


Figure 3.5: Geometry used for the Comsol simulations of the entrance and outlet of an inlet capillary.

with an uniform electrical potential in the SIMION model. While the capillary had an adjustable potential, the end cap was kept grounded. The gas volume was considered as ideal vacuum for the electrical field calculation, since the permeability of nitrogen is very close to unity.

In Comsol the viscous interaction between the ions and the background gas was modeled by an elastic collision force. For the capillary inlet a pressure of 1013 mbar and a resulting collision frequency of $1 \times 10^9 \text{ s}^{-1}$ was assumed. At the outlet, the pressure was set to 400 mbar and the collision frequency to $0.5 \times 10^9 \text{ s}^{-1}$. The electrical potential on the capillary wall was approximated in the Comsol model by an analytical function which models the buildup of charge on the capillary wall in the inlet area. The end cap was always grounded. The electrical gradient on the capillary was described by a starting value of 500 to 1000 V at the inlet of the capillary ('arc length' = 1 cm in figure 3.6) and a scaling factor dependent on the distance of the inlet, given by the equation $f(s) = 1 - \exp(-(1-s) \cdot k)$, with the local coordinate at the capillary inner wall (s) and an adjustable parameter (k). The function is plotted with different k values in figure 3.6. As only the last centimeter of the capillary was considered in the model the spatial parameter (s) is in the range of 0 to 1 cm. With increasing (k) values the gradient increases, a (k) value of 100 leads to a nearly stepped course of the electrical potential.

3 Experimental

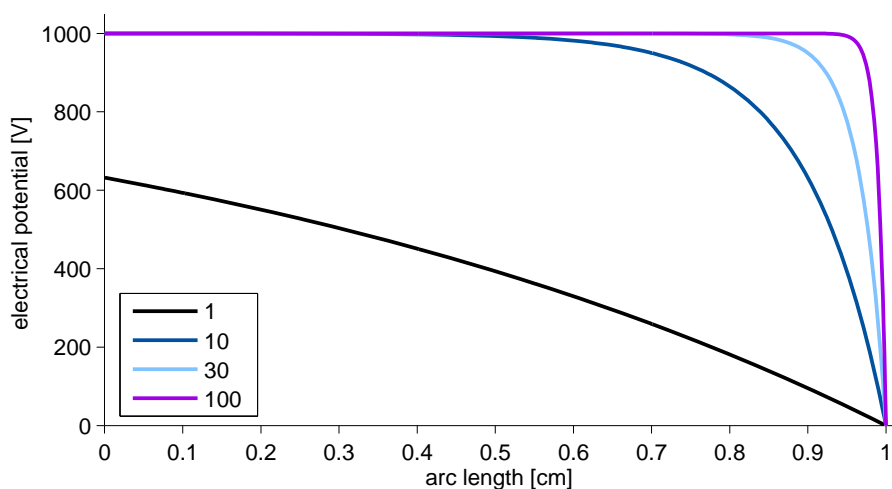


Figure 3.6: Analytical functions used to describe the potential on the capillary wall. The different colors indicate different k values. A voltage of 1000 V directly on the wall was assumed.

As gas flow velocities values between 10 to 100 ms^{-1} at the inlet of the capillary and 100 to 300 ms^{-1} at the outlet were assumed. The Comsol model was solved with the standard solver settings.

3.5 The Photoelectric Effect at Atmospheric Pressure

To examine the photoelectric effect at atmospheric pressure a rather simple setup was chosen. For measurements of the work functions of different metals at atmospheric pressure a tunable light source is necessary. A frequency tripled Nd:YAG (*neodymium-doped yttrium aluminum garnet*; 355 nm, 10 Hz; Spitlight 600, Innolas GmbH, Krailing, Germany) pumped *optical parametric oscillator* (OPO) (VisIR2, GWU-Lasertechnik GmbH, Erfstadt, Germany) with a *second harmonic generation* (SHG) stage (SHG VisIR2; GWU Lasertechnik GmbH, Erfstadt, Germany) provided light in the range of 205 to 412 nm. The OPO consists of a non-linear optical crystal (*beta-bariumborat*, BBO) that converts the incoming laser light to two output light waves with lower frequencies as the input light by a non-linear process. The sum of both output frequencies is equivalent to the input frequency. One of the output frequencies is chosen and frequency doubled in the following second harmonic generation stage. This process is not very efficient and without elaborate optimization the output energy is less than 1 mJ even though the output pulse energy of the 355 nm Nd:YAG laser light is approximately 80 mJ. To cover a wavelength range from 205 to 412 nm two non-linear crystals are necessary. At 257 nm the crystals are changed, which results

3.5 The Photoelectric Effect at Atmospheric Pressure

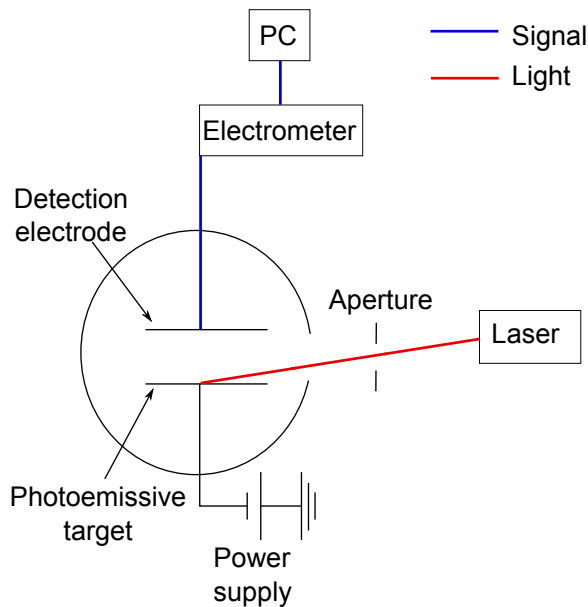


Figure 3.7: Schematic of the measurement setup to determine work functions at atmospheric pressure.

in a step in light intensity. The intensity of the laser light was monitored with a pyroelectric joulemeter (Orion PE 25-V2, Ophir Optonics LTD, Jerusalem, Israel). Other experiments were carried out with a fixed frequency unfocused *diode pumped solid state* (DPSS) laser (FQSS 266–50, Crylas GmbH, Berlin, Germany). The light has a wavelength of 266 nm at a frequency of 100 Hz, with pulse energies of 50 μJ per pulse.

A home-built measurement chamber was used to enable the examination of different metals with minimal external influence, shown in figure 3.7. Inside the chamber the metal probe plate was mounted on a *polyvinyl chloride* (PVC) holder, parallel to the measurement electrode. An adjustable acceleration voltage was applied to the metal plate (± 0 to 80 V) to accelerate the emitted photoelectrons toward the electrode plate. The detector electrode was connected to a sensitive electrometer (602 electrometer, Keithley Instruments Inc., Cleveland, OH, USA). The laser light was partially blanked out with an adjustable aperture. The small laser spot was directed at the metal probe plate through a silica window. Care was taken to avoid that the reflection of the laser light falls onto the detector electrode. The detection electrode was made of a cable shoe connected to the electrometer via a copper cable creating a small electrode that is spatially adjustable. The chamber was filled with laboratory air, if not otherwise stated. To avoid perturbances of the ion current measurements the chamber was closed, as air drafts can easily interfere the measurements with the sensitive electrometer at atmospheric pressure. The blind current of the electrometer was lower than 0.01 pA.

Different metals were used and had all standard technical purities. The sterling

3 Experimental

silver was a ten Euro coin from 2007, which has a stated purity of 92.5 %. Nickel plating of copper and gold plating of steel was carried out electrochemically. The surfaces were polished with abrasive paper of different grain sizes and washed in some cases deionized water or organic solvents. Two different approaches were used for the deposition of nickel on surfaces: one technique uses 30 g nickel chloride, 10 g sodium hypophosphite, 55 g ammonium chloride and 100 g sodium citrate for 1 L electrolytic solution, resulting in a pH of 8 to 9. A temperature of 90°C is needed to obtain an increase in nickel film thickness of 10 $\mu\text{m h}^{-1}$. This first procedure was mainly used for the coating of the glass capillaries, as it cannot be used for aluminum, which would slowly dissolve in alkaline solutions. Nickel will only deposit on glass capillaries if the glass surface was mechanically roughened (sand paper, 400 grit) beforehand and aluminum powder was polished into the roughened glass surface to provide seeding crystals for the deposition of nickel.

In the second technique to deposit nickel on surfaces a one liter solution containing 40 g nickel sulfate, 80 g sodium acetate, 20 g adipic acid and 20 g sodium hypophosphite was used. As this solution is not alkaline, it was used for the deposition of nickel on aluminum. The process took place at a temperature of 95°C, the film growth per hour is the same as for the first technique. This second technique was also used for the aluminum target for the cAPECI source design 1.

Variation of the laser power density was carried out by focusing or expanding the laser beam, using lenses or by adjusting the lamp voltage of the flash lamp pumping the OPO-laser system. Integration of the signals to calculate the peak area was done with Matlab version R2013a (The MathWorks Inc., Natick, MA, USA). Measurement of ozone mixing ratios was done with a Thermo Environmental 49 O3 Analyzer (Thermo Environmental Instrument Corporation, Waltham, MA, USA).

3.6 Reaction Mechanism in Negative Mode API-MS

3.6.1 Ionization Mechanism

For the examination of the ionization mechanism in negative mode API-MS a commercial reflectron TOF (HTOF, TOFWerk AG, Thun, Switzerland) was used as mass spectrometer, equipped with custom inlet stage and ion optics, allowing the use of an inlet capillary for sampling at atmospheric pressure. Furthermore, the ion optics were modified to be able to circumvent CID due to the high reduced field strength and clustering reactions appearing in supersonic jet expansions. Nearly thermal sampling is thus possible with this instrument. A schematic of the inlet stage is shown in figure 3.8. It consists of a glass inlet capillary (ID 0.6 mm, length 18 cm, volume flow around 1.4 L). The background pressure in the first vacuum stage was adjustable via a pressure control valve and was held constant at 5 mbar for the experiments described in this work. At a distance of 6 mm from the capillary exit a skimmer is placed to separate the first and second vacuum stage. The skimmer has an orifice diameter of 0.8 mm. With a downstream pressure of 1×10^{-3} mbar after the skimmer and 5 mbar upstream, the

3.6 Reaction Mechanism in Negative Mode API-MS

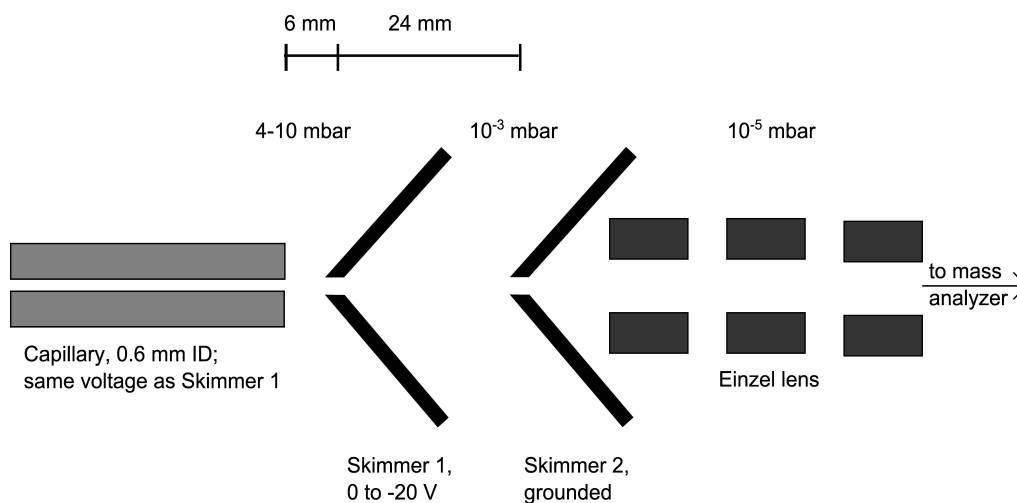


Figure 3.8: Schematic view of the custom designed inlet stage of the TOFwerk HTOF [7].

expansion through the orifice does not become supersonic. Thus, extensive cluster growth in this section of the mass spectrometer is avoided. The pressure values given for both regions are only measured near the pumps, the local pressure in the gas stream may be considerably higher. 24 mm behind the first skimmer a second skimmer separates the second differential pumping region from the high vacuum region of the mass spectrometer. The pressure in this region is approximately 1×10^{-5} mbar, which means that hardly any collisions occur downstream of the second skimmer, due to the long mean free paths of the molecules of several meters. After the ions pass through the second skimmer an Einzel lens is used to focus the ion beam before it enters the time-of-flight analyzer. The voltages applied to the ion optical devices are adjustable over wide ranges.

CID processes only occur if the reduced field strengths are well above 100 Td, as described in section 1.1.2. Between the capillary and the first skimmer voltages of more than 100 V would be necessary to reach this value. In the region between the skimmers voltages of up to 20 V are sufficient due to the low gas pressure. Voltages in the range of 0 to 200 V were applied to the metalized end cap of the capillary. In all the experiments described here the second skimmer was grounded. If CID processes between the two skimmers were desired, voltages between 0 to 20 V were applied to the first skimmer and to the capillary end cap. The voltage applied to the first skimmer was always the same as that on the capillary end cap to avoid CID reactions in the region between capillary and skimmer.

The TOF analyzer is able to measure m/z ratios down to m/z 1 with very little discrimination against small masses. The instruments calibration only allows nominal masses to be obtained from the mass spectra. The mass spectrometer setup is de-

3 Experimental

scribed in detail by Albrecht et al. [247]. In summary, the instrument has the following features:

- the voltages on the focusing elements are fully adjustable to control the level of CID processes
- it can measure down to m/z 1
- the pressures in the different pressure regions are adjustable
- the distances between capillary and skimmers are adjustable to control the occurrence of adiabatic expansions

APLI was used to generate ions with an unfocused diode pumped solid state laser (FQSS 266–50, Crylas GmbH, Berlin, Germany) with toluene as dopant (cf. section 3.5). APLI was chosen for the generation of thermal electrons because only toluene cations and thermal electrons are produced during the ionization process. Photolysis of neutral compounds such as oxygen or water is negligible, so that neutral radical formation can be neglected. A laminar flow ion source was mounted in front of the capillary [27, 38]. This ion source avoids the large gas volumes present in common ion sources and increases the light path for laser ionization, so that the ionization volume inside the LFIS is much larger than in common AP ion sources. The volume flow into the LFIS was kept equal to the capillary inflow by flow controllers (Mass-Flow-Controller; MKS Instruments, Andover, MA, USA) of different ranges. The overall gas flow was 850 mLmin^{-1} of synthetic air.

To demonstrate the operation two analytes were used. One that preferentially produces radical anions, p-benzoquinone (108 Da) and one that produces mainly $[M-H]^-$ ions, 3-methyl-2-nitrophenol (153 Da). A stream of the main gas at room temperature over the solid analyte deposited on the wall of the laminar flow ion source gave flows containing saturated vapor pressures of the analyte corresponding to mixing ratios of 130 ppmV for p-benzoquinone and 56 ppmV for 3-methyl-2-nitrophenol. To increase the number of negative charge carrying species, toluene was used as dopant. The mixing ratio was adjusted by taking the vapor over liquid toluene by a gas stream of synthetic air at room temperature. Then this gas stream was diluted by mixing it with the main gas flow, resulting in a mixing ratio of 650 ppmV. These rather high analyte and dopant mixing ratios were necessary due to the low sensitivity of the mass spectrometer under CID free conditions. To avoid CID processes very low voltages were applied to the ion optical elements in the inlet region, so that the focusing of the ions by these elements was virtually non-existent. Under normal conditions voltages of some hundred volts are applied to the capillary end cap and some tens of volts to the skimmers.

The mass spectra recorded with the thermally sampling TOF are compared with spectra obtained with a commercially available mass spectrometer. For this purpose, a quadrupole ion trap, described in detail in section 3.3, was used. As stated previously, CID free conditions are not possible with this instrument (cf. section 3.3). A cAPECI ion

source, with silver as target material, was used for ion generation in these experiments. The ion source is described in detail in section 6.5. Similar to APLI, cAPECI is a clean source for thermal electrons.

3.6.2 Dinitrotoluenes

For the investigation of the ion-molecule/radical reactions of the dinitrotoluene isomers two different reaction times are necessary, which means that two ionization positions are required. Two ionization positions were achieved by using the laminar flow ion source and a silica capillary that was partially silver plated on the inside. Photoelectron emission was used for the production of primary ions. A comparison between both ionization positions is shown in figure 3.9. Ionization inside the LFIS was carried out in the same way as described in section 3.6.1. The LiF window was mounted at the closest possible point to the inlet capillary. The transfer time of ions from this point to the reaction free high vacuum region of the mass spectrometer is approximately 5 ms [248]. A reduced transfer time of less than 1 ms was achieved with the second ionization position inside the partially silver-plated silica inlet capillary. The silica capillary (Hilgenberg GmbH, Malsfeld, Germany) had the same length as common inlet capillaries, but had a slightly smaller capillary channel (0.4 mm) resulting in volume flows of 0.75 L min^{-1} . It was chemically silver plated on the inside to provide a photoemissive material for photoelectron generation. This was done using the "Tollens' reagent". For this procedure silver nitrate was dissolved in distilled water to give a 0.6 mol L^{-1} solution. The same volume of sodium hydroxide solution (2.5 mol L^{-1}) was added, so that silver oxide precipitates. Aqueous ammonia was added until the precipitation redissolves. In the last step some milliliters of a saturated glucose solution were added. This solution was gently heated, leading to a thin silver coating on a metal target or on the channel walls when pumped through a capillary. A detailed description can be found in [249]. Subsequently the silver was partially removed by a wire with a diameter of 0.3 mm, so that the UV light could enter into the capillary channel. For detailed information on this inlet capillary see section 6.4.

When ionization was performed inside the LFIS a standard glass capillary was used as inlet stage because the ion transfer properties of the silica capillary are unsatisfactory for ions that are produced in front of the silica capillary. The reasons for this behavior are not fully understood, see chapter 5 for a detailed description of the transfer characteristics of different capillary types.

A gas stream of synthetic air was mixed with a gas stream containing the vapor of the solid analyte at room temperature. Mixing ratios in the range of 9 ppmV^4 to 28 ppbV^5 were obtained. The number of generated thermal photoelectrons was not comparable for both ionization positions. Only a very small fraction of the UV light

⁴For 2,4-dinitrotoluene, vapor pressure 133 Pa at 293 K [101], main gas flow 1.4 L min^{-1} , gas flow over analyte 10 mL min^{-1} .

⁵For 3,5-dinitrotoluene, vapor pressure 0.17 Pa at 293 K [101], main gas flow 0.6 L min^{-1} , gas flow over analyte 10 mL min^{-1} .

3 Experimental

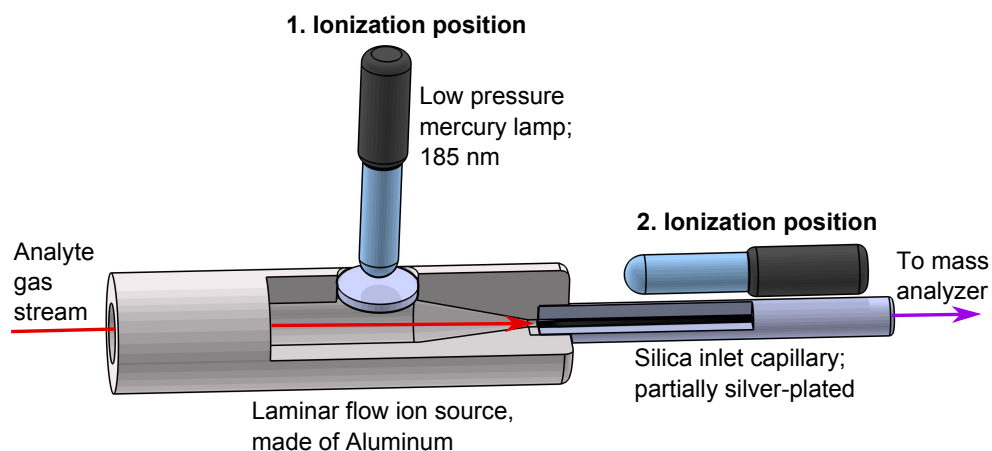


Figure 3.9: Schematic showing the two ionization positions; 5 ms position inside the LFIS and 1 ms position inside the inlet capillary.

enters into the LFIS and is therefore used for electron generation, so only the relative signal distribution, but not the absolute signal intensities are compared in this study.

The measurement of the signal dependence on the oxygen mixing ratio was obtained by adding small volumes of synthetic air to the nitrogen main gas flow. The analyte was added to a nitrogen gas flow as mentioned before. All gas flows were adjusted by flow controllers, 10 mL min^{-1} for the analyte gas stream, 50 mL min^{-1} for synthetic air and 2 L min^{-1} for the main gas flow (Mass-Flo-Controller; MKS Instruments, Andover, MA, USA). Table 3.2 lists the used gas flows and the resulting oxygen mixing ratios for a total flow of 1.23 L min^{-1} .

To investigate the influence of sulfur hexafluoride on the ion-molecule/radical reactions of dinitrotoluene the LFIS was used in combination with the ion trap mass spectrometer. The photoelectric effect was used for ionization; a low pressure mercury lamp (Pen-Ray LSP035, LOT-Oriel GmbH & Co. KG, Darmstadt, Germany) provided UV light (for details see section 3.7). The setup is similar to that shown in figure 3.9 but with an untreated glass inlet capillary instead of a silver-plated silica capillary. The purity of the sulfur hexafluoride used for these experiments was 99.90 %, the main impurities being nitrogen and oxygen at a level of approximately 500 ppmV. Water was present with a mixing ratio of approximately 10 ppmV. To remove these impurities and water which was also present in the compressed nitrogen (purity 5.0; $[\text{H}_2\text{O}] < 3 \text{ ppmV}$) both gases were mixed and then passed through a cooling trap held at 77 K with liquid nitrogen. The flow of both gases was adjusted with flow controllers (Mass-Flo-Controller; MKS Instruments, Andover, MA, USA) with ranges of 2 L min^{-1} for nitrogen and 2.6 ml min^{-1} for sulfur hexafluoride.

Table 3.2: Adjusted gas flows and resulting oxygen mixing ratios.

Nitrogen flow [L · min ⁻¹]	Synthetic air [mL · min ⁻¹]	Oxygen mixing ratio [%]
1.23	0	0
1.225	5	0.08
1.223	7	0.11
1.22	10	0.16
1.215	15	0.24
1.21	20	0.33
1.205	25	0.41
1.2	30	0.49
1.195	35	0.57
1.19	40	0.65
1.175	55	0.90

3.7 Ion Source Development

The development of a stable and sensitive ion source was the main aim of this work. The detailed description of the developed ion sources and the associated setups can be found in section 6. All measurements during the development process were done with the ion trap mass spectrometer described in section 3.3. Ion current measurements were performed with a sensitive electrometer (602 electrometer, Keithley Instruments Inc., Cleveland, OH, USA). The measurement setup was the same as already described in section 3.4.2, where the ion source substitutes the inlet capillary or is placed in front of it.

3.7.1 Sample Introduction

Analytes, e.g., 3-methyl-2-nitrophenol, were added by flowing synthetic air or nitrogen over the thermally equilibrated vapor over the solid analyte at room temperature. This gas flow was then diluted with the main gas flow, consisting of the same gas as used for the analyte delivery. All gas flows were adjusted with mass flow controllers (Mass-Flo-Controller, MKS Instruments, Andover, MA, USA). It was attempted to keep the total gas flow equal to the gas flow generated by the mass spectrometer. To avoid contamination of the system with laboratory air a slightly higher inflow into the ion source was used. The overflowing gas escaped through an overflow outlet.

3 Experimental

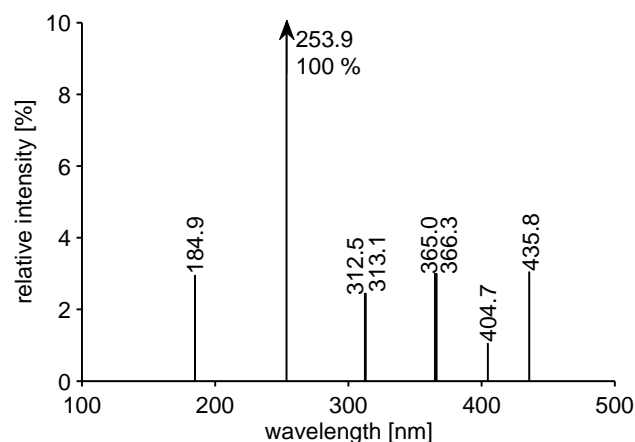


Figure 3.10: Emission spectrum of the mercury Pen-Ray lamp, the argon lines that lie in this range are not shown; adapted from [250].

3.7.2 UV Lamp

Unless otherwise stated a low pressure mercury lamp (Pen-Ray®LSP035, LOT-Oriel GmbH & Co. KG, Darmstadt, Germany) providing light in the UV range was used for all experiments during the ion source development. The lamp is a cold cathode UV lamp that consists of a silica double bore tubing. The tubing contains argon at a low pressure. Mercury droplets are present as source for Hg gas which constitutes the UV emitting species. When the lamp is switched on the high electrical field between the electrodes at both ends of the tube is sufficient to ionize argon and establish a discharge arc between both electrodes. This leads to heating of the mercury droplets which evaporate and ionize in the argon arc. When enough ionized mercury is present the arc between the electrodes is sustained mainly by the mercury ions. It takes several minutes until this process is established, which means that this type of lamp cannot be switched on and be used directly, it has to "warm up" for up to ten minutes until the arc is a bright bluish violet. The main emission of these lamps is at 253.6 nm, a second emission in the UV range is at 184.9 nm with 3% intensity of the 253.6 nm line. Other emission lines are at longer wavelengths (see figure 3.10), however, none of them has sufficient energy for the generation of photoelectrons with common metals. Mercury has emission lines up to 435.8 nm. The emission of argon is not shown in figure 3.10, here, the emission lines start at 404.4 nm and extend to the *infrared* (IR) range with more than 800 nm, a range that is not used during this work.

A UG 5 ultraviolet band pass filter (Schott AG, Mainz, Germany, relative transmission $< 10^{-5}$ at 185 nm and 83% at 254 nm) was used to determine which of the two emission lines contributes predominantly to the photoelectron generation. When this band pass filter was placed between lamp and photoemissive material virtually no 185 nm

photons reach the photoemissive material. Therefore, the recorded ion current under these conditions, as described in section 3.4, was entirely attributable to the 254 nm line.

3.7.2.1 Monitoring of the lamp stability

The stability of the emission of the low pressure mercury lamp was examined using two assemblies. An avalanche photodiode (SD 200-12-22-041, Advanced Photonics, Inc., Camarillo, CA, USA) which was connected to a multimeter (VC820 Digital-Multimeter, Voltcraft, Conrad Electronic SE) was used to measure the current produced inside the photodiode by the incoming light. The multimeter was connected to a PC to record the data. The photodiode was sensitive to the visible light range only. As is shown in figure 3.10, the low pressure mercury lamp also has emission lines in the visible range, all with less than 3 % intensity compared with the 253.6 nm line. It was assumed that all emission lines have the same temporal intensity profile.

A VUV spectrometer (ARC VM-502, Acton Research Corporation, Acton, MA, USA) [251] was used for the monitoring of the 184.9 nm and 253.6 nm emission lines. The light emitted by the lamp passed through a LiF window into an evacuated chamber (1×10^{-6} mbar) with an optical grid, which selected the wavelength that reached the detector (photomultiplier tube, R955, Hamamatsu Photonics K. K., Hamamatsu City, Japan). The signal was amplified by a factor of 1000 and then digitized by a multimeter (VA18B, V&A, ELV Elektronik AG, Leer, Germany) and recorded using a personal computer.

3.7.3 Laminar Flow Ion Source

The LFIS was introduced by Barnes et al. in 2010 [27, 38]. A profile view of the laminar flow ion source is shown in figure 3.11. The source is made of an aluminum tube with an inner diameter of 4 mm that is nickel plated for some experiments. It was built for gaseous sample introduction and is tightly attached to the inlet capillary. To facilitate a laminar gas flow through the ion source a cone shaped reduction of the inner diameter to 0.8 mm is implemented at the end of the LFIS. As the inner diameter of the capillary channel is 0.6 mm the gas flow remains laminar until it reaches the inlet capillary [38]. The volume inside the laminar flow ion source is small in contrast to common ion sources. As the LFIS has no drains the entire inflow into the ion source is pumped into the mass spectrometer. The neutral analyte is not diluted by high gas flows as in common ion sources. A lithium fluoride window is mounted close to the cone at the end of the metal tube. A flute is drilled into the LiF window to match the tube channel. For ionization, the low pressure mercury lamp or an APPI krypton discharge VUV lamp (Waters Corporation, Milford, MA, USA) is placed above the LiF window. The transfer time from this point to the high vacuum region of the mass spectrometer, where reactions are negligible due to the low collision frequencies, is approximately 5 ms [248].

3 Experimental

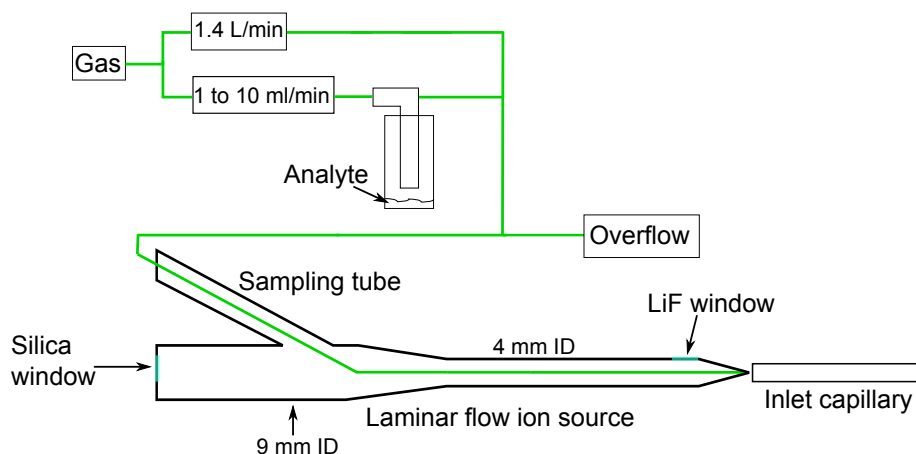


Figure 3.11: Setup of the measurements with the LFIS, with sample introduction and inner profile of the laminar flow ion source.

The laminar flow ion source was originally built for atmospheric pressure laser ionization. The laser is coupled into the ion source coaxially through a silica window, leading to a long ionization path of approximately 20 cm that gives rise to high ionization efficiencies. The sampling tube is used to supply the analyte, while maintaining a laminar flow. The LFIS was not used with APLI during this work except for the examination of the ionization mechanism in the negative ion mode as described in section 3.6.1. For the development of an ionization method based on the photoelectric effect the upstream part of the LFIS is used for sample introduction through the sampling tube and the UV lamp was placed on top of the LiF window near the capillary duct.

3.7.3.1 Metal Coated Windows

Metal coating of silica windows was carried out in the group “Experimental Physics - Condensed Matter” of Prof. Dr. Frahm at the University of Wuppertal. Both, *physical vapor deposition* (PVD) and sputtering were used to form thin films on the silica windows. For PVD the target was introduced into a high vacuum chamber (pressure around 1×10^{-6} mbar). A sample scoop made of tungsten, filled with pellets of the coating metal was conductively connected with a high current power supply inside the vacuum chamber. The metal was evaporated by electrical heating of the tungsten scoop. The metal vapor deposited on all cooler surfaces inside the vacuum chamber and on the walls of the chamber itself, so that a thin metal film also formed on the window. The film thickness is directly proportional to the time the target is exposed to the metal vapor. The film thickness was not determined experimentally, the PVD process was stopped when the window was optically intransparent. For the experiments described in section 6.3.1 copper was used as the metal.



Figure 3.12: Photograph of the silica inlet capillary with casing to match the capillary socket in the mass spectrometer and a common Bruker Daltonik inlet capillary made of lead silicate glass.

3.7.4 Silica Capillary

To generate photoelectrons inside the inlet capillary, the common glass capillary was replaced by a silica capillary (Hilgenberg GmbH, Malsfeld, Germany) of the same length (18 cm). This was necessary as glass is not transparent for UV photons which are mandatory for the photoelectric effect as the work function of most metals falls into the UV range. The inner diameter of the silica capillary (0.4 mm) was slightly smaller than that of common inlet capillaries, resulting in a choked flow of approximately 0.75 L min^{-1} . The silica capillary had a slightly smaller outer diameter of 4 mm compared to 6.5 mm for common glass capillaries. As the silica inlet capillary was supposed to replace the glass inlet capillary, metal casings of 3 cm length, with an outer diameter of 6.5 mm and an inner diameter of 4.1 mm were plugged on both ends of the silica capillary and made airtight using two-component adhesive. The casing had a 0.7 mm bore drilled into the end face that matches the capillary channel. To provide a photoemissive material, the capillary channel was chemically silver plated as described previously in section 3.6.2. After this treatment the capillary channel was fully silver plated. To enable entry of the UV light into the capillary channel so that it can fall on the silver surface for the production of photoelectrons, the silver mirror was partly removed mechanically using a wire with a diameter of 0.3 mm. As this procedure is not reproducible, all measurements were conducted with the same silica inlet capillary. Figure 3.9 shows a schematic view of the partly silver-plated silica capillary. A photograph of an unplated silica capillary with the metal casings is shown in figure 3.12.

3.7.4.1 Branched Capillary

In a second capillary ion source the ion generation region and the analyte introduction were separated. The transfer time from the region where reagent ions and the neutral analyte were mixed to the nearly collision free vacuum region in the mass spectrometer was as short as possible. An unmodified glass inlet capillary was used to deliver

3 Experimental

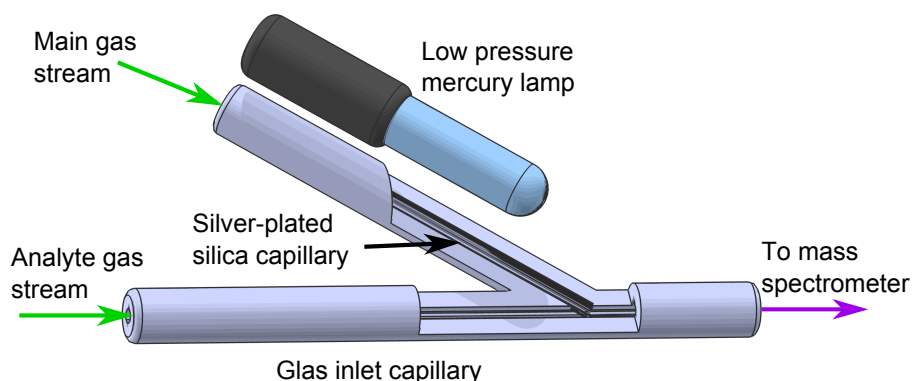


Figure 3.13: Schematic view of the branched capillary.

the analyte and to guide the mixed gas into the mass spectrometer. This had the advantage that the modified ion source directly fits into the desolvation stage of the mass spectrometer. Primary ion production took place by photoelectron generation inside a silica capillary that was partially silver plated on the wall of the capillary channel (see figure 3.13). The low pressure mercury UV lamp was used as light source. The silica capillary was connected to the glass capillary at a distance of 5 cm from the exit end of the capillary. At this point, a wedge shaped opening was drilled in the glass capillary. One end of the silica capillary was ground down to form a wedge-shaped counterpart. Both capillaries were joined together with adhesive chemically setting cement (No. 31, Liquid No. 31A; Sepp Zeug GmbH & Co. KG, Böblingen, Germany), which is a mixture of silica powder and modified sodium silicate solution. Flow controllers (Mass-Flo-Controller; MKS Instruments, Andover, MA, USA) were used to adjust the analyte gas stream through the glass capillary (10 mL min^{-1}) and the main gas flow of synthetic air (1.4 L min^{-1}) through the silica capillary.

3.7.5 cAPECI Design 1

An ideal ion source generates reproducible ion currents and furthermore, a cAPECI source should have an exchangeable photoemissive material. This was not the case for the silver-plated silica capillary. The custom built cAPECI source partly replaced the common glass inlet capillary, but used capillary segments at both ends to match the overall length of a normal inlet capillary. Thus, it was compatible with the capillary mount of the mass spectrometer, which allowed the combination with common ion sources and analyte supply techniques. Figure 3.14 shows a schematic view of the ion source. It consisted of an aluminum housing, with sockets at both ends for an airtight attachment of the capillary segments. An insert made of aluminum was attached to

the housing with a sealing ring. The attachment did not result in any additional gas volume. Plates made of different photoemissive materials could be mounted on the insert. A flute was milled into these plates which had a similar diameter as the capillary channel 0.6 mm. A UV transparent window made of silica, lithium fluoride or sapphire (all: Korth Kristalle GmbH, Altenholz, Germany) was mounted on top of the photoemissive material. To complete the capillary channel, a flute was also milled into the window with the same diameter as in the photoemissive material. The combination of the flutes formed a channel through the ion source, similar to the capillary channel. However, also windows without flute were used, forming only a half channel and gave similar results. Gas flows of 938 mL min^{-1} for a complete capillary channel inside the ion source and 909 mL min^{-1} for a half channel were measured. The window was mounted onto the photoemissive material by a cover plate and sealed with a silicone flat gasket. Thus, the capillary channel went straight through the ion source and the capillary segments. In the following this setup is referred to as *cAPECI design 1*.

The insert was designed to ensure that the photoemissive material was easily interchangeable, as can be seen in figure 3.15. Different materials were used as photoemissive materials. For some metals the plates were directly made of the specific metal (e.g., aluminum, copper, steel or silver), other metals were electrochemically or chemically applied to the target plates. Nickel was chemically deposited on an aluminum target as described in section 3.5. To deposit gold on the silver plate, a cyanide free gold electrolytic solution was used (gold electrolyte, Conrad Electronic SE). An electroplating device (Conrad Electronic SE) was dipped into the electrolytic solution. The electroplating device and the workpiece were connected to the positive and the negative pole of a power supply. The same procedure, but with a silver electrolyte solution (Conrad Electronic SE) was used for silver deposition on metal targets. Another way to deposit silver on surfaces was the use of the Tollens' reagent as described in detail in section 3.6.2.

Samarium is a lanthanide that has a low work function of 2.7 eV [101]. It is not stable in air because of surface oxidation, however, samarium oxide Sm_2O_3 , may also have a comparatively low work function. To examine its characteristics as photoemissive material for the cAPECI ion source it was physically vapor deposited on a copper target. The physical vapor deposition was carried out as described in section 3.7.3.1. The film thickness was not determined experimentally, the PVD process was stopped when the copper surface was visibly coated with samarium. The metalized target is shown in figure 3.16.

Another promising material with a low work function was a tungsten inert gas welding electrode that was alloyed with a lanthanide to reduce the work function of the composition (Techweld Multistrike®, Huntingdon Fusion Techniques Limited, Bury Port, UK). It was not stated which lanthanide was used for the alloy, but the manufacturer quotes a work function of 2.9 eV [252]. Tungsten has a work function of 4.35 eV [101], the work function of an alloy lies somewhere between the work function of the pure metals [253, 254]. However, the exact dependence of the work function

3 Experimental

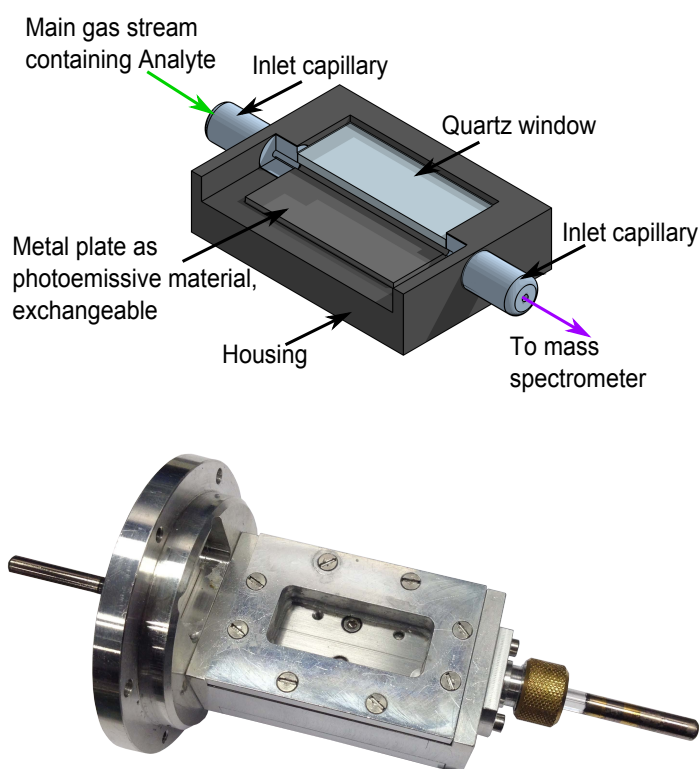


Figure 3.14: Schematic view (top) and photograph (bottom) of the capillary ion source design 1 for atmospheric pressure electron capture ionization developed during this work.

on the composition has to be found experimentally [253, 254]. The electrodes had a diameter of 2.4 mm. To use them as a photoemissive material in the cAPECI source design 1 one of the aluminum targets was modified by drilling a channel with a diameter of 2.5 mm through it, in a way that the flute that was intended to be the capillary channel is slightly opened, as is shown in figure 3.16 (left). In this setup both the tungsten-lanthanide electrode and the aluminum, which was still part of the capillary channel serve as photoemissive materials. An increased photoelectron yield should have been measurable compared to the target consisting fully of aluminum. To verify this, a non-photoemissive material (polyvinyl chloride coated cable) of the same diameter as the electrode was used for one measurement instead of the tungsten-lanthanide electrode. In this case, only the aluminum from the capillary channel walls provided photoelectrons, giving a photocurrent reduced by a factor of 3.

The capillary channel that was milled in the metal target has a length of 4.9 cm. In

3.7 Ion Source Development

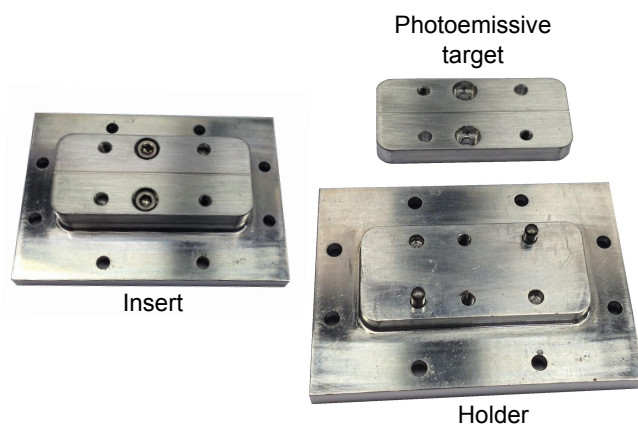


Figure 3.15: Picture of the insert of the cAPECI source design 1 with an aluminum plate as photoemissive material, Left: mounted; right: disassembled.

an attempt to increase the photoelectron yield the capillary channel on the target was to lengthened, as is shown in figure 3.17. As photoemissive material aluminum was used. The length of this capillary channel was 2.5-fold that of the commonly used channel length. For this target a window without flute was used, as it would be difficult to match the curved channel in the target. However, not only the illuminated capillary channel was lengthened, but also the transfer time of ions through the capillary ion source.

To provide a surface that does not chemically change with time an anodized aluminum target with a normal channel length was made. The aluminum target was placed in a 20 % sulfuric acid solution and was attached to the negative pole of a laboratory power supply (PS3030, Conrad Electronic SE). Typical anodization currents were 1 A per 90 min for every 10 cm² surface. During the anodization the solution is cooled by an ice bath. The thickness of the aluminum oxide layer is directly proportional to the electrolysis time until the layer thickness saturates and the layer growth stops. The aluminum target was anodized sufficiently long to reach the maximum aluminum oxide thickness. To close the pores of the aluminum oxide surface, the work-piece was placed in a distilled water bath with a temperature of 100°C for one hour. The conductivity of the anodized aluminum surface was measured with a multimeter (Votcraft VC820, Conrad Electronic SE).

Besides the photoemissive target, an entire cAPECI source design 1 was anodized to have the same conductivity on all surfaces that were in contact with ions. The anodization process was the same as described for the aluminum target. For this ion source a sapphire window (Korth Kristalle GmbH) was used instead of a silica or lithium fluoride window.

3 Experimental



Figure 3.16: Picture of the modified aluminum insert to use the tungsten electrodes as photoemissive material (left) and of the samarium-plated target directly after the PVD process (right).



Figure 3.17: Picture of the aluminum target with a 2.5-fold increased capillary channel length.

3.7.6 cAPECI Design 2

The second cAPECI source design avoided the necessity of modifying the inlet capillary, but maintained the advantage of short transfer times. This had been achieved by moving the ion source upstream of the inlet capillary and by separating ion generation and analyte introduction. Figure 3.18 shows the layout of the new ion source. The analyte was added to the gas stream with the primary reactant ions at a point where the diameter of the ion source is similar to the capillary channel 0.6 mm. Thus, the gas velocity at this point was already large, resulting in short transfer times of the ions from the mixing region to the high vacuum region of the mass spectrometer. The primary ion generation took place by photoelectron generation by the interaction of the UV mercury lamp with anodized aluminum as photoemissive material. An airtight sealing of the UV lamp was ensured by a sealing ring. The inner side of the tubular ion source was used as photoemissive material; this had the advantage of using the entire light

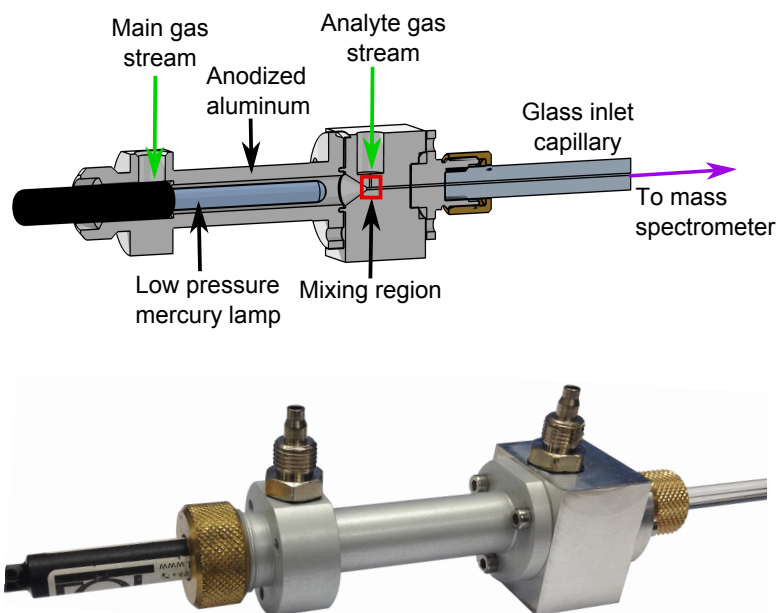


Figure 3.18: Schematic setup and picture of the cAPECI source design 2.

that was provided by the mercury lamp, in contrast to the cAPECI source design 1, which used only a small fraction of the UV light. The tubular ion source had an inner diameter of 8 mm. Synthetic air or other gases were introduced as the main gas flow. The reactant ions were formed with the main gas components by electron capture processes. At the end of the main tube containing the UV lamp the inner diameter was conically narrowed to 0.6 mm. The 0.6 mm channel was 1.5 cm long. For most experiments the main gas stream was in the range of 1 to 1.5 Lmin⁻¹, while the analyte gas stream was 1 to 10 mLmin⁻¹. The inlet capillary of the mass spectrometer was attached airtight to the ion source in the same way as in the cAPECI source design 1. Gas flows were adjusted using flow controllers of 2 Lmin⁻¹ for the main gas flow and 10 mLmin⁻¹ for the analyte gas stream (Mass-Flo-Controller; MKS Instruments, Andover, MA, USA).

3.7.6.1 Comparison of Transfer Times

To examine the influence of the transfer time on the extent of ion molecule/radical reactions and therefore also on the signal distribution obtained with this ion source, a second ion source was designed. As can be seen in figure 3.19 mixing of the main gas stream, containing the primary ions and the analyte gas stream took place before the inner diameter of the ion source is reduced. Thus, the transfer time from this point to the high vacuum region of the mass spectrometer was significantly increased.

3 Experimental

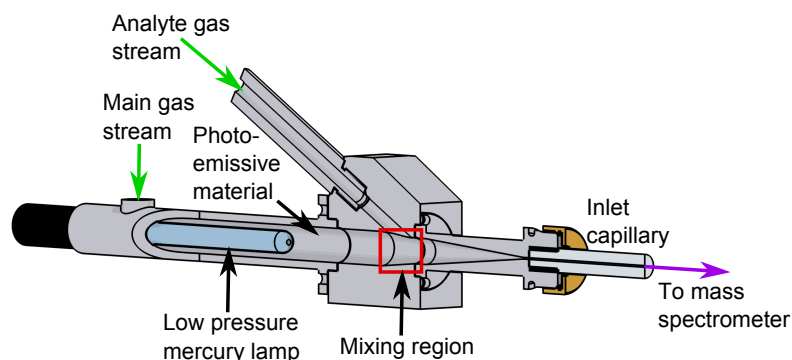


Figure 3.19: Schematic setup of the cAPECI source design 2 with a longer transfer time.

Ionization was carried out in the same way as in the cAPECI source design 2, i.e., with a UV mercury lamp in combination with anodized aluminum. With this ion source the photoemissive material was exchangeable, as it was inserted into the ion source as a tube with an inner diameter of 9 mm, an outer diameter of 1.2 cm and a length of 4.8 cm. Different materials were investigated: silver, copper, aluminum, anodized aluminum, nickel-plated aluminum and gold-plated silver. The strongest photoemission signal was obtained with anodized aluminum as photoemissive material. The introduction of gases and the attachment to the mass spectrometer inlet capillary were as already described for the ion source in section 3.7.6. Variation of the oxygen mixing ratio of the gas stream passing through the ion source was accomplished by mixing different amounts of synthetic air to pure nitrogen. The volume flow of synthetic air was adjusted by a 2 L min^{-1} mass flow controller. This led to oxygen mixing ratios between some ppmV and 20 %. The mixed gas was also used to deliver the analyte.

3.8 GC-cAPECI-MS Hyphenation

A GC coupling with the novel ionization method was built, by means of a custom GC-transfer line [255]. A schematic view is shown in figure 3.20. The GC used for all experiments described in this work was an Agilent 7890 A (Agilent Technologies Inc., Shanghai, China) with a multi purpose column (Zebron ZB-5HT Inferno™, 30 m, 0.25 mm inner diameter and 0.25 mm film thickness (Phenomenex Inc., Torrance, CA, USA)). The heated transfer line was used to deliver the GC capillary from the GC oven to the ion source. It was held at a constant temperature of 350°C , unless otherwise stated. A microprocessor controlled PID (*proportional integral derivative*) controller was used for temperature control of the transfer line. The transfer line is described in detail by Schiewek [255] and Klink [256]. The transfer line was tightly attached to the

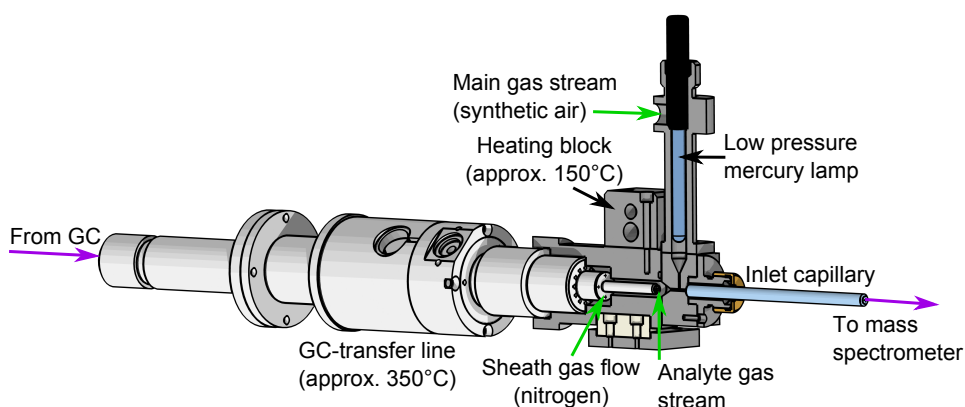


Figure 3.20: Schematic setup of the cAPECI-GC coupling with custom built GC-transfer line and heated cAPECI source.

cAPECI ion source. The GC capillary ran straight through the transfer line and ended directly in the ion source cone. A sheath gas flow of nitrogen in the range of 100 to 500 mLmin⁻¹ enveloped the analyte gas stream from the GC, which was normally set to 1.5 to 3 mLmin⁻¹. As described in section 3.7.6 for the cAPECI source design 2, the region for primary ion generation was separated from the sample introduction. Primary ions were generated in the main gas stream of synthetic air via electron capture of photoelectrons, as described previously (see section 3.7.2). The tube dimensions were the same as for the cAPECI source design 2 (see section 3.7.6). The main gas stream was mixed with the analyte gas stream coming from the GC in a region of the ion source where the inner diameter was already reduced to the dimension of the capillary channel, enabling short transfer times of the analyte ions, which results in a strongly reduced extent of ion-molecule/radical reactions. To prevent condensation of the analyte coming from the heated GC capillary, the ion source was also heated to approximately 150°C by a temperature controlled heating cartridge that is placed on top of the transfer line holding fixture. The temperature was controlled by a resistance thermometer (PT100) connected to a PID device that regulates the resistance heating elements (Horst GmbH, Lorsch, Germany).

GC injection was done manually with a 10 µL syringe (Model 701, Hamilton Messtechnik GmbH, Höchst, Germany) with an injection volume of 1 µL. The temperature of the injector was held constant at 350°C throughout the measurements. Splitless injection was used. The temperature program and other settings of the GC oven were selected for the individual measurements, but mainly two programs were used, as shown in table 3.3. The first (“fast run” in table 3.3) was used for samples containing only one or two analytes, since the separation efficiency was not crucial. The other temperature program (“separation” in table 3.3) was used for more complex samples, i.e., samples

3 Experimental

Table 3.3: Temperature programs for GC-cAPECI experiments.

	Fast Run	Separation
Capillary flow [mLmin^{-1}]	1.5	1.5
Initial temperature [$^{\circ}\text{C}$]	80	60
Initial time [s]	0.5	0.5
Temperature rate [$^{\circ}\text{C min}^{-1}$]	30	6
Final temperature [$^{\circ}\text{C}$]	350	350
Final time [s]	1	5

containing several analytes.

A slightly modified second cAPECI ion source for the coupling with GC was compared with the ion source described above. In this ion source the gas stream directions were changed, so that the main gas stream, containing the primary ions, went straight through the ion source and into the inlet capillary. The analyte gas stream coming from the GC was added at an angle of 90° . This arrangement had the advantage that the largest gas stream did not have to change direction after the reagent ions were generated. All other parameters were held constant. A nitro-aromatic-explosive mix investigated was purchased from Dr. Ehrenstorfer GmbH (Augsburg, Germany).

These two GC-cAPECI setups were compared to ionization inside the inlet capillary as applied in the cAPECI ion source design 1 (see section 3.7.5). The ion source described above was used for the tight attachment of the transfer line and the transition from the transfer line to the inlet capillary.

3.9 Atmospheric Chemistry Studies

Before atmospheric chemistry studies were carried out, the performance of the cAPECI source was compared with a common ionization method, proton transfer reaction ionization. As cAPECI source the partly silver-plated silica capillary was used, which is explained in detail in section 3.7.4.

Proton transfer reaction mass spectrometry was performed with a PTR-HRTOF-MS (Ionicon Analytik GmbH, Innsbruck, Austria), which has a resolution in the 1×10^4 range. The PTR-MS was used without further modification. A schematic view of the hollow cathode ion source and the PTR-drift-tube is shown in figure 3.21 a). A hollow cathode discharge generates proton bound water clusters, $[\text{H}(\text{H}_2\text{O})_n]^+$, from water vapor that is introduced into the ion source. The proton bound water clusters are directed into the drift tube where the analyte gas stream is added. The gas inflow

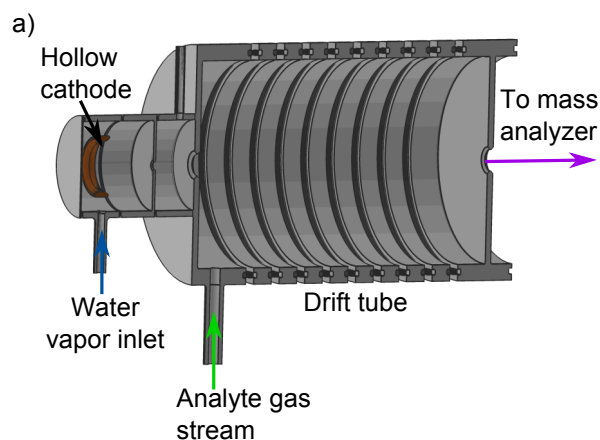


Figure 3.21: Schematic view of the PTR ion source and drift tube.

into the PTR sampling line is approximately 300 mL min^{-1} , from which only a small fraction is fed into the drift tube. Inside the drift tube a pressure of 3 mbar is established. A homogeneous electrical field inside the drift tube is established by applying a DC gradient over the concentric electrode rings inside the drift tube. The voltage applied to the drift tube can be varied over a wide range, resulting in reduced field strengths of 0 to 200 Td. This is necessary to decrease the cluster size of the proton bound water cluster distribution. H_3O^+ has the highest acidity of all proton bound water clusters and is able to protonate most analytes. However, not only the mean cluster size decreases due to the field strength inside the drift tube, but analyte ions are also affected. This potentially leads to fragmentations and thus to additional signals in the mass spectrum. The optimization of the reduced field strength in terms of ionization efficiency and minimization of analyte fragmentation is required. For all measurements described in this work a reduced field strength of $E/N = 130 \text{ Td}$ was used. PTR and cAPECI measurements were performed simultaneously from the same sample line. A detailed description of the PTR used for these experiments is given by Sonderfeld [257].

Figure 3.22 shows the two setups used a) for the comparison of the different ionization methods and b) for the photo-oxidation study. For the comparison measurements the solid or liquid analyte was put into a bubble counter that was held at a constant temperature. The synthetic air gas stream was flown over the analyte. The flow contained the saturation vapor pressure of the analyte and was adjusted by a flow controller (Mass-Flo-Controller; MKS Instruments, Andover, MA, USA) to 2.5 L min^{-1} . The gas stream was divided into three different sample lines, going to the PTR-MS (300 mL min^{-1}), to the ion trap for cAPECI measurements (0.75 L min^{-1}) and the balance to a *Fourier transform infrared spectrometer* (FTIR; Nicolet Nexus, Thermo Scien-

3 Experimental

tific, Waltham, MA, USA). The FTIR spectrometer was used to measure the absorption of the sample over a broad wavenumber range (4000 to 600 cm^{-1}). It is coupled to a long path absorption White type multi reflection optics set to a total path length of 32.8 m housed in a photoreactor leading to sensitivities in the ppmV range. Spectra were obtained by co-addition of 128 scans over a period of 2 minutes. The FTIR setup is described in detail by Barnes et al. in [258].

The FTIR was also used for concentration linearity measurements. As the sensitivity of the instrument does not allow measurements in the sub-ppmV range, the PTR-MS was used for mixing ratio determination for lower concentrations. This procedure is possible as the PTR-MS shows a good linearity over large mixing ratio ranges, as widely reported in the literature [193, 259]. The range in which FTIR and PTR were able to be used simultaneously is sufficient for the precise determination of all the mixing ratios investigated for the mass spectrometric measurements. In addition the mixing ratio of the analyte can be calculated using the saturation vapor pressure as described for the comparison measurements, however this approach does not take wall losses into account. These may significantly affect the actual mixing ratio present in the system particularly for low analyte mixing ratios. As the determination of the exact mixing ratio was not crucial for the comparison measurements, the mixing ratios were thus calculated for this type of experiment. Furthermore, the use of the FTIR would have been experimentally much more demanding since the recording of calibration curves for each analyte would have been necessary.

Figure 3.22 b) shows the setup used for the photo-oxidation study. The experimental setup of the photoreactor and the FTIR system has been described in detail by Bejan et al. [226], so that only a brief description is given here. A 1.12 L glass tube (length 45.3 cm, inner diameter 5.6 cm), which was conically shaped at both ends was used as photo-oxidation reactor. It was surrounded by six super actinic fluorescent lamps (20 W, length 57 cm, TL/05, Koninklijke Philips N.V., Eindhoven, The Netherlands), which emit light in the range of 290 to 460 nm with a maximum emission at $\lambda_{max} = 360$ nm. The glass reactor and lamps were mounted in an aluminum housing, which was equipped with a fan to keep the temperature constant during the measurement. As analyte 2-methyl-3-nitrophenol was used. The analyte was delivered by flowing a synthetic gas stream over the solid analyte resulting in a gas stream containing the saturated vapor pressure of the analyte. This stream was diluted with synthetic air to a constant mixing ratio of some hundred ppbV. Previous experiments have shown that this analyte needs a comparatively long irradiation time until photo-oxidation products are observed. Thus, a reaction time of approximately 22 min within the photoreactor was adjusted by using only a low gas stream of 50 mLmin^{-1} from the reactor and diluting it afterwards with a synthetic air make up gas stream of approximately 1.1 Lmin^{-1} to match the total gas stream needed for both mass spectrometers. This gas stream was split for the direct and simultaneous comparison of PTR (0.3 Lmin^{-1}) and cAPECI at the ion trap (0.75 Lmin^{-1}). The mixing ratio of 2-methyl-3-nitrophenol was too low to allow comparison measurements with the FTIR.

3.10 Determination of Reaction Rate Constants

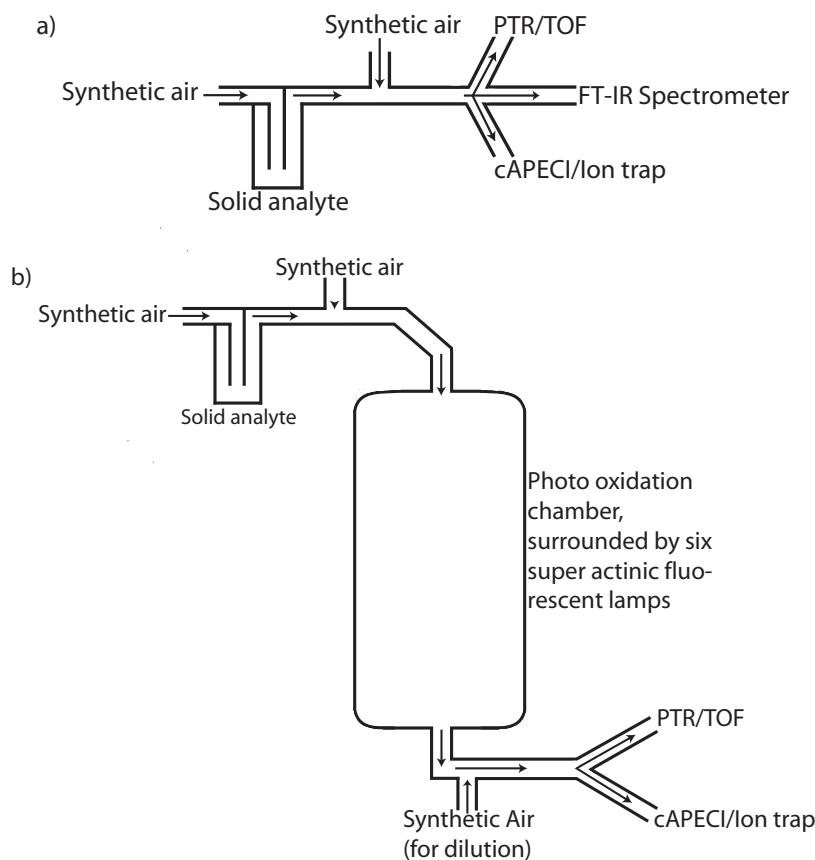


Figure 3.22: Schematic view of a) the experimental setup for the linearity measurements and the comparison of PTR and cAPECI and b) the photo-oxidation measurement setup.

3.10 Determination of Reaction Rate Constants

The determination of rate constants were made with the cAPECI source design 1 mounted at the ion trap mass spectrometer. Silver was used as photoemissive material. Synthetic air and the analyte mixing ratio were adjusted with flow controllers, as described in the previous sections.

Monte Carlo simulations were carried out with the *Reaction Simulation* (RS) extension for the charged particle solver Simion [243] [26, 65, 260] to calculate the concentration evolution of superoxide and the reaction products during the reaction. The parameters used for the simulations are described in section 7.3.

3 Experimental

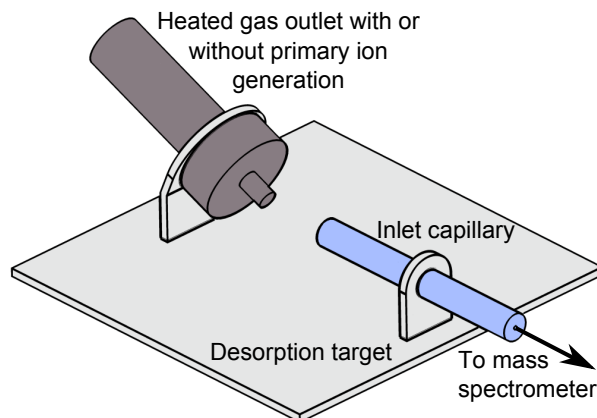


Figure 3.23: Schematic view of the desorption APECI source.

3.11 Desorption APECI

A *desorption APECI* (DAPECI) source was constructed using the anodized aluminum tube and the UV mercury lamp described in section 3.7.6 and a custom extension, which is shown in figure 3.23. At the downstream exit of the tube in which the photoelectron generation was performed, the inner diameter was conically reduced to 1 mm to increase the gas velocity and to decrease the spot size of the emitted gas. Gas flows of 1 to 1.5 L min⁻¹ synthetic air were adjusted with a 2 L min⁻¹ flow controller (Mass-Flo-Controller; MKS Instruments, Andover, MA, USA). The gas stream was directed onto a target on which the analyte was applied. Plates made of stainless steel or glass were used as targets for most experiments; also desorption from skin was carried out. Different analytes were each dissolved in hexane or ethylacetate and the resulting solutions were applied to the target in 10 μ L droplets. After drying of the solvent, the targets were investigated using desorption APECI. The distance between the DAPECI source and the target was varied to find the optimum position; the same optimization was performed for the distance between target and inlet capillary. Some targets were placed on a heated metal block (around 100°C) to increase the vapor pressure of the analytes. This setup was compared with desorption by a gas stream of synthetic air that was directed onto the target in front of the inlet capillary. The setup was basically the same as that described above, the only difference being the Pen-Ray lamp switched off. Which desorption method was used is indicated in the description of the measurements in section 7.4.

4 Ionization Mechanism in Negative Mode API-MS

While the ionization mechanisms in positive ion mode mass spectrometry are largely clarified, the reaction mechanisms leading to negative ions at atmospheric pressure is still open to debate (cf. section 1.3.1). As stated in the introduction, the presence of primary ion water clusters for most negative ionization methods is widely accepted, but as the examination of these species is difficult with commercially available mass spectrometers their role in the mechanism is not yet known. In commercially available mass spectrometers the voltages applied to the ion optical devices are sufficiently high to allow distinct CID processes to occur. These high voltages are necessary to increase the ion transfer efficiency from the atmospheric pressure ion source to the high vacuum region where the analyzer is located. Furthermore, due to adiabatic expansions between regions of different pressures, cluster growth can easily occur. Thus, the observed cluster distribution is mostly shifted from the thermal cluster distribution obtained with standard instruments. Furthermore, the cut off of small m/z ratios is common for these instruments and cannot be easily circumvented, but the reagent ions of interest are present in this mass region. The experiments described in the following were therefore carried out with a thermally sampling mass spectrometer [247] to examine the ionization mechanisms in the negative ion mode under relatively clean conditions and with oxygen as the electron capturing species [7, 261]. With this instrument mass spectra are obtained that closely resemble the ion distribution in the ion source (see sections 1.1.2 and 1.1.4).

4.1 Verification of Thermal Sampling

To verify that the custom ion optics of the mass spectrometer are indeed nearly thermally sampling, the well described proton bound water cluster system, $[\text{H}(\text{H}_2\text{O})_n]^+$, was examined in the positive ion mode. This system is ideal for a validation of the properties of the mass spectrometer: The ions are easily formed under the present conditions, the cluster distribution is easily varied by both CID and adiabatic gas expansions and the kinetics of this system are well known.

Formation of the cluster system was achieved using the same conditions applied for the examination of the negative ionization mechanism, i.e., laser ionization of toluene at atmospheric pressure, described in section 3.6.1. The use of a corona discharge

4 Ionization Mechanism in Negative Mode API-MS

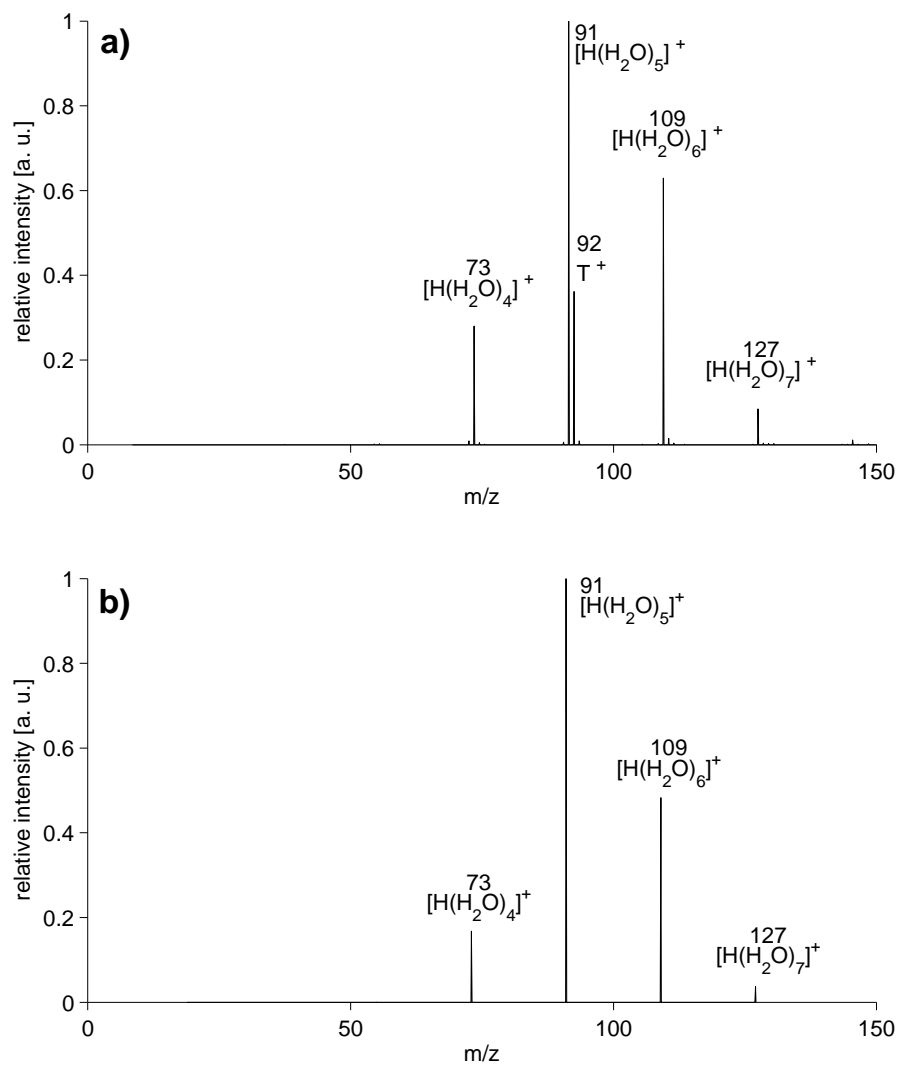


Figure 4.1: a) Primary ion distribution in the positive ion mode for APLI of toluene with roughly 500 ppmV water mixing ratio. b) Calculated cluster distribution (500 ppmV water, standard conditions).

for ion generation gave similar results. As expected, the proton bound water cluster distribution showed a high dependence on the water mixing ratio present in the ion source and on the voltages applied to the ion optics. Furthermore, a dependence on the pressure of the first two vacuum stages was observed, when the pressure difference and the distances between the skimmers were adjusted in a way that adiabatic expansions penetrated through the orifice. A detailed description of the proton bound water cluster system examined with this instrumental setup is given by Albrecht et al. [247] and Klee et al. [56]. The upper mass spectrum in figure 4.1 shows an exemplary cluster distribution for a pressure of approximately 3 mbar in the first pumping stage and a voltage of 5 V applied to the first skimmer while the second skimmer is grounded. A thermal cluster size distribution is observed. The signal at m/z 92 corresponds to the toluene radical cation. The water mixing ratio is about ppmV as the ion source was opened frequently and no efforts were made to lower the water mixing ratio, e.g., by flushing the source with the boil-off of liquid nitrogen. The lower panel of the figure shows a calculated signal distribution, using the rate constants from Kebarle et al. [57] and Lau et al. [262]. A water mixing ratio of 500 ppmV and a mixing ratio of 100 pptV (at standard conditions) for the initial charge carrying species, H_3O^+ , were assumed, which is reasonable for the given conditions. Only cluster sizes up to $n = 6$ were considered, as rate constants for the cluster growth and the reverse reaction for larger clusters were not available in the literature.

The comparison of the measured and the calculated cluster distribution clearly shows that thermal sampling is achieved with this setup, as the observed and calculated intensities of the cluster signals are nearly identical. Thus, the instrument is suitable for the examination of the ionization mechanism in negative ion mode.

4.2 Reagent Ions

Initially, the reagent ion distribution obtained from the ionization of toluene by APLI was studied. Nitrogen, oxygen and water were present in the ion source, as synthetic air was used to provide a clean gas stream and water is inevitably present in atmospheric pressure ion sources. Figure 4.2 a) shows the primary ion distribution when only background water is present (around 0.05 %V) and a voltage of -3 V is applied to the first skimmer. This voltage is not sufficient to induce CID processes but leads to a significant increase of the ion transmission. A thermal superoxide water cluster distribution, $[\text{O}_2(\text{H}_2\text{O})_n]^-$, is observed, with cluster sizes up to $n = 3$ and the maximum at $n = 2$. In addition an O_4^- signal is present. The water cluster distribution is in agreement with kinetic simulations using rate constants known from the literature [263]. As expected no signal that corresponds to the dopant molecule was detected. Toluene exhibits a negative electron affinity ($E_A = -1.11$ eV [101]) and a very low gas-phase acidity [264]. A weak signal at m/z 32, corresponding to O_2^- , is observed with an intensity of ~ 0.07 %.

Dependence of the Signal Distribution on the Water Mixing Ratio Similar to the proton bound cluster distribution, the superoxide cluster distribution is highly dependent on the water mixing ratio inside the ion source as predicted by the kinetic simulations. Figure 4.2 shows the primary ion distribution with a) less than 500 ppmV water present and b) with 0.2 % water added. All other conditions were held constant for both measurements.

On addition of water, the cluster maximum shifts from $n = 2$ to $n = 3$ and cluster sizes up to $n = 5$ appear. When the water mixing ratio is further increased, the cluster distribution shifts to even higher cluster sizes, in agreement with the kinetic model.

The reactivity of the superoxide water clusters changes with the cluster size. The electron affinity increases with increasing cluster size, as calculated from the Gibbs free enthalpies obtained from experiments [265] or theoretical calculations [266]. The results are in agreement with *ab initio* calculations carried out during this work. The latter also show that the gas-phase basicity of the larger clusters decreases significantly. The ionization efficiency decreases when the water mixing ratio in the ion source is increased because charge transfer or proton abstraction reactions are less likely to occur.

This effect is directly observed when the water mixing ratio inside the ion source is varied and the normalized signal intensity of the analyte signal peak is monitored. Figure 4.3 shows the normalized signal intensity of the $[M-H]^-$ signal of 3-methyl-2-nitrophenol (3M2NP) for water mixing ratios from 0.2 to 1.9 %, measured with the ion trap mass spectrometer. It is clearly evident that the signal intensity decreases drastically as the water mixing ratio is increased. The water mixing ratio is around 100 ppmV in pure synthetic air. For mixing ratios higher than 1.5 % the ionization efficiency decreases almost to zero. This experiment strongly supports the assumption that the water mixing ratio is a crucial parameter for the ionization efficiency of negative ionization methods when oxygen is used as reagent gas.

Measurements with the ion trap mass spectrometer and cAPECI source design 1 (see section 3.7.5) with different water mixing ratios gave similar results. To compare the sensitivity for different water mixing ratios, a 5 Å molecular sieve was placed upstream of the ion source gas inlet. Water is efficiently captured by the molecular sieve so that the water mixing ratio inside the ion source was considerably reduced compared to ambient air. Since an exact water mixing ratio was not measured only qualitative conclusions are drawn in the following.

Figure 4.4 shows the extracted ion chromatogram of the $[M-H]^-$ ion of 3-methyl-2-nitrophenol when measured in ambient air (0 to 5.5 min) and when the molecular sieve was used to reduce the water mixing ratio (5.5 to 10 min). Reducing the water mixing ratio inside the ion source results in an increase of the signal intensity by a factor of 3. The signal peak at the beginning of the measurement with the molecular sieve (at 5.5 min) is attributed to charging effects on the capillary walls which are described in detail in chapter 5.

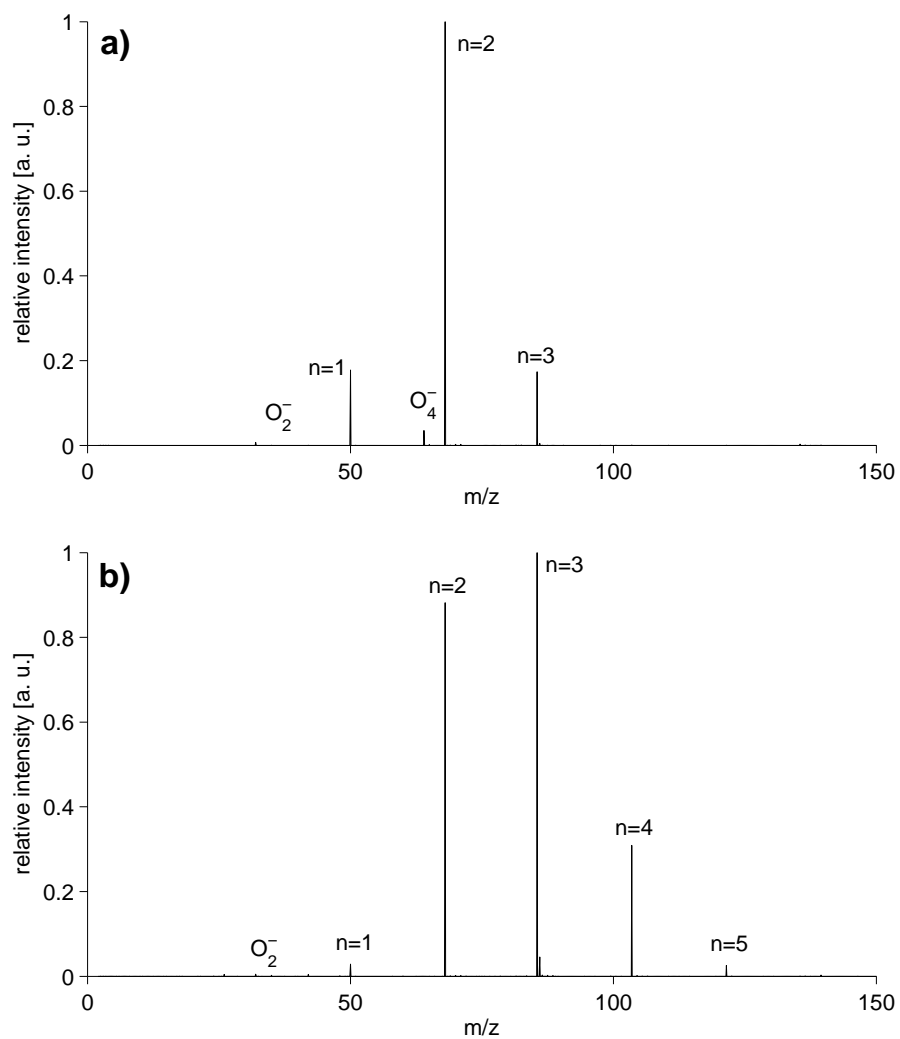


Figure 4.2: Superoxide cluster distribution when a) no additional water is present in the ion source (≤ 500 ppmV) and b) with 0.2 %V water added under otherwise similar conditions.

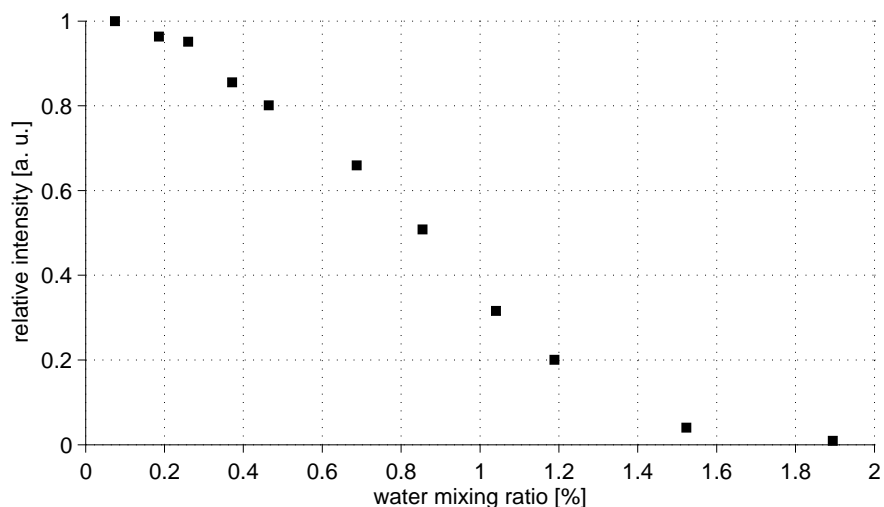


Figure 4.3: Dependence of the normalized signal intensity of the most abundant $[M-H]^-$ signal of 3-methyl-2-nitrophenol on the water mixing ratio.

A comparison of the mass spectra of 3-methyl-2-nitrophenol for the two different water mixing ratios inside the ion source is shown in figure 4.5. A decreased water mixing ratio results in a highly increased signal intensity of the $[M-H]^-$ ion. However, for elevated water mixing ratios, as in ambient air (lower panel of figure 4.5, around 1.5 % water) additional signals appear in the mass spectrum. The $[M+O_2]^-$ signal is present in the spectrum even when the level of CID processes is increased. The other two signals at m/z 137 and 167 are attributed to ion molecule reactions which were not further investigated.

Ionization via the Photoelectric Effect A low pressure mercury UV lamp was used to provide photons for photoelectron generation (see section 3.7.2). The main wavelengths emitted by this lamp are 254 nm and 185 nm in addition. Thus, ozone is generated by photolysis, when oxygen is present in the ion source. When water is present, hydroxyl radicals are generated by photolysis of water as well. The primary ion distribution may be shifted to these radical ions when ionization takes place via the photoelectric effect and not by laser ionization. To ascertain if this is the case kinetic simulations were performed.

The corresponding reactions are shown in R 3.5 to R 3.14. Many of the radicals and reaction products cause ion-transformation processes. However, a short reaction time can minimize their occurrence in the mass spectra, as stated previously. The ion-molecule/radical reactions and photolysis products can also act as primary charge carrying species. These products can alter the ionization mechanism described in the following in which superoxide, O_2^- , is the main reagent ion. In the following, an

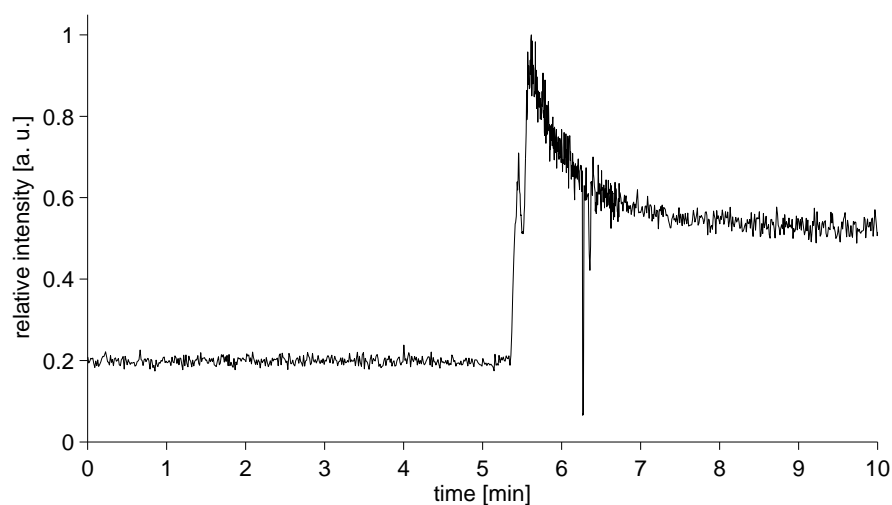


Figure 4.4: Extracted ion chromatogram of the $[M-H]^-$ signal of 3-methyl-2-nitrophenol measured in ambient air (0 to 5.5 min) and when the water mixing ratio is reduced by a 5 Å molecular sieve (5.5 to 10 min).

estimation based on kinetic data is made to investigate to what extent these radicals play a role as electron capturing species. As ion source the cAPECI source design 1 was assumed (for further details regarding the simulation conditions see section 3.2).

The kinetic simulation predicted a linear increase of the hydroxyl and ozone mixing ratio. Ozone is produced relatively fast with a rate of 2×10^{13} molecule $\text{cm}^{-3} \text{s}^{-1}$ compared to 4×10^{12} molecule $\text{cm}^{-3} \text{s}^{-1}$ for OH radicals. The residence time of molecules in the irradiated area in the cAPECI source design 1 is 400 μs . This is the maximum photolysis time. The mixing ratios of ozone and hydroxyl radicals present inside the reaction volume within this time (see figure 4.6) were 6.7×10^9 molecule cm^{-3} and 1.8×10^9 molecule cm^{-3} , respectively, corresponding to mixing ratios of 270 pptV ozone and 380 pptV hydroxyl radicals. Compared to these values oxygen is present in a 1×10^8 fold excess.

In a further simulation the electron capture process was also taken into account (reactions R 3.1 to R 3.4). A mixing ratio of 100 pptV for the thermalized photoelectrons was assumed, which represents an upper limit as the experimentally determined electron mixing ratios were considerably lower. The simulation resulted in concentrations of 2.4×10^9 molecule $\text{cm}^{-3} \text{s}^{-1}$ for O_2^- and essentially zero for O^- and OH^- . Their concentrations only start to rise after several microseconds. Provided the charge transfer from O_2^- to OH is feasible, which is speculated to be highly efficient because of the higher electron affinity of OH compared to O_2 [101], along with a collision controlled reaction rate constant of 1×10^{-9} cm^3 molecule $^{-1} \text{s}^{-1}$, an OH^- concentration of 5.3×10^6 molecule cm^{-3} after 400 μs results. Even in this case O_2^- is in 500-fold

4 Ionization Mechanism in Negative Mode API-MS

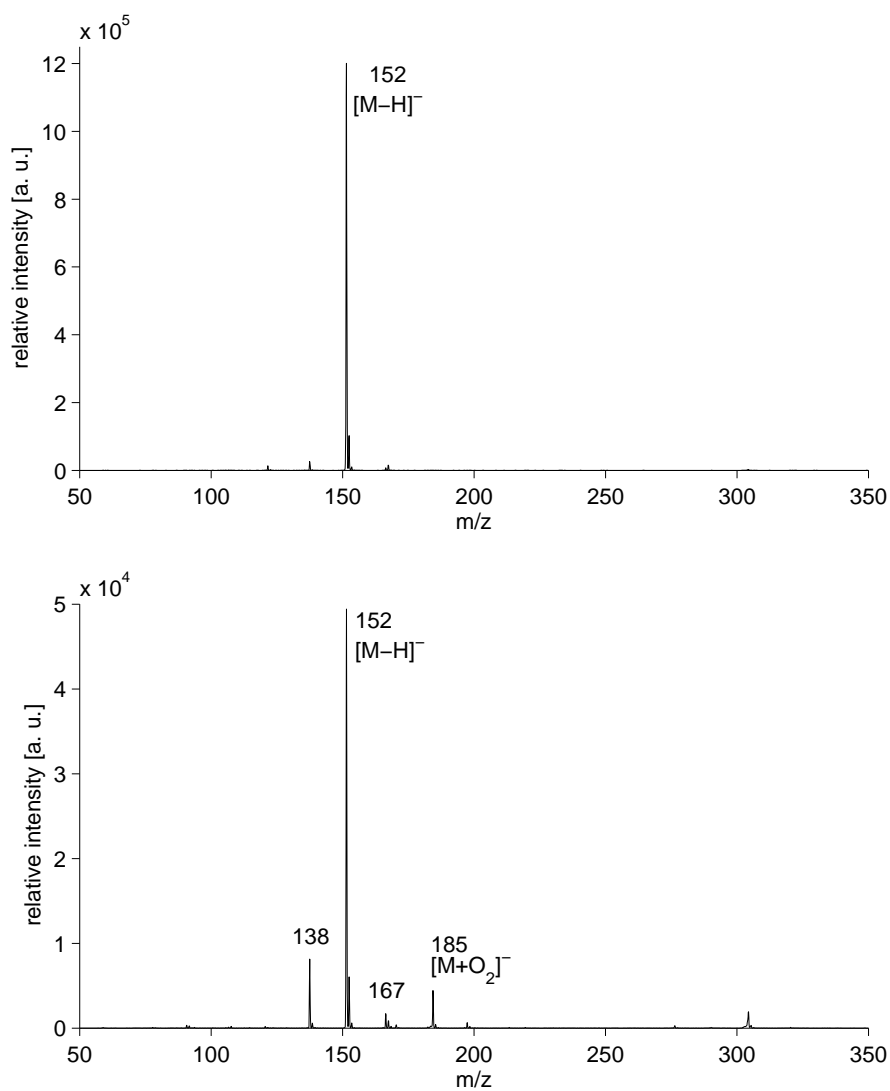


Figure 4.5: Mass spectra of 3-methyl-2-nitrophenol recorded with the ion trap mass spectrometer for two different water mixing ratios: Low water mixing ratio due to the use of a 5 Å molecular sieve (upper panel) and ambient air (approximately 1.5 %, lower panel).

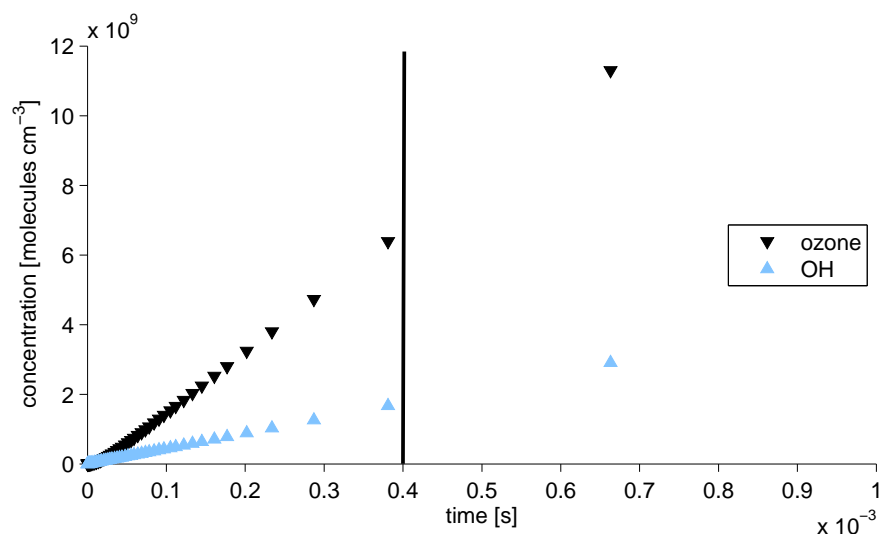


Figure 4.6: Concentration profiles obtained from kinetic simulations of O_3 and OH when 20 % O_2 , 79 % N_2 and 1 % water are present.

excess.

The kinetic simulations clearly show that even when a low pressure mercury lamp is used for ionization the only important reactive species is O_2^- with air as carrier gas. The low concentrations of ozone and hydroxyl radicals generated cannot compete with oxygen molecules in electron capture reactions to any significant extent.

4.3 Formation of Molecular Anions

To examine the ionization mechanism leading to M^- ions, p-benzoquinone (108 Da) was chosen as analyte, due to its high electron affinity (1.9 eV [264]). In figure 4.7 a) the thermally sampled mass spectrum of p-benzoquinone is shown. A mixing ratio of approximately 130 ppmV p-benzoquinone was present in the ion source. The high mixing ratio of the analyte leads to low intensities of the reagent ions in this mass spectrum. Besides the distribution of reagent ion clusters, the M^- of the analyte and an analyte water cluster, $[M(H_2O)]^-$, are observed. The analyte anion has the highest abundance. There are three signals (m/z 142, 217 and 249) in the spectrum which are not easily explainable. The signal at m/z 142 could possibly be ascribed to $[M(H_2O)+O]^-$, but as this signal was not observed in all other mass spectra it is more likely that it is not attributable to the analyte. For both signals at higher masses neither the intensity nor the m/z ratio change with the voltage applied to the first skimmer, which makes it most likely that these signals are due to contaminations in the ion source and not to cluster or adduct ions.

4 Ionization Mechanism in Negative Mode API-MS

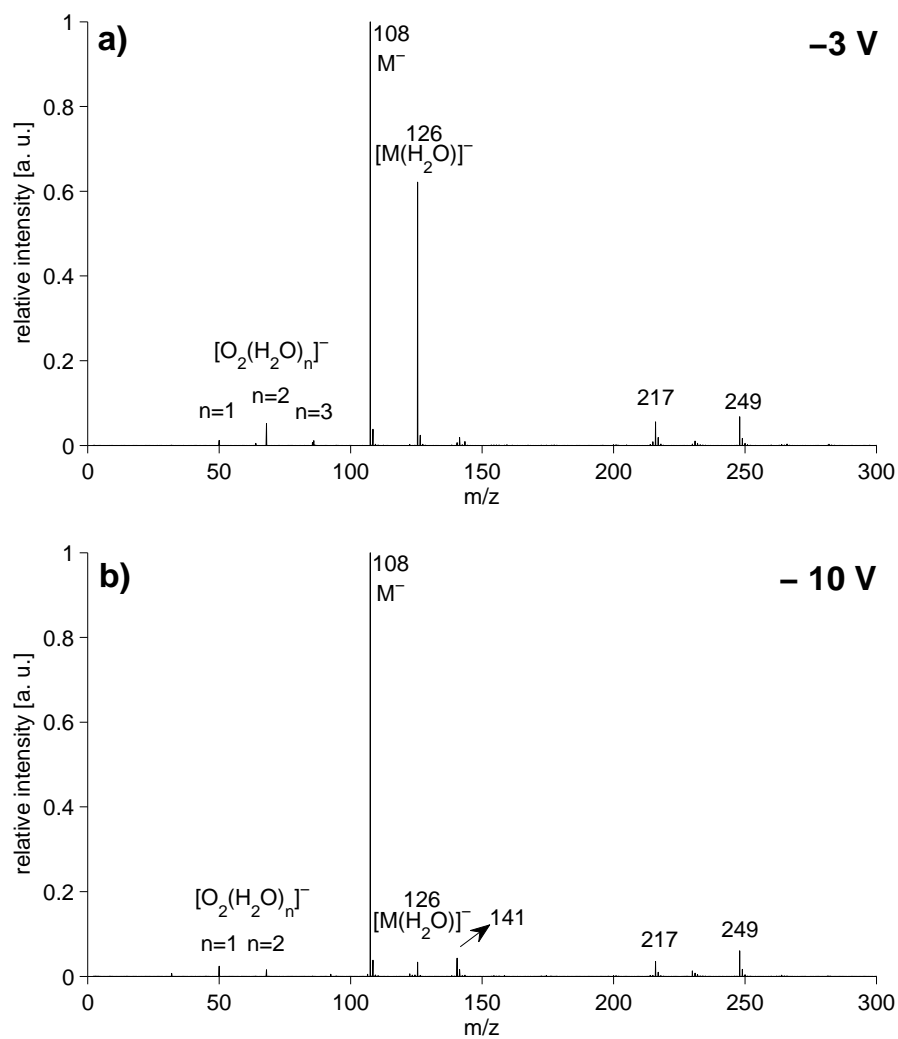


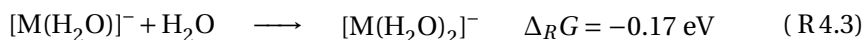
Figure 4.7: Mass spectra of p-benzoquinone in a) the absence of CID processes (-3 V) and b) when -10 V are applied to the first skimmer.

Collision Induced Dissociation In figure 4.7 a thermally sampled mass spectrum is compared with a spectrum recorded with a slightly increased level of CID in the mass spectrometer inlet stage. This was achieved by applying a voltage of -10 V to the first skimmer. The increased kinetic energy in the second vacuum region gives rise to CID processes, which lead to a decrease in cluster size. The mass spectrum shows only superoxide clusters of size $n = 1$ and $n = 2$. With a voltage of -10 V the analyte water cluster abundance is decreased to approximately 5% of the initial intensity and the M^- signal becomes the only intense signal in the mass spectrum. The unidentified signals at higher masses remain unchanged. The signal at m/z 142 has shifted to m/z 141 which contradicts the notion that it is assigned to an $[M(\text{H}_2\text{O})+\text{O}]^-$ ion. The spectrum under increased CID conditions is very similar to the results obtained with the commercially available ion trap mass spectrometer, were CID processes inevitably occur. Here, M^- is the only signal recorded. A significant difference between the spectra from both instruments is the superoxide peak that is not observed with the ion trap mass spectrometer, due to the cut off of low mass-to-charge ratios.

The base peak in the mass spectrum is the analyte anion even under CID-free conditions. This strongly supports the notion that the ionization mechanism leading to M^- does not proceed via adduct formation with primary charge carrying species. No analyte-oxygen adduct ions are observed under any of the conditions employed during these experiments. Direct charge transfer is thus the most likely ionization pathway:



Small superoxide water clusters may also lead to charge transfer, depending on the electron affinity of the analyte. For p-benzoquinone, the reaction with O_2^- is exothermic by -1.45 eV^1 , therefore no additional energy is necessary for this reaction to proceed. The analyte-water adduct is thus most likely formed after the charge transfer to benzoquinone from superoxide has taken place. As water exhibits a negative electron affinity, a benzoquinone anion and a neutral water molecule are the reactants for the cluster formation. This reaction scheme is also supported by *ab initio* calculations, shown in the values of the Gibbs free energies of the reactions.



Dependence on the Water Mixing Ratio As stated previously, the increase of the water mixing ratio leads to a shift of the cluster distribution to larger cluster sizes. Furthermore, when p-benzoquinone is present, the analyte water cluster distribution, $[\text{M}(\text{H}_2\text{O})_n]^-$, is also shifted to larger water cluster sizes. This is seen in figure 4.8 with a

¹As calculated from the values found in [264], *ab initio* calculations gave a value of -1.61 eV .

4 Ionization Mechanism in Negative Mode API-MS

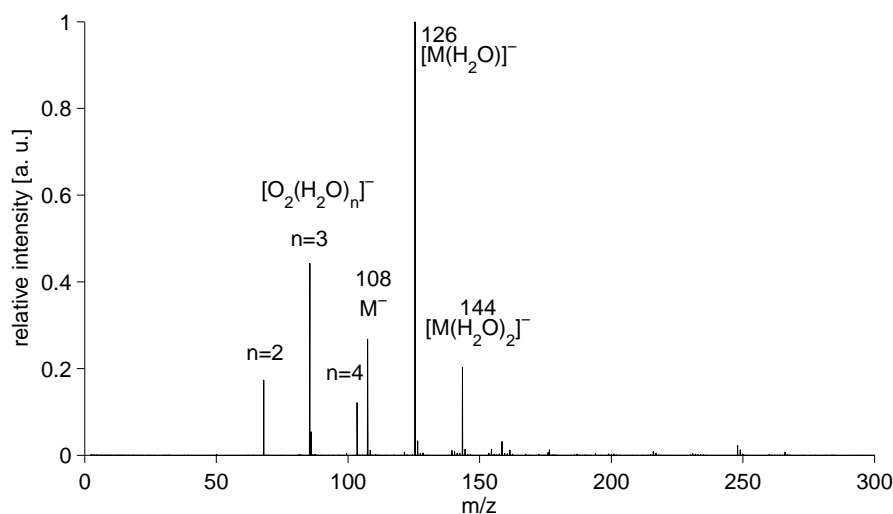


Figure 4.8: Mass spectrum of p-benzoquinone when 0.2 % water is present in the ion source.

water mixing ratio of 0.2 % present. The signal with the highest abundance shifts from M^- for relatively dry conditions (see figure 4.7 a) approximately 0.05 %) to the smallest analyte-water cluster and the cluster with $n = 2$ is observed as well. The superoxide water cluster distribution also shifts to larger cluster sizes, as expected.

Ambient Air With the ion source developed during this work it should be readily possible to detect analytes in laboratory air. Thus, the thermal ion distribution of laboratory air was also studied for p-benzoquinone, as shown in figure 4.9. Due to the comparably high water mixing ratio in laboratory air, the cluster distribution for the reagent ion clusters and the analyte water clusters is shifted to larger cluster sizes. Both, the superoxide water cluster distribution and the analyte water cluster distribution exhibit a maximum at $n = 3$. In figure 4.9, the light blue curve traces the distribution of analyte water clusters. For this cluster type, even clusters with more than five water molecules are observed. The dark blue curve traces a second water cluster distribution at higher mass-to-charge ratios with a maximum at m/z 234. The signal at m/z 216 is possibly due to the $[M(H_2O)_6]^-$ ion and thus associated to the first cluster distribution (light blue dotted curve) or to the p-benzoquinone dimer, $[M+M]^-$. This dimer may be the starting point for the second distribution, i.e., dimer water clusters of the type $[M+M(H_2O)_n]^-$. However, as the TOF instrument did not allow controlled CID experiments, the identification of these signals was not possible. The increase of the voltage applied to the first skimmer from -3 V to -15 V gave no conclusive results.

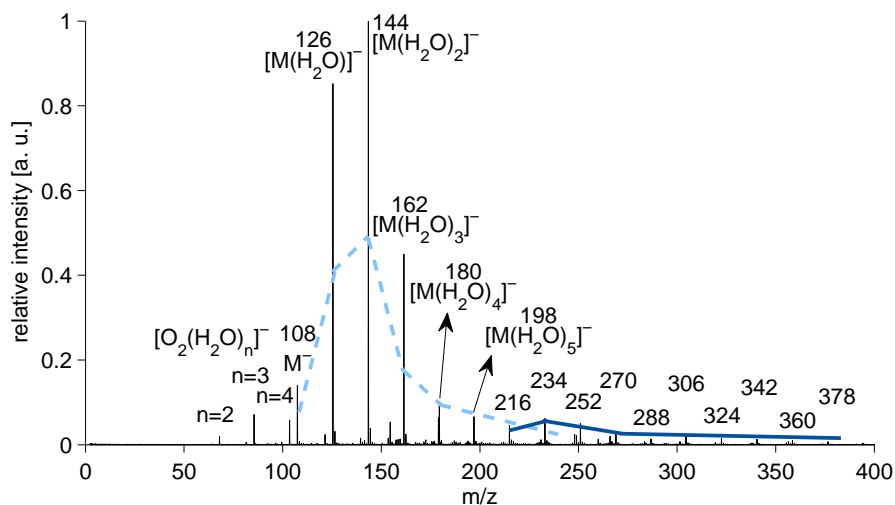


Figure 4.9: Mass spectrum of p-benzoquinone measured in ambient air.

4.4 Formation of Deprotonated Anions

While analytes with high electron affinities form mainly M^- signals in the negative ion mode, analytes with a high gas-phase acidity form $[M-H]^-$ ions when oxygen is used as primary charge carrying species. To examine the ionization mechanism 3-methyl-2-nitrophenol was chosen as a representative analyte (molecular mass of 153 g mol^{-1}).

Under nearly CID free conditions, i.e., -3 V applied to the first skimmer, the mass spectrum shown in figure 4.10 is obtained. Due to the lower mixing ratio of the analyte compared with the p-benzoquinone experiment, the abundance of the reagent ion clusters is much larger than in figure 4.7. Furthermore, O_2^- and O_4^- signals are observed. Three signals are assigned to the analyte, i.e., an analyte oxygen adduct, $[M+O_2]^-$, an analyte dimer, $[M+M-H]^-$ and an analyte dimer oxygen adduct, $[M+M+O_2]^-$. In contrast to p-benzoquinone, there are no adduct signals that contain the analyte and water molecules. While $[M-H]^-$ is the most intense signal for this compound with commercially available mass spectrometers, no such signal is observed under nearly CID free conditions.

A hypothetical pathway leading to $[M-H]^-$ ions is a reaction cascade similar to the “ligand-switching/ligand-association” mechanism, that has been confirmed for many ionization methods in positive ion mass spectrometry (cf. reactions R 1.10 and R 1.11 in section 1.3.1) [56, 112–115]. This is also the case in NI-MS, if one of the following reactions take place:

4 Ionization Mechanism in Negative Mode API-MS

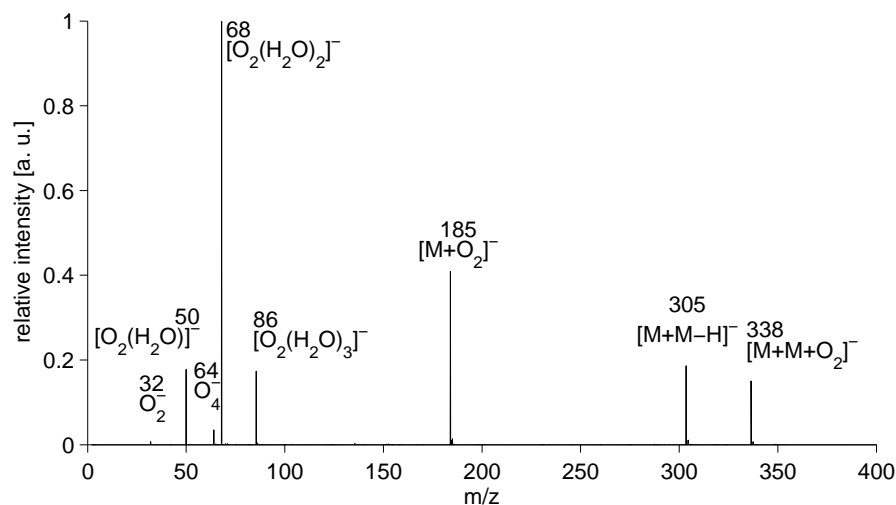
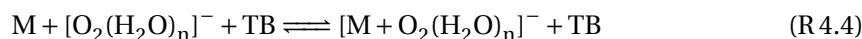


Figure 4.10: Mass spectrum of 3-methyl-2-nitrophenol under CID free conditions.



with TB denoting a third body reaction partner. The cluster ions then dissociate to the $[\text{M}-\text{H}]^-$ ion through CID processes inside the ion optics of the mass spectrometer. When this mechanism is valid, analyte oxygen water clusters should be observed under CID free conditions. However, these clusters are not observed in the mass spectra, which strongly supports that this mechanism is not a major pathway.

Even though there is no $[\text{M}-\text{H}]^-$ ion signal present in figure 4.10 the dimer signal at m/z 305 is formed. The most likely explanation for the occurrence of this ion is the decomposition of $[\text{M}+\text{M}+\text{O}_2]^-$ to $[\text{M}+\text{M}-\text{H}]^-$ and HO_2 which takes place even at the very low voltages applied to the first skimmer. This assumption is supported by the fact that, even under the comparably high CID conditions of common mass spectrometers, $[\text{M}+\text{M}+\text{O}_2]^-$ cannot be observed in the mass spectrum, while both of the other analyte signals are present, i.e., $[\text{M}+\text{O}_2]^-$ and $[\text{M}+\text{M}-\text{H}]^-$ (see figure 4.12).

Another possible rate leading to $[\text{M}+\text{M}-\text{H}]^-$ is the dissociation of the analyte oxygen adduct to $[\text{M}-\text{H}]^-$, which then clusters with a neutral analyte molecule. However, $[\text{M}-\text{H}]^-$ is virtually absent in the mass spectrum and in addition the mixing ratio of the analyte is comparably low. Furthermore, the ratio of both signals does not show a dependence on the mixing ratio of 3-methyl-2-nitrophenol.

There are two possible reaction pathways leading to the signal with the highest abundance that includes analyte molecules, $[\text{M}+\text{O}_2]^-$: adduct formation of the neutral

analyte with superoxide ions and direct charge transfer from superoxide to the analyte followed by adduct formation of the analyte anion with neutral oxygen. The absence of a M^- signal in the mass spectrum does not necessarily exclude the second reaction pathway as oxygen is in large excess over the analyte ions with a mixing ratio of approximately 20 %, which shifts the reaction to the side of the adduct. In the investigation of the ionization of trinitrotoluene by ^{63}Ni - β -radiation by Daum et al. [267] both pathways are proposed to take place simultaneously. *Ab initio* calculations carried out in this work support these reaction pathways.

Another hint on the ionization pathway is the absence of analyte oxygen water clusters. Adduct formation only takes place with superoxide and not with superoxide water clusters. Alternatively all water molecules leave the cluster when cluster and analyte react. However, this is energetically not favored as shown by *ab initio* calculations. Furthermore, the ionization efficiency decreases drastically when the superoxide water cluster size increases (see figure 4.3), which merely rules out this pathway. An increase of the water mixing ratio present in the ion source only shifts the superoxide cluster distribution to larger cluster sizes and decreases the ionization efficiencies of the analyte.

Collision Induced Dissociation The increase of the voltage applied to the first skimmer increases the level of CID processes during the transfer of the ions. Figure 4.11 demonstrates this effect of mass spectra of 3-methyl-2-nitrophenol. Due to the change in ion transfer efficiency the intensity of each spectrum is normalized to the largest signal. With increased CID the superoxide cluster distribution is shifted to the bare superoxide signal. The decrease of the total reagent ion intensity is due to the instrument's ion transmission characteristic. It decreases for small mass-to-charge ratios when the voltages applied to the ion optical devices, e.g., skimmers, is increased, while the overall ion transmission improves.

More interesting is the shift of the recorded analyte signals: while a slight increase of the voltage applied to the first skimmer to -7 V does not change the mass spectrum significantly, a further increase to -10 V leads to the appearance of the $[\text{M}-\text{H}]^-$ signal and a decrease of the dimer oxygen cluster. With higher voltages, the intensity of this signal decreases to zero, supporting the assumption that the stability of this ion is comparably low. For extensive CID, the $[\text{M}-\text{H}]^-$ signal is the most abundant signal, the dimer and the analyte oxygen adduct are present only with a very low intensity. This observation supports an ionization mechanism that proceeds via the dissociation of $[\text{M}+\text{O}_2]^-$ by CID processes² for the formation of the $[\text{M}-\text{H}]^-$ signal. The mass spectrum with extensive CID (-20 V) is nearly identical to the mass spectrum of this compound obtained with the commercially available ion trap mass spectrometer shown in figure 4.12. Standard settings for this instrument were selected for the recording of this spectrum. The superoxide signal is not observed with the ion trap due to the low mass-to-charge ratios cut off.

²DFT calculation yield an energy of 0.71 eV necessary to dissociate the $[\text{M}+\text{O}_2]^-$ to the $[\text{M}-\text{H}]^-$.

4 Ionization Mechanism in Negative Mode API-MS

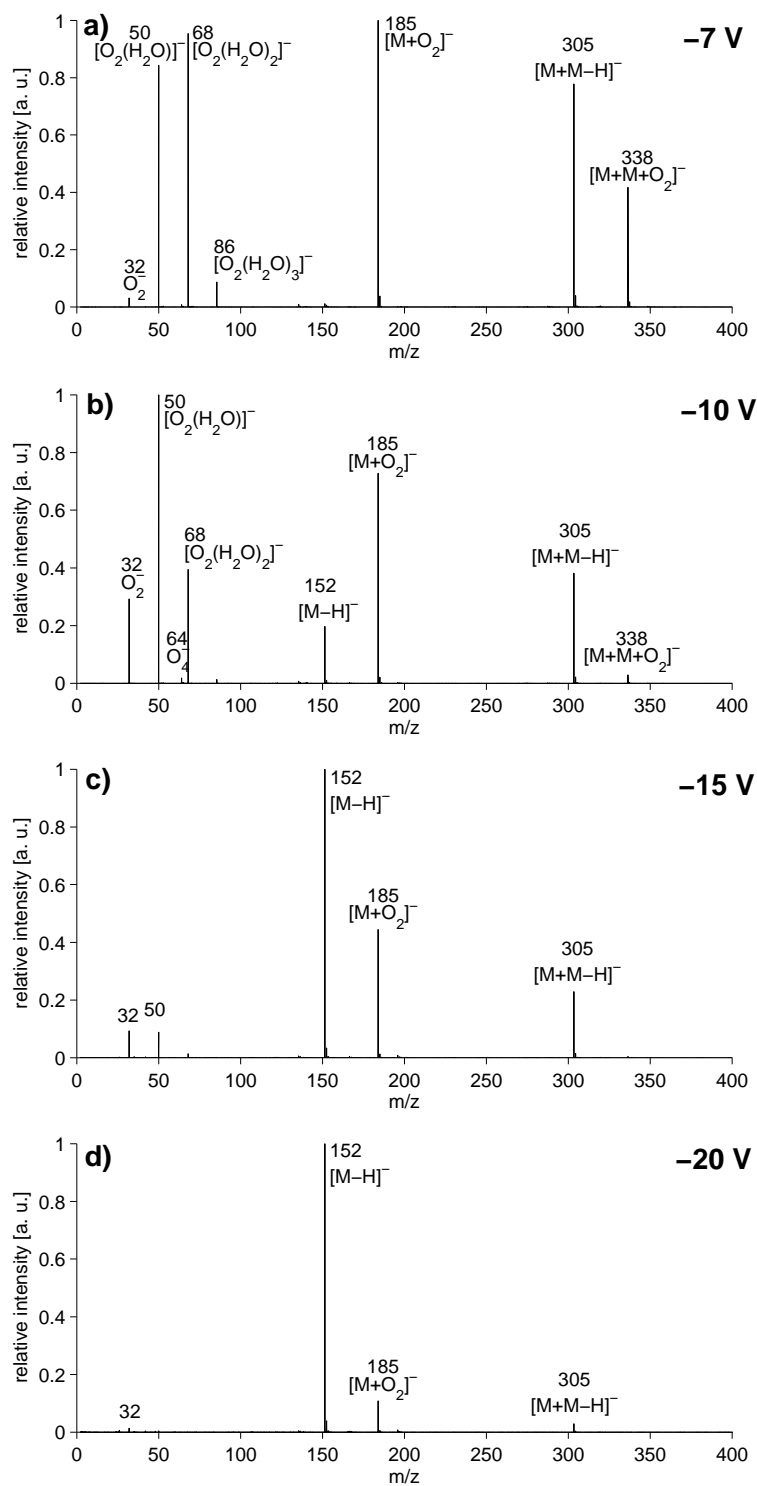


Figure 4.11: Mass spectra of 3-methyl-2-nitrophenol for different extents of CID. Voltages of a) -7 V, b) -10 V, c) -15 V and d) -20 V were applied to the first skimmer.

4.4 Formation of Deprotonated Anions

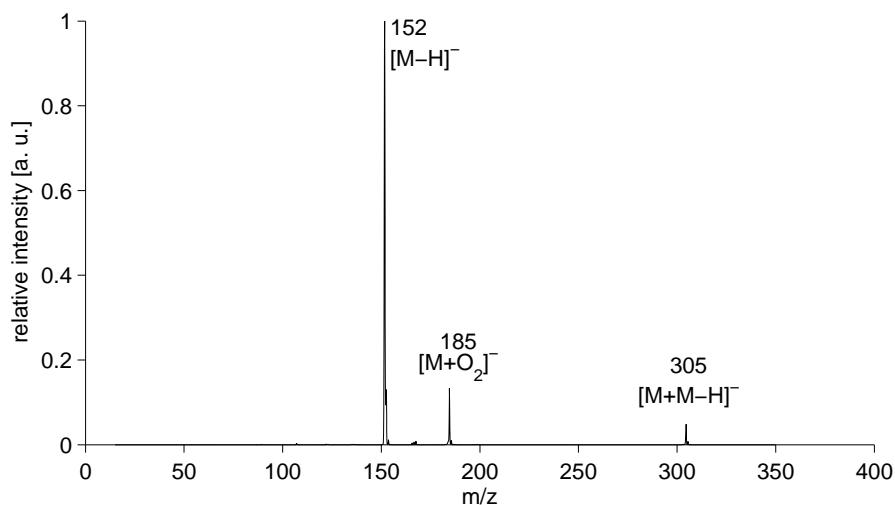
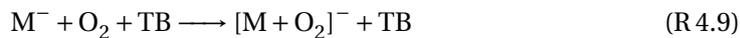
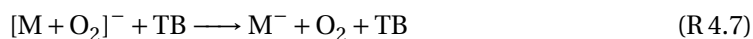
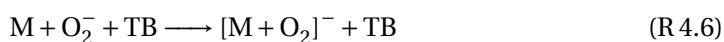


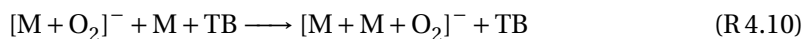
Figure 4.12: Mass spectrum of 3-methyl-2-nitrophenol recorded with the ion trap mass spectrometer.

When 2-methyl-4-nitrophenol is used as analyte similar signal patterns are obtained with the ion trap mass spectrometer. This indicates that the formation of oxygen adducts is not due to an “ortho effect” caused by the ortho position of the hydroxyl- and nitro-groups. The position of substituents on the aromatic ring is known to affect the reactivity of the aromatic analyte [226].

The proposed ionization mechanism leading to $[M-H]^-$ derived from the experimental results mentioned, which are supported by *ab initio* calculations is as follows:



For elevated analyte mixing ratios reactions R 4.10 and R 4.11 must also be taken into account.



4 Ionization Mechanism in Negative Mode API-MS

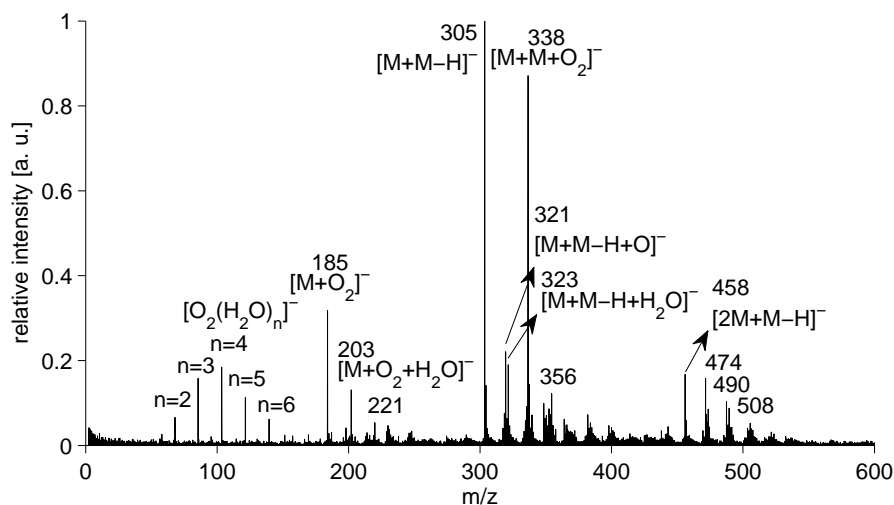


Figure 4.13: Mass spectrum of 3-methyl-2-nitrophenol in laboratory air.

Reactions R 4.7 and R 4.8 only proceed when additional energy is delivered. For CID free conditions $[M+O_2]^-$ is the most abundant signal in the mass spectrum and $[M-H]^-$ upon CID. For higher mixing ratios, dimer clustering with oxygen and the $[M+M-H]^-$ signal are observed under essentially CID free conditions. With commercially available instruments, i.e., CID processes inevitably occur during transfer thus only the $[M+M-H]^-$ cluster is present, as the stability of the $[M+M+O_2]^-$ ion is insufficient.

With the ion trap mass spectrometer the same ion distribution is obtained for other representatives of this compound class. For typical levels of CID in transfer stages the $[M-H]^-$ signal has the largest intensity. The analyte oxygen adduct and the $[M+M-H]^-$ signal are also observed, especially when the voltages applied to the ion optics and inside the ion trap are reduced. The ionization mechanism is most likely applicable to the entire compound class.

Ambient Air The mass spectrum of 3-methyl-2-nitrophenol in laboratory air was recorded (see figure 4.13). A voltage of -7 V was applied to the first skimmer. The water mixing ratio has been comparably high during this measurement as the maximum of the superoxide water cluster distribution is at $n = 4$ and even clusters with $n = 6$ were observed. Many more identifiable signals occur compared with the spectrum recorded in synthetic air. The most abundant signal is the $[M+M-H]^-$ signal at m/z 305, followed by the $[M+M+O_2]^-$ signal. In addition to the signals observed in synthetic air, one cluster distribution and several other signals are observed. The cluster distribution consists of the $[M+O_2+(H_2O)_n]^-$ progression which may be abundant due to the strongly increased water mixing ratio. However, in synthetic air this cluster type

was not observed even for high water mixing ratios. Furthermore, signals assignable to $[M+M-H+O]^-$, $[M+M-H+H_2O]^-$ and $[M+M+M-H]^-$ are present. The trimer ion signal is due to the relatively high analyte mixing ratio, but the mechanism leading to the other ions remains unclear and needs further investigation. In addition signals occur that cannot be assigned to a specific ion, for example, the signal at m/z 474 and the following three signals (cf. figure 4.13), which may be an $[3M-H+O_n]^-$ cluster distribution. Therefore, no rationale on the formation of these ions is given here.

In the literature, reagent ions other than superoxide and O_4^- are proposed when ionization takes place in laboratory air, since for example, OH^- , CO_2^- or water clusters of these ions [89, 119, 120]. However, none of these ions were observed in laboratory air, the ionization mechanism in laboratory air should be similar to that proposed for the measurements in synthetic air.

4.5 Dinitrotoluenes

Ionization of the different dinitrotoluene isomers is reported in the literature with various ionization methods. The use of different ionization methods leads to different signals particularly for 2,4-dinitrotoluene, with the M^- or the $[M-H]^-$ as main signals. All other dinitrotoluene isomers show the M^- signal for nearly all experimental conditions [104, 268–270]. The result for 2,4-dinitrotoluene is surprising as it does not contain an acidic proton.

When 2,4-dinitrotoluene is ionized with cAPECI both ions are observed. The signal ratio is highly dependent on the transfer time. Different reaction times were realized using two different ionization positions. For ionization inside the inlet capillary the reaction time is less than 1 ms. When the ionization takes place inside an ion source that is attached to the inlet capillary, the reaction times are considerably higher. The second ionization position is inside the laminar flow ion source, close to the entrance of the inlet capillary, leading to a reaction time of approximately 5 ms.

Ionization of 2,4-dinitrotoluene inside the inlet capillary leads to the expected M^- ion, while ionization inside the laminar flow ion source in front of the capillary results in the $[M-H]^-$ signal, as shown in figure 4.14. Furthermore, in addition to the $[M-H]^-$ ion, a signal at higher mass-to-charge ratios is observed in the mass spectrum for the longer reaction time, probably due to oxidation reactions [3].

Why 2,4-dinitrotoluene behaves differently than the other dinitrotoluene isomers is rationalized in terms of the Gibbs free enthalpies of reaction for the proton abstraction and electron capture, respectively. The Gibbs free enthalpies for these reactions were obtained from DFT calculations. The electron capture reaction is a feasible route for all isomers, but 2,4-dinitrotoluene has the most favorable Gibbs free enthalpy of reaction for the proton abstraction with -0.92 eV compared to the other isomers (-0.75 eV and 0.04 eV).

The measurements shown in figure 4.14 were carried out in synthetic air. As expected, in purified nitrogen only the M^- signal is observed independent of the reaction

4 Ionization Mechanism in Negative Mode API-MS

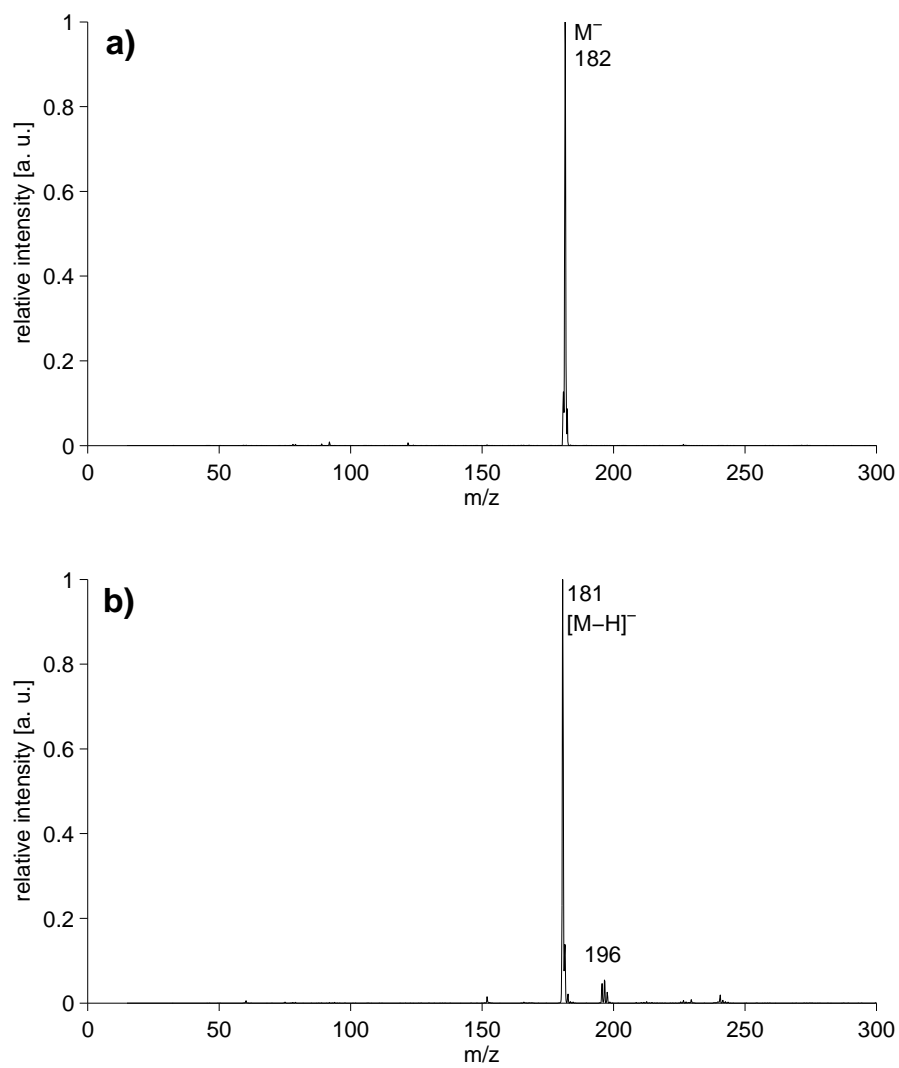


Figure 4.14: Mass spectra of 2,4-dinitrotoluene with a) 1 ms and b) 5 ms reaction time.

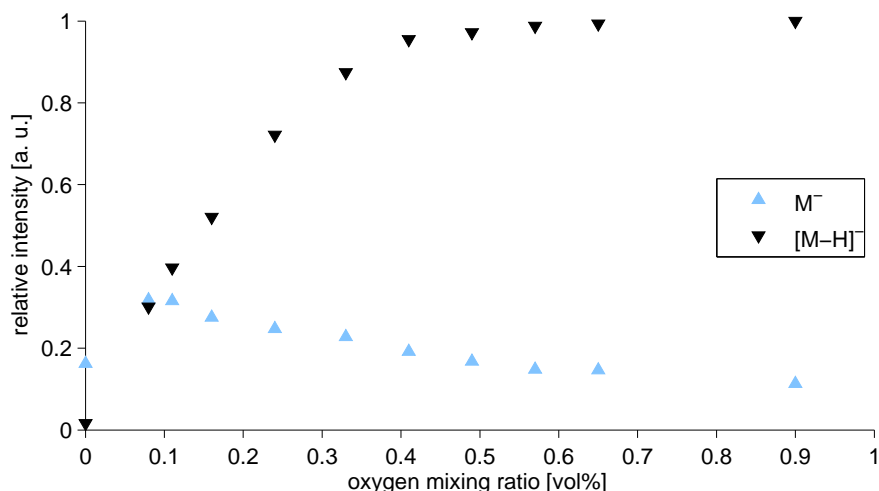
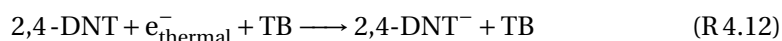


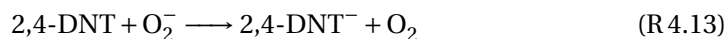
Figure 4.15: Measured signal intensities of the M^- and the $[M-H]^-$ of 2,4-dinitrotoluene as a function of the oxygen mixing ratio.

time. When small amounts of oxygen are added to the nitrogen gas stream, the intensity of the $[M-H]^-$ increases slowly for the longer transfer time. The dependence of the normalized signal intensities of both ions on the oxygen mixing ratio are shown in figure 4.15. Up to a mixing ratio of approximately 0.5 % the intensity of the $[M-H]^-$ signal increases and then remains constant. Surprisingly, the intensity of the M^- signal also increases slightly when small amounts of oxygen are added (around 0.1 %). When the oxygen mixing ratio is further increased, the intensity decreases again.

The formation of the M^- signal of 2,4-dinitrotoluene in pure nitrogen is ascribed to direct electron attachment, as no species that could capture the thermal electrons and as primary charge carrying species are present in this case.



As stated in the previous section and according to Daum et al. [267], the following reactions are involved in the formation of $[M-H]^-$ when oxygen is present with 5 ms reaction time:



4 Ionization Mechanism in Negative Mode API-MS

It is proposed that the oxygen adduct is quantitatively converted to $[M-H]^-$ by CID processes inside the ion optics of the ion trap. The formation of superoxide water clusters is not taken into account in the kinetic simulation. As mentioned before, the water clusters exhibit a lower reactivity with respect to charge transfer or proton abstraction compared to bare superoxide. Thus, these species serve as a charge sink and are not explicitly considered.

The system, described by reactions R 4.12 to R 4.15, is described by kinetic simulations to determine the ratio between the rate constants. Reactions R 3.1 and R 3.2 are used for the description of the generation of O_2^- . In the simulations, mixing ratios of 200 ppbV for 2,4-dinitrotoluene and 500 pptV for thermal electrons are assumed. The rate constants of the electron capture reactions of oxygen were taken from the literature, as stated in table 3.1. Rate constants for the other four reactions including 2,4-dinitrotoluene are estimated based on literature data and were iteratively adjusted to give a similar dependence of the signal intensities as for the experimentally obtained distribution shown in figure 4.15. From the simulations, which are depicted in figure 4.16, the following rate constants were calculated:

Reaction R 4.12	$4 \times 10^{-32} \text{ cm}^6 \text{ molecule}^{-2} \text{ s}^{-1}$
Reaction R 4.13	$5 \times 10^{-12} \text{ cm}^3 \text{ molecule}^{-1} \text{ s}^{-1}$
Reaction R 4.14	$1 \times 10^{-31} \text{ cm}^6 \text{ molecule}^{-2} \text{ s}^{-1}$
Reaction R 4.15	$2 \times 10^{-34} \text{ cm}^6 \text{ molecule}^{-2} \text{ s}^{-1}$

Oxygen mixing ratios lower than 0.1 % are naturally possible in the simulations but not in the experiments. Except for this mixing ratio range the simulated signal distribution for the addition of small amounts of oxygen is similar to that obtained by the measurements, with the rate constants given above. This strongly suggests that the proposed reaction scheme is a reasonable representation of the processes occurring. The rate constants determined in this study have a considerable uncertainty, as the mixing ratios for the thermal electrons and the analyte are only roughly estimated from the experimental conditions. The determination of exact values for the rate constants is subject to further investigations.

Sulfur hexafluoride has a considerably high thermal electron capture rate constant of $2.5 \times 10^{-7} \text{ cm}^3 \text{ s}^{-1}$ [271]. When small amounts of SF_6 are added to a nitrogen gas stream and ionization takes place with cAPECI, the main ion observed in the mass spectrum is SF_6^- (m/z 146). The use of synthetic air leads to a competitive situation between oxygen and sulfur hexafluoride for the electron capture. Due to the higher electron affinity (1.05 eV for SF_6 and 0.451 eV for oxygen) and the higher rate constant for the electron capture reaction, SF_6^- is formed preferably to O_2^- . This effect is observed when 2,4-dinitrotoluene is used as analyte, only small amounts of oxygen are present in a clean nitrogen gas stream and a considerably long reaction time of the ions

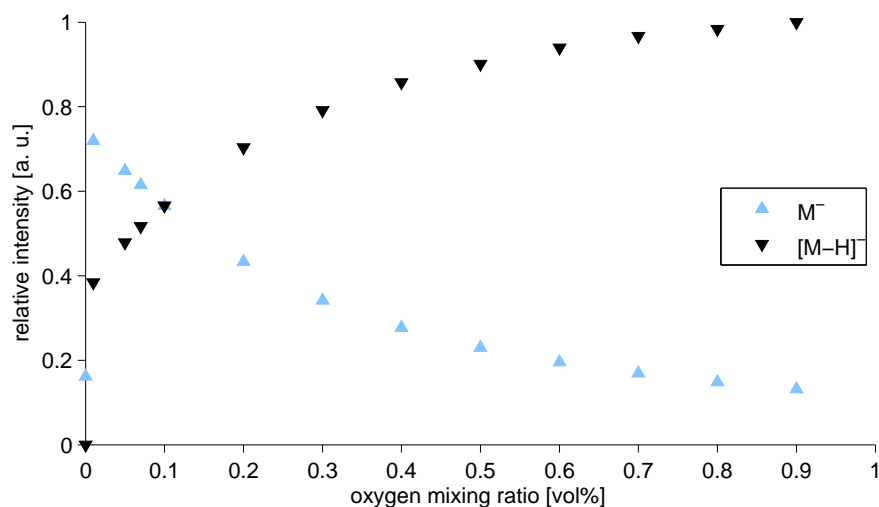


Figure 4.16: Dependence of the M^- and the $[M-H]^-$ of 2,4-dinitrotoluene on the oxygen mixing ratio obtained by kinetic simulations.

exists. In this setup, 2,4-dinitrotoluene forms $[M-H]^-$ due to proton abstraction by superoxide (see section 4.5). When small amounts of sulfur hexafluoride are added, the ion distribution shifts to the M^- ion as SF_6^- acts as electron transfer agent and does not possess a sufficient gas-phase basicity for proton abstraction from the analyte. Figure 4.17 shows the mass spectra when 0.5 % oxygen and 0.08 % sulfur hexafluoride are mixed into the nitrogen gas stream at a transfer time of 5 ms.

The oxygen mixing ratio is considerably high and should be sufficient to form the $[M-H]^-$ ion of 2,4-dinitrotoluene. However, the small amount of sulfur hexafluoride is enough to hinder the formation of superoxide and thus formation of the deprotonated analyte. The signal at m/z 146 corresponds to the SF_6^- ion. The signal at m/z 124 is also attributable to sulfur hexafluoride. In the literature a reaction between sulfur hexafluoride and water is reported which leads to the formation of the SF_4O^- ion [16].



The identity of the signal at m/z 124 as SF_4O^- ion was confirmed by MS^n experiments. Fragmentation of the m/z 124 signal yields solely a signal at m/z 105 and the difference in the mass-to-charge ratio can readily be explained by the loss of a fluorine atom.

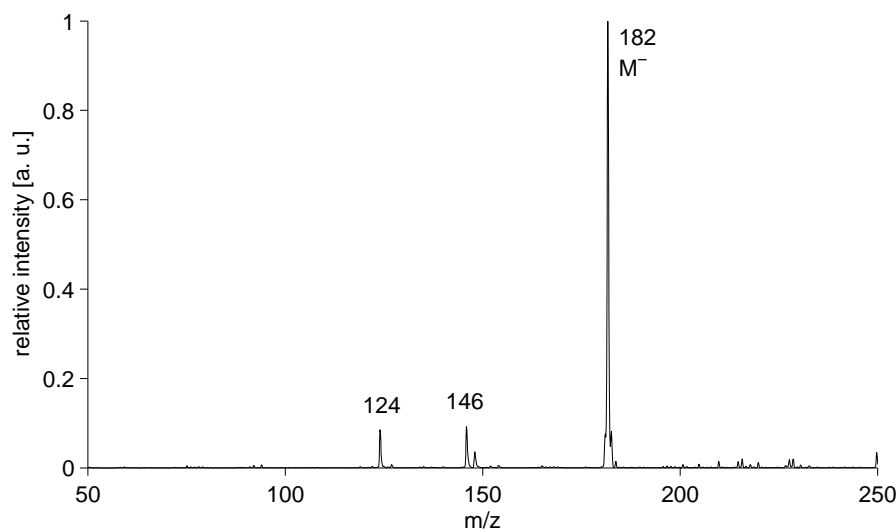


Figure 4.17: Mass spectrum of 2,4-dinitrotoluene with 5 ms transfer time when SF₆ (0.08 %) and oxygen (0.5 %) are present in a nitrogen gas stream.

4.6 Summary and Outlook

The ionization mechanism in the negative ion mode under comparably clean conditions was examined using dopant assisted APLI with a custom built quasi-thermally sampling mass spectrometer. Adiabatic expansions inside the ion optics of the mass spectrometer are minimized and collision induced dissociation processes are controlled, leading to mass spectra that are close to the ion distribution inside the ion source.

With synthetic air, the primary charge carrying species was identified as superoxide, O₂⁻ which subsequently forms water clusters, [O₂(H₂O)_n]⁻. At mixing ratios present in atmospheric pressure ion sources O₄⁻ was also observed. It is shown that the water mixing ratio is a crucial factor for the ionization efficiency of the instrument, as larger clusters are formed at higher mixing ratios which are less reactive. Furthermore, the voltages applied to the ion optics govern the level of CID processes and thus have large influence on the observed signal distribution.

With increasing CID the cluster distribution shifts to smaller cluster sizes. When analyte ions are present, M⁻ or [M-H]⁻ become the most intensive signals. The reaction pathways leading to these analyte ions were determined. *Ab initio* calculations for ion-molecule/radical reactions were carried out to examine, which reaction pathway is energetically most favored and fully support the experimental results. For the formation of the M⁻ ion of analytes with high electron affinity and low gas-phase basicity, direct electron transfer from superoxide and probably small superoxide water clusters

is assumed. After M^- is formed, cluster formation with water may occur, with the size of the cluster distribution depending on the water mixing ratio inside the ion source. The generation of $[M-H]^-$ ions takes place via $[M+O_2]^-$ adducts. When the voltages applied to the ion optics are sufficient for CID processes to occur, the adducts dissociate to $[M-H]^-$ and HO_2 or to M^- and neutral oxygen. The M^- quickly reverts to the oxygen adduct due to the high oxygen mixing ratio inside the ion source. Thus, the M^- is not observed in the mass spectra. For higher analyte mixing ratios dimer or even trimer ions occur. These are present as oxygen adducts or dissociate to the $[M_n+M-H]^-$ ion, as these clusters do not exhibit a high stability.

Two representative analytes were used during these experiments, thus, further investigations should be carried out with a broader range of analytes. Furthermore, the rather complex signal distribution in laboratory air needs to be examined in more detail. Other ionization methods, e.g., APPI or APCI, produce a large amount of different neutral radicals during the ionization process, for example, OH-radicals. An investigation whether or not these radicals participate in the ionization mechanism would make an interesting research study.

The examination of the signal distribution of 2,4-dinitrotoluene for different ion transfer times and different oxygen mixing ratios with cAPECI gave valuable insights into the ionization mechanism at atmospheric pressure and confirms the proposed pathways. For reaction times ≤ 1 ms, the M^- ion was the main signal at all conditions. When the reaction time was considerably longer, i.e., 5 ms, M^- was the only observed ion in pure nitrogen. Adding small amounts of oxygen led to the occurrence of the $[M-H]^-$ signal. For mixing ratios higher than 0.5% oxygen, the signal intensity did not increase further. Adding small amounts of sulfur hexafluoride to this gas stream resulted in a shift to the M^- ion of the analyte even for longer reaction times. Sulfur hexafluoride captures the thermal electrons instead of oxygen, so that proton abstraction reactions from the analyte are no longer possible.

Kinetic simulations were performed to describe the reaction system and to determine the ratio of the reaction rate constants. For the simulation, the direct electron capture of 2,4-dinitrotoluene, electron transfer from superoxide to the analyte, adduct formation of neutral analyte with superoxide and adduct formation of the negatively charged 2,4-dinitrotoluene with neutral oxygen were taken into account. Using iteratively optimized rate constants, an oxygen dependence of the signal distribution was calculated which is similar to that obtained experimentally. This agreement supports that the reaction scheme is reasonable. However, exact values for the rate constants need to be determined in future studies, as the mixing ratios of electrons and the analyte were only roughly estimated.

5 Ion Transmission Measurements

Inlet capillaries made of glass or metal are widely used as first pressure restriction stages in AP-MS. They guide the ions from the ion source at atmospheric pressure to the first vacuum stage held at some millibars. However, the dynamics of ion transmission through these capillaries is not fully understood.

In previous studies the gas flow through the standard glass capillaries used in Bruker Daltonik mass spectrometers was identified as fully developed turbulent. It is generally assumed in the literature that the gas flow through capillaries is laminar, regardless of the specific inner diameter and length of the capillary, as ions that collide with the wall are assumed to be neutralized. However, ions that pass through the inlet capillary almost certainly collide with the capillary walls due to molecular diffusion regardless of the flow state in the capillary, i.e., turbulent or laminar. In turbulent gas flows the molecular diffusion is negligible compared to the turbulent mixing. In all cases molecular diffusion is the lower limit for the number of collisions of molecules with the walls. This number is calculated using the velocity of the diffusion described by the Einstein-Smoluchowski relation [272]. The mean distance of diffusion of each molecule is given by:

$$x = \sqrt{2 \cdot D \cdot t} \quad (5.1)$$

with: x = distance of diffusion
 D = diffusion coefficient
 t = time

The diffusion coefficient is pressure and temperature dependent. While the temperature inside the capillary remains constant to our knowledge, the pressure decreases throughout the capillary. As a mean pressure 500 mbar is assumed (see figure 1.2). The diffusion coefficient is calculated using the following equation.

$$D = \frac{1}{3} \cdot \lambda \cdot \bar{v} \quad (5.2)$$

with: λ = mean free path
 \bar{v} = mean velocity

With a mean velocity of 460 ms^{-1} (assuming a mean molecular weight of 30 gmol^{-1}) and a mean free path of 200 nm a diffusion coefficient of $0.303 \text{ cm}^2 \text{ s}^{-1}$ is calculated. As most ions are larger than the normal constituents of air, their diffusion coefficients

should be slightly smaller. With this diffusion coefficient and a transfer time through the capillary of 1.2 ms, equation 5.1 gives a distance of 0.3 mm for the molecular diffusion of each molecule. Thus, the collision probability with the wall of ions that are at the center axis of the capillary is very high, i.e., most ions will collide with the walls, but not all. However, as stated before, this calculation only specifies the lower limit of collisions with the walls and does not take any other mixing processes into account. Thus, in turbulent gas flows the number of collisions of ions with the walls should be much higher.

At atmospheric pressure both metal and glass surfaces are covered with water [273–275] and other air constituents [273]. The water coverage is highly dependent on the relative humidity of the surrounding gas. In most atmospheric pressure ion sources the water mixing ratio is in the high ppmV up to the percentage range. The water coverage at normal conditions is at least one or two molecular layers [276]. In a turbulent gas flow the ions collide several times with the water layer on the capillary surface. However, the ion transmission through an inlet capillary is surprisingly high, up to 50 % for a bipolar ion gas stream through a glass capillary with an inner diameter of 0.5 mm and a total length of 18 cm [73,277].

Ion currents in the low picoampere range are measured with an electrometer with the experimental setup used for both cAPECI and APLI. A signal of 2×10^{-13} A corresponds to an ion current of $1.25 \times 10^6 \text{ s}^{-1}$ elementary charges. The transfer time of ions through the capillary is 1.2 ms for a capillary with 18 cm length. Thus, the total number of charges traveling within the inlet capillary is 1500 ions for a continuous ionization method as cAPECI. For APLI a pulsed laser beam is used for ionization. The ion pulses that pass through the inlet capillary must contain a higher concentration of ions to generate the same mean ion current. The laser pulse has a duration of approximately 10 ns, but the ion pulse broadens to experimentally determined widths of 25 to 75 ns. A typical repetition rate for the experiments carried out during this study is 10 Hz. A typically shaped ion pulse is not symmetric, the maximum number of ions that are traveling inside the capillary is thus much higher than 1500 ions, but nevertheless the number of ions that are traveling within the inlet capillary is small. At considerably higher repetition rates the ion pulses merge into a virtually continuous ion current [47,278]. From the small number of ions that are traveling the capillary follows that potential gradients and other disturbances can severely affect the ion population.

Ion transmission measurements of unipolar ion gas streams for various inlet capillaries and for capillaries composed of different materials show that charging effects are likely to occur, but not for bipolar gas streams. In the following sections two possible consequences of charging effects are described in detail. These are the signal peak slope at the beginning of the measurement and/or the lack of long term signal stability. Bipolar ion gas streams never showed any of these effects regardless of the material combinations or of the capillary pretreatment.

Virtually all ionization methods used for atmospheric pressure mass spectrometry generate both positive and negative ions. Which ion polarity passes through the

5 Ion Transmission Measurements

capillary into the mass spectrometer is determined by the voltages applied within the ion source. Only one polarity is attracted by electrical fields towards the capillary entrance through the bulk gas inside the ion source. In most AP mass spectrometers purely unipolar ion gas streams pass through the inlet capillary, however, in most cases the long term stability is not affected. The signal peak at the beginning of a measurement should occur with common mass spectrometers, but is seldom observed. The reason for this is not yet known. Charging effects gain importance for composite capillaries that consist of materials with different conductivities. These effects are described in detail in the following sections, where mostly unipolar ion gas streams were used in the experiments.

5.1 Ion Transmission of Different Materials

5.1.1 Intact Inlet Capillaries

Inlet capillaries are made of different materials as described in sections 1.2 and 3.4.2. Two different effects from surface charging are observed when unipolar ion gas streams pass through inlet capillaries. The ion signal often declines over time and often a relatively short signal pulse is observed at the beginning of the measurement. A hypothesis for the explanation of the behavior of different inlet capillaries and for the observed charging effects is given, followed by a description of the experimental evidence for this rational.

5.1.1.1 Qualitative Ion Transmission Model

The central factor for the model to explain the charging effects occurring in inlet capillaries is the electrical conductivity of the capillary material. The inner capillary wall is generally covered with water, but also with oxygen and other molecules. While the conductivity of many capillary materials is rather low, the conductivity inside the water layer at the capillary wall may be higher by some orders of magnitude. However, different capillary materials also behave differently, indicating that the thickness of the water layer is determined by the capillary material. Glass and silica have many free OH groups from silicate on the surface, which means that water can easily form hydrogen bonds to the surface. The lead oxide coated lead silicate capillary has a layer of reduced lead silicate glass on its surface where all molecular groups are present in their reduced form. Thus, hydrogen bonds are not preferentially formed, leading to thinner water layers. Ions that enter the water layer do not see the capillary wall, they therefore do not necessarily get neutralized, but lead to an overall charging of the water layer. It is assumed that some of the ions move through the water layer to the capillary wall or to the ends of the capillary where they get discharged. The capacity of the water layer to absorb ions depends on the thickness of the layer and the polarity of the ions. For bipolar ion gas streams no effective potential will form, as positively and negatively charged ions enter the water layer. If unipolar ion gas streams pass

5.1 Ion Transmission of Different Materials

through the capillary, the effective charge inside the water layer increases as more ions enter the water layer. Ions that approach the charged water layer are influenced by the resulting electrical fields, so that the inflow of ions decreases with increasing potential. Furthermore, with increasing potential the number of ions that reach the capillary wall or the end caps and discharge increases. After some time an equilibrium establishes in which the number of ions discharging and entering the water layer is identical. The equilibrium potential is dependent on the thickness of the water layer, the conductivity of the capillary, the flow of ions into the water layer, the potential applied to the end caps.

If these processes would be the sole influences on the ion transmission, the ion current would differ significantly from the ion signals shown in the following section. At the beginning of a measurement many ions would enter the water layer as its effective charge is initially low, resulting in a low ion transmission. The ion transmission would then increase with time as the potential of the water layer increases and the number of ions entering the water layer decreases. When equilibrium is established, the ion transmission would remain constant. However, this behavior is not observed in most experiments, which means that an additional process must be involved.

A further process influencing the ion transmission of an inlet capillary is a consequence of the other process noted above. When the effective charge of the water layer increases, a potential will form between the capillary with low conductivity and the highly conductive metallic end caps at each end of the capillary. In the following it is assumed that both end caps are grounded. Naturally, this is not the case in common mass spectrometers, but was the case for nearly all the experiments carried out with the measurement chambers described here (cf. section 3.4). However, if a voltage is applied to the end cap, the model is still applicable, only the potential difference between capillary and end cap changes. The potential difference between capillary and end cap is assumed to be in the range of 500 to 1000 V. This value is rationalized by the observation that this is the voltage range which is applied to the glass of an inlet capillary without changing the ion current that passes through the capillary. The experiments leading to this assumption are explained in detail in section 5.3. When the conductivity of the capillary material and the end cap differs and the water layer on the capillary surface is charged by absorbed ions a potential gradient will form, leading to an electrical field at the entrance and the outlet of the capillary. This electrical field, when sufficiently strong, influences ions that come close to the inlet of the capillary. Without electrical fields ions near the entrance are dragged into the capillary duct by viscous flow forces. With increasing potential difference and increasing slope of the potential gradient between capillary material and end cap an increasing number of ions are discharged at the end cap. The potential gradient depends on the conductivity of the capillary material. A steep gradient will result for materials with a low conductivity. Materials with a high conductivity, such as the lead oxide coated lead silicate capillary, will only generate a flat potential gradient, which will have a lower influence on the ions.

Numerical simulations of this process were carried out with the Simion and Comsol

5 Ion Transmission Measurements

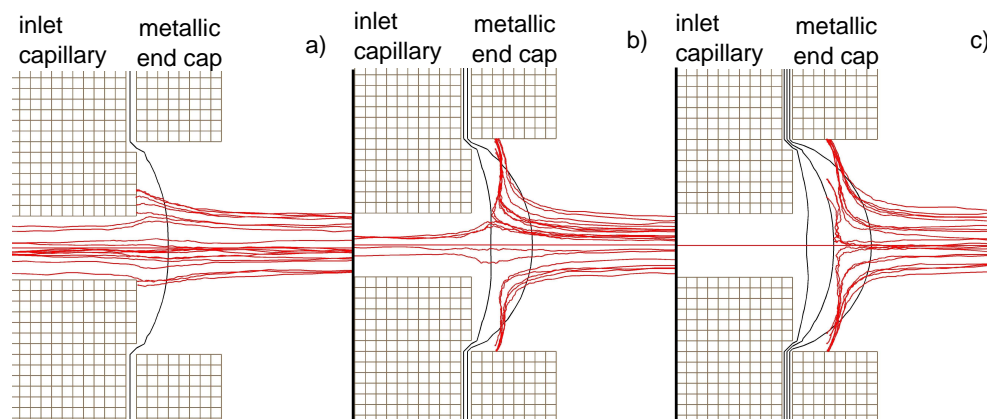


Figure 5.1: Numerical simulation with Simion of the influence of a potential gradient on the ion motion at the entrance of an inlet capillary. The potential of the capillary is set to a) 150 V, b) 250 V and c) 350 V.

programs. A variation of the potential, the gradient slope and the gas velocity in a reasonable range (see section 3.4.2) show that sufficiently high electrical fields can force charged molecules onto the grounded end cap, reducing the number of ions that enter the capillary. This result is given by both calculation methods. An exemplary calculation with Simion is shown in figure 5.1. The parameters for this simulation are an ion mass-to-charge ratio of 60, a velocity of the inflowing gas of 80 m s^{-1} and a pressure of 1013 mbar. The metallic end cap has a potential of 0 V in the simulations shown. Three different potentials on the capillary wall are assumed, i.e., a) 150 V, b) 250 V and c) 350 V. As seen, a voltage of 350 V is sufficient to quantitatively deflect all ions from the capillary entry port. When the gas velocity is decreased a lower potential or a lower electrical gradient is necessary to force ions on the metallic end cap. The numerical model shows that the model described above is in principle reasonable.

Furthermore, the simulations showed that ions are not deflected at the exit port of an inlet capillary. The pressure at the end of the capillary is considerably lower, the gas density is comparatively low and the ion mobility is increased. However, the gradient between capillary material and metallic end cap does not lead to a deposition of ions on the end cap, as can be seen in figure 5.2. For this Simion simulation a gas velocity of 300 m s^{-1} , which may be higher in reality, an ion mass-to-charge ratio of 60 and a pressure of 400 mbar is assumed. The potential is 0 V on the metallic end cap and 1000 V on the inner wall of the capillary. The black lines in figure 5.2 depict the potential lines. The ion stream is narrowed at the material boundaries and broadens in the vacuum region. The charging effect has a considerable influence on the ion transmission of an inlet capillary only at the entrance of the capillary.

5.1 Ion Transmission of Different Materials

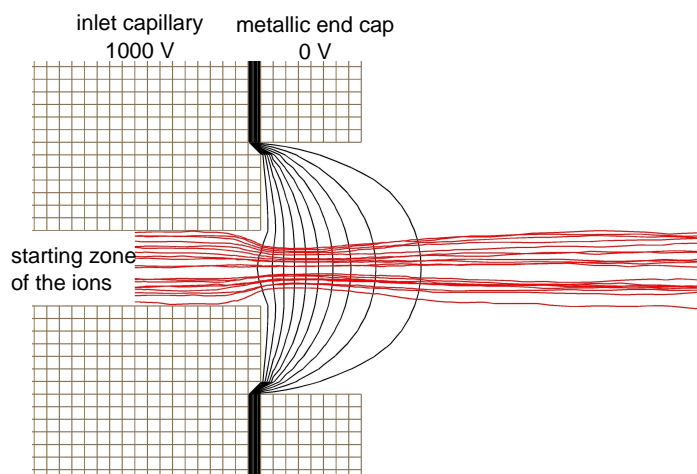


Figure 5.2: Numerical simulation with Simion of the influence of a potential gradient on the ion motion at the outlet of an inlet capillary.

At the beginning of a measurement the potential on the capillary wall is low, so that ions enter the inlet capillary without hindrance. As the potential increases until the equilibrium between charge uptake of the water layer and discharge of ions is established, the number of ions that enter the inlet capillary decreases. When equilibrium is reached a constant potential is established and the ratio of ions entering the inlet capillary and colliding with the end cap remains constant. This process leads to an ion transmission behavior which reaches a constant intensity after a time period of decreasing signal. The time until the equilibrium is reached is strongly dependent on the used material.

5.1.1.2 Experimental Results

The long term stability of the ion signal for a constant analyte concentration is an important characteristic of an inlet capillary, as a varying signal intensity with time renders analytical quantification measurements difficult. Common borosilicate glass inlet capillaries show excellent long term stabilities for unipolar ion gas streams. However, external influences from electrical fields disturb the ion transmission and even signal drop outs occur. These effects are described in detail in section 5.3. The reduced form of the lead silicate glass prevents signal drops due to electrostatic fields and also has a sufficiently good long term stability. However, the unreduced lead silicate glass capillary does not provide a constant signal intensity over longer time periods. The upper panel of figure 5.3 shows the ion current through the lead oxide coated lead silicate capillary over 80 min, in the lower part of the figure a long term ion signal stability of the lead silicate capillary is shown.

5 Ion Transmission Measurements

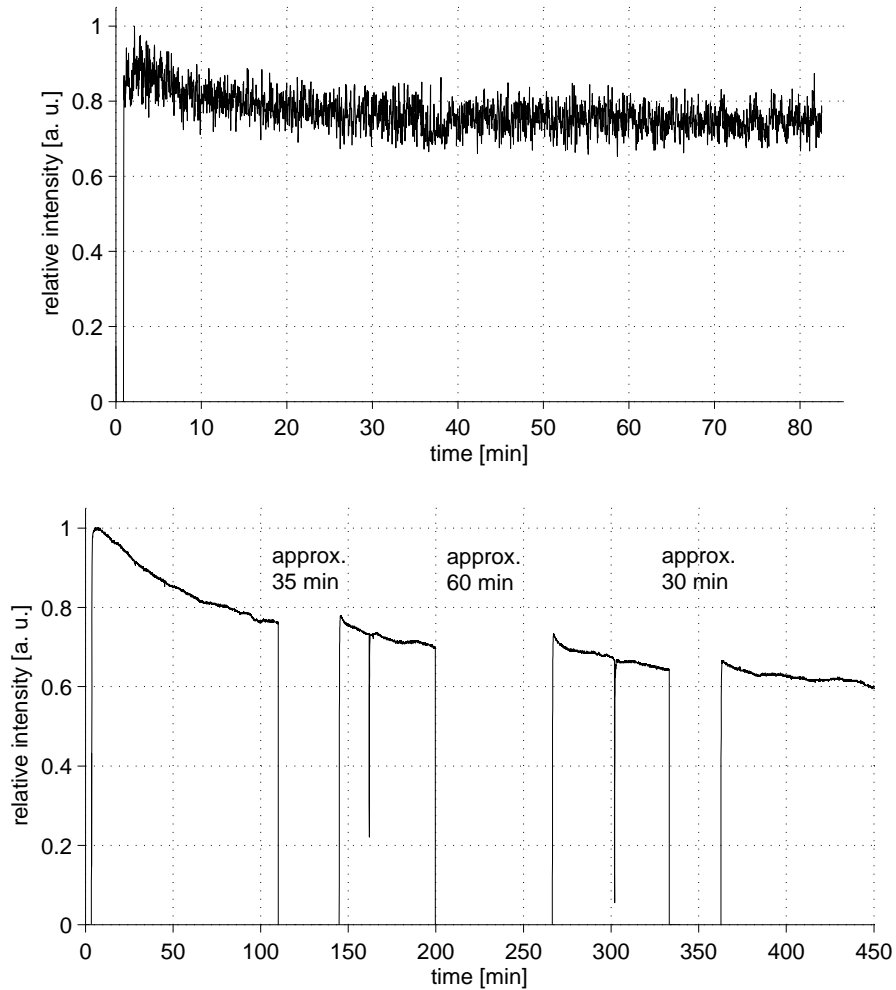


Figure 5.3: Long term behavior of the lead oxide coated lead silicate glass capillary (upper panel) and the lead silicate glass capillary (lower panel). For the lead silicate capillary the laser beam was blanked out for different time periods to observe the signal recovery.

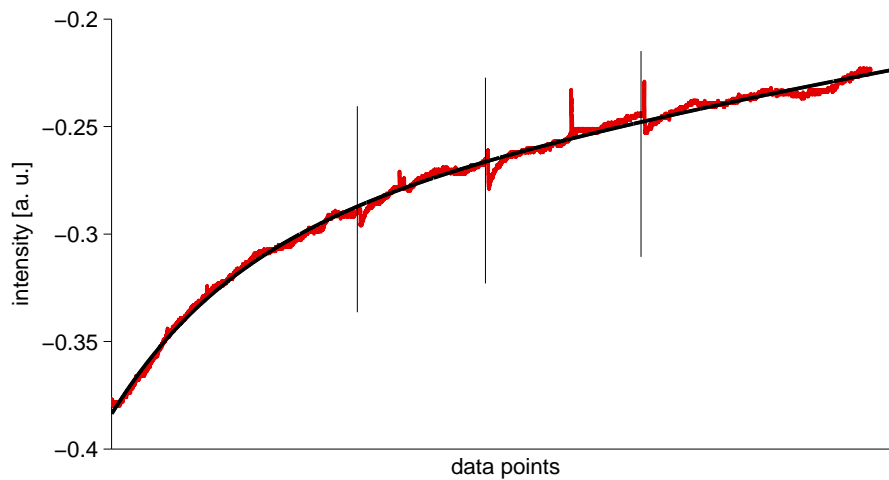


Figure 5.4: The same measurement as shown in the lower panel of figure 5.3, but without the periods where the laser beam was blanked out, resulting in a continuous signal intensity-time profile.

Even though the lead oxide coated lead silicate capillary shows a signal peak at the beginning of the measurement, the signal remains constant after an adjustment period of approximately 30 min. Periods of this length only occur during the first measurement of a day, the signal intensity of later experiments remains constant after considerably shorter time periods. The high noise of this measurement is due to the low ion current and the associated high amplification of the electrometer to measure in the low picoampere range. The low signal intensity is not caused by a poor transmission efficiency of the inlet capillary, but from the adjustment of the laser beam inside the ionization chamber and the low voltages applied to focus the ions onto the capillary entrance.

The transmission through the lead silicate capillary shows a distinct decline with time. As lead silicate has the lowest conductivity of all materials used, the time until the equilibrium is reached is very long. In the first thirty minutes the signal decreases stronger than the signal through the lead oxide coated lead silicate capillary. However, the most striking difference in the observed ion transmission is that the signal decay does not stop in the case of the lead silicate capillary after a short initial period. Instead, the signal decays over the entire experiment of more than seven hours to approximately 60 % of the initial signal intensity. During the measurement, the laser beam was blanked out for different time periods to examine whether the signal recovers when no ions pass through the inlet capillary. With blocked laser beam, ions inside the water layer should reach the capillary wall or the metallic end caps and get discharged while no additional ions enter, keeping the effective charge inside the water layer constant.

5 Ion Transmission Measurements

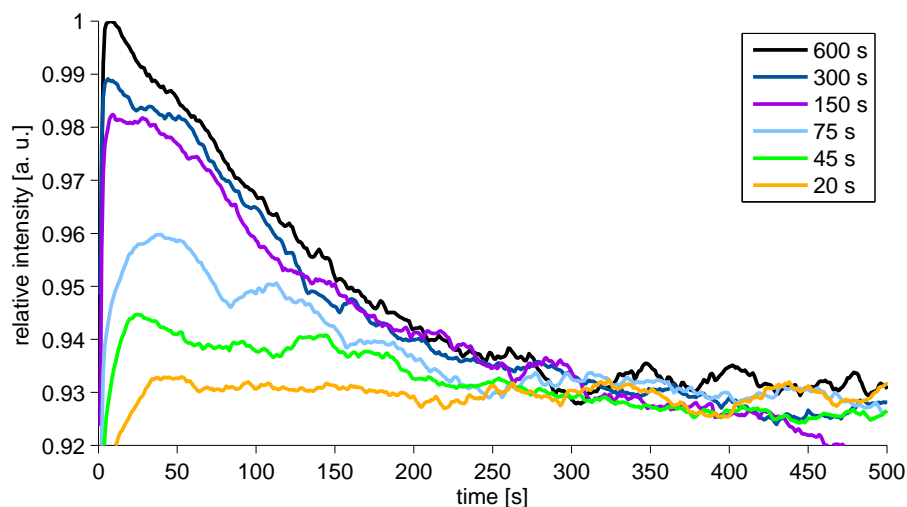


Figure 5.5: Close up view of the normalized initial signal peak with a standard glass capillary after different blank out times of the laser light.

This should lead to an increase in ion transmission efficiency compared to the ion transmission before the laser beam was blanked out, but the signal intensity should recover to the previous level quickly as the potential forms again. This is exactly what is observed (figure 5.3), the signal starts at a higher intensity when the laser is switched on again compared to the signal intensity just before the laser beam is blanked out. The signal recovery is dependent on the time the laser beam is blanked out.

Even though the signal recovers after a period in which no ions pass through the inlet capillary, the signal decay remains the same as is shown in figure 5.4. Here, the time periods in which the laser beam was blanked out have been removed, the vertical lines indicate where the laser beam was blocked in the previous experiment. After each break the signal recovers slightly but the signal decreases quickly to the intensity that would be observed without the blanked out period. Except for the signal peaks after the breaks, the signal is described well by a combination of two exponential terms of the general form $f(x) = a \cdot \exp(b \cdot x) + c \cdot \exp(d \cdot x)$ ¹, indicating that the overall signal behavior is not affected by the disruptions.

An initial peak was observed for all materials used during this study of unipolar ion gas streams, even when the signal intensity became constant after some time. One example is shown in the upper part of figure 5.3 in the signal intensity-time profile for the lead oxide coated lead silicate capillary. The size and the duration of the initial

¹The exact form for the non-normalized data shown is $f(x) = -0.07982 \cdot \exp(-3.14 \cdot 10^{-3} \cdot x) - 0.304 \cdot \exp(1.54 \cdot 10^{-4} \cdot x)$, with a correlation coefficient of $R^2 = 0.9967$.

5.1 Ion Transmission of Different Materials

peak depends on different parameters, e.g., the capillary material. For the lead oxide coated lead silicate capillary the initial peak is always rather long with several minutes. Even intact glass capillaries, which are commonly used in mass spectrometers, showed a short signal peak at the beginning of many measurements, especially for the first measurements of each day or when the laser beam was blanked out for some time. The intensity of the initial peak is dependent on the time the laser beam was blanked out, i.e., on the time period where no ions pass through the inlet capillary. This is shown in figure 5.5. For this experiment, a standard glass capillary with APLI as ionization method was used, the laser beam was blanked out for time periods between 20 and 600 s. Figure 5.5 shows the moving average of the data points as the fluctuation of the signal intensity during each measurement was too high to yield a clear presentation of all ion signals in one figure. Furthermore, the data is normalized as the total signal intensity varied between the measurements.

A short dark time does not lead to an initial signal peak (see yellow line '20 s' in figure 5.5), but already a doubling in time ('45 s') leads to an apparent initial signal peak. With increasing time the height of this peak increases, however, with dark times longer than 600 s no further significant increase in the peak occurs (not shown here). While the peak area increases with the dark time, the decay time until the signal reaches a constant intensity is apparently similar for all five profiles and is thus independent of the dark time of the laser light. However, the transmission efficiency after the initial peak declines is still relatively high with 93 % of the highest signal intensity of the initial peak for the longest dark time. The constant decay time is rationalized as follows: Short dark periods barely change the potential gradient and the ratio of ions that enter the inlet capillary remains almost constant. Furthermore, the effective charge of the water layer reduces the number of ions that enter the layer to reach the equilibrium potential. The equilibrium state is thus only reached very slowly. If the time period in which no ions enter the inlet capillary is longer, most of the charges inside the water layer are lost. Thus, the potential that hinders ions entering the inlet capillary is low, which means that many ions pass through. Some of the ions entering the inlet capillary move into the water layer. This increases the potential and increases the number of ions that are discharged. The increase of the potential leads to a decrease in the number of ions that enter the capillary.

The peak area is proportional to the number of surface charges that drain from the inner wall of the capillary during the dark time. The longer no charges enter the capillary, the more surface charges drain from the walls. Figure 5.6 shows the integrated areas of the initial peaks for different time periods in which the laser was blanked out. As seen in this figure, the drain of charges does not proceed linearly with time, but reaches saturation for longer dark times, most likely because nearly all charges are eventually removed.

Different dark times are associated with different starting concentrations of charges at the wall before the first ions pass through the capillary. This situation corresponds to the variation of starting concentrations carried out in the field of reaction kinetics to determine the rate constant of a second order reaction. Even though the exact reaction

5 Ion Transmission Measurements

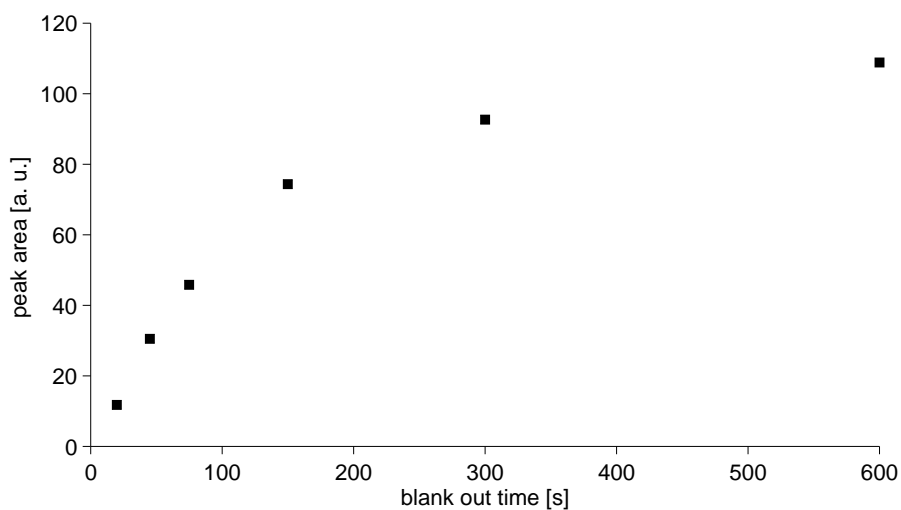


Figure 5.6: Dependence of the integrated peak area of the initial signal peak on the laser blank out time period.

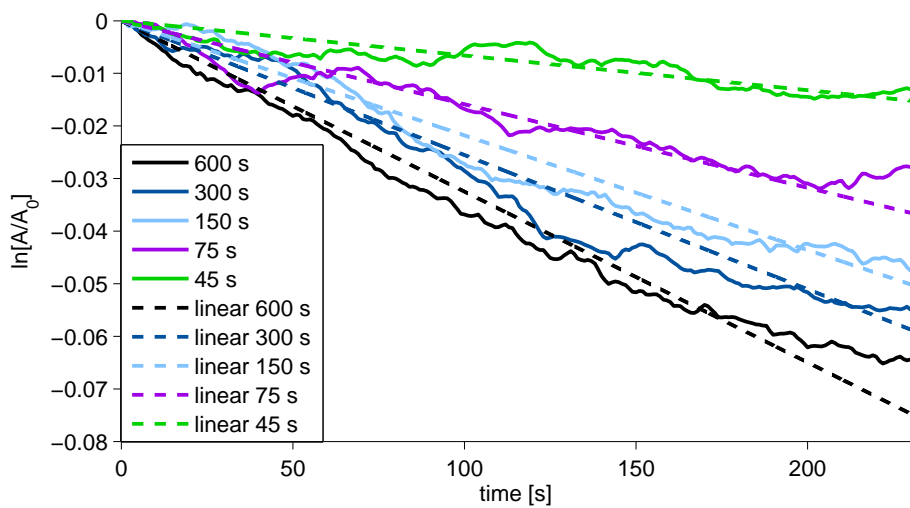


Figure 5.7: Determination of the pseudo-first order rate constant for different starting concentrations that are proportional to the blank out times.

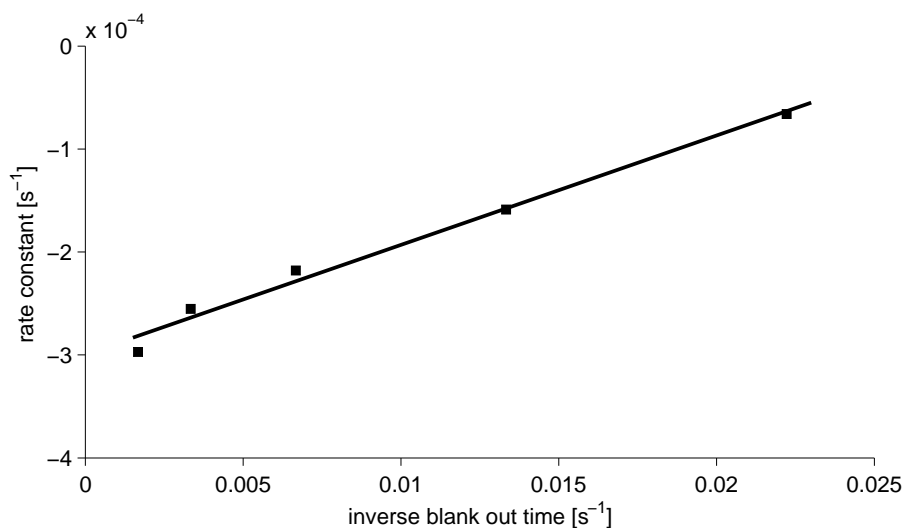


Figure 5.8: Determination of the second order rate constant by the pseudo-first order rate constants and the starting concentrations, represented by the inverse blank out times.

pathway is not known, a second order reaction is assumed, with one concentration in large excess over the other, representing a pseudo-first order reaction condition². The decreasing part of each signal intensity-time profile from 5.5 has been taken and the natural logarithm of the respective signal intensity divided by the initial signal intensity plotted against time (figure 5.7). The slope of the linear regression of each data set corresponds to the pseudo-first order rate constant for that particular dark time. These pseudo-first order rate constants were then plotted against the concentration, as shown in figure 5.8 yielding the second order rate constant. The dark times correspond to an inverse concentration, as longer dark times lead to a smaller number of charges that remain at the capillary wall.

As long as the process of charge deposition at the wall and the loss process of ions inside the surface water layer is not fully understood the determined rate constant is of little use only. However, the knowledge that the process has an overall reaction order of two may be helpful for the further investigation of the processes involved.

5.1.2 Composite Capillaries

Due to the turbulent gas flow inside the capillary, the construction of an inlet capillary consisting of several segments, potentially made of different materials, is possible without severely affecting the transmission efficiency. However, the use of different materials can lead to charging effects, which are described in the following sections.

²The treatment of second order reactions is explained in standard kinetics textbooks, for example [279].

5 Ion Transmission Measurements

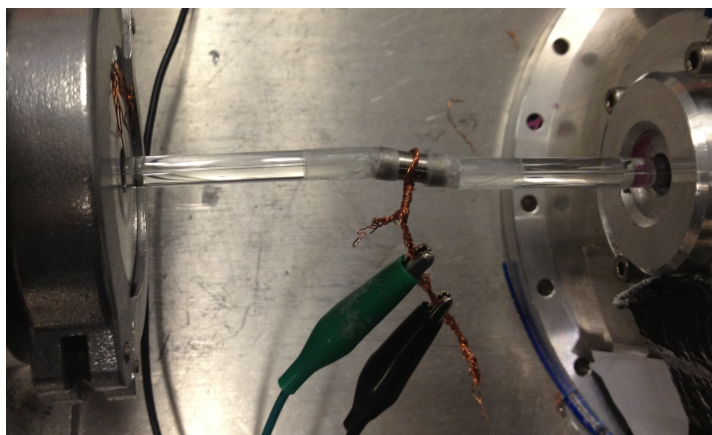


Figure 5.9: Buckled inlet capillary with a metal capillary piece between two glass capillary segments, fastened with adhesive tape.

When capillary segments are combined the segments must be assembled airtight. This was achieved by two different means, i) using an adaptor that presses the segments together and ii) using adhesive tape that is wrapped around the point of contact of two segments. The adaptor forces the capillary segments to result in a straight alignment, while the adhesive tape allows moderate bending, as shown in figure 5.9. Even with a slight bend the ion transmission through the inlet capillary is still sufficiently high. The metal capillary piece is grounded. In the bent section the volume increases between the capillary channels, which means that the gas velocity decreases and the dwell time of the ions in this volume is strongly increased. However, the ion transmission efficiency is hardly affected compared to the same setup with a straight alignment; the same holds true for the occurrence of charging effects. The results obtained using either the adhesive tape or the adaptor were basically identical.

The influence of contact resistance at the contact point of two materials with different conductivities was examined. For this investigation capillaries were assembled with segments made of different materials but with approximately the same inner diameters. While nearly all material combinations gave good ion transmission efficiencies, the signal intensity-time profiles differ significantly. Figure 5.10 shows the normalized ion transmission for different combinations of capillary segments. These consist of two segments of standard glass capillaries and a metal segment in between two glass capillary segments or a silica segment that is cased by a metal husk. In all cases the metallic adaptor was grounded. The signal intensity-time profile with an intact standard glass capillary is also shown for comparison. The ionization conditions were not reproducible after modification of the setup. Additionally, the gas flow through the capillary differs for the different inlet capillaries, thus a comparison of the

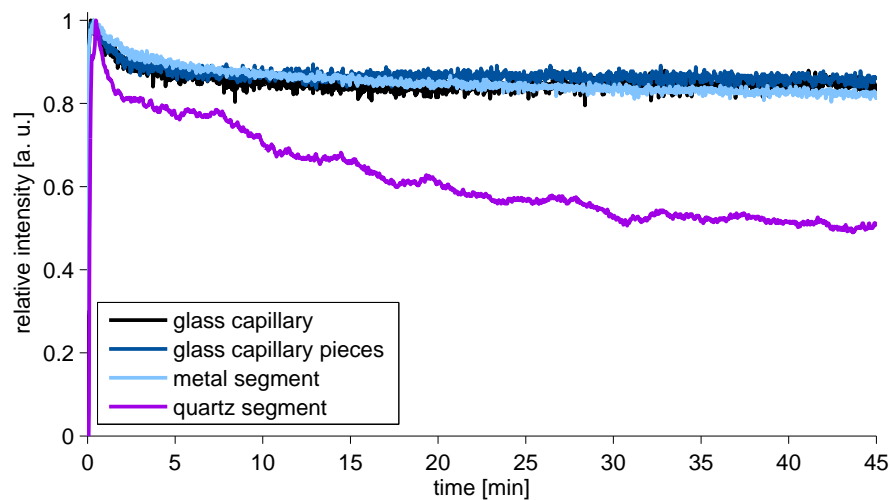


Figure 5.10: Ion transmission signal with time for different combinations of capillary segments compared to a standard glass capillary.

absolute signal intensities was not possible.

As mentioned above, standard glass capillaries lead to an initial signal peak when an unipolar ion gas stream starts passing through it. This was also the case for all the inlet capillaries that were assembled using different segments.

The long term signal intensity is remarkably different for the capillaries. Except for the capillary that contained the silica segment, all segment combinations showed a long term signal stability that was comparable to an intact glass capillary. A PVC segment led to similar results (data not shown). The absolute signal intensity with a PVC segment however is considerably lower than with all other materials used. For the capillary with the silica segment the signal did not reach a constant value even after 45 min, indicating that the equilibrium of a constant potential at the capillary wall is only reached very slowly. For some material combinations the long term transmission through inlet capillaries is not influenced by charging effects. This is easily understandable for an additional brink as in the inlet capillary made of two glass capillary segments which does not provide a transition between materials of different conductivity. However, when the relative humidity inside the capillary is considerably high, this could change the transmission characteristics, as a water layer with a higher conductivity than the capillary material in this brink may increase the transport of charges from the capillary surface to the grounded metal of the adaptor.

With the insertion of a metal segment the conductivity inside the capillary changes considerably. However, these different conductivities do not lead to charging effects, which may be due to the higher conductivity of metal compared to glass. Charges that reach the wall of the metal segment get discharged and as the metallic segment is

5 Ion Transmission Measurements

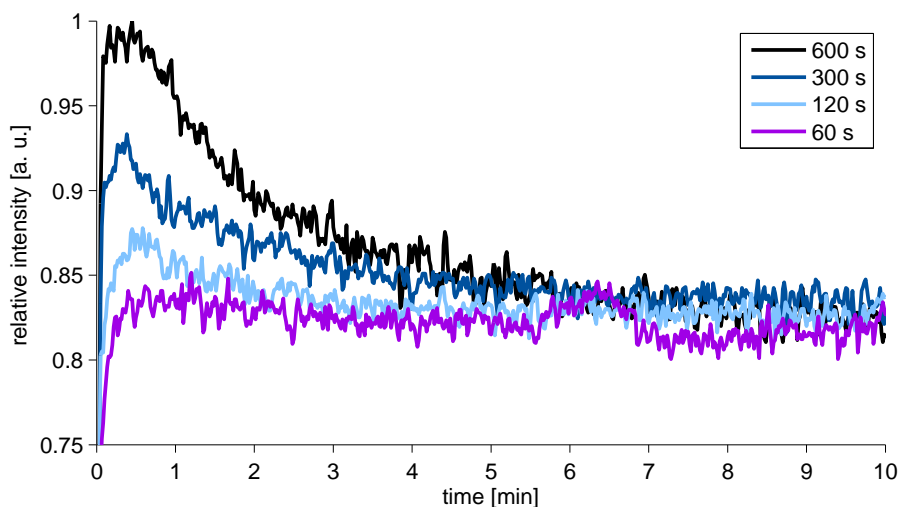


Figure 5.11: Normalized transmission curves with initial signal peak after different blank out times of the laser light with a metal capillary section between two glass capillary segments.

grounded by the adaptor, no electrostatic potential is formed with time. A potential gradient should be formed between glass and metal. However, the reason that ions are not influenced may be that a water layer on the metal surface balances the conductivity of both materials and prevents the formation of a gradient or that the gradient forms, but the ions are not forced to move in the direction of the wall. It is not possible to simulate the ion motion inside the capillary with numerical methods because the boundary conditions are still unknown. Thus, it is speculated which processes are responsible. For the transition from glass to metal the gradient may have the same influence on the ions as shown in figure 5.2 for the outlet of the capillary, which means that the ion gas stream is constricted by the electrostatic fields. The potential gradient at the transition from metal to glass should have a similar effect as shown in figure 5.1, but it is reasonable to assume that the ions are traveling fast enough to cross the electrostatic field without the deposition of a considerable number of ions on the wall. However, the behavior of this capillary assembly needs further investigations for deeper insights.

The initial peak when using a capillary with a metal segment is similar to that observed with a common glass capillary. Figure 5.11 shows the dependence of the initial peak on the time period in which no ions pass through the capillary before a new measurement is started. The dark times were varied between 60 to 600 s (normalized data are shown). In contrast to the glass capillary, even a dark time of 60 s does not lead to an initial signal peak. However, the time period after which nearly all charges are removed from the wall, identified by the stagnating size of the initial signal peak

5.1 Ion Transmission of Different Materials

is approximately 600 s for both capillaries. The time after which a constant signal intensity is reached is the same for all three dark times. With around 6 min this time is approximately doubled compared to the decay time for the glass capillary. This may be due to the lower total ion intensity that passed through the metal capillary, as determined by the position of the laser inside the ionization chamber. Whether or not the different decay times depend on the material or on the ionization conditions needs to be further investigated.

Only the capillary with the silica segment shows a signal decay over a long time. To investigate the influence of the material transition in more depth, three different silica/metal segments were used. The results are shown in figure 5.12 together with their ion transmission signals. The three signal intensities are normalized to the highest signal intensity. The highest intensity occurred for the silica segment that had a husk made of metal, but where the silica protrudes on both sides, so that the ions are not exposed to metal. Initially the signal increases slowly until it reaches a constant intensity after approximately 10 min. This signal behavior is similar for the silica segment where the silica protrudes only on one end of the metal husk (light blue curve). The signal increases less steep than for the segment described before, but also reaches a constant signal intensity. A signal intensity-time profile with an initial peak and a signal decay with time has only been observed for the third segment used, where the silica is inside the metal husk but the husk is a little longer than the silica piece. The ions pass from the glass capillary through a hole inside the metal husk with the same inner diameter as the capillary channel. After they pass through the silica capillary piece there is a larger volume where the metal husk protrudes for some millimeters before they reach the glass capillary.

The observation that the signal intensities remain constant after some time for two of three silica segments and only one segment shows a signal peak at the beginning of a measurement is inconsistent with the previous measurements with silica segments, where a signal decay and an initial peak is observed in most cases. The slowly increasing signal for two of the silica segments may be due to a thicker water layer on the walls (cf. section 5.2). However, the effects are not yet fully understood and capillaries that contain silica have always shown unpredictable signal behavior with time. In depth investigations of silica capillaries and silica containing capillaries are planned for the future.

5.1.2.1 Signal Drop Outs

In a segment, where the silica protrudes on both sides of the metal husk (dark blue curve in figure 5.12), random signal drop outs occurred during a measurement (see figure 5.13). Surprisingly they occurred after an alteration of the setup and remained until the setup was modified again.

To examine this effect different approaches were used to intentionally induce drop outs. This was finally achieved by wrapping adhesive tape around the metal husk, so that the metal was no longer in contact with the grounded metal of the adaptor. The

5 Ion Transmission Measurements

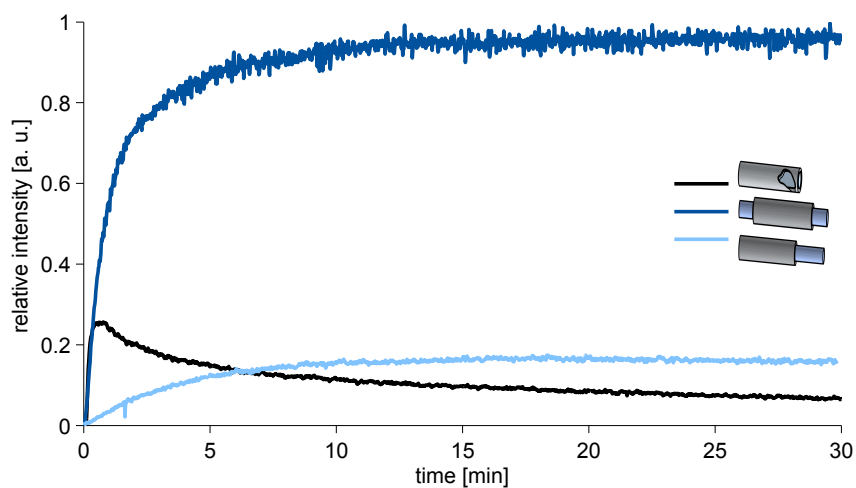


Figure 5.12: Normalized ion transmission-time profiles for different silica/metal capillary segments between two glass capillary segments.

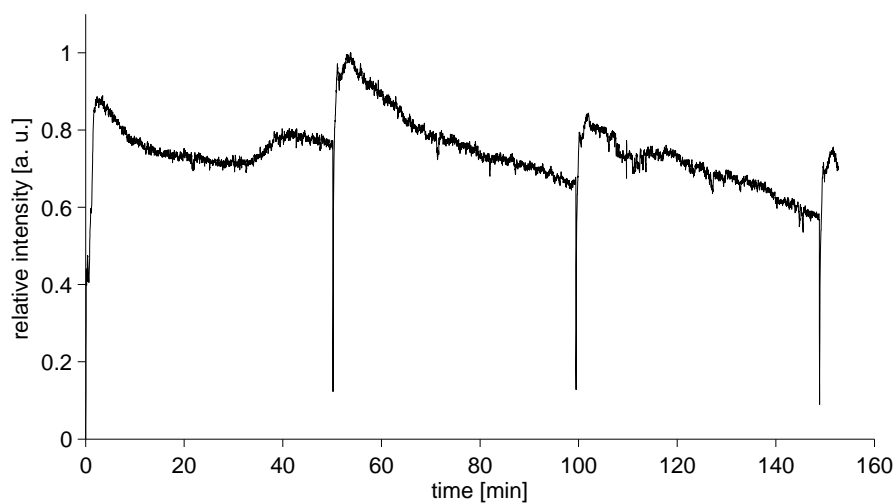


Figure 5.13: Randomly occurring signal drop outs with an inlet capillary that consisted of a silica segment between two glass capillaries.

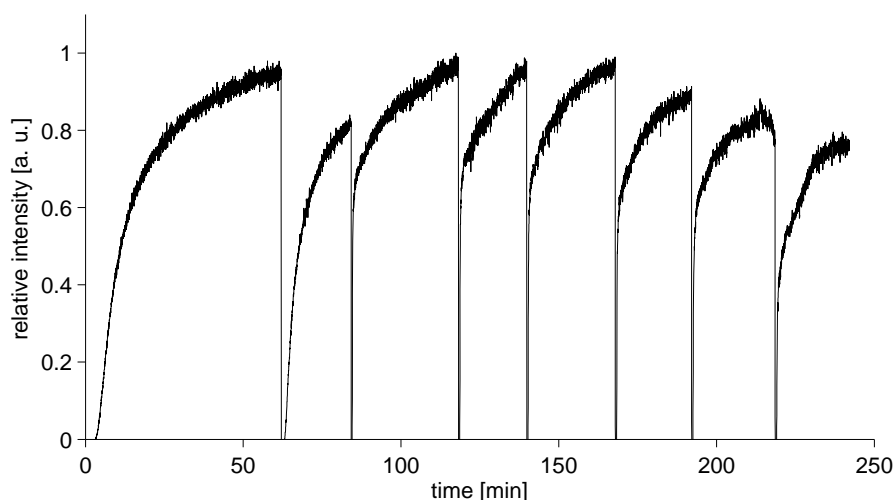


Figure 5.14: Intentionally caused signal drop outs which occurred when the metallic husk of the silica segment was wrapped with adhesive tape to prevent contact between the metal and adaptor.

drop outs are shown in figure 5.14. Most striking is that they show exactly the opposite signal shape to that obtained for the randomly occurring drop outs. Here, the signal intensity starts with a signal peak after a drop out, after which the signal intensity decreases slowly until the next drop out occurs. The drop outs that were observed after isolating the metal husk from the adaptor show a slowly rising signal after a drop out. The drop outs occur more or less periodically in each case. For the intentionally induced drop outs the first two signal recoveries have significantly different slopes than the following which have all very similar slopes.

While the reason for the difference in the peak shapes is not yet understood, a qualitative explanation for signal drop outs is that the resistance between the metal husk and the grounded adaptor is considerably increased, due to the adhesive tape or to an assembly where the metal is not in direct contact with the adaptor. When the contact resistance is increased, the charges residing on the capillary wall cannot drain easily. If the accumulated potential is high enough to overcome the contact resistance the surface is abruptly discharged. The different peak shapes may be due to different ways in which the charges are removed from the surface. Possible explanations are i) that the adhesive tape is no longer isolating for high potentials, ii) that the charges drain by an electrical breakdown through the air between the metal and adaptor or iii) that the charges are transported from the silica capillary to the glass capillary and then to the adaptor where they drain.

Similar signal drop outs were observed with a commercially available time-of-flight mass spectrometer equipped with a common glass capillary and APLI as ionization

5 Ion Transmission Measurements

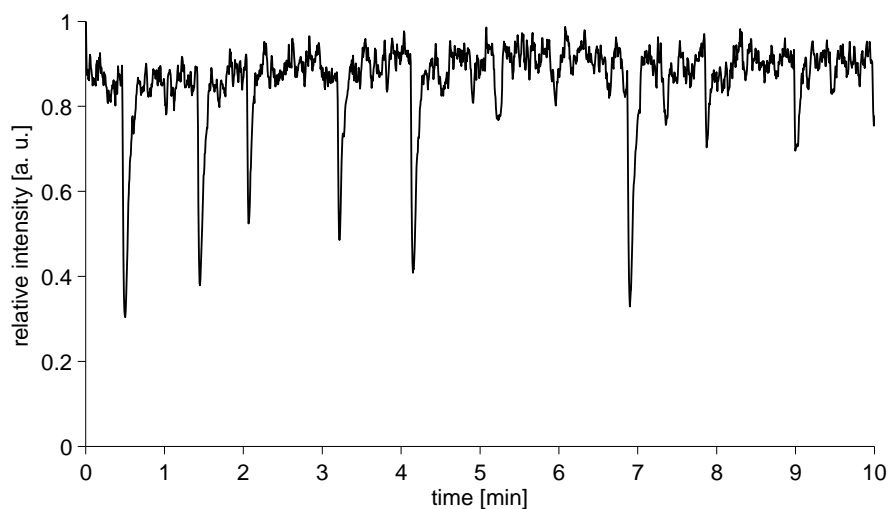


Figure 5.15: Signal drop outs that occurred randomly with a TOF mass spectrometer equipped with a common glass capillary and APLI as ionization method.

method [81]. These signal drop outs are shown in figure 5.15. The reason for these signal drop outs, which occurred prior to the investigations of the capillaries described here, is still not fully understood. It was not possible to force these effects to occur intentionally. However, a reason may be that the glass capillary has a high contact resistance at some point, maybe at the transition from the glass capillary to the end cap. The signal drop outs occurred mainly when high purity gases passed through the capillary for a longer time period. This leads to a thinner water layer that electrically connects the glass and metal, resulting in an increased contact resistance. When the potential on the capillary wall reaches a critical value a discharge occurs.

To avoid these signal drop outs at the measurement chambers, a borosilicate glass capillary was completely nickel plated at the outside. This conductive coating has no influence on the transmission characteristics of the capillary. The signal intensity and the long term stability were comparable to that of a common glass capillary with and without nickel-plated end caps. The nickel-plated capillary could not be used in the mass spectrometer, because different voltages are applied to both ends of the capillary. The manufacturer of the mass spectrometer showing signal drop outs, recommended the use of a lead oxide coated lead silicate capillary instead of a common borosilicate glass capillary to suppress these effects. This supports the assumption that the conductivity affects the occurrence of drop outs, as the conductivity of the lead oxide coated lead silicate capillary is considerably higher than that of the glass capillary, so that the charges can drain much more easily.

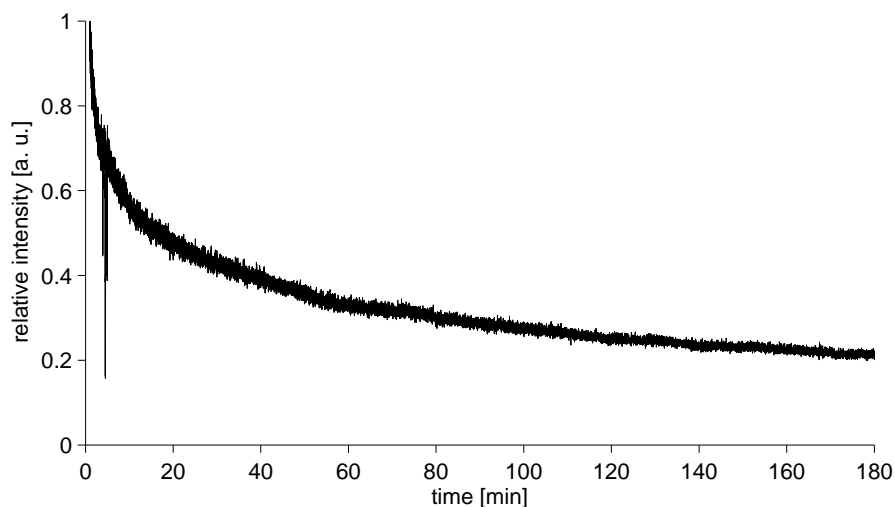


Figure 5.16: Signal intensity-time profile of the cAPECI source design 1 recorded with the quadrupolar ion trap.

5.1.3 cAPECI Source Design 1

The initially designed cAPECI source in its standard configuration consisted of two glass capillary segment, an aluminum housing, a lithium fluoride window and a photoemissive plate made of silver or anodized aluminum. Consequently, there are several transitions where materials with rather different conductivities are in contact, which may lead to significant surface charging. The generation of photoelectrons with UV light, may also be a source for fluctuating signal intensities with time, thus the ion source was used with both, ionization inside the ion source and ionization with APLI in front of the capillary ion source.

Figure 5.16 shows the dependence of the signal intensity with time for ionization inside the cAPECI source recorded with the Bruker Daltonik ion trap. The normalized total ion current is shown, the signal intensity of the monitored extracted ion chromatograms showed a similar behavior. The signal intensity decreases over the whole measurement period of about 3 h by around 70 %. However, upon ionization in front of the inlet capillary containing the cAPECI source, the signal behavior is similar, indicating that the signal decay with time is not caused by the photoelectron ionization method, but again by charging effects due to the material transitions as described in the previous section.

When ionization in front of the capillary with APLI is used, the number of ions passing through the cAPECI source is readily adjusted. This can be seen in figure 5.17 where the number of ions is adjusted by varying the repetition rate of the laser. For higher repetition rates the signal intensity-time profile is similar to that obtained with

5 Ion Transmission Measurements

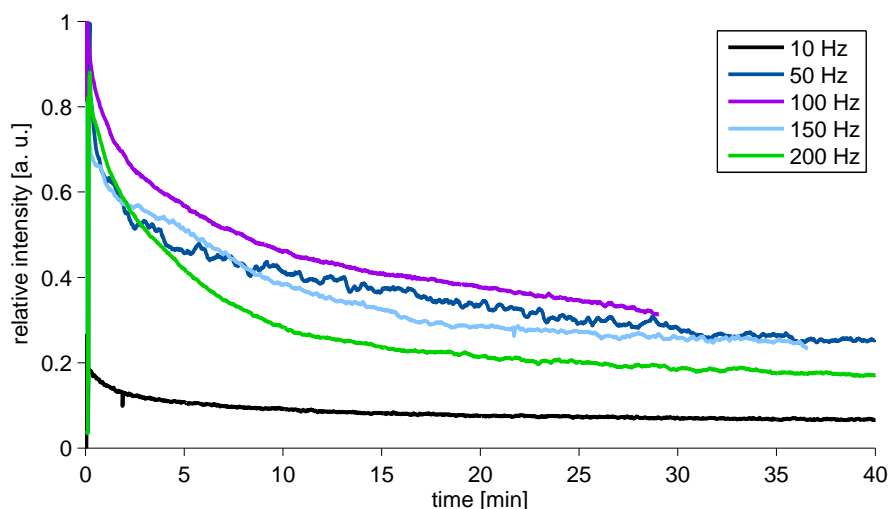


Figure 5.17: Ion transmission signals for laser ionization in front of the cAPECI source design 1 for different repetition rates.

ionization by cAPECI. The half life period is considerably shorter, but this may be due to the larger number of ions that pass through the capillary with APLI compared to cAPECI. It is striking that the signal intensity for repetition rates of 150 and 200 Hz is considerably lower than that for 100 Hz. This effect was observed for all APLI measurements. This may be caused by space charge effects inside the ionization volume. Even though it looks as if lower repetition rates lead to a less distinct signal decay and nearly constant signal intensities with time after one run (see the black line for 10 Hz) the ratio of the ion loss is the same for all repetition rates. The signal intensities do not reach a constant value even after an hour of measurement. The ratio of signal intensity after 30 min and initial signal intensity is approximately 0.4 for all five repetition rates. Laser ionization in front of the capillary leads to a higher transmission ratio. After 40 min the signal has still not reached a constant intensity, but the decrease in signal intensity is comparatively slow. When all five transmission-time profiles are scaled to the same initial intensity they are nearly identical, which indicates that the underlying charging effect does not change with the number of ions passing the inlet capillary. Thus, space charge effects do not affect the ion transmission. Furthermore, the ratio of charges that are deposited on the wall to the number of charges that drain remains the same over the range of repetition rates.

Dependence on the Pretreatment of the Inlet Capillary During the variation of the repetition rates the signal evolutions were not fully reproducible. When a lower number of ions passed through the capillary prior to the next measurement, the transmission signal had a shape as shown in figure 5.17. When a measurement with

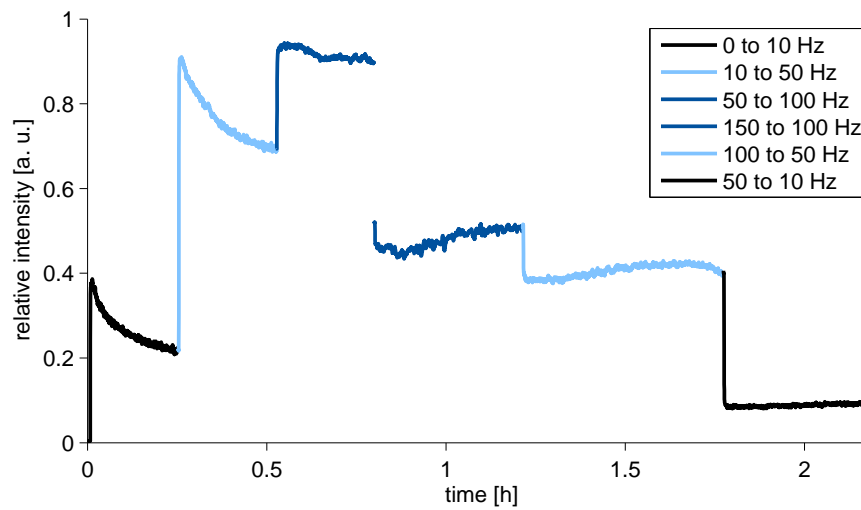


Figure 5.18: Ion currents in dependence on the number of ions that passed through the capillary prior to the measurement caused by different repetition rates of the laser.

a higher repetition rate was performed beforehand, a signal slowly increasing with time was recorded. A systematic study of this behavior is shown in figure 5.18, where the measurements with the same repetition rate are shown in the same color. It is clearly seen that the shape of the signal is highly dependent on the pretreatment of the capillary. Considering the light blue curves, representing the measurements carried out with 50 Hz, a decreasing signal intensity with time is observed when the previous measurement was carried out at 10 Hz, but a slowly increasing signal intensity is recorded when the prior repetition rate was set to 100 Hz. They are always higher for the measurement in which the number of ions is increased. However, it is most probable that both measurements reach the same equilibrium signal intensity if the measurement period would have been extended.

The different signal shapes are in agreement with the model describing the charging effects presented at the beginning of this section. The condition inside the capillary when pretreated with a lower ion current is similar to the situation when the laser beam was blocked for some time. When the measurement starts, the number of charges on the walls is lower than the equilibrium concentration according to the selected ion current. Thus, as mentioned before, the potential is low enough and more ions pass into the capillary as it would be the case in the equilibrium state, resulting in a decreasing signal intensity with time (see the first three signal-time profiles in figure 5.18). In the opposite case the potential inside the inlet capillary is higher than that corresponding to the equilibrium of the specific repetition rate. When a smaller number of ions passes through the inlet capillary, the drain of ions from the wall is

5 Ion Transmission Measurements

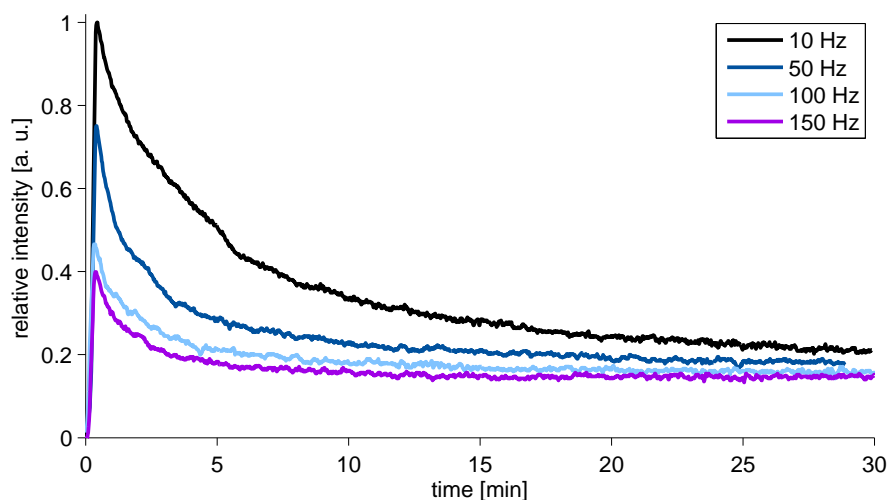


Figure 5.19: Dependence of cAPECI ion currents on the pretreatment of the inlet capillary by variation of the laser repetition rate.

higher than the number of ions that are deposited on the walls. The potential on the wall slowly decreases until the equilibrium is reached, resulting in a slowly increasing signal intensity with time.

Upon ionization with cAPECI, the signal evolution also shows a dependence on the number of ions that passed through the capillary previous to the measurement. Since the number of ions is not reproducibly adjustable with the cAPECI source, APLI was performed with different repetition rates in front of the ion source. Figure 5.19 shows the signal evolutions of the cAPECI source for four different mixing ratios of ions that passed through the capillary before the measurement started. All four signals show an initial signal peak and a slowly decreasing ion current with time. After around 30 min the signal intensities of the four profiles reach approximately the same value. This indicates that an equilibrium state has been reached and that the equilibrium potential that forms on the capillary wall is independent of the ion “pretreatment” of the capillary. However, the time required before the equilibrium is established differs considerably. With lower number of ions that pass through the capillary prior to the cAPECI measurement, the initial signal peak height and the time until the equilibrium state is reached increases. This is explained in the same way as the effects shown in figure 5.18. When a low number of ions passed through the capillary before the UV lamp was switched on, the number of charges on the wall is lower than it would be in the equilibrium state of the photoelectron ionization. Higher amounts of ions, as for example, when the capillary was pretreated with APLI at a repetition rate of 150 Hz, led to shorter equilibration times. For these conditions, the number of charges on the wall is close to the equilibrium value for the ionization with

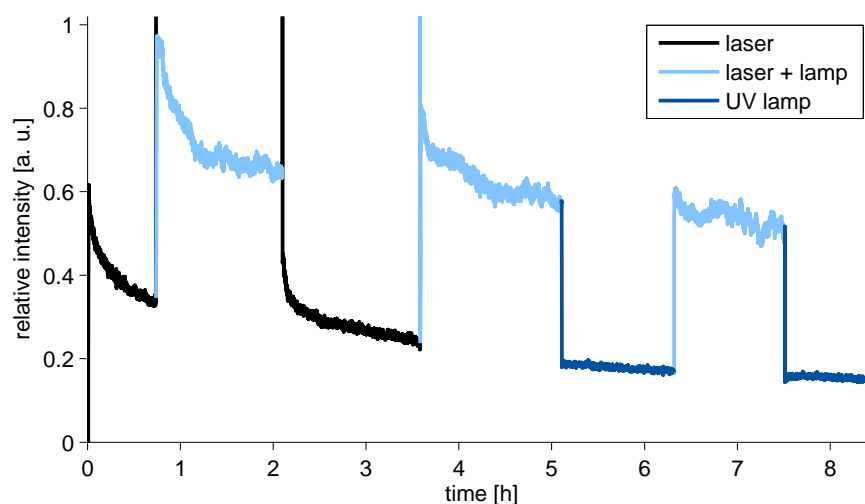


Figure 5.20: Ion transmission intensity-time profiles for APLI, cAPECI and the simultaneous combination of both methods.

cAPECI, resulting in only a short time until the signal intensity becomes constant.

Combination of Ionization Methods A combination of both ionization methods, laser ionization in front of the inlet capillary and the generation of photoelectrons inside the cAPECI source was carried out in different ways. While cAPECI always leads to negative ions, the ion polarity with APLI is selected. Figure 5.20 shows the ion transmission from the combination of photoelectron generation and a purely negative ion stream from laser ionization. The ion current of APLI was adjusted so that it was in the same range as that resulting from cAPECI. The black curves, corresponding to laser ionization and the dark blue curves, representing photoelectron ionization, show the expected transmission evolution for an inlet capillary containing a cAPECI source design 1. When the measurement is started with photoelectron generation and laser ionization follows, the transmission evolution looks very similar, indicating that it is solely dependent on the number of ions passing through the inlet capillary, but not on the ionization method.

The combination of both ionization methods, i.e., the light blue curves in figure 5.20, leads to an increase in intensity as expected because the number of ions is roughly doubled. However, the relative intensity is larger than the sum of both individual signals. The number of ions is increased compared to the previous measurement when both ionization methods are used simultaneously, so the transmission shows an initial peak at the beginning.

APLI is a pulsed ionization method, while cAPECI generates ions continuously. To determine which of both ionization methods has a larger impact on the signal

5 Ion Transmission Measurements

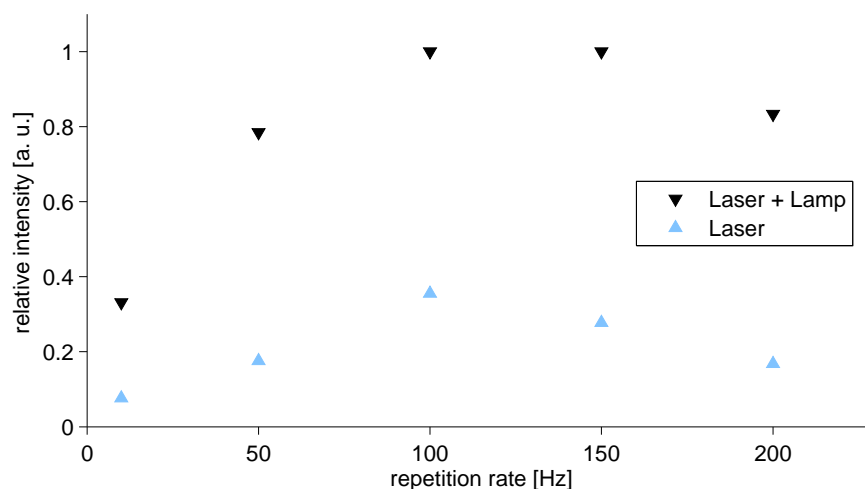


Figure 5.21: Dependence of the relative intensity of the laser signal and the signal of both laser and photoelectron generation on the repetition rate of the laser.

amplification the repetition rate of the laser was varied. The relative intensity from the combination signal of lamp and laser correlates with the dependence of the laser signal on the repetition rate, as shown in figure 5.21. However, the difference between both signal intensities is a constant factor, except for the signals obtained from a repetition rate of 10 Hz. Thus, the ions generated by photoelectrons add a constant number to the variable APLI signal when a certain threshold of ions is present. The reason for this effect may be that the ions generated by cAPECI increase the transmission through the capillary ion source for externally generated ions, by charging the surfaces in a way that leads to a higher transmission.

When only positive ions generated by APLI pass through the capillary and the UV lamp is switched on and negative ions are detected an amplification of the signal is also observed. Figure 5.22 shows the dependence of the ratio of the sum of cAPECI signal when positive ions pass through the capillary to the pure lamp signal on the repetition rate of the laser. With increasing repetition rate of the laser, an increasing number of positive ions is mixed into the continuous negative ion stream. The ion stream inside the capillary becomes more and more bipolar with higher repetition rates, resulting in an increased ion transmission. The ratio plotted in figure 5.22 reaches a constant value for higher repetition rates. It was shown previously that the ion cloud becomes a nearly continuous ion stream inside the capillary for high repetition rates [47]. Thus, bipolarity is nearly continuously established for higher repetition rates, leading to the highest possible transmission for a certain number of negative ions, due to the minimization of charging effects, which lower the transmission of unipolar ion streams.

5.1 Ion Transmission of Different Materials

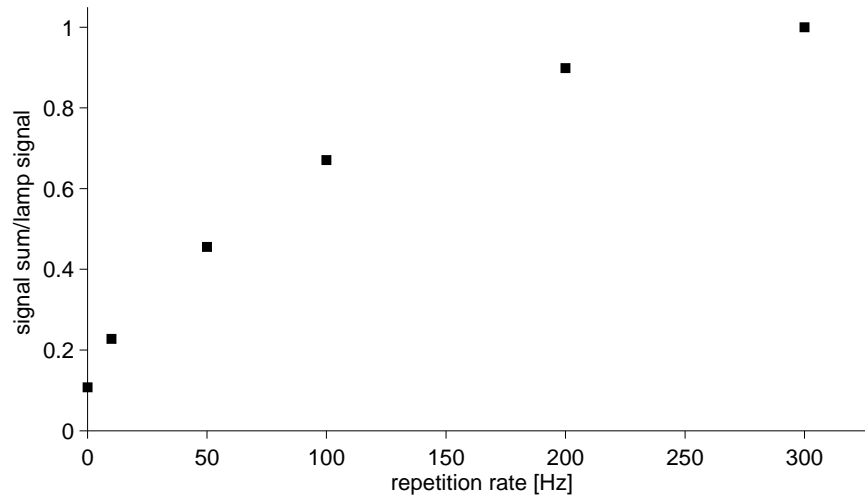


Figure 5.22: Dependence of the amplification of the negative cAPECI signal on the repetition rate of the laser for the generation of positive ions.

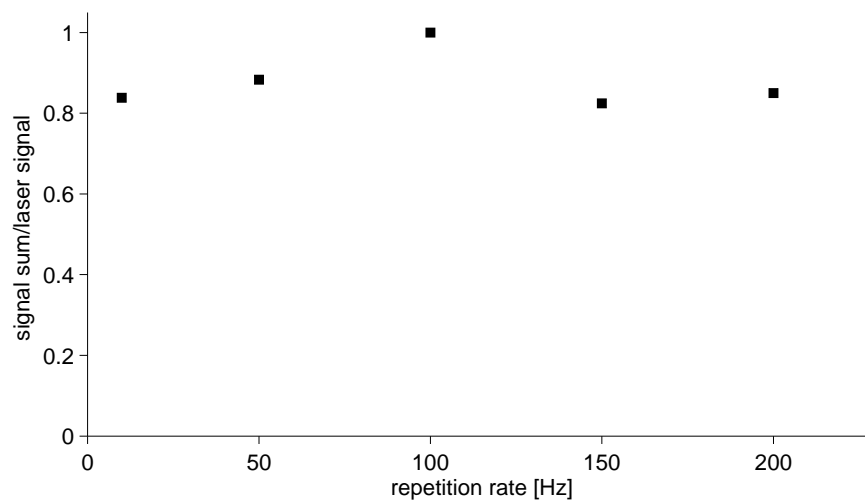


Figure 5.23: Dependence of the amplification of the positive ion signal by negative ion generation with cAPECI on the laser repetition rate.

5 Ion Transmission Measurements

For low repetition rates, the bipolarity of the ion gas stream is only given during the ion pulses generated by APLI.

Amplification of the measured ion current also occurs for the positive ion current generated by laser ionization. As the amount of negative ions from the cAPECI source remains constant for all measurements, independent of the repetition rate of the laser, the amplification factor is nearly the same for all adjusted repetition rates. This is seen in figure 5.23 where the ratio of the positive ion current when the UV lamp is switched on to the purely positive ion current is plotted against the repetition rate. Despite a small variation, the amplification is constant over the whole repetition rate range. It should be emphasized that the positive ion signal certainly shows an increasing signal intensity with an increased repetition rate, but this dependence is the same for the purely positive ion current and the bipolar ion current when negative ions are generated with cAPECI, resulting in a constant amplification factor for all repetition rates.

5.1.3.1 Temperature Dependence

The experiments described in the previous section suggest that the influence of the ionization method on the transmission signal is small because similar initial peaks and long term transmission evolutions are obtained for ionization with cAPECI and APLI. However, during cAPECI the UV lamp heats up considerably, leading to a heating of the ion source, which may lead to changes in the transmission characteristics. The change in temperature potentially changes the surface covering with molecules, which may influence the capability of the photoelectrons escape to the gas phase. Whether or not this causes a decreasing signal intensity with the run time of the cAPECI source is investigated by heating the source to different temperatures. The resulting ion current for different temperatures of the source is shown in figure 5.24. With increasing temperature, the ion current decreases significantly. However, the heating of the ion source also leads to an increase of the viscosity of the gas that passes through it. This effect has been observed before, when the total gas flow through an inlet capillary was measured as a function of the temperature of the capillary [85]. The decrease of the ion current should be similar when ionization is performed in front of the capillary. This would lead to an increased viscosity with rising temperature, but a changing surface coverage would not have an influence on the ionization process. Figure 5.25 shows the dependence of the ion current generated with APLI on the source temperature. Here, the signal also shows a strong dependence on the temperature. At approximately 150°C the signal decreased to around 10 % compared to the signal at room temperature. This is roughly the same value as for ionization with cAPECI, indicating that the change of the gas flow due to the increase in viscosity potentially covers other effects that may be caused by a variation of the source temperature. Furthermore, even though the relative intensity changes with increasing temperature no variation in the signal intensity evolution with time was observed.

When a cAPECI measurement begins, the lamp needs some time to reach its working

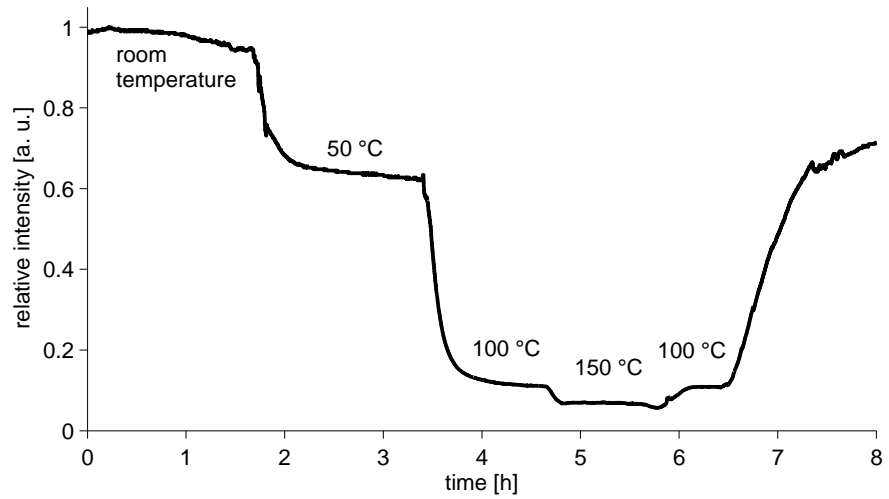


Figure 5.24: Photoelectron transmission signal for different temperatures of the CAPECI source design 1.

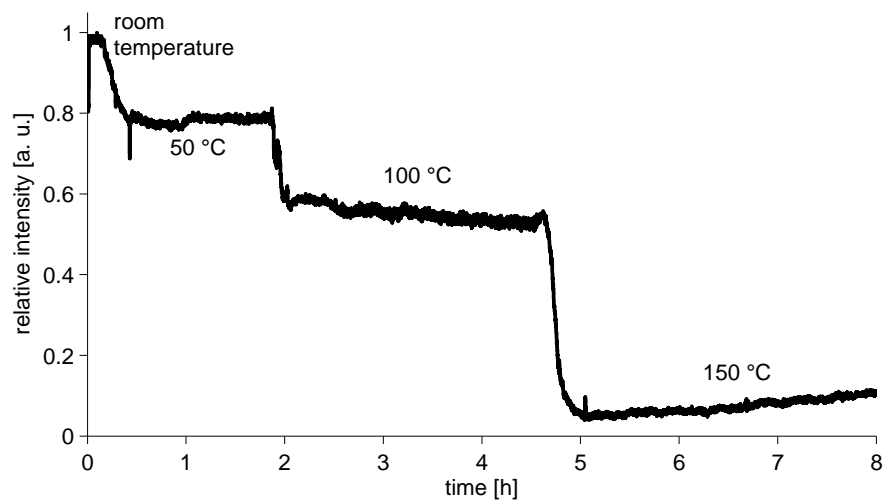


Figure 5.25: Transmission signal of ions generated with APLI for different temperatures of the CAPECI source design 1.

5 Ion Transmission Measurements

temperature. The ion source also heats up, which takes a considerably long time, as it is relatively large compared to the heat output of the lamp. During this time it is possible that the decreasing signal intensity with time is caused by the heating of the metal, resulting in an increase in viscosity and thus on a reduction of the total gas flow through the inlet capillary. Replacing the window inside the cAPECI source by a metal plate made of brass and performing APLI in front of the inlet capillary allowed to investigate the heating of the source due to the lamp without the generation of photoelectrons. The resulting ion transmission when the lamp was switched on was constant and did not show a declining signal intensity with time. The constant signal, even though the cAPECI source is included, is understandable as the ion source consists only of metal and does not contain a silica or lithium fluoride window which are necessary for photoelectron generation. Experiments with the different capillary segments between two glass capillary pieces yielded a similar result; a signal decay with time was only observed with the silica capillary segment.

5.2 Dependence on Relative Humidity

For all capillary types the signal evolution of the first measurement of each day and after larger modifications of the setup differed significantly from later measurements. It is therefore very likely that the amount of water inside the capillary significantly influences the ion transmission.

Figure 5.26 shows the signal evolution for two experiments. Two capillary segments were connected and attached to the ionization or detection chamber. The capillaries were separated and individually flushed with different gases. The detailed description of the setup is given in section 3.4. In the first experiment, dry air was flown through the capillary that was connected to the detection chamber, before the capillaries were assembled (green curve). In the second experiment, water saturated air was used to flush the capillary for two minutes (blue curve). When dry air was used, the signal is similar to measurements where only the laser beam was blanked out (see figure 5.5). The decay time for the initial peak is longer with approximately 5 min, but that may be due to the lower number of charges that passed through the capillary. The use of humid air changes the signal-time profile drastically. The ion signal is first detected after about 3 min. The signal rises for one minute and reaches a constant value without a considerable signal peak at the beginning.

The drastic change of the ion transmission signal when humid air is used confirms the assumption that the different result for the first measurement of a day is due to the change in the water concentration inside the capillary, as the measurement chambers were held open over night in most cases. Possible reasons for the changes are i) that the transmission of ions through the capillary is hindered until the film thickness of the water layer is thin enough or ii) that the water layer must take up a certain number of charges such that the repulsion of the potential formed by these charges is high enough to allow ions to pass through the capillary.

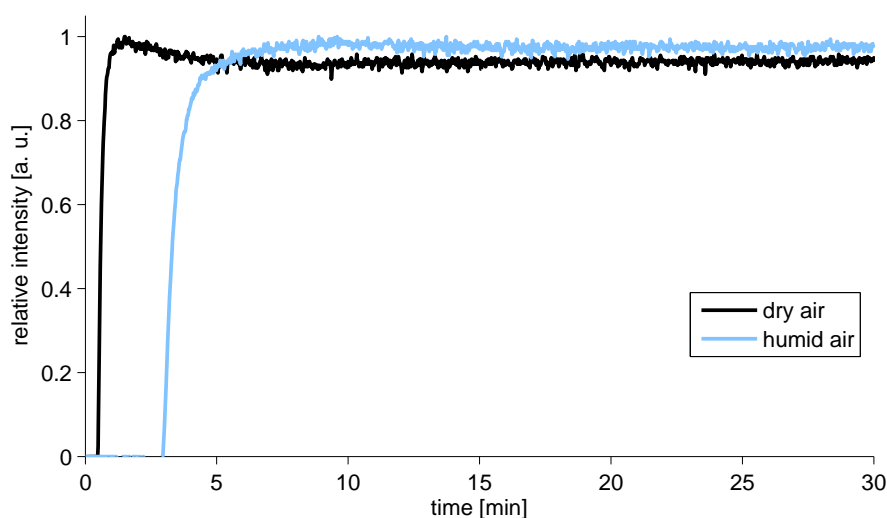


Figure 5.26: Ion transmission-time profile after dry or humid air passed through the second part of an inlet capillary consisting of two glass capillary segments.

5.3 Application of Voltages

External electrical fields may also disturb the ion transmission and signal drop outs may occur. High statical electrical fields near the capillary are easily generated by touching the capillary or by electrostatically charged plastic parts. In both cases, the electrostatic voltage cannot be quantified. As the systematic investigation of these effects would involve extensive investigation, only a brief overview over the influence of electrical fields on the ion transmission is given in the following.

To examine the influence of electrical fields on standard inlet capillaries, the adaptor, normally used to assemble inlet capillaries from different segments, was pushed onto the capillary with a voltage applied. With increasing voltage the ion current measured with the ion trap decreased. However, the level of the signal decrease depended on the respective polarities of the voltage and the ion current. Figure 5.27 shows the influence of the polarity of the electrical field on the negative total ion current. The ion gas stream through the capillary is purely negative (cf. section 3.4). When a voltage of -6 kV is applied, the signal decrease is much larger than when a positive potential of the same value is applied. Two observations are striking: Firstly, the signal regenerates after the voltage is applied and the signal was dropping to zero. Secondly, the shape of the signal regeneration is different if a positive or a negative field is applied. The signal regeneration is much larger for the negative ion current when the electrical field is negative. After the voltage is applied, no ions pass through the capillary for approximately 10 min, then the total ion current increases almost to the value when

5 Ion Transmission Measurements

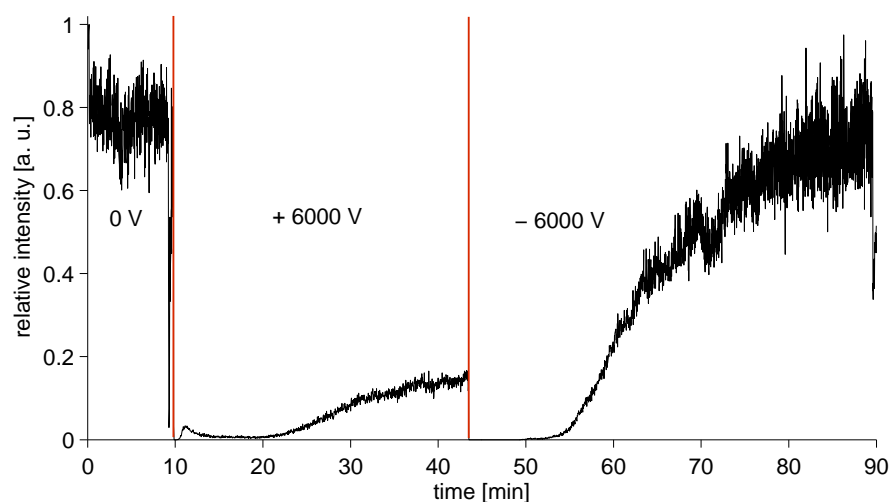


Figure 5.27: Dependence of the negative TIC of a common glass capillary on the voltage applied to a metallic adaptor that was placed over the capillary.

the adaptor is grounded. When the applied voltage polarity is changed a regeneration of the intensity occurs, but not to the same extent. Furthermore, the signal-time profile when a positive voltage is applied differs significantly to that of the negative voltage. The signal not only decreases and then increases again after some time, but shows a signal peak after the voltage is switched on. Subsequently the signal decreases and starts to recover after some time. Voltages of more than ± 9 kV resulted in the complete disappearance of the signal, which did not recover even after an extended time period.

When two capillary segments were assembled to an inlet capillary with the adaptor and a voltage is applied similar effects were observed. However, the main difference is the voltage that is needed for a vanishing signal intensity. This was approximately ± 4 kV, which is less than half of the voltage that is necessary for an intact capillary. With a metallic capillary segment between the glass capillary pieces the influence of the voltage on the ion transmission is further increased. In this case, a voltage of ± 3 kV is sufficient to prevent ions passing through the capillary. Figure 5.28 shows the dependence of the negative and the positive total ion currents on the voltage applied to the metal segment. Again, the polarity of the electrical field in relation to the polarity of the ions is important for the extent of the signal decrease. In contrast to the intact capillary, the ion current with the opposite sign to the polarity of the field shows a higher transmission when a voltage is applied. A voltage of -1 kV on the adaptor leads to a large signal decrease by more than a factor of ten for the negative ion current. The ion current of the positive ions is only halved. With a voltage of 1 kV the signal intensities switch and the negative ion current is much larger than the positive ion current. Voltages higher than ± 1 kV lead to a disappearance of the ion current for ions

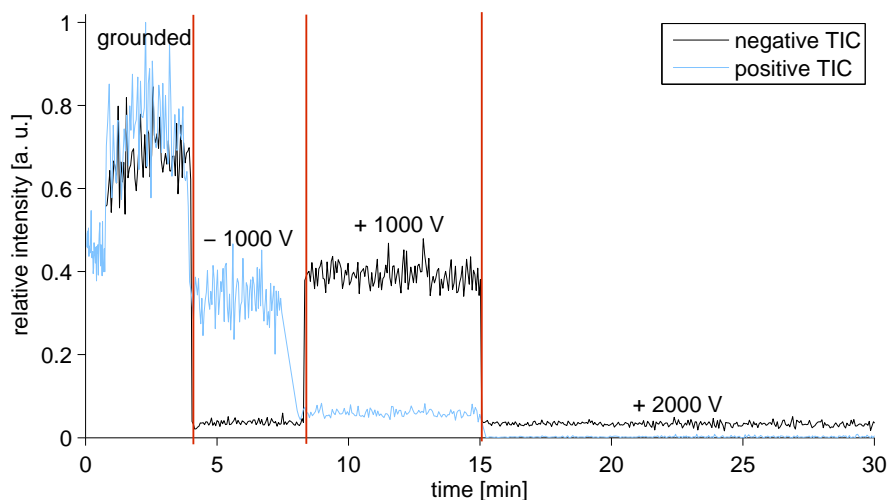


Figure 5.28: Dependence of the voltage applied to the metallic capillary segment between two glass capillary segments on the total ion current.

of the same polarity.

With a silica capillary segment inside a metal husk mounted between two glass capillary segments the effect of applying a voltage on the metallic adaptor is significantly different. Firstly, the voltage that is needed to decrease the ion current to zero is less than ± 1 kV. Secondly, as can be seen in figure 5.29, the signal intensities of the negative and positive ions when the capillary is grounded are very different. A voltage of -100 V leads to a decrease of the positive TIC by a factor of three and to an increase of the negative TIC by a factor of three, so that both TICs have then almost the same intensity. For voltages higher than ± 300 V the signal intensities decrease again.

The influence of electrical fields on the ion transmission of differently composed capillaries is yet not fully understood. For an intact capillary, the static electrical field must have a considerably high voltage to influence the ion transmission. It must pass through the glass to influence the number of charges on the inner wall of the capillary to the extent that no ions pass through. When the inlet capillary is composed of two glass capillary segments, the voltage that is necessary to decrease the ion current to zero is lower. The electrical field influences the ions more pronounced as it i) passes through the air between the contact surface of the two segments and ii) at normal conditions, the glass surface at the contact area of the capillary is covered with water and other molecules, so that the conductivity is enhanced. The ions are easily discharged at the metallic adaptor through this surface layer. The introduction of a metallic capillary segment decreases the required voltage further. The electrical field does not have to penetrate through insulators or air to influence the ions inside the capillary channel by changing the surface potential as the voltage is directly applied

5 Ion Transmission Measurements

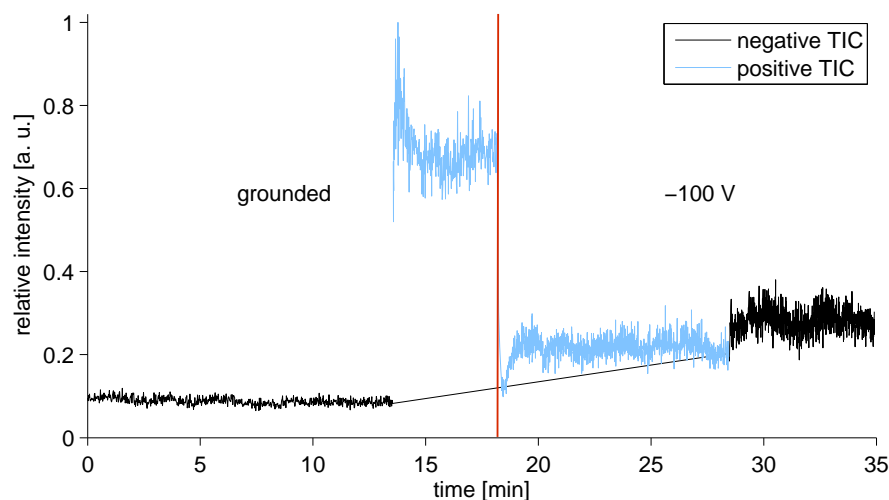


Figure 5.29: Dependence of the ion current through an inlet capillary containing a silica segment on the applied voltage.

to the metallic segment. However, the very low voltage that is necessary to deflect all ions when a silica capillary segment is introduced into the inlet capillary does not fit to the assumptions described above. Silica has a high electrical resistivity, so that it should show a behavior that is similar to glass. The two transitions of materials inside the capillary facilitate the influence of the electrical field, but that does not explain the factor of ten in the voltages between the capillary assembly. An explanation may be that the metallic husk was a little larger than the silica capillary piece at one side, which resulted in an increase of the volume in this section. This decreases the gas velocity and the ions are influenced to the same extent by lower voltages.

The experiments were carried out with unipolar and partially bipolar ion currents. When both TICs are shown in the figure, the ions of different polarities pass through the capillary consecutively within some milliseconds, due to the voltages applied inside the ion source. This time is not long enough to change the surface potential significantly, so that a bipolar surface coverage is assumed. However, the observations when voltages are applied to different capillaries do not differ considerably for each polarity if a unipolar or quasi-bipolar ion current passes through the capillary.

For an intact inlet capillary, the negative ion current is larger when a negative voltage is applied to the outside of the capillary. The electrical field changes the equilibrium potential on the capillary wall. After the potential is changed nearly all ions that enter the inlet capillary are forced into the surface layer. When the number of charges approaches the new equilibrium potential, more and more ions pass through the inlet capillary until the maximum potential is reached. The ion current recovers to nearly the same intensity as before with the new equilibrium potential. This behavior is

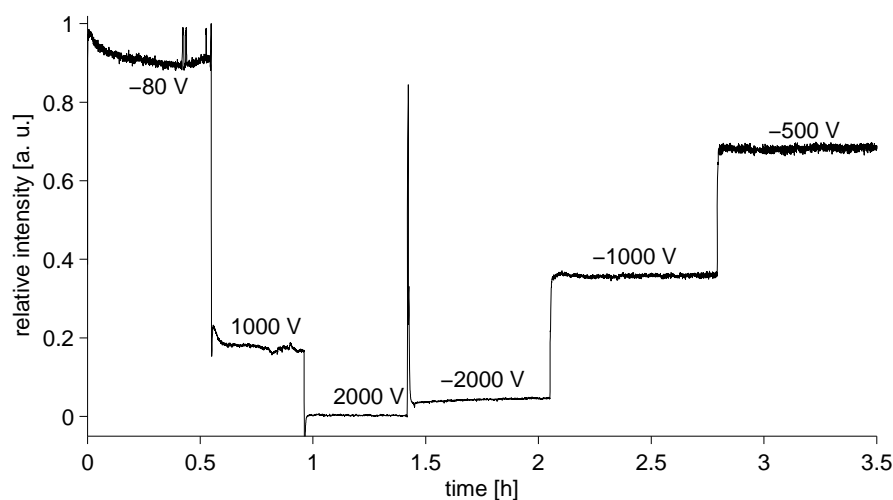


Figure 5.30: Dependence of the normalized negative ion current of an inlet capillary containing two glass capillary segments and a metal capillary segment on the voltage applied to the metal segment; recorded with the measurement chambers.

not consistent with the explanation given in the previous section, as it was assumed that the equilibrium signal intensity depends on the surface potential. It may be the case that the number of surface charges is only changed in the area where the voltage is applied, so that the potential at the inlet of the capillary remains unchanged. Thus, the number of ions entering the capillary is constant during the measurement and the signal decrease is caused by a high intake of ions into the surface layer. For combined inlet capillaries, the applied voltage causes the same effect, but as ions can get discharged at the metallic adaptor through the contact surfaces, an enhanced potential leads to similar effects as described above for the inlet of the capillary. This means that the decrease of ions is caused by the changed potential at the capillary wall and that the signal does not recover because the enhanced potential leads to a deflection of the ions towards the walls where many are discharged.

When the experiment with voltage applied to the metallic capillary segment between to glass capillary segments was carried out with the measurement chamber, the results were not in agreement with that obtained with the mass spectrometer. Figure 5.30 shows the negative ion current where different voltages are applied to the metallic capillary part. A positive electrical field leads to a larger decrease of the transmission than a negative voltage applied to the metal. Thus, the dependence on the voltage polarity is exactly the opposite to the behavior with the ion trap. The reason for this effect is not understood and is a topic for further investigations.

5.4 Summary and Outlook

Even though the results obtained by the measurements described in this chapter did not yield a comprehensive explanation for the observed effects, the investigation of the ion transmission characteristics gave crucial insights for the utilization of composite capillaries.

Experiments were carried out with a setup, which mimics a simplified desolvation stage of a mass spectrometer. The experiments showed that the gas flow inside the inlet capillary is fully developed turbulent for the conditions prevailing in Bruker Daltonik mass spectrometers. Calculations of the minimal molecular diffusion inside the capillary were carried out showing a large number of ions collide with the capillary wall during transport through the capillary in both, laminar and turbulent gas streams. Ions that reach the wall are not necessarily discharged. The surface of the capillary is covered with a layer of water and other molecules with a thickness which is dependent on the capillary material.

It was shown that the ion transmission-time profiles are different for unipolar and bipolar ion streams. Bipolar ion flows are barely affected by modifications of the inlet capillary, only the external application of voltages results in a change of transmission efficiency.

The model to describe the charging effects that occur when unipolar ion gas streams pass through different kinds of inlet capillaries describes most experiments fairly accurately. A fraction of the ions that are transported through the inlet capillary enter the water layer always present at the capillary wall. These charges result in the built-up of a potential; the magnitude is dependent on the material of the capillary and the amount of water in the gas stream. A potential forms between the capillary material and the metallic end caps, which were grounded under most of the experimental conditions. Some of the ions inside the surface layer discharge at the end caps. In the equilibrium state, the intake of ions at the water layer and the number of ions that are discharging is constant. The potential between the capillary and end cap influences the inflow of ions at the entrance of the capillary, by forcing a fraction of the ions toward the end cap instead of following the fluid dynamical forces. Numerical simulations support this assumption. The fraction of ions that does not enter the capillary, but follows the electrical field to the end cap as determined by the electrical gradient and the velocity of the inflowing gas. At the exit of the capillary the ion stream is not affected significantly. During the time in which the potential increases the number of ions that enter the capillary decreases. This process leads to a signal peak at the beginning of the measurement. For materials where the equilibrium is only slowly reached the signal slowly decreases with time. Both effects were observed in the experiments.

The signal peak at the beginning of the measurement was present in nearly all experiments with unipolar ion streams, even when using standard glass capillaries. For these capillaries, the signal intensity-time profile of the initial peak follows second order kinetics. The size and the decay time of the initial signal peaks are dependent on

the capillary material.

While the initial signal peak was observed in nearly all experiments for different materials, the long term stability was considerably changed. While a constant signal was reached for most materials, the lead silicate capillary and composite capillaries containing silica segments exhibited a signal decline over the whole measurement period. Other composite capillaries, containing metal or PVC segments did not show this behavior. This was also the case for the cAPECI source design 1 when the window was exchanged with a metal plate. A lack of long term stability is thus potentially related to materials with a very low conductivity, indicating that the equilibrium is only slowly reached in such circumstances.

The conductivity of the capillary material and especially the contact resistance between two materials are important factors for the occurrence of charging effects. Furthermore, signal drop outs may occur when the contact resistance between two materials becomes too high. Signal drop outs were observed for an inlet capillary containing a silica segment. The signal drop outs were then forced intentionally, by isolating the metallic husk of the silica segment from the grounded adaptor, which has been used to obtain an airtight connection between the capillary segments. There is a considerable difference in the transients of the signal drop outs, one being almost the inverse to the other. The reason for this behavior is not yet fully understood. Similar drop outs occurred with a commercial mass spectrometer. Generally, signal drop outs are caused when there is a high resistance between the capillary (or a part of the capillary) and a material with a high conductivity. In such cases, the potential increases up to a certain value and discharges suddenly.

Both charging effects, the initial signal peak and the long term stability are independent of the applied ionization method. The signal evolutions are identical for both laser ionization in front of the capillary and photoelectron generation inside the cAPECI source. The ionization method, developed during this work, provides a constant number of ions with time, however the design of the ion source is a crucial parameter for the long term stability.

The intensity and shape of the initial signal peak is highly dependent on the pre-treatment of the capillary, particularly on the number of ions that passed through the capillary prior to the actual measurement. When a lower number of ions passed through the capillary during the previous measurement, the signal showed an initial signal peak followed by a slowly decreasing signal intensity with time. In contrast, when the number of ions prior to the measurement was high the signal rose slowly to the equilibrium signal intensity. It was assumed that in both cases the signal intensity reaches the same value after a sufficiently long time period. As mentioned before, the number of charges inside the water layer and the potential between capillary and materials with a high conductivity, e.g., the metallic end caps, determine the signal evolution. When the potential at the beginning of the measurement is higher than that in the equilibrium state, a smaller number of ions enters the inlet capillary at the beginning than during the further course of the measurement.

Laser ionization was used for both, negative and positive ion generation. The com-

5 Ion Transmission Measurements

combination of a selected ion polarity generated by APLI and the negative ions generated by cAPECI inside the capillary ion source yielding surprising results. The amplification of the purely negative signal was higher than the sum of both individual signals. The amplification of the positive APLI ion current is readily explained as the combination with the negative ions generated by cAPECI results in a partially bipolar ion current, which was more stable and had a higher signal intensity compared with unipolar ion streams in previous measurements. However, the combination of two negative ion streams also led to an amplification of the ion signal. The signal intensity showed a dependence on the repetition rate of the laser. For higher repetition rates, the cAPECI ion stream added a constant offset to the ion current generated by laser ionization. The reason for this amplification is still not fully understood, it may be the case that the ions generated inside the cAPECI source reduce the loss of ions generated in front of the capillary within this source. To examine this effect in detail further investigations will be carried out.

In atmospheric pressure ionization the amount of water is always high when no special drying procedures are applied. As the capillary always has a water layer on the inner wall, the influence of the water mixing ratio on the transmission of ions was investigated. When a gas stream with an increased water mixing ratio passed through the capillary prior to the measurement, the ion signal needed several minutes to appear. The signal evolution was rising to exact the same signal level as for dry gas. A possible explanation is that all ions are forced to enter the water layer at the beginning in order to charge it or that the surface layer needs some minutes to become thin enough.

External heating of the cAPECI ion source increases the viscosity of the gas leading to a decrease in gas volume that passes through the capillary. However, this is not the reason for the decreasing signal intensity with time, which was often observed for the cAPECI source, as the increase in temperature did not lead to a decreasing signal intensity with time. Other effects, as the regeneration of the surface at different temperatures were not observed, due to the large influence of the change in total gas flow.

The influence of the application of voltages to capillaries made of different materials is a large field to investigate and was only briefly touched on in this work. The voltage level that needed to be applied until the ion signal vanished varied considerably for different capillaries. While for intact glass capillaries ions were able to pass through until the voltage reached approximately 9 kV, capillaries containing a metal segment only needed around 2 kV until the ion current dropped to zero. Astonishingly, the voltage was lowest for a capillary containing a silica segment. The reason for this behavior is not fully understood.

For intact glass capillaries, the signal recovered after some time when a voltage was applied. A total recovery was only observed when the applied voltage had the same polarity as the ions passing through the capillary. For the opposite polarity, the signal also recovers, but reaches only a small fraction of the initial intensity. When a metallic segment is introduced, the negative TIC is decreased more than the positive TIC

5.4 Summary and Outlook

when a negative voltage is applied and vice versa. As mentioned before, the behavior of the capillary containing the silica segment is not understood when voltages are applied. When a negative voltage of only a hundred Volt is applied, the positive TIC decreases, while the negative TIC increases. Experiments at the measurement chambers gave results which are not in agreement with those obtained with the ion trap mass spectrometer. This topic will be investigated in detail in the future.

The transmission measurements with inlet capillaries containing silica segments were also not fully reproducible. The signal intensities did not always show a decrease with time, but an increasing signal intensity in the first minutes of the measurement followed by either a constant or very slowly decaying signal intensity with time. With the cAPECI source containing a lithium fluoride or silica window, the signal intensity showed a decreasing signal with time for all measurements. Thus, further investigations on inlet capillaries containing silica segments are necessary to understand the various processes leading to this behavior.

6 Ion Source Development

An ion source which uses the photoelectric effect for the generation of ions was developed. The ion source should have the following characteristics:

- generation of solely negative ions
- long term stability
- short reaction times between reagent ions and neutral analyte
- good sensitivity and selectivity

Furthermore, the ion source should ideally be made of readily available materials, easy to handle and not involve the use of potentially dangerous components, e.g., radioactive sources or high voltages.

Four ion sources were iteratively developed during this work, each source improving the disadvantages of the previous one. Figure 6.1 gives an overview over the developed ion sources (for details see sections 3.7.3 to 3.7.6.1), including a variant of the cAPECI source design 2 with longer reaction times. These sources are described in the following.

6.1 The Photoelectric Effect at Atmospheric Pressure

Work functions of metals are generally measured under high vacuum conditions. In the ionization method that was developed during this work, ionization takes place at or near atmospheric pressure. Thus, work functions of different metals were also determined at such pressure. The influence of different conditions, e.g., the oxidation state of the surface, organic substances on the surface or different laser powers, on the work functions and signal intensities is examined. This is important as all metals exhibit a surface layer of water and other molecules at atmospheric conditions. The photoelectrons generated by the photoelectric effect have to pass through this layer to escape into the gas phase, where they are captured and measured. The thickness and the molecular composition of the surface layers will thus influence the measured work function (cf. section 1.4) [89, 280].

6.1 The Photoelectric Effect at Atmospheric Pressure

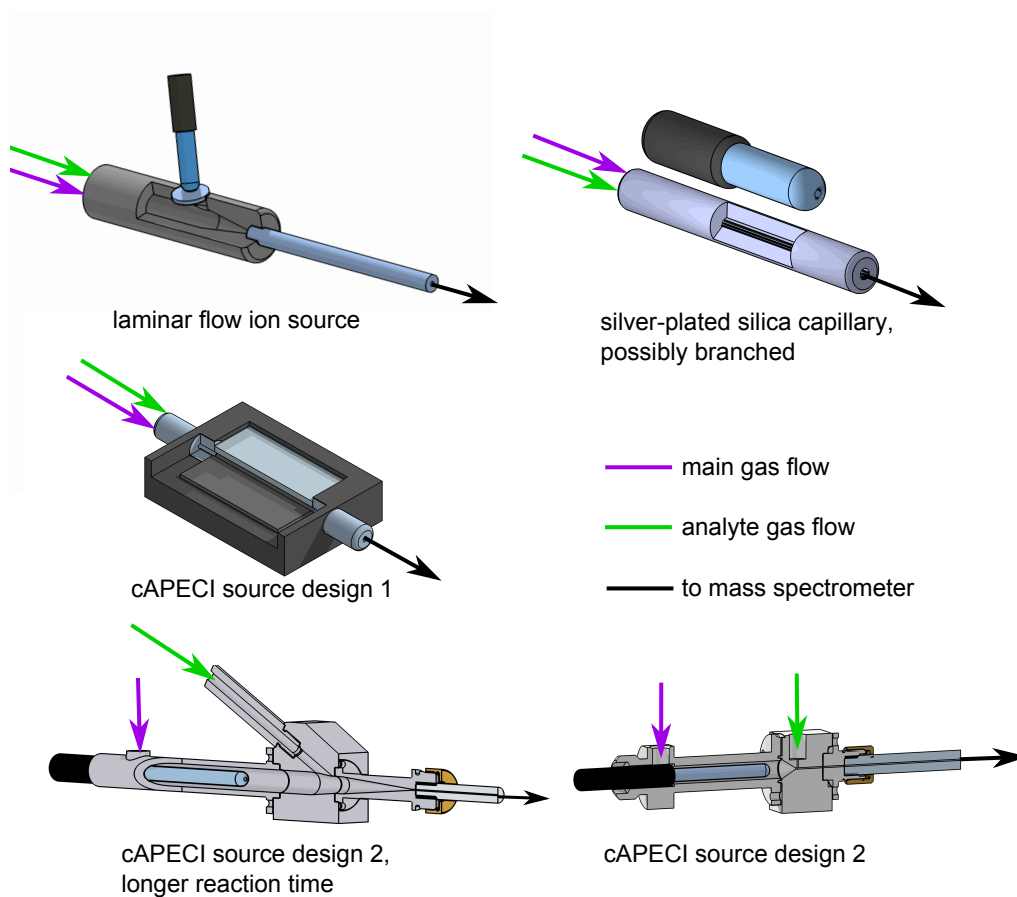


Figure 6.1: Overview about the different ion sources developed during this work.

Table 6.1: Work functions of different metals at atmospheric pressure, measured in synthetic air (accuracy ± 0.05 eV).

Metal	Work Function [eV]	
	Measured	Literature [101]
Aluminum	4.17	4.06-4.28
Titanium	4.34	4.33
Lead	4.23	4.14-4.25
Tantalum	4.35	4.0-4.80
Copper	4.37	4.48
Nickel-plated copper	4.37	5.04
Gold	4.37	4.74-5.31
Gold-plated steel	4.37	4.74-5.31
Sterling silver	4.62	4.25-4.74

6.1.1 Tunable Laser System

The work functions reported in table 6.1 were measured at atmospheric pressure in synthetic air. For most metals, the measured work function and the value found in the literature, determined under vacuum conditions, are in good agreement. Due to the different measurement conditions the work functions found in the literature exhibit generally a broad range, thus, a correlation between measured and literature values is not surprising. However, two results are striking: Firstly, nickel-plated copper and copper have the same work function. For gold-plated steel, this effect is not observed, which shows the same work function as pure gold. Secondly, the work function of gold differs significantly from the literature value. The investigation of this second effect will be discussed later in this section. Photoelectron generation with a nickel surface should be possible up to 246 nm. However, even with 284 nm photons electrons are detected. A possible explanation is that a thin nickel layer allows photons to pass through and reach the copper atoms, which then eject photoelectrons. For gold-plated steel a different result is obtained. Here, the work function is the same as for gold. As is shown later, gold behaves differently than the other metals, which may also explain this effect.

The airtight measurement chamber could be evacuated to approximately 1.3 mbar. Work functions measured under this condition are perfectly in agreement with the results measured at atmospheric pressure. However, the signal intensity and especially the peak shapes are significantly different under reduced compared to atmospheric pressure as seen in figure 6.2. In this figure, each grid line of the y-axis corresponds to a signal intensity of 100 mV recorded with the oscilloscope. The upper channel shows the laser trigger pulse to which the photoelectron signal (lower channel) is synchronized. The signal intensity of each signal is determined relative to the base line

6.1 The Photoelectric Effect at Atmospheric Pressure

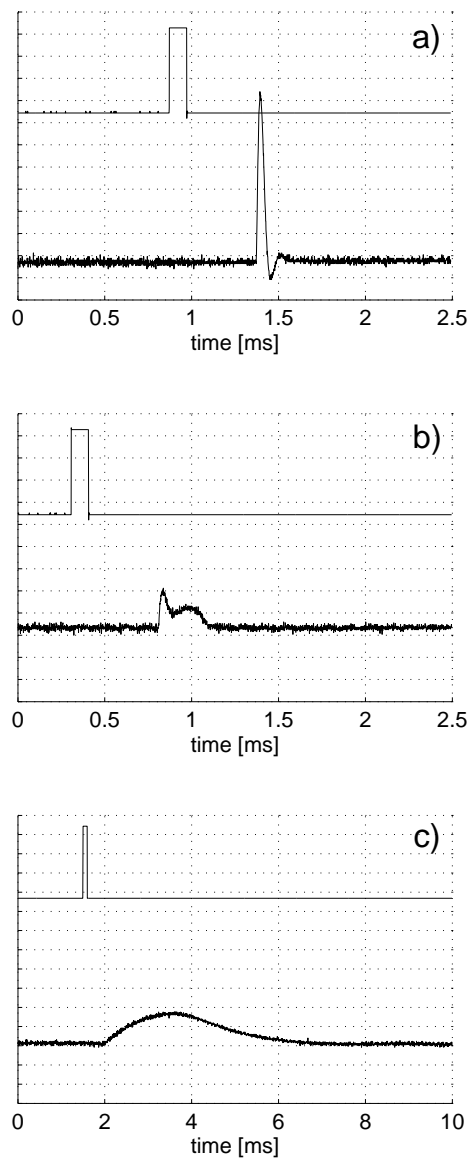


Figure 6.2: Photoelectron signal transients at 266 nm with 80 V acceleration voltage recorded under different pressures: a) 0.7 mbar, b) 7 mbar and c) 985 mbar. The upper channel shows the trigger pulse of the laser, the lower one the photoelectron signal. On the y-axis one grid line represents 100 mV.

6 Ion Source Development

of the specific channel. As the intensity recorded with the oscilloscope depends on the amplification factor of the electrometer, a direct comparison of signal intensities and peak areas is difficult. With different amplification factors adjusted at the electrometer, the peak shape also changes. An increase of the measurement range from 1×10^{-7} to 1×10^{-9} A broadens the signal considerably. Thus, the measurement range should not be changed, if possible, when signal shapes or signal intensities are to be compared. In figure 6.2 the signals at reduced pressure (a and b) are recorded with an amplification of 1×10^{-7} A, while the signal at atmospheric pressure was too small to be recorded in this measurement range, so that a range of 1×10^{-8} A was used. The broadening of the signal is therefore not only attributable to the increased pressure, but also to the measurement system. However, the broadening of the signal is already observed when the signals at 0.7 mbar and 7 mbar are compared. Not only a broadening of the formerly very sharp photoelectron signal is observed for increased pressures, but also two individual signals. The first signal remains sharp and rather small, while a broader peak overlaps. A possible explanation is that at low oxygen concentrations the first sharp signal is assigned to a photoelectron peak, while the broader signal is produced by superoxide ions. As these two species exhibit drastically different electrical mobilities, they are detected as individual signals. With increasing pressure, the sharp signal disappears, as all photoelectrons are captured by oxygen during their passage from the photoemissive material to the measurement electrode.

Influence of Different Gases When the measurement chamber is filled with gases other than oxygen, it is expected that although the peak shape may change, the signal intensity should show the same pressure dependence compared to synthetic air. However, this is not the case. Figure 6.3 shows the photoelectron signal at 266 nm with an acceleration voltage of 80 V and a measurement range of the electrometer of 1×10^{-7} A in the presence of helium as background gas. The signal at reduced pressure is nearly ten times larger than the signal at elevated pressure. In air the signal under vacuum conditions was approximately a hundred times more intense than at atmospheric pressure. Furthermore, even though the signal intensity decreases with increasing helium pressure, the peak shape does not change significantly, i.e., no broadening is observed.

The use of sulfur hexafluoride leads to a different effect. With increasing SF₆ pressure the signal peak becomes broader and loses intensity. At a pressure of approximately 260 mbar the signal is no longer observed, even when the measurement range is decreased from 1×10^{-7} to 1×10^{-10} A. A decrease in signal intensity may be explainable by the formation of SF₆⁻, which is a comparably large ion and thus has a low ion mobility. However, this can not explain the disappearance of the signal at higher SF₆ pressures, as the formed ions will not disappear but reach the measurement electrode at a later time than smaller ions.

For argon a similar behavior is observed. At an argon pressure of 800 mbar, the photoelectron signal has decreased to zero under otherwise similar conditions as

6.1 The Photoelectric Effect at Atmospheric Pressure

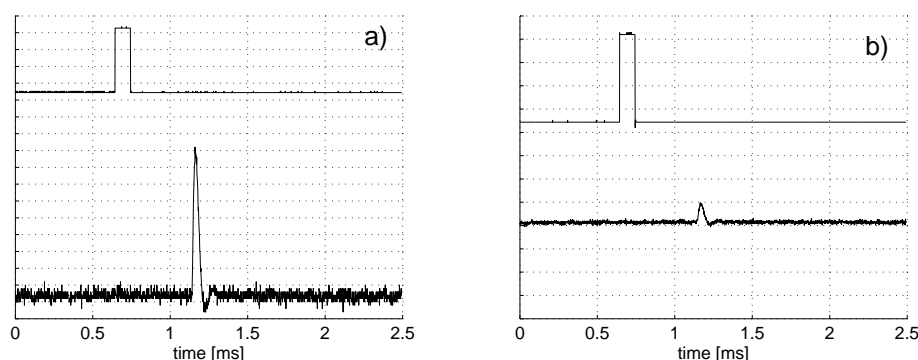


Figure 6.3: Photoelectron signals at 266 nm with 80 V acceleration voltage recorded under different helium pressures of a) 0.7 mbar and b) 976 mbar. On the y-axis one grid line represents 100 mV.

described previously for sulfur hexafluoride and helium. As argon does not react with the photoelectrons this effect is not easily explainable. The diffusion coefficient of thermal electrons in argon is three times higher than that of electrons in helium¹ [281], so that the signal should be even more confined at the same reduced electrical field strength as in helium. Astonishingly, the same behavior is observed with increased nitrogen pressures, when the signal is no longer observed for pressures above approximately 400 mbar. Nitrogen also does not react with electrons and there is no obvious reason as to why the generated electrons vanish. To examine the reason for the disappearance of the signal at enhanced pressures further investigations are needed. During this study maximum acceleration voltages of 80 V were applied, it is possible that the signal may be observed with higher acceleration voltages. The generated photoelectrons may return into the metal surface if the acceleration voltage is not able to pull the electrons away from the surface.

When the pressure is increased and the acceleration voltage is kept constant, the reduced field strength decreases from 125 Td at 1.3 mbar to 0.16 Td at 1013 mbar. To test if this influences the shape or the intensity of the photoelectron signal different acceleration potentials were applied at the same pressure. The results of this experiment are shown in figure 6.4. For the signal peaks at 80 to 60 V acceleration voltage, one grid unit of the y-axis corresponds to 10 mV, while for the lower three acceleration voltages, 50 to 30 V, one grid unit corresponds to only 5 mV, which means that these

¹For a reduced electrical field of approximately 0.21 Td (80 V acceleration voltage and an electrode distance of around 1.5 cm), an electron drift velocity of $1.5 \times 10^3 \text{ ms}^{-1}$ in helium and 1.75 ms^{-1} in argon and diffusion coefficients to mobility ratios, D/μ , of $6 \times 10^{-2} \text{ V}$ for helium and $2 \times 10^{-1} \text{ V}$ for argon, a diffusion coefficients of $45 \text{ cm}^2 \text{ s}^{-1}$ for electrons in helium and $175 \text{ cm}^2 \text{ s}^{-1}$ for electrons in argon is obtained. The values for the electron drift velocity and the diffusion coefficient to mobility ratios were taken from the data in Pack et al. [281].

6 Ion Source Development

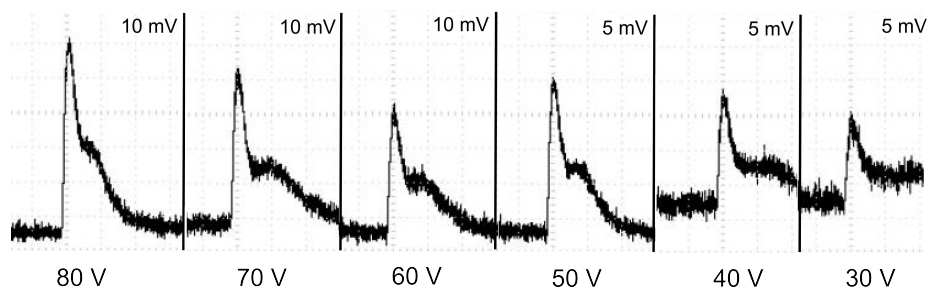


Figure 6.4: Signal shapes at 970 mbar synthetic air with different acceleration voltages between the electrodes, separated by 2 mm. One grid in the x-axis corresponds to 100 μ s, in the y-axis to 10 mV for 60 to 80 V and 5 mV for 30 to 50 V acceleration voltage.

signal peaks have only half of the intensity of the other signals. In the x-axis one grid unit corresponds to 100 μ s for all signals. It can be seen that the general signal shape does not change much with increased acceleration voltage. However, the signal intensity increases considerably resulting in a clearer distinction of the two peaks that compose the detected signal. This supports the assumption that the photoelectron signal in enhanced argon pressures may be observed at higher acceleration voltages.

Influence of the Surface Properties An important factor affecting the work function and the signal intensity is the chemical surface state and structure of the metal surface. Aluminum shows an extensive oxidation of its surface in a relatively brief time period. Thus, the examination of the signal dependency on the oxidation of the surface has been mostly studied with aluminum and was compared with silver. Its surface is only slowly oxidized with time. An aged aluminum surface, which means a completely oxidized surface, exhibits a 400 times lower signal intensity compared to freshly polished aluminum. When a freshly polished surface oxidizes, only during one night the signal intensity decreases by a factor of two. Silver also shows a dependence of the signal intensity with the surface condition, but the decrease in intensity between a freshly cleaned and an aged surface is only 25%. Even though these measurements were performed at approximately 2 mbar the comparison of the signal intensities should be approximately transferable to atmospheric pressure.

The second part of this examination regards the dependence of the work function on the surface condition. While freshly polished aluminum exhibits a work function of 4.12 eV (301 nm), oxidized aluminum did not show a photoelectron signal for wavelengths longer than 285 nm. Leaving the freshly polished aluminum in laboratory air over night led to a work function threshold of 4.25 eV (292 nm). Silver always shows the same work function of 287 nm, independent of the age of the surface. Copper has a slowly reacting surface with time compared to aluminum. With an old, unpolished surface the work function was measured to be 4.38 eV (283 nm), polishing of the surface

Table 6.2: Signal intensities at 266 nm for silver and aluminum for water and toluene on the metal surface.

Solvent	Relative signal intensity	
	Aluminum	Silver
“clean”	1	1
Water	0.4	0.4
Toluene	10	8

resulted in a small increase of the work function to 4.35 eV (285 nm).

The change of signal intensity or work function due to solvents on the surface of a photoemissive material is reported in the literature, for example, by Inumaru et al. [162], Hubert et al. [155] and DeRenzi et al. [282]. There, the work function changes significantly when organic materials cover the metallic surface. Different solvents gave changes of the signal intensity in the range of -98 to 73 % and a change of the work function of -0.09 to 0.25 eV [162]. Reasons for the changes were identified as i) solvent clusters that form stable negative ions which transport electrons to the measurement electrode, ii) molecules at the surface that form stable anions which decrease the photoelectron current and iii) the ionization of molecules or clusters that contribute to the measured ion current. However, in the experiments carried out during this work, the application of water and organic solvents on the surface of aluminum and silver did not result in changes of the work function, but had a large impact on the signal intensity, cf. table 6.2. Water vapor on the metal surface decreased the signal intensity for both metals nearly equally. In contrast, toluene vapor on the metal surfaces led to an increase in the photoelectron yield for both metals.

There are possible explanations for these effects: UV light is used for photoelectron generation and water is able to absorb this wavelength range with an absorption cross section of $4.7 \times 10^{-20} \text{ cm}^2 \text{ molecule}^{-1}$ at 295 nm [283], reducing the generation of photoelectrons. Furthermore, a water layer may hinder the electrons from escaping into the surrounding gas phase. Toluene has a different effect as its ionization potential is attainable by resonant enhanced two photon ionization with the wavelength used in this experiment (266 nm). Thus, the enhanced measured ion current may be due to ionization of toluene instead of photoelectron generation. If that notion is correct would be easily verifiable since a positive ion current should be also detectable. However, this was not done in the present experiments, so that further investigations are needed, which should also cover a broader range of organic solvents.

Enhanced Laser Power Density Another factor that potentially influences the recorded signal is the intensity of the laser beam interacting with the photoemissive material. Firstly, the shape and intensity may be affected. Secondly, an increased laser

6 Ion Source Development

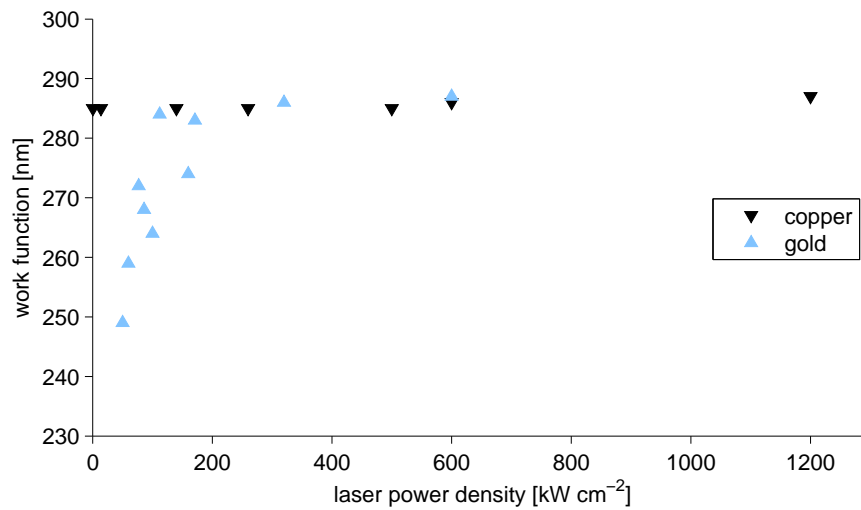


Figure 6.5: Dependence of the measured work function threshold on the laser power density for copper and gold.

intensity may influence the work functions.

When the measured ion current is entirely the result of the photoelectric effect, which means that photons interact with the metal atoms and electrons are ejected, the work function should not be dependent on the laser power. However, at enhanced laser powers different effects possibly occur. These are, i) the *two photon photo effect* (2PPE), where a photoelectron is generated by two photons instead of one and ii) second harmonic generation, where a photon with a doubled frequency is generated by two primary laser photons. Figure 6.5 shows the dependence of the ion current on the laser power density for copper and gold for laser power densities in the range 0.56 to 1200 kW cm^{-2} . The measured work function of copper barely changes with increasing laser power. In contrast, the work function threshold of gold increases from 4.98 eV (249 nm) to 4.32 eV (287 nm), when the power density is increased from 50 kW cm^{-2} to 600 kW cm^{-2} . While the work function at low power densities is in agreement with the literature values, an enhanced laser power density leads to measured ion currents much higher than those found in the literature for gold.

Gold There are several possible explanations for the decreased work function of gold, including the effects mentioned above. However, the ion current that is detectable at wavelengths above the work function threshold cannot be due to a decrease in the work function, as the work function is a material specific value which can only be changed by changing the chemical structure of the surface of the photoemissive material.

The energy of photons with 287 nm (4.32 eV) is much lower than the ionization po-

6.1 The Photoelectric Effect at Atmospheric Pressure

tential of all the molecules that are possibly present inside the measurement chamber. Within the power density range used, resonance enhanced two photon ionization is only capable of ionizing aromatic species. This effect is ruled out as the signal intensity with gold with this specific wavelength is the same i) in laboratory air, ii) after intense cleaning of the measurement chamber and iii) in synthetic air or nitrogen with a purity of 99.995 %. To ionize molecules one photon with sufficient energy is required. This photon may be formed by second harmonic generation of the 287 nm photons on the metal surface [284–287]. The quantum yield of SHG is reported to be small, 1×10^{-9} to 1×10^{-11} [285]. However, the resulting ion current should be measurable with a sensitive electrometer. When VUV photons of the doubled frequency are formed, they should be able to ionize impurities that are inside the measurement chamber. When second harmonic generation of the incoming laser beam, followed by ionization of impurities in the gas phase is the reason for the detectable ion current, the signal should not be greatly affected when a lithium fluoride window is mounted in front of the gold electrode. While photoelectrons generated on the metal surface are not able to pass through the window, VUV photons in the range of 140 nm generated on the metal surface should pass through it and should then lead to ionization of molecules. However, the results of this experiment are not fully conclusive. Although the signal intensity with 287 nm was considerably lower (2 to 10 times) when a LiF window was mounted in front of the gold electrode, it was still observed. A positive ion current was also detectable. If the normally recorded signal was completely caused by photoelectrons, no signal should be observed. Furthermore, the VUV light should photolyze oxygen and thus lead to generation of ozone inside the chamber. An ozone analyzer was used to prove if SHG takes place by measuring the ozone mixing ratio inside the measurement chamber. It has a stated limit of detection of 2 ppbV, but even for very high laser power densities no ozone signal above the normal background level was observed, indicating that SHG is negligible.

To further test if the signal comes from generated VUV photons, the laser beam was positioned such that no light impinged on either electrode. An ion current signal was still observed, which was up to ten times smaller than the signal measured when the laser directly irradiated the metal surface. Table 6.3 shows the relative signal intensities for different wavelengths and laser beam paths, i.e., the laser beam is directed to the electrode or not. For wavelengths longer than the work function threshold and low laser power densities, an ion current is only observed when the laser beam is directed to the electrode. In this case only a negative ion current is detected. When the gold electrode is not directly irradiated, no ion current signal is observed. Increasing the laser power density results in an increase in signal intensity for the negative ion current and a small positive ion current is also detected when the laser beam is directed on the gold electrode. Directing the laser beam between the electrodes results in a decrease in the negative ion current, which is most likely due to the missing photoelectron current, while the positive ion current remains more or less constant. With a wavelength larger than the work function threshold of gold, e.g., 283 nm, only very small signals are observed in both cases when the power density is low. A higher power density gives

Table 6.3: Dependence of the signal intensity on the wavelength, the laser power density and the pathway of the laser beam.

Wavelength [nm]	Power density [kW·cm ⁻²]	Directed on electrode		Not directed on electrode	
		rel. intensity		rel. intensity	
		negative	positive	negative	positive
235	0.5	0.83	0.02	0.01	0.01
235	200	1	0.42	0.39	0.49
283	5	0.06	0.04	0.07	0.03
283	600	0.78	0.80	0.75	0.84
312	3	0.0	0.0	0.0	0.0
312	2000	0.0	0.02	0.01	0.01

roughly the same signal intensity independent of ion polarity and the orientation of the laser beam. Further increase of the wavelength does not give any ion currents, even for very high laser power densities. An ion current that is fully attributable to photoelectron generation is thus only detected for wavelengths lower than the literature value of the work function and low power densities.

The ion current which is detected when the LiF window is mounted between both electrodes is very likely not caused by second harmonic generation of VUV photons, as it has the same value as when the laser beam is directed between both electrodes. Even when the measurement chamber is evacuated to a pressure of approximately 1 mbar and the laser beam is directed in a way that it does not irradiate the electrodes negative and positive ion currents are measurable. As single laser photons are not able to ionize molecules directly, the source for the measured ion current remains unknown.

Another possible explanation is the two photon photoelectric effect, which is reported to occur at elevated laser power densities [168, 169, 172, 284, 287]. As in the case at second harmonic generation, this effect would lead to a quadratic dependence of the signal intensity on the laser power density. However, the dependence of the integrated signal peak area on the laser power density shows a similar behavior for wavelengths below and above the work function threshold, 235 nm and 283 nm, respectively (see figure 6.6). Furthermore, the measured signal intensity does not change significantly when the laser beam is not directed to the electrodes.

For a power density range up to 400 kW cm⁻² both measurements show a linear dependence of the peak area with the power density. For higher laser power densities, the results for 283 nm are not fully conclusive, due to a high variation of peak areas for power densities between 400 to 800 kW cm⁻². The signals at very high power densities do not fit to a quadratic dependence of the peak area. The anomalous behavior of gold is still not understood and further investigations are needed.

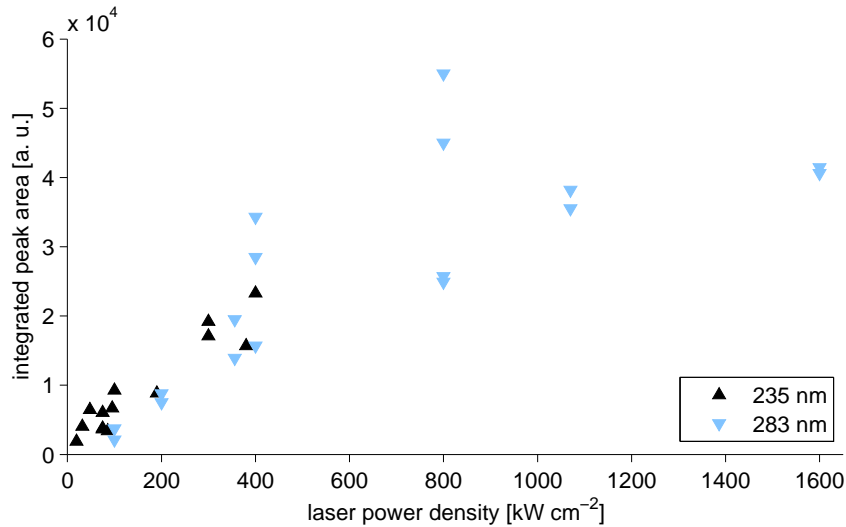


Figure 6.6: Dependence of the integrated peak area on the laser power density for two wavelengths, one with an energy above (235 nm) and one below (283 nm) the work function threshold of gold (4.77 eV; around 260 nm).

6.1.2 Low Pressure Mercury Lamp

The use of a low pressure mercury lamp, providing photons at mainly 254 nm, corresponding to 4.88 eV, should provide photoelectrons with most metals, as the energy is almost always well above the work function. Furthermore, the lamp provides photons with 185 nm with an intensity of 3 % of the main emission at 254 nm. However, with a band pass filter, that has a relative transmission of $\leq 1 \times 10^{-5}$ at 185 nm and 0.83 at 254 nm, between lamp and metal no photoelectron current was detectable with any of the metal used. This indicates that the ion current measured without the band pass filter is fully attributable to the emission at 185 nm. The differences between these experiments and the experiments described in the previous section, where a wavelength of 254 nm was sufficient for photoelectron generation for all the metals tested, are the photon density of the light source and the voltage applied between the measurement electrode and the photoemissive electrode.

The application of -200 V on a silver electrode resulted in a measurable ion current when photons with 254 nm irradiate the metal. A possible explanation is that molecules on the surface, that are always present at atmospheric pressure, hinder the ejection of electrons from the metal into the air. Besides this, for metals less noble than silver an oxidized layer will quickly form at atmospheric pressure. Photoelectrons are emitted by the metal and possibly need sufficient kinetic energy to pass through the surface layer, as discussed in the literature for organic layers [288] or layers of water [289]. With 254 nm the emitted electrons exhibit a kinetic energy of 0.14 eV in

the case of silver as the photoemissive material, while 185 nm photons lead to kinetic energies of 1.96 eV. A voltage that pulls the electrons from the metal towards the measurement electrode may also facilitate the transition through the surface layer.

6.2 Light Source

For the generation of electrons by the interaction of photons and photoemissive materials a light source that provides UV photons is required. The quantum yield of the photoelectric effect is rather low, as stated in section 1.4, but it increases when the photon energy becomes sufficiently larger than the work function. However, for photons with an energy higher than approximately 7 eV single photon ionization of organic compounds becomes possible, resulting in unwanted positive ion generation. When the photon densities are sufficiently high, e.g., with lasers, multi photon ionization can take place even for photon energies of less than 7 eV and can lead to the generation of positive ions. Furthermore, an ideal light source should provide a constant continuous number of photons.

A Pen-Ray low pressure mercury lamp was chosen as a light source since it combines all of the desired properties. This lamp provides light with a main emission line at 254 nm and a minor emission line at 185 nm, which has an intensity of 3 % of the main line (see emission spectrum, figure 3.10). Even though the energy of the 254 nm photons (4.88 eV) should be sufficient to overcome the work function of most metals, only the 185 nm emission generates photoelectrons as stated in the previous section.

The 6.7 eV energy of the 185 nm photons, is not high enough for single photon ionization of the compounds typically present in atmospheric pressure ion sources. Photon densities of 6×10^{15} photon $\text{cm}^{-2} \text{s}^{-1}$ at 254 nm are not sufficient to allow multi photon ionization. Thus, positive ion generation will not take place when the Pen-Ray-lamp is used as a light source. This was verified by measuring the positive ion current with the measurement chambers using a sensitive electrometer (see section 3.4). The measured current was in the same range as the background signal of the instrument in the positive mode. Furthermore, with the mass spectrometer no ions were observed in the positive ion mode when this lamp was used for photoelectron generation.

Low pressure mercury lamps are commonly used to generate ozone. The dependence of the amount of ozone produced on the oxygen mixing ratio is shown in figure 6.7. It was measured for a gas flow of 1 L min^{-1} with the cAPECI source design 2 (see section 3.7.6 for details on the ion source and section 3.5 for details on the ozone measurement). The ozone mixing ratio increases slowly until an oxygen mixing ratio of approximately 2 % is reached. For higher oxygen mixing ratios the ozone mixing ratio continue to increase linearly. When synthetic air is used as carrier gas, 20 % oxygen is present inside the ion source, resulting in the production of a steady state mixing ratio of 1.6 ppmV ozone.

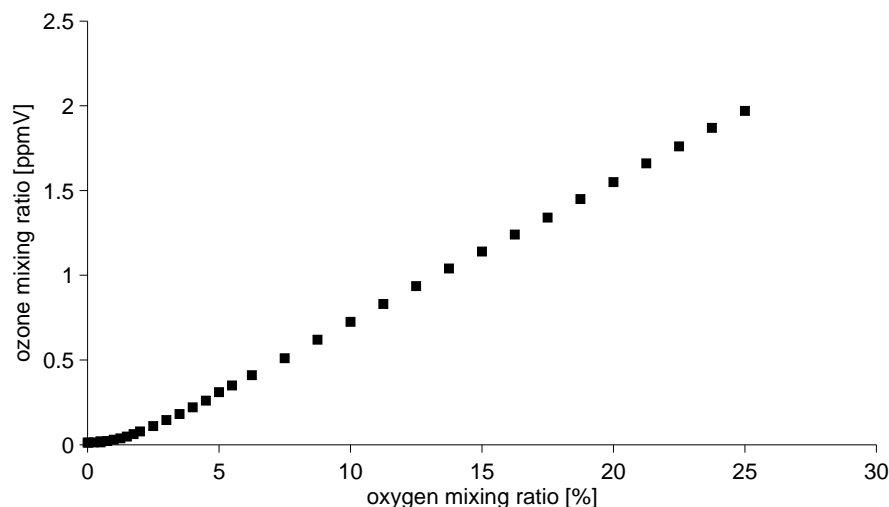


Figure 6.7: Measured ozone mixing ratio in dependence of the oxygen mixing ratio inside the cAPECI source design 2.

6.2.1 Calculation of the Photolysis Rate

In most of the ion sources described in the following sections the analyte was also irradiated by the UV-light of the Pen-Ray-lamp. The energy of the photons is not sufficient for photoionization, but potentially induces photolysis, which would reduce the mixing ratio of the neutral analyte. In the following an estimation is made of the amount of analyte molecules which are photolyzed. 3-methyl-2-nitrophenol is used as analyte

First of all, the photolysis frequency at the main wavelengths emitted by the UV lamp (i.e., 254 nm and 365 nm) must be determined.

$$J_{\lambda} = \sigma \cdot \phi \cdot I \quad (6.1)$$

with: J_{λ} = photolysis frequency at wavelength λ
 σ = absorption cross section
 ϕ = quantum yield
 I = photon flux

The absorption cross sections at both wavelengths were obtained from absorption measurements in the liquid phase where 3-methyl-2-nitrophenol was dissolved in dichloromethane [226, 290]. Values of $\sigma_{254nm} = 4.31 \times 10^{-18} \text{ cm}^2 \text{ molecule}^{-1}$ and $\sigma_{365nm} = 4.40 \times 10^{-18} \text{ cm}^2 \text{ molecule}^{-1}$ were obtained from the spectra. To determine the upper limit of the photolysis frequency a quantum yield of 1 molecule photon⁻¹ was assumed for the analyte photolysis for both wavelengths. Photon fluxes of both

6 Ion Source Development

wavelengths were calculated from the light intensity data provided by the lamp manufacturer, $I_{254nm} = 6 \times 10^{15}$ photon $\text{cm}^{-2} \text{s}^{-1}$ and $I_{365nm} = 3.4 \times 10^{14}$ photon $\text{cm}^{-2} \text{s}^{-1}$, respectively [250]. With these values photolysis frequencies for both wavelength are calculated to $J_{254nm} = 2.586 \times 10^{-3} \text{s}^{-1}$ and $J_{365nm} = 1.496 \times 10^{-3} \text{s}^{-1}$.

Typical mixing ratios are in the ppbV-range, thus, a mixing ratio of 10 ppbV was assumed, which corresponds to a density of 1×10^{11} molecule cm^{-3} under the conditions of the experiments. The rate of reaction is given by

$$-\frac{d[M]}{dt} = [M] \cdot J_{\lambda} \quad (6.2)$$

where $[M]$ denotes the concentration of the analyte. Insertion of the concentration and the photolysis frequency results in 2.6×10^9 molecule $\text{cm}^{-3} \text{s}$ at 254 nm and 2.6×10^9 molecule $\text{cm}^{-3} \text{s}$ at 254 nm.

To calculate the total amount of photolyzed analyte, the irradiated time is a crucial factor. Ionization inside the cAPECI source design 1 is considered in the following (section 6.5). In this design, the irradiated area has a length of approximately 5 cm. With figure 1.2 a mean velocity in between an axial capillary position of 5 and 13 cm of 125ms^{-1} is calculated, giving a transfer time through the irradiated area of $400 \mu\text{s}$. The amount of photolyzed analyte is calculated to 1.03×10^6 molecule cm^{-3} at 254 nm, 5.98×10^4 molecule cm^{-3} at 365 nm and 1.09×10^6 molecule cm^{-3} in total. This corresponds to 0.0011 % of the analyte, i.e., a negligible photolysis loss.

The photolysis at 185 nm should also be taken into account, but unfortunately no absorption cross sections were available for the VUV range from the literature. However, the contribution of this wavelength to the amount of photolyzed molecules is assumed to be small, since the relative intensity of the emission at this wavelength is 3 %. Even with a photolysis frequency a hundred times higher than that at 254 nm the percentage of photolyzed molecules would be only doubled.

6.2.2 Lamp Stability

An important characteristic of the light source is its long term stability. To have a constant ion signal, the quantity of emitted photons with time should be constant. Therefore, the stability of the emissions at 185 nm and 254 nm were monitored. For both emissions a VUV spectrometer was used (see section 3.7.2). Figure 6.8 shows the signal intensity with time for three measurements of the 185 nm line.

After a short period in which the signal intensity increases at the beginning of the measurement, all three measurements show a decrease in the signal intensity with time. The lamp heats up during the first minutes until the mercury inside the lamp housing is completely evaporated and the maximum emission intensity is reached. The decrease of the signal intensity with time is not readily explainable. However, if this signal behavior is caused by a decrease in the photon emission with time the signal intensity should recover when the lamp is switched off for a certain time period. The resulting light intensity signal is shown in figure 6.9. It is clearly seen that the

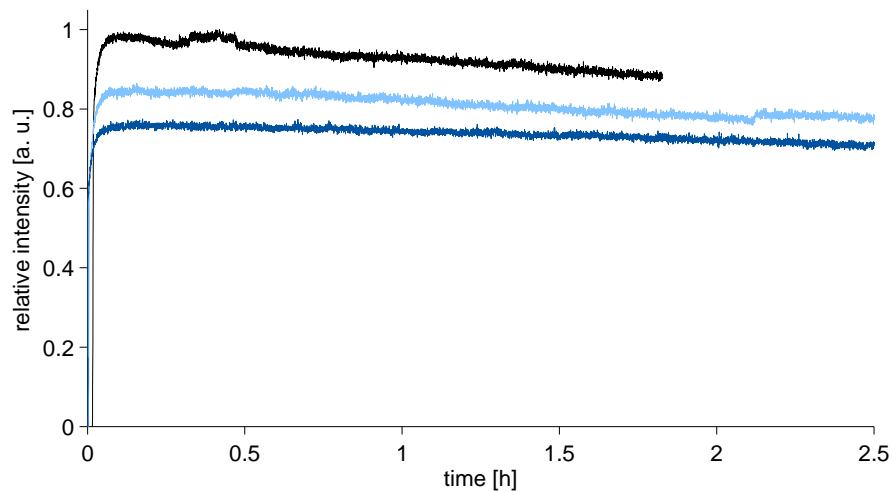


Figure 6.8: Intensity of the 185 nm emission line of the Pen-Ray-UV lamp with time. Three measurements are shown.

signal does not recover, even when the lamp is switched off for 160 min. Thus, the decreasing emission intensity with time cannot be caused by a decrease in the photon emission, but must be due to the instrumental setup. This assumption was confirmed by a measurement where the power supply of the photo multiplier was switched off for different time periods (see figure 6.10). When the photomultiplier was switched on again, a regeneration of the signal intensity was observed. The reason for this behavior is currently not known but tentatively attributed to the age of the employed photomultiplier.

Because of this behavior a photodiode was used to monitor the 365 nm emission line. With the assumption that the emission intensity-time profile is identical for all emission lines this setup was an alternative approach to monitor the lamp intensity. With the modified setup, the light intensity signal remained constant with time, as is shown in figure 6.11 for three measurements. The different intensity of each data set is caused by a different orientation of the photodiode to the UV lamp. The measured photo current shows a peak in the first seconds, most probably due to electrical disturbances induced by switching on the UV lamp. After the transient period the signal intensity is constant except for small fluctuations.

All experiments shown in the following were carried out with the described light source.

6 Ion Source Development

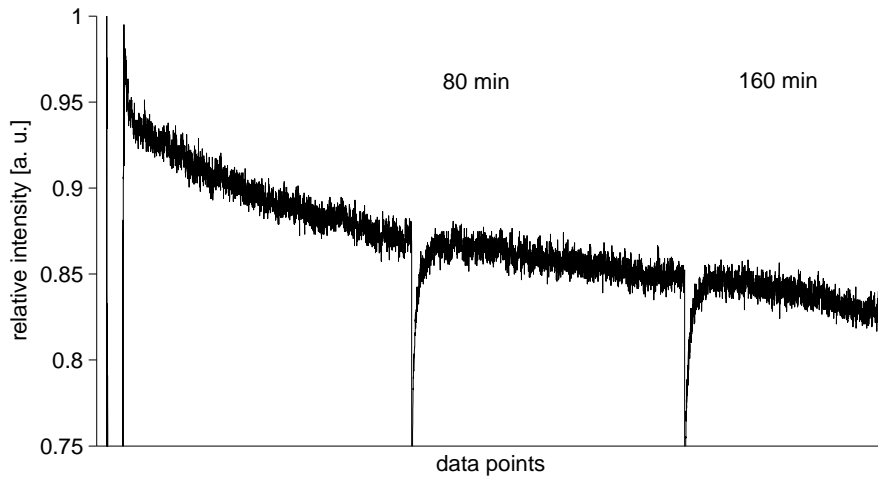


Figure 6.9: Emission intensity-time profile of the 185 nm line when the lamp is switched off for 80 min and 160 min.

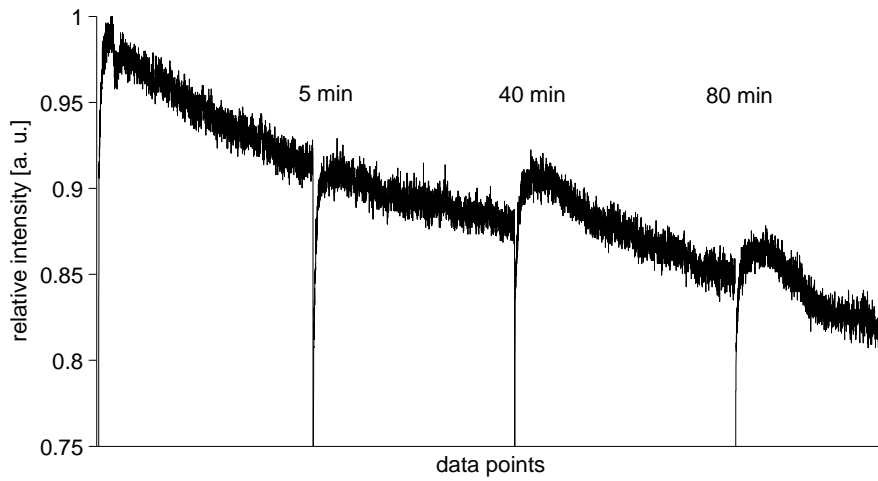


Figure 6.10: Emission intensity-time profile when the power supply to the photo multiplier of the VUV spectrometer was switched off for different time periods.

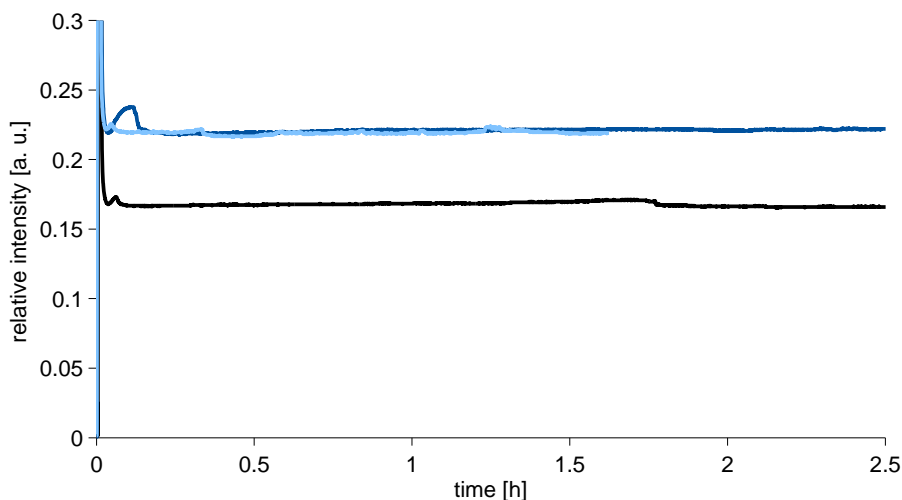


Figure 6.11: Emission intensity of the 365 nm line with time, recorded with a photodiode. Three measurements are shown.

6.3 Laminar Flow Ion Source

The first ion source was made of existing parts and was mainly used to characterize the generation of ions by the photoelectric effect (cf. section 6.3). A laminar flow ion source, described in detail in section 3.7.3 was used. Photoelectron generation inside the LFIS takes place near the capillary duct. However, transfer times to the high vacuum region from this point of ionization are rather long, approximately 5 ms, which probably leads to additional signals in the mass spectra due to ion-molecule/radical reactions. An example for a mass spectrum obtained with this setup is shown in figure 6.12. As expected, for 2-nitrophenol in synthetic air the $[M-H]^-$ signal has the highest abundance, but additional ion signals are observed. These are the deprotonated dimer ion, $[M+M-H]^-$, and oxygenated analyte molecules. The observed ion signals are expected due to the high concentration of oxygen radicals produced by the UV lamp and are in agreement with the proposed ionization mechanism for negative ionization at atmospheric pressure (see chapter 4).

As mentioned in section 1.1.2, the voltages applied to the ion transfer optic inside the mass spectrometer have a large impact on the recorded mass spectrum, as they can shift the signal distribution of the mass spectrum to a large extent. All measurements shown in this work were carried out with optimized voltage settings, so that the degree of fragmentation of the analyte ion was minimized and the signal intensity of the M^- or $[M-H]^-$ was maximized. According to the ionization mechanism proposed in chapter 4 this means that for analytes with a phenolic OH groups the deprotonated dimer ion and the $[M+O_2]^-$ adduct ions are fragmented to $[M-H]^-$ inside the ion

6 Ion Source Development

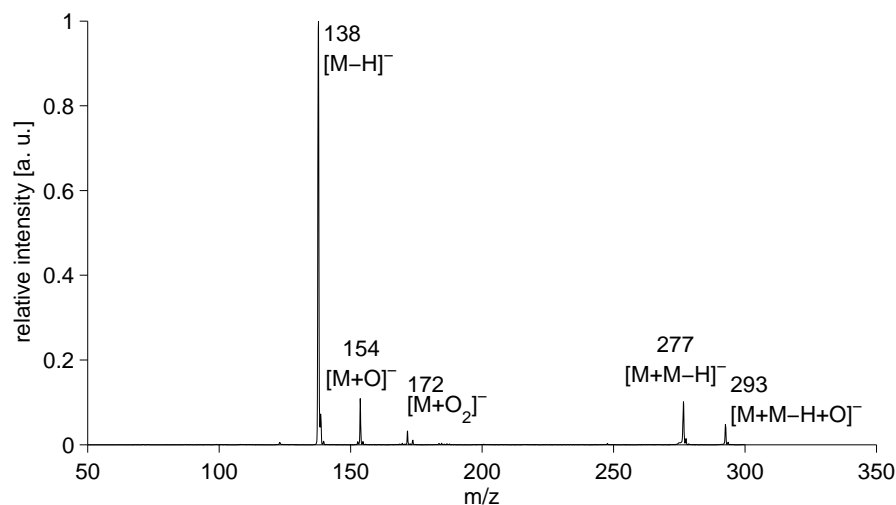


Figure 6.12: Mass spectrum of 2-nitrophenol in synthetic air with ionization by photoelectron generation inside the laminar flow ion source.

optics.

Recording the mass spectrum of 2-nitrophenol in pure nitrogen leads to a mass spectrum with M^- as the only signal. However, the signal intensity is reduced by a factor of ten compared to the spectrum in synthetic air.

The UV lamp is positioned perpendicular to the LiF window, thus only a very small fraction of the emitted photons are used for photoelectron generation inside the ion source. Furthermore, the distance between the window and photoemissive surface is 4 mm. The near VUV light is absorbed to a large extent by oxygen during its passage through the ion source before it interacts with the metallic surface². Both effects result in low sensitivities for this ion source.

When the lamp is placed upstream inside the laminar flow ion source, where the laser would be coupled with the ion source (cf. figure 3.11 in section 3.7.3), the entire quantity of emitted photons is available for photoelectron generation and the distance to the ion source walls is reduced. However, the large increase in the transfer time from the place of ion generation to the inlet capillary leads to mass spectra that show many additional signals and are not very useful (see figure 6.13). Apart from the $[M-H]^-$ and the $[M+O]^-$ ions at m/z 138 and m/z 154, respectively, the remaining signals cannot be assigned to the analyte and have not been identified.

²The absorption cross section of oxygen at 185 nm is $3 \times 10^{-19} \text{ cm}^2 \text{ molecule}^{-1}$ [291]. With an oxygen molecule density of $5 \times 10^{18} \text{ molecule cm}^{-3}$ and a layer thickness of 4 mm, the Beer-Lambert law [33] gives a transmission of 54.88 %.

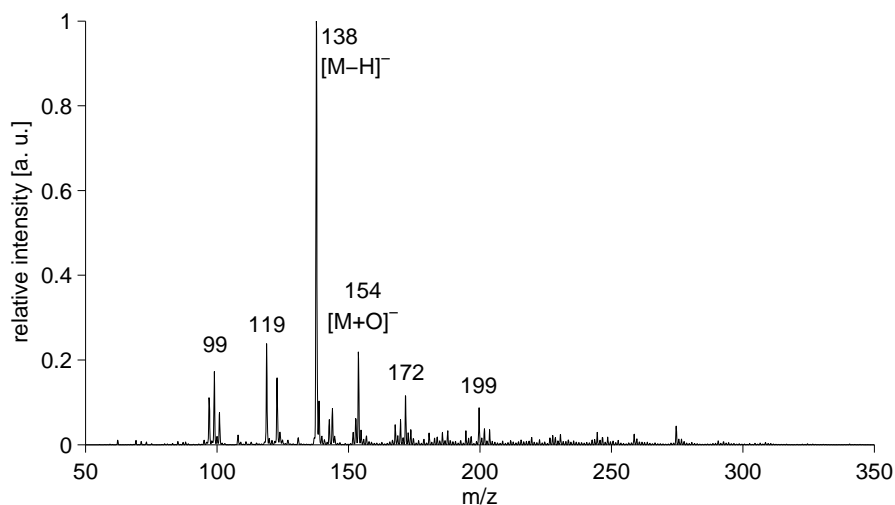


Figure 6.13: Mass spectrum of 2-nitrophenol in synthetic air when ionization takes place upstream inside the LFIS.

6.3.1 Metal Coated Windows

To reduce the concentration of oxygen atoms and ozone inside the laminar flow ion source the LiF window inside the LFIS near the capillary duct was replaced by a silica window, which has a thin metal coating on the side facing the ion source volume (cf. section 3.7.3.1). Irradiation of this window with the UV lamp produces photoelectrons inside the LFIS and no light penetrates into the ion source. Therefore, no photolysis of oxygen takes place, which would lead to oxygen atoms and ozone production.

While the mass spectra obtained with this setup show much less additional signals under constant conditions, the sensitivity is much lower than with direct photoelectron generation inside the LFIS. Figure 6.14 shows the mass spectrum of sulfur hexafluoride in nitrogen, when a copper coated silica window is used. In addition to the SF_6^- ion at m/z 146, the SF_5^- ion is observed at m/z 127. The third signal at m/z 89 is most likely caused by impurities from previous measurements. The fact that SF_6^- is the primary ion in the photoelectron mass spectrum indicates that the generated electrons are actually thermalized. For electron attachment with electrons that exhibit a kinetic energy of more than 0.3 eV, SF_5^- is preferably formed [100]. When SF_6^- is formed by thermal electron capture, the energetically excited ion SF_6^{*-} is generated in the first step. It is then quenched to the stable ion by collisions with background gas particles, which is only possible at enhanced pressures [100]. This demonstrates, that photoelectron generation is a soft ionization method under the given conditions.

Interestingly, ions were only observed with this setup when a low voltage was applied to the metal coating. This may be due to a fast charging of the layer when

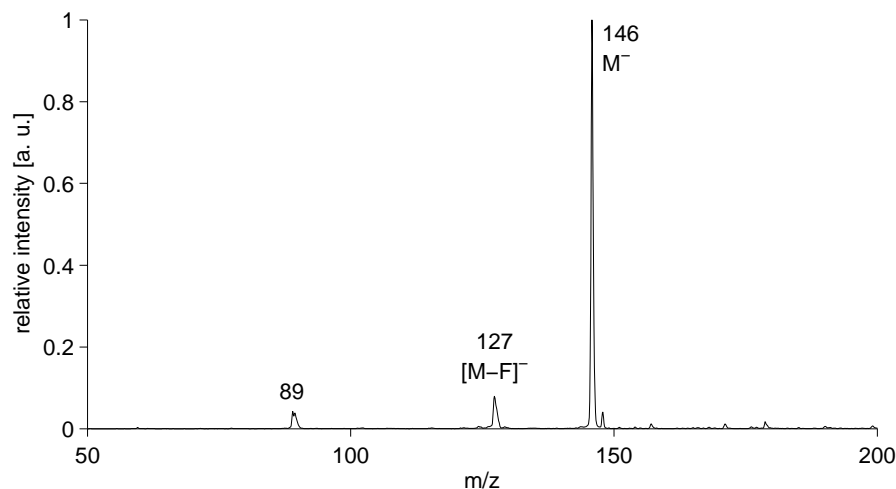


Figure 6.14: Mass spectrum of sulfur hexafluoride in nitrogen obtained with photoelectron generation from a copper coated silica window.

photoelectrons are ejected from the metal, as the coating has a thickness of only several nanometers, possibly necessitating the delivery of new electrons from an external source. When the laminar flow ion source was used, no voltages were needed for photoelectron generation. However, the LFIS was always conductively connected to the mass spectrometer so that electrons could be delivered to the ion source from the point of generation along the potential gradient.

The signal intensities obtained with the coated windows are generally very low. To increase the sensitivity with this setup a laser with a wavelength of 266 nm is used for photoelectron generation instead of the UV lamp. This is possible, as the light does not penetrate the laminar flow ion source, due to the coating of the window. Thus, it is not able to induce multi photon ionization of aromatic compounds. Even though the sensitivity is increased by several orders of magnitude by the use of a laser, the metal coating was damaged after only a few laser pulses. No difference of the stability of the metal coating between both coating methods, PVD and sputtering, is observed. Increasing the thickness of the metal coating results in a better stability with respect to laser light irradiation, but leads to a drastic decrease in sensitivity.

6.4 Silica Capillary

The transfer time of at least 5 ms inside the laminar flow ion source inevitably leads to ion-molecule/radical reactions. Reduction of the transfer time is possible when ionization takes place inside the inlet capillary, as was shown by Kersten et al. [38, 74]. For photoelectron generation a silica inlet capillary was used, which was partially

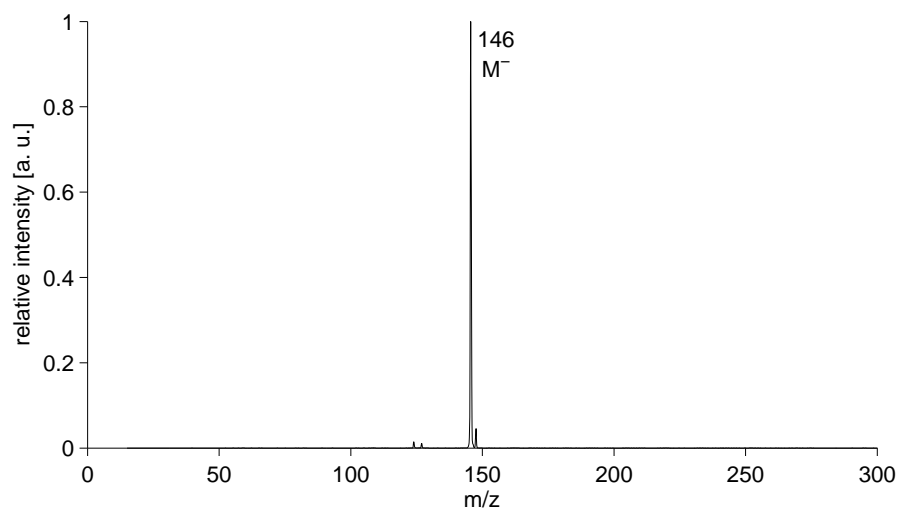


Figure 6.15: Mass spectrum of sulfur hexafluoride in synthetic air obtained with ionization within the partially silver-plated silica capillary.

silver plated on the inner capillary wall (for details see section 3.7.4).

Figure 6.15 shows a mass spectrum of sulfur hexafluoride measured in synthetic air with the partially silver-plated silica capillary. In contrast to the mass spectrum of sulfur hexafluoride shown in figure 4.17, where the SF_6^- ion at m/z 146 and the reaction product SF_4O^- ion at m/z 124 are present, this spectrum only shows the molecular anion of sulfur hexafluoride. The absence of ion-molecule/radical reaction products is most likely due to the shorter reaction times.

Almost none of the experiments performed with this ion source reveals any fragmentation or product signals from ion-molecule/radical reactions. The M^- or $[\text{M}-\text{H}]^-$ ions are the only signals in the mass spectra. In agreement with the proposed reaction mechanism in chapter 4, the deprotonated dimer ion, $[\text{M}+\text{M}-\text{H}]^-$, and the oxygen adduct ion, $[\text{M}+\text{O}_2]^-$, are observed for analytes containing a hydroxyl group. However, by the adjustment of the level of CID processes occurring inside the transfer stage of the mass spectrometer, i.e., the voltages applied to the capillary end cap, the skimmer and the trap drive, the intensities of these signals can be minimized to virtually zero.

A major drawback of this ion source is the inhomogeneous silver surface on the inner wall of the capillary, which is due to the manufacturing process. Thus, the positioning of the UV lamp is a crucial factor for the amount of generated electrons. It varies significantly for different positions and unfortunately positioning of the lamp was not reproducible. The ion current inside the capillary was measured at every centimeter along the capillary axis with a sensitive electrometer. The results are shown in figure 6.16. The bars represent the number of ions generated at each position,

6 Ion Source Development

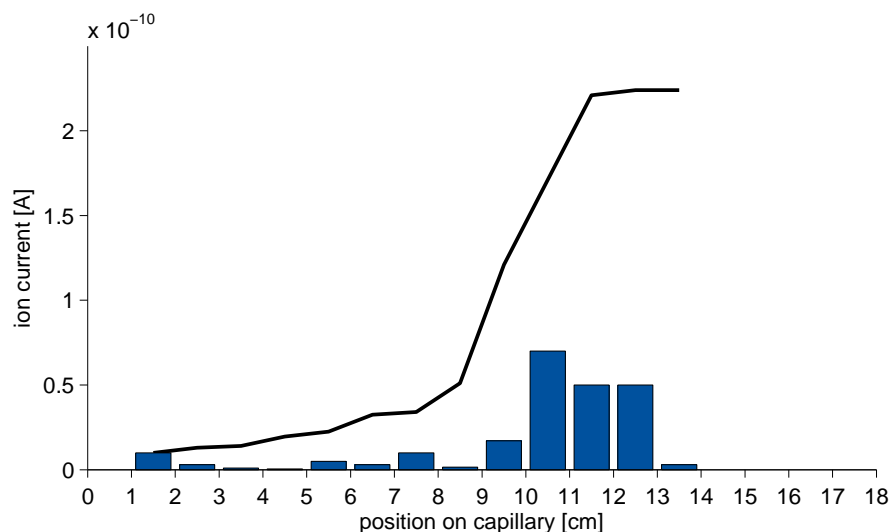


Figure 6.16: Measured ion current along the silica capillary axis (bars) and the sum of the ion currents up to the specific positions (line). The entrance of the inlet capillary is at 0 cm, the exit into the mass spectrometer at 18 cm.

the line depicts the sum of the ion current at the specific position. It is shown that most ions are generated between 10.5 and 13.5 cm and hardly any ions are generated in the first part of the capillary. From 14.5 cm onwards the capillary is inside the measurement chamber, thus no ion current can be measured in this range. Normally, the lamp was positioned in the range of 9.5 to 13.5 cm where most ions are generated. Rotation of the capillary along the main axis was found to lead to a different ion current distribution. A second capillary was partially silver plated in the same way gave a completely different ion current distribution as expected. Thus, reproducible amounts of ions are not generated with this ion source.

A second drawback of this ion source is that in the first measurement of each day or after modifications of the setup the signal does not appear immediately after switching on the UV lamp. It only appears after several minutes or when a 127 nm VUV-photoionization lamp is positioned in front of the capillary duct producing a large number of ions. This indicates that a charging of the capillary channel is necessary, which means that a certain number of ions had to enter the inlet capillary before ions are able to pass through it.

Furthermore, the signal intensity decays with time, which occurs even though the mixing ratio of the analyte and all other conditions were held constant. An example of this signal decay is shown in figure 6.17. The signal drop outs in the measurement are due to touching, i.e., grounding the capillary. As long as the capillary is grounded the signal disappears, when the finger is removed the signal recovers instantaneously.

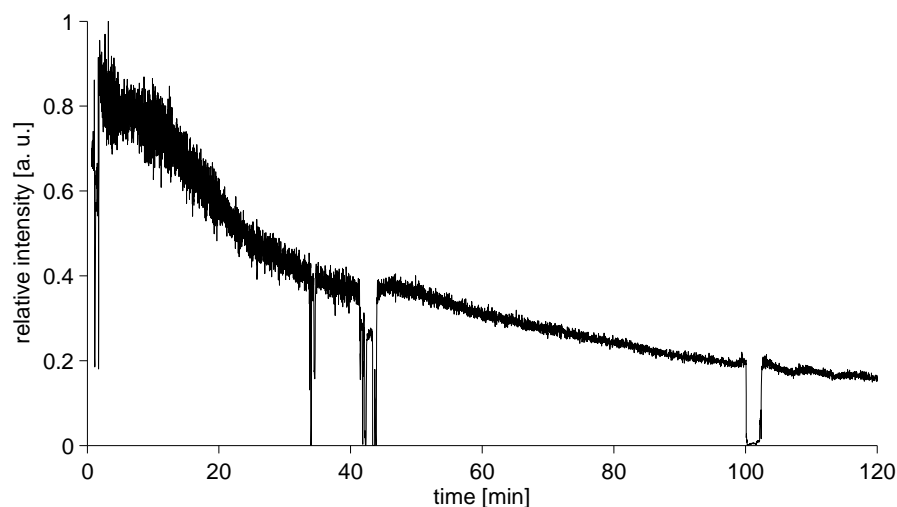


Figure 6.17: Decreasing signal intensity with time for ionization within the partially silver-plated silica capillary.

Only after very long time periods when the capillary is grounded constantly the signal recovers slowly. The signal decay varies for different measurements, but after a time period of 60 to 120 min the signal intensity always decreases to approximately 20 % of the maximum intensity.

The characteristic feature of this ion source is the ionization inside the inlet capillary by an electron capture mechanism at atmospheric pressure. Thus, the method is termed *capillary Atmospheric Pressure Electron Capture Ionization* and is abbreviated to *CAPECI*.

6.4.1 Branched Capillary

The mass spectra obtained with the partially silver-plated silica capillary were promising as ion-transformation processes are minimized. Furthermore, calculations showed that illumination of the analytes with UV light does not lead to considerable photolysis (cf. section 6.2). However, a capillary ion source was developed where the neutral analyte is added to the main gas stream after primary ion generation, by connecting two inlet capillaries in a way that is explained in detail in section 3.7.4.1.

With this ion source mass spectra are recorded that are comparable to those obtained with the partially silver-plated silica capillary. The signals for all measured analytes are identical to that obtained before; ion-transformation processes are thus minimized. Sensitivities are in the same range, although this parameter is difficult to compare because of the non-reproducible silver plating inside the silica capillary. No analyte exhibited a significant improvement in terms of sensitivity or fragmentation

Table 6.4: Comparison of the different metals used as photoemissive materials in the cAPECI source design 1.

Metal	Relative intensity (± 0.1)
Silver	1
Aluminum (long channel)	1
Silver plated (long channel)	0.9
Gold plated	0.8
Gold plated (long channel)	0.6
Aluminum	0.6
Steel	0.6
Copper	0.6
Nickel plated	0.5
Silver plated	0.3
Tungsten welding electrode	0.3
Samarium plated	0.2

compared to the silica capillary ion source described previously. However, there may be analytes for which this ion source is advantageous, e.g., if they are thermally unstable or readily undergo photolysis, as no interaction with the UV light and the heat from the mercury lamp takes place.

6.5 cAPECI Design 1

The cAPECI source design 1 was intended to provide a homogenous, reproducible and exchangeable metal surface to avoid the disadvantages of the partially silver-plated silica capillary. Thus, different metals were investigated as photoemissive materials and the resulting sensitivities were compared. Although the analyte mixing ratio was held constant, the instruments performance varied from day to day, leading to variable sensitivities for each metal. The averaged relative intensities are shown in table 6.4.

The silver target and the aluminum target which has a 2.5-times longer channel than the normal targets (cf. section 3.7.5 for details), show on average the highest intensity. Surprisingly, the silver-plated aluminum target with the longer capillary channel leads to a lower sensitivity than the target made of solid silver with the normal channel length. The reason is most likely the surface cleanliness of the silver plating as the silver-plated target with the normal channel length also shows a very low relative signal intensity. This may also be the case for the gold-plated aluminum. However,

why the gold-plated target with the longer channel leads to a lower sensitivity than the shorter capillary channel length remains unclear. Aluminum, steel, copper and nickel-plated aluminum all lead to comparable sensitivities. The theoretically most promising materials, a samarium-plated copper target and a tungsten-lanthanide welding electrode, which was inserted into an aluminum target below the capillary channel (for details see section 3.7.5), give the lowest relative intensities. Samarium has a comparably low work function of 2.7 eV [101] and the tungsten welding electrode contains a lanthanide, which also reduces its work function. However, even though these properties should lead to high quantum yields with the employed VUV light, the signal intensities are the lowest compared with the other metals. This may be due to the very fast oxidation of the lanthanides on the surface.

The influence of oxidation or other forms of aging of the surfaces on the photoelectron yield were also studied for other metals. Most photoemissive materials show surface changes with time, e.g., steel and silver. While the signal intensity of the copper target does not change after several days, the sensitivity of the aluminum target increases by a factor of two when the surface was freshly polished. However, an anodized aluminum target, i.e., aluminum with a relatively thick layer of aluminum oxide on the surface, gives a signal intensity comparable to that of freshly polished aluminum.

The effect of “aging” of the aluminum surface is not only due to the oxidation of the surface. Other effects are involved, which were not further investigated during this work. The anodized aluminum target does not show any dependence of the signal intensity on the age of the surface. With this target an ion current of 4×10^{-10} A is measured with the electrometer. Compared with an ion current of around 1.5×10^{-11} A measured for the partially silver-plated silica capillary, this is a considerable improvement in sensitivity.

With the cAPECI source design 1 and the silver-plated silica capillary short reaction times were achieved. Laser ionization in the center of the ionization area of the cAPECI ion source leads to transfer times of approximately 0.7 ms.

As a simple means to increase the sensitivity of the ion source the capillary channel that is milled into the metal target was extended, increasing the area where the photoelectrons are generated. Figure 6.18 shows the mass spectra of the aluminum target with the straight capillary channel (upper panel) and that of the aluminum target with a 2.5 fold longer capillary channel (lower panel).

Even though the channel length is more than doubled the signal intensity is increased by less than a factor of two. Besides the larger signal intensity of the $[M-H]^-$ signal of the analyte, an additional signal is observed at m/z 168. The transfer time of the ion source with the longer capillary channel is increased on average to 1.2 ms, which also increases the occurrence of ion-molecule/radical reactions. A possible explanation for the signal at m/z 168 is an $[M-H+O]^-$ ion, which may form due to the high mixing ratio of ozone and oxygen radicals generated by the VUV light of the low pressure mercury lamp. Whether the increased sensitivity is more important than a

6 Ion Source Development

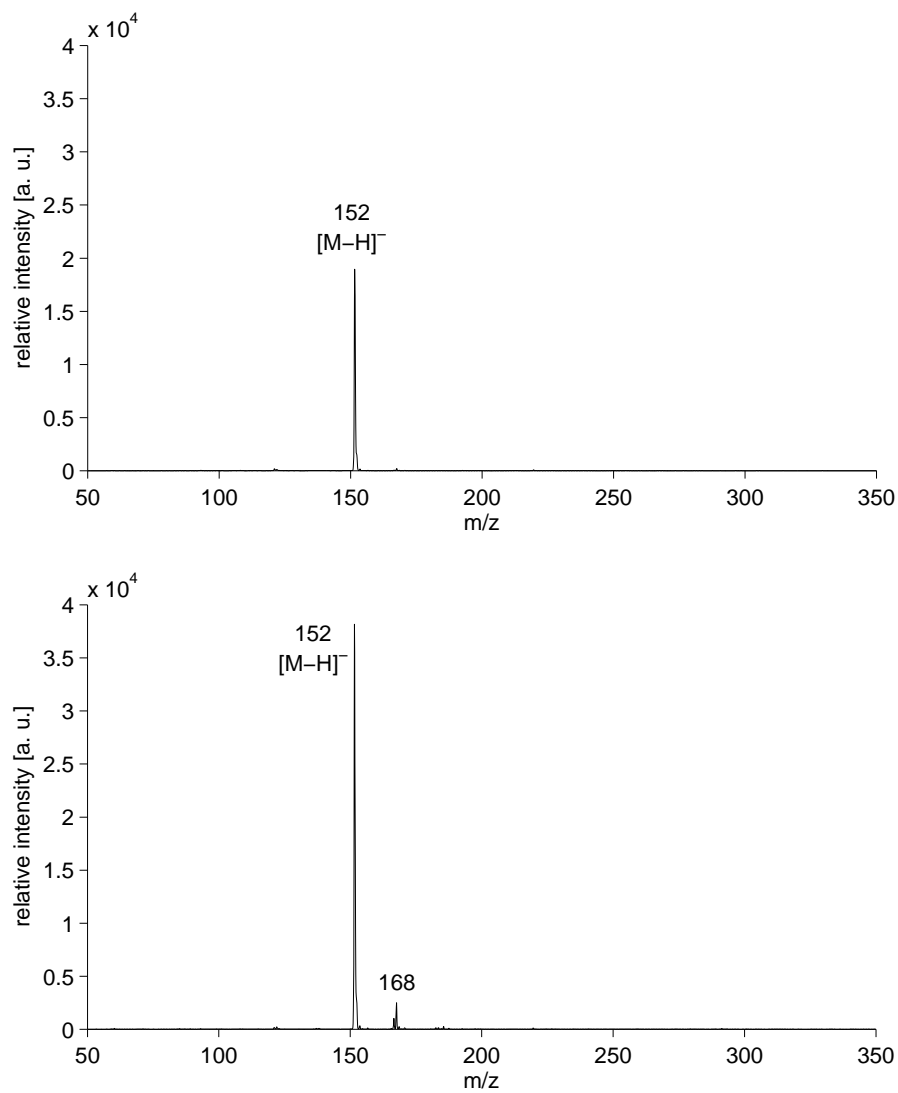


Figure 6.18: Comparison of the mass spectra of 3-methyl-2-nitrophenol obtained with an aluminum target with a straight capillary channel of 4.9 cm (upper panel) and with a 2.5 times longer capillary channel (lower panel).

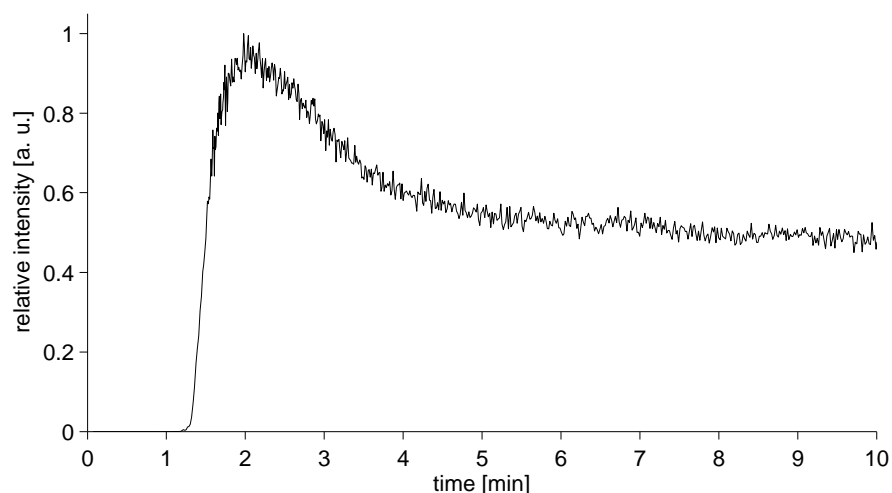


Figure 6.19: Total ion current for a first measurement of a day. The UV lamp was switched on at $t=0$.

mass spectrum without signals attributable to ion-transformation processes needs to be decided on a case by case basis. However, the comparison of the two mass spectra shows again that the transfer time is a crucial factor for the development of an efficient ion source.

For the first measurement of the day or when the ion source was disassembled prior to a measurement, activating the UV lamp does not immediately lead to an ion signal in the mass spectrometer. The signal only starts to increase after several minutes, as is shown in figure 6.19. The time after which the signal starts to rise varies from less than a minute up to several minutes. This behavior is explainable similarly to the observed characteristics of the silver-plated silica capillary. A “charging” of the ion source must take place before ions can pass through and are then detectable in the mass spectrometer (see chapter 5 on ion transmission effects for details).

The signal evolution is characteristic for the cAPECI source design 1; after a fast increase the signal starts to decrease slowly with time and reaches a constant value after long measurement times up to more than an hour. During this time the signal decreases by a factor of 2 to 3 from its initial maximum to a nearly constant intensity. Figure 5.16 shows the signal evolution for an extended time period. The reason for the decreasing signal intensity with time are described in detail in chapter 5. The non reproducible signal intensities hamper an analytical use of this ion source. Usage of an ion source, which is completely made of anodized aluminum, in combination with a sapphire glass window gave nearly constant signal intensities with time. The conductivities of both materials are very similar and thus charging effects are minimized.

6 Ion Source Development

However, the transmission of sapphire for the 185 nm line of the low pressure mercury lamp, which is responsible for photoelectron generation, is only around 50 % [292], leading to lower sensitivities.

The limit of detection was determined for an anodized aluminum target. The setup ran for approximately two hours before the calibration curve was measured in order to ensure that a steady state was reached. Due to the pseudo-first order kinetics taking place during the ionization process a non-linear calibration curve is obtained as shown in figure 7.14 in section 7.3. However, this curve is reproducible and a limit of detection (3σ [293]) of less than 250 pptV is calculated for an acquisition time of less than 1 s. The fitting function of the calibration curve is

$$y = 9.11 \cdot 10^4 \cdot \left[1 - (1 - 1.14 \cdot 10^{-3} \cdot [M]_0) \cdot e^{(-2.28 \cdot 10^{-3} \cdot [M]_0)} \right] \quad (6.3)$$

6.6 cAPECI Design 2

The decreasing signal intensity with time of the cAPECI source design 1 hinders its applicability for reproducible quantification. Thus, the next stage in the development of an cAPECI source should lead to a design that maintains the characteristics and advantages of the previous ion source, but also exhibits a stable signal intensity with time. The results of the investigation on ion transmission properties of composite inlet capillaries made of different materials suggested that an ideal inlet capillary for the use with unipolar ion gas streams should be made of only one material. Therefore, photoelectron generation inside the inlet capillary is not a viable option. To maintain the short reaction times ionization takes place directly in front of the capillary duct in a region of the improved ion source where the inner diameter of the source tubing matches the diameter of the capillary channel (see section 3.7.6 for details). With this setup, the signal intensity remains constant, an exemplary signal progression is shown in figure 6.20. After an initial signal peak of 5 min and a short dip of the intensity, the signal remains constant over the whole measurement period. The initial peak is observed for nearly all measurements carried out with purely unipolar ion gas streams (cf. chapter 5 on ion transmission measurements).

Figure 6.21 shows a mass spectrum of 3-methyl-2-nitrophenol. As expected, the spectrum shows only one signal, the $[M-H]^-$ of the analyte. Furthermore, the sensitivity of this setup is comparable to that obtained with the cAPECI design 1.

The cAPECI source design 2 allows the addition of the analyte gas stream to the main gas stream before or after the reagent ions are formed. However, mixing after the reagent ions are generated is advantageous as the sensitivity is considerably increased compared with the addition of the analyte before the gas passed the UV lamp.

Reaction Time To compare the influence of the reaction time, a second ion source was build in which the primary ions and the analyte gas stream were mixed in a larger

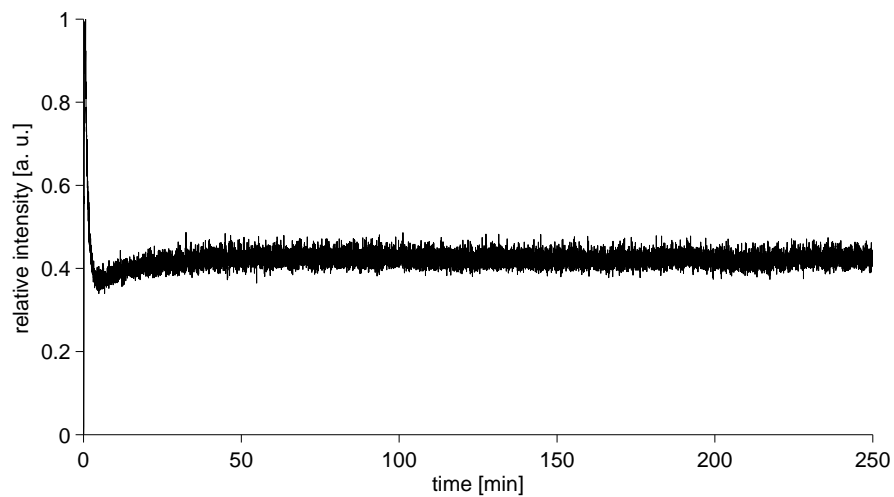


Figure 6.20: Temporal evolution of the signal intensity for a measurement with constant conditions with the cAPECI design 2.

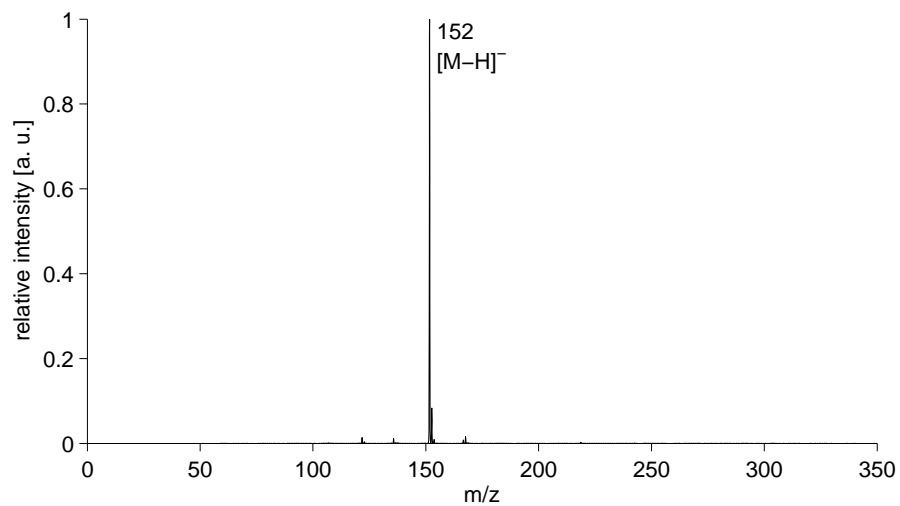


Figure 6.21: Mass spectrum of 3-methyl-2-nitrophenol obtained with the cAPECI source design 2 measured in synthetic air.

6 Ion Source Development

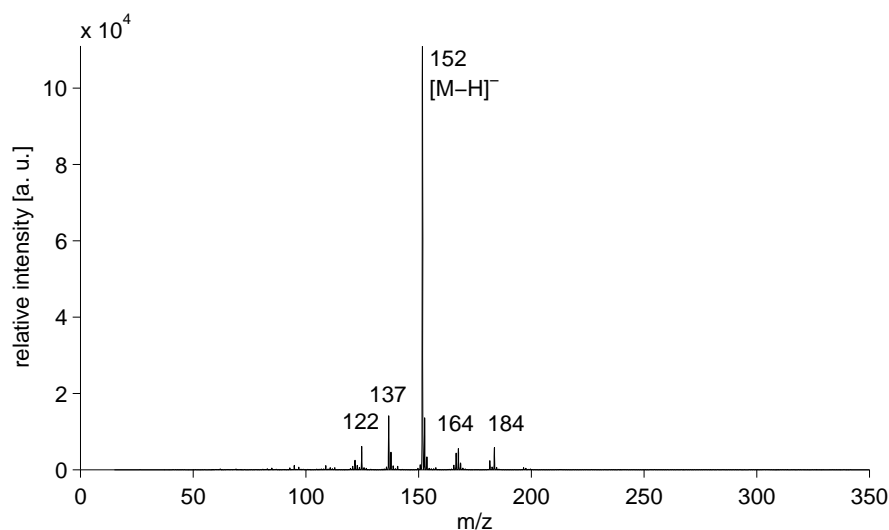


Figure 6.22: Mass spectrum of 3-methyl-2-nitrophenol obtained with a cAPECI source design 2 with a longer reaction time.

volume, leading to reaction times of more than 5 ms. Due to the longer transfer time a large number of ion-molecule/radical reaction products are observed in the mass spectrum shown in figure 6.22.

However, even for the setup with the longer reaction times of the generated ions, an almost “clean” mass spectrum with a minor abundance of ion transformation products is obtained when the oxygen mixing ratio is reduced. Figure 6.23 shows a mass spectrum of the same analyte when only 0.2 % oxygen is present inside the ion source. The $[M-H]^-$ ion of 3-methyl-2-nitrophenol is the only significant signal. Interestingly, the signal intensity is only 0.8 times lower than that obtained with synthetic air (20 % oxygen, see figure 6.22).

The dependence of the deprotonated anion of the analyte and the fragment ions on the oxygen mixing ratio is shown in figure 6.24. As indicator for the total amount of ion-transformation processes taking place after ionization, the yellow line represents the sum of all additional signals in the mass spectrum except for the $[M-H]^-$ signal at m/z 152. The desired m/z 152 signal has an intensity maximum at an oxygen mixing ratio of approximately 3.5 %. All the ion transformation products show a similar intensity dependence on the oxygen mixing ratio, albeit the maximum intensities do not match exactly with respect to the O_2 mixing ratio. The ions at m/z 122 and m/z 168 reach their intensity maxima at roughly the same oxygen mixing ratio as the deprotonated anion of the analyte. The other two ions do not reach the maximum until a mixing ratio of 6.5 %. As these two ions show the higher absolute signal intensities, the sum of the product ions also has its maximum intensity at this mixing ratio. The coincidence of the signal behavior of the two ion pairs with the maximum at the same

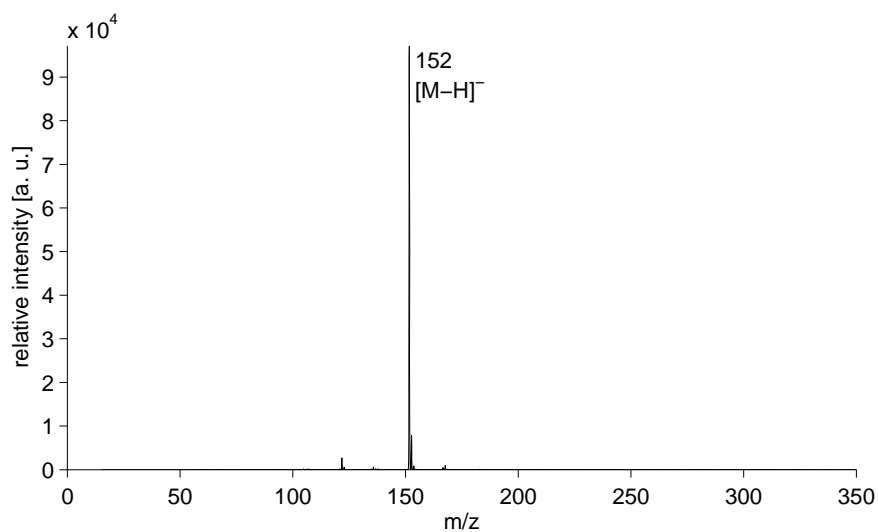


Figure 6.23: Influence of a decreased oxygen mixing ratio (0.2 %) on the mass spectrum of 3-methyl-2-nitrophenol obtained with the cAPECI source design 2. Compare with figure 6.22 for the spectrum with 20 % oxygen.

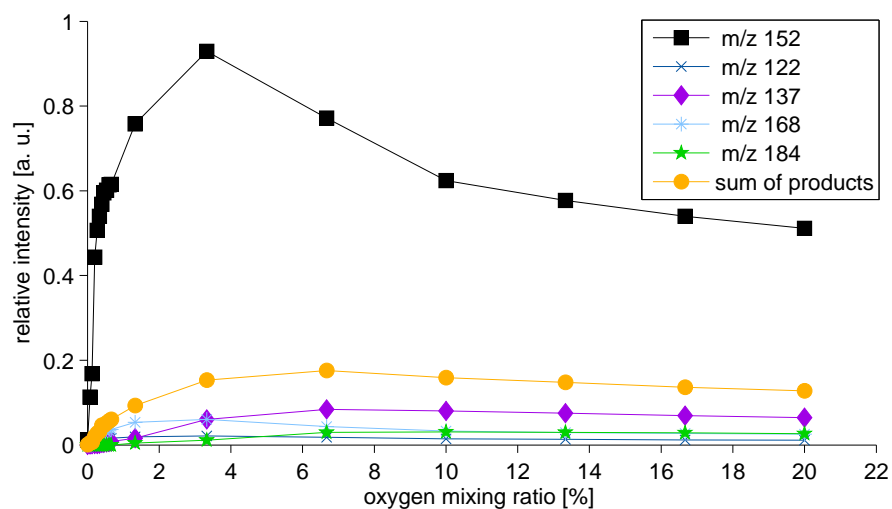


Figure 6.24: Dependence of the observed signal intensities with the cAPECI source design 2 with a longer reaction time on the oxygen mixing ratio. The yellow line represents the sum of the reaction products.

mixing ratio is striking. It is most likely that the ions with the lower mass-to-charge ratio both are fragments from the other ions.

6.7 Summary and Outlook

The measurement of work functions at atmospheric pressure led to similar values as obtained at low vacuum conditions and those reported in the literature for high vacuum conditions. As expected, the signal intensity was highly dependent on the laser intensity and the voltage applied to the photoemissive electrode. Only the work function of gold showed a variation with the power density. The examination of different surface conditions revealed a high dependence of the signal intensity not only on the surface oxidation, but also on the presence of water or organic molecules on the surface. The work function was observed to change with the surface condition of the metal. The largest change was observed for aluminum, the surface of which is quickly oxidized. Metals with more noble character, e.g., silver, which have an almost inert surface, did not show a variation of the work function.

Gold is the only metal for which a deviation between the measured work function and the literature value was observed. Even though the reason for this difference could not be determined, several possible explanations were ruled out. As a quadratic dependence of the signal intensity on the power density was not observed, second harmonic generation, leading to VUV photons and the two photon photoelectric effect were excluded. The effect occurred only at enhanced power densities and also when the laser beam did not irradiate the metal electrode. To determine the cause for this effect detailed investigations are necessary.

To built an ion source, which generates ions based on the photoelectric effect, a suitable light source was chosen and characterized. A low pressure mercury lamp provides light in the required wavelength range with emission lines at 254 nm and 185 nm. Due to the absence of VUV light no direct photoionization takes place and due to the low photon densities compared with laser light, no multi photon ionization can occur. Furthermore, photons are emitted continuously with a good long term stability. However, large amounts of ozone are generated by the UV lamp. For oxygen mixing ratios present in synthetic air a mixing ratio of 1.6 ppmV ozone is established. This high ozone mixing ratio and the resulting high oxygen radical mixing ratio show that a short transfer time from the place of ion generation to the vacuum part of the mass spectrometer is crucial to circumvent the occurrence of extensive ion-transformation processes.

Several ion sources were designed, each iteration addressing the disadvantages of the previous source. The first laminar flow ion source showed that ionization via the photoelectric effect is feasible, but due to long reaction times signals attributable to ion-molecule/radical reactions were observed in the mass spectrum, rendering a clear

6.7 Summary and Outlook

signal identification difficult. To decrease the transfer time the region of ionization was moved into the inlet capillary and a partially silver-plated silica capillary was used as ion source. This had the desired effect and for nearly all analytes only one signal was observed in the mass spectrum, i.e. the M^- or $[M-H]^-$. However, the signal intensity decreased over the measurement period by a factor of 2 to 3 and the silver plating inside the inlet capillary could not be performed reproducibly. In an attempt to have an exchangeable, homogenous photoemissive material in the irradiated region the cAPECI source design 1 was build. Here, ionization still takes place in the inlet capillary. This led to sensitive, reproducible mass spectra. Aluminum, anodized aluminum and silver gave the highest sensitivities, while only anodized aluminum did not show a variation of the signal intensity with the age of the targets surface. However, the signal intensity also decreases with time for this ion source. The latest version, the cAPECI source design 2, gives a constant signal intensity with time because the glass inlet capillary is not modified as ionization takes place in front of it. To maintain the short reaction times the inner diameter of the ion source tubing is reduced to the dimension of the capillary channel where the analyte gas stream and the reagent ion gas stream are mixed.

The newly developed ionization source combines all the desired characteristics. It gives low limits of detection of less than 250 pptV for an acquisition time of less than 1 s, provides “clean” mass spectra with high signal-to-noise ratios and a high selectivity towards analytes with high electron affinities or acidic protons.

7 Applications

In the previous chapter, the newly developed ionization method and several ion sources were characterized. To show the adaptability for “real-world problems”, several applications in different fields were carried out and are described in the following. The coupling of the mass spectrometer with a gas chromatograph adds a preceding separation stage before the ionization takes place. This allows the measurement of complex samples containing different analytes and matrix components. An important application is the use of cAPECI in atmospheric chemistry, where the measurement of (nitro-)phenols is crucial in many areas. Proton transfer reaction mass spectrometry is a widespread technique in atmospheric chemistry, therefore a comparison of cAPECI with PTR was performed. With the cAPECI ion source design 1 rate constants for reactions between analyte and primary reactant ions, e.g., O_2^+ , were determined. The procedure is described in detail in section 7.3 and an example is given. The last application described here was the use of the novel ionization method as an “ambient” method that can be used for the desorption and ionization of analytes from surfaces.

7.1 GC-cAPECI-MS Hyphenation

The hyphenation of GC with a mass spectrometer is a common analytical method for the analysis of complex samples. It is widely used for the detection of nitro-aromatic compounds and explosives [209, 294–298]. For nearly all common ionization methods, ion sources exist which allow easy coupling between GC and MS. An ideal ion source should be heated to prevent condensation of low volatile analytes coming from the GC on cold surfaces in the ion source. It should have a small gas volume and require minimal amounts of additional gas in order to prevent unnecessary dilution of the analyte. Furthermore, the short reaction times realized with the cAPECI ion sources should be retained. Two different setups for the coupling of cAPECI with a GC were investigated. In the first setup, the transfer line, transporting the analyte from the GC oven to the ion source while maintaining the separation performance, was mounted in a straight line with the inlet capillary (see section 3.8). The reagent ion gas stream was mixed downstream with the GC effluent where the tubing size has the same inner diameter as the inlet capillary, similar to the cAPECI source design 2. In the second setup, the transfer line was mounted perpendicular to the inlet capillary. Thus, the main gas stream (0.9 to 1.5 Lmin^{-1}) entered straight into the inlet capillary and the analyte containing GC effluent (100 to 400 mLmin^{-1}) was added from the side. The

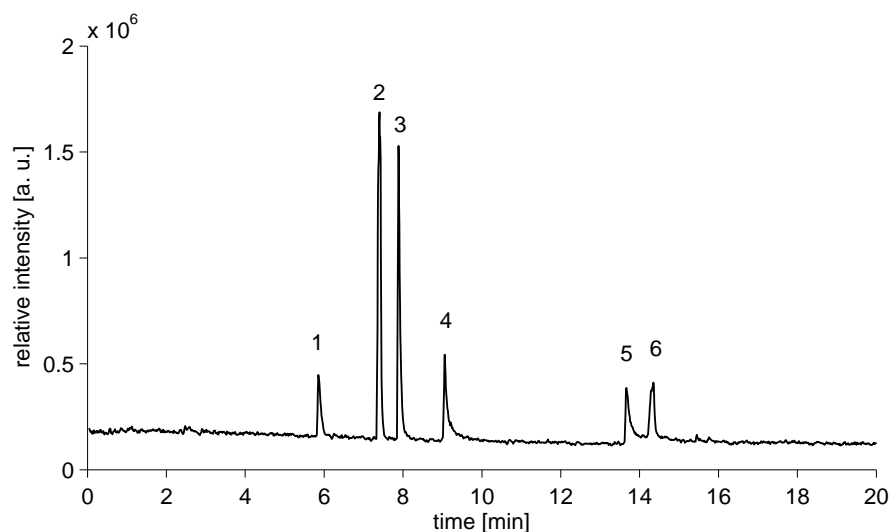


Figure 7.1: GC-cAPECI-MS chromatogram of a mixture of six compounds dissolved in hexane. For the measurement conditions see section 3.8. For peak assignment see table 7.1.

results obtained with these two setups were compared with that of the ion source implemented directly within the capillary (cAPECI source design 1).

Setup 1 First of all the separation efficiency of the setup was determined using a mixture of six analytes dissolved in hexane. The compounds are listed in table 7.1. All analytes show only one mass signal, either the M^- or $[M-H]^-$ signal. Thus, the TIC of the chromatographic run is shown in figure 7.1 and not the mass traces of the individual ions. Six signal peaks with different intensities are recorded. The chromatographic properties are summarized in table 7.1. Peak widths are in the range of 2.2 to 7.4 s, which is a favorable result but leaves room for further improvements. This is also the case with respect to the sensitivity, as the concentrations of the analytes are comparably high. A volume of 1 μL was injected, resulting in 53 to 436 pmol of analyte on the column. As expected, the signal-to-noise ratios are high, due to the “clean” mass spectra with low background noise.

One major advantage of the newly developed ionization method is that generally only one signal peak per analyte is detected. The mixture used for the GC-MS measurement shown in figure 7.1 was also analyzed without chromatographic separation. As is shown in figure 7.2, except for 2,4-dinitrotoluene, signals of all analytes are present in the mass spectrum. One signal peak per analyte is observed and one additional signal at m/z 196, which has not been identified. 1,4-benzoquinone shows a M^- signal (BQ, m/z 108) and the phenols show the $[M-H]^-$ signals. These were 2,4,6-trimethylphenol (TMP, m/z 135), 2-nitrophenol (NP, m/z 138), 3-methyl-2-nitrophenol (152, m/z 152)

Table 7.1: Assignment of the GC peaks in figure 7.1 and the corresponding chromatographic properties.

Peak number	Compound	Molar mass [g · mol ⁻¹]	Peak width (FWHM) [s]	Peak area [a. u.]	Signal-to-noise ratio	Concentration [mg · μL ⁻¹]
1	2-nitrophenol	138	4.8	1045000	427	10
2	2,4,6-trimethylphenol	136	2.2	8121000	306	10
3	3-methyl-2-nitrophenol	153	2.9	5446000	709	10
4	2,4-benzoquinone	108	4.1	2343000	124	50
5	2,4-dinitrophenol	184	5.7	1744000	114	10
6	2,4-dinitrotoluene	182	7.4	2002000	104	50

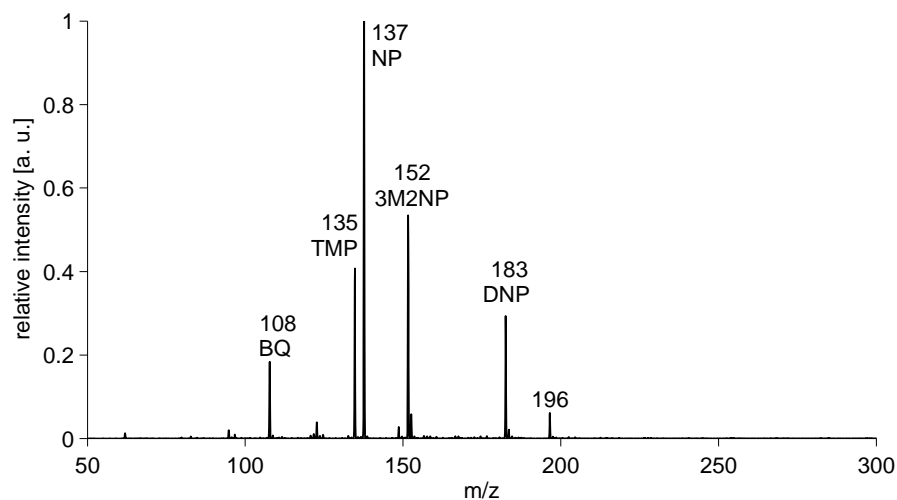


Figure 7.2: Mass spectrum of the same mixture as in figure 7.1, but without chromatographic separation.

and 2,4-dinitrophenol (DNP, m/z 183). The absence of a 2,4-dinitrotoluene signal in the resulting mass spectrum may be due to the low vapor pressure compared to the other compounds, which are 6.8×10^{-3} mbar at 20°C for 2,4-dinitrotoluene [299] and 1.3 mbar at 49.3°C for 2-nitrophenol [101].

To demonstrate the dynamic range and the limit of detection exemplary measurements were made for one analyte. Figure 7.3 shows the linear range of 2-nitrophenol for a concentration range of 0.6 to $150 \mu\text{mol L}^{-1}$ and an injection volume of $1 \mu\text{L}$. The linear fitting function is $[\text{Peak Area}] = 1.32 \cdot 10^4 \cdot [\text{Conc.}] + 2.18 \cdot 10^4$ with a regression coefficient of $R^2 = 0.998$. With the method of Kaiser and Specker (3σ) [293] a limit of detection of 187 nmol L^{-1} is calculated.

Setup 2 The second setup differs from the first in the orientation of the gas feedings. The primary ion gas stream ($\approx 1 \text{ L min}^{-1}$) goes straight into the inlet capillary and the neutral analyte gas stream ($\approx 300 \text{ mL min}^{-1}$) perpendicularly. This should reduce the loss of reagent ions. However, the modification turned out to have only a small impact on the sensitivity of the GC-MS coupling.

A mixture of seven nitro-aromatic compounds was used to test if the chromatographic performance of the setup changed. A list of the compounds present in the mixture and their chromatographic characteristics is given in table 7.2, the chromatogram is shown in figure 7.4. Hexogen (RDX) and Octogen (*High Molecular Weight RDX*, HMX) are not observed in the mass spectrum. They were also not present in the GC *flame ionization detector* (FID) spectrum which was provided with the analytical standard certificate of the mixture by the manufacturer. Both compounds are

7 Applications

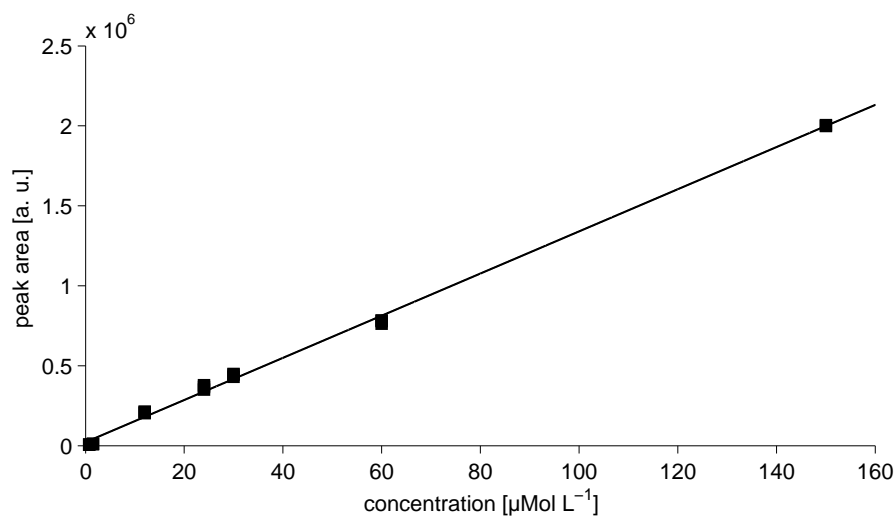


Figure 7.3: Determination of the linear range of the GC-cAPECI-MS setup version 1 for 2-nitrophenol.

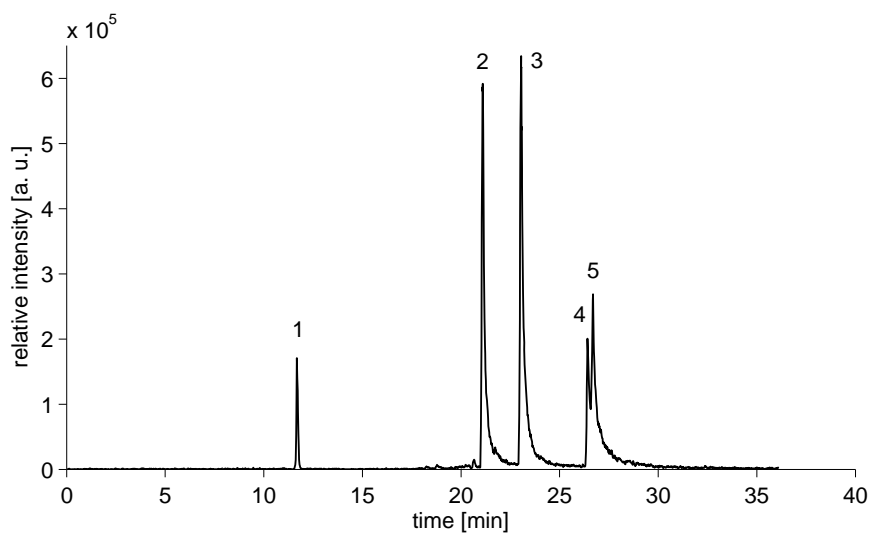


Figure 7.4: GC-cAPECI-MS chromatogram of a certified nitro-aromatic explosives mixture of seven compounds. Hexogen and Octogen are not observed. The peaks are assigned in table 7.1.

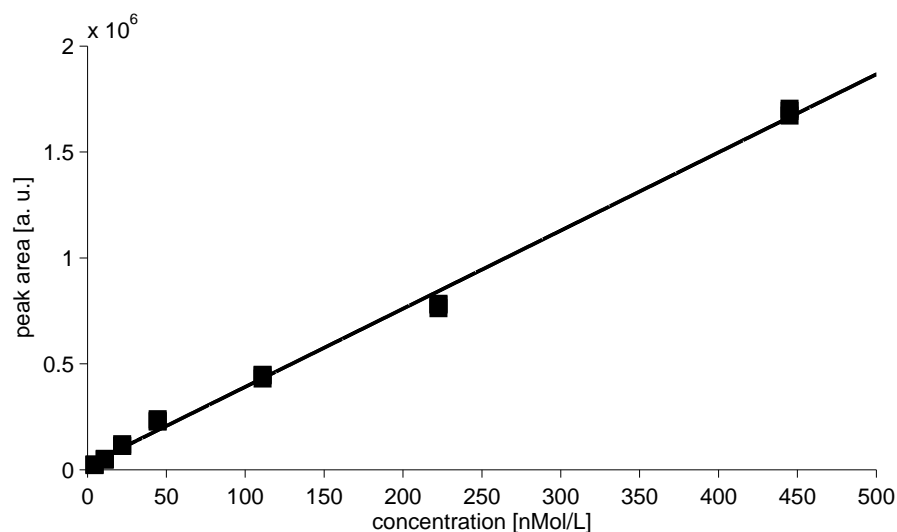


Figure 7.5: Determination of the linear range of 2,4,6-trinitrotoluene detection with the second GC-cAPECI-MS setup.

thermally unstable and it is often reported in the literature that they are not readily measurable with GC-MS without significant fragmentation occurring [294, 297, 298]. Compared with GC-cAPECI setup 1 the chromatographic performance is not affected.

The limit of detection and the linearity for 1,3,5-trinitrotoluene in the nmolL^{-1} range were determined, as is shown in figure 7.5. The linearity is well acceptable over the concentration range investigated. The linear fit yields a calibration line of $[\text{Peak Area}] = 3689.5 \cdot [\text{Conc.}] + 21775$ with a correlation coefficient of $R^2 = 0.996$. The limit of detection was calculated to be 2 nmolL^{-1} with the method of Kaiser and Specker (3σ) [293]. With an injection volume of $1 \mu\text{L}$ this corresponds to a LOD of 2 fmol.

As many nitro-aromatic compounds and particularly explosives are thermally more or less unstable, the temperature of the transfer line and the ion source are crucial factors for the sensitivity of the setup. Figure 7.6 shows the impact of the temperature of the transfer line on the signal intensity of 2-nitrophenol. A decrease of the temperature from the commonly used 300°C to 200°C leads to a doubling of the peak area. The peak width is unaffected. Compared with compounds as for example RDX, 2-nitrophenol should be thermally much more stable, thus this change of the peak area with temperature should be more distinct for explosive compounds than for nitrophenol.

This setup was compared to the coupling of GC with the cAPECI source design 1, which has the ion source integrated into the inlet capillary (cf. section 6.5). Neutral analyte was delivered by the GC. However, neither the sensitivity, nor the chromato-

Table 7.2: Assignment of the GC peaks in figure 7.4 and the corresponding chromatographic properties.

Peak number	Compound	Molar mass [g · mol ⁻¹]	Peak width (FWHM) [s]	Peak area [a. u.]	Signal-to-noise ratio	Concentration [ng · μL ⁻¹]
1	nitrobenzene	123	3.2	1685000	607	10
2	1,3-dinitrobenzene	168	4.5	6293000	502	10
3	2,4-dinitrotoluene	182	8.3	7342000	535	10
4	1,3,5-trinitrobenzene	213	10	1846000	166	10
5	2,4,6-trinitrotoluene	227	10.5	3673000	228	10
	Hexogen	222			10	
	Octogen	296			10	

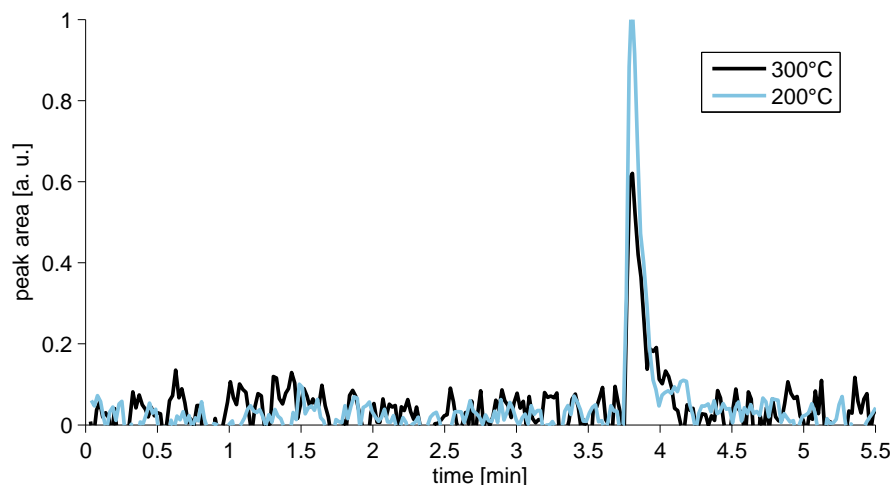


Figure 7.6: Signal peaks of 2-nitrophenol for two different temperatures of the GC transfer line.

graphic characteristics, e.g., the peak capacity, change when using this setup. The reduced reaction time gives a slightly lower background noise level. The main advantage of this setup is that changing to direct sampling or desorption sampling is straight forward. Furthermore, also other ion sources can be mounted in front of this ion source.

7.2 Atmospheric Chemistry

The detection of nitro-aromatic compounds is an important field in atmospheric chemistry (section 1.7). A relatively new, but already widespread method used especially in atmospheric chemistry is proton transfer reaction mass spectrometry introduced by Hansel in 1995 [192]. To examine the applicability of cAPECI in the field of atmospheric chemistry for the selective detection of nitrophenols, phenols and other compounds with elevated electron affinity or high gas-phase basicity, cAPECI was directly compared to the performance of a PTR-TOF-MS and the limit of detection was exemplary determined for one compound with both instruments. Furthermore, as an example for an application in atmospheric chemistry a photo-oxidation study of 3-methyl-2-nitrophenol was carried out with simultaneous monitoring of the processes using both instruments [82, 257, 300, 301].

7 Applications

7.2.1 Comparison of cAPECI and PTR

Different compounds were simultaneously measured with the PTR-TOF-MS and the cAPECI ion source coupled with the ion trap mass spectrometer. The analyte chosen as representative for the compound class of nitrophenols was 2-nitrophenol (139 Da). Mass spectra obtained with cAPECI and PTR in ambient air are shown in figure 7.7. The PTR generates only positive ions. All mass spectra shown here from the PTR-MS were recorded in the positive ion mode, while all the cAPECI mass spectra were obtained in negative ion mode.

As expected, the cAPECI mass spectrum shows only one peak, the $[M-H]^-$ ion of the analyte. In the PTR mass spectrum the signal with the highest intensity is the $[M+H]^+$ signal of the analyte. A second signal assignable to the analyte is recorded with a relative intensity of 60% at m/z 122 and identified as the $[M+H-H_2O]^+$ ion. This ion is generated inside the drift tube of the PTR-MS by CID processes. During the measurements shown a reduced field strength of 130.5 Td was used. This can easily lead to CID processes, for example, the dissociation of water from compounds that contain hydroxyl groups. A third signal is observed in the PTR mass spectrum at m/z 78.

The second compound class studied was the group of nitro-aromatic compounds without hydroxyl functions. The mass spectra of 2-nitro-isopropylbenzene (165 Da) measured with cAPECI and PTR are shown in figure 7.8. With cAPECI M^- is the only signal in the mass spectrum. PTR generates the $[M+H]^+$ ion for most analytes. This is also the case for 2-nitro-isopropylbenzene where $[M+H]^+$ is the most intense signal in the PTR mass spectrum. The additional signal at m/z 106 remains unidentified.

An exemplary limit of detection was determined for both ionization methods using 3-methyl-2-nitrophenol. The LOD is determined by the method of Kaiser and Specker [293] and a threefold standard deviation (3σ) is used. For the PTR-MS, a limit of detection of ≤ 250 pptV during a measurement period of 30 s is obtained [257]. For cAPECI the limit of detection is ≤ 1 ppbV, for a measurement period of less than 1 s.

It is worth noticing that the measurements described here for cAPECI were carried out with the silica capillary which was partially plated with silver on the inside (cf. section 6.4). Compared to this ion source, the stages developed later during the course of this work showed significantly higher sensitivities (cf. section 6.6). Unfortunately the PTR instrument was not available for comparison measurements during the further development stages of the cAPECI ion source.

7.2.2 Photo-Oxidation Study

To investigate the applicability of cAPECI for atmospheric chemistry measurements under realistic conditions, a photo-oxidation study was carried out [82, 257, 300]. As analyte, 3-methyl-2-nitrophenol was chosen. The residence time of the analyte in the photo-oxidation chamber was approximately 22 min. For details on the experimental setup see section 3.9.

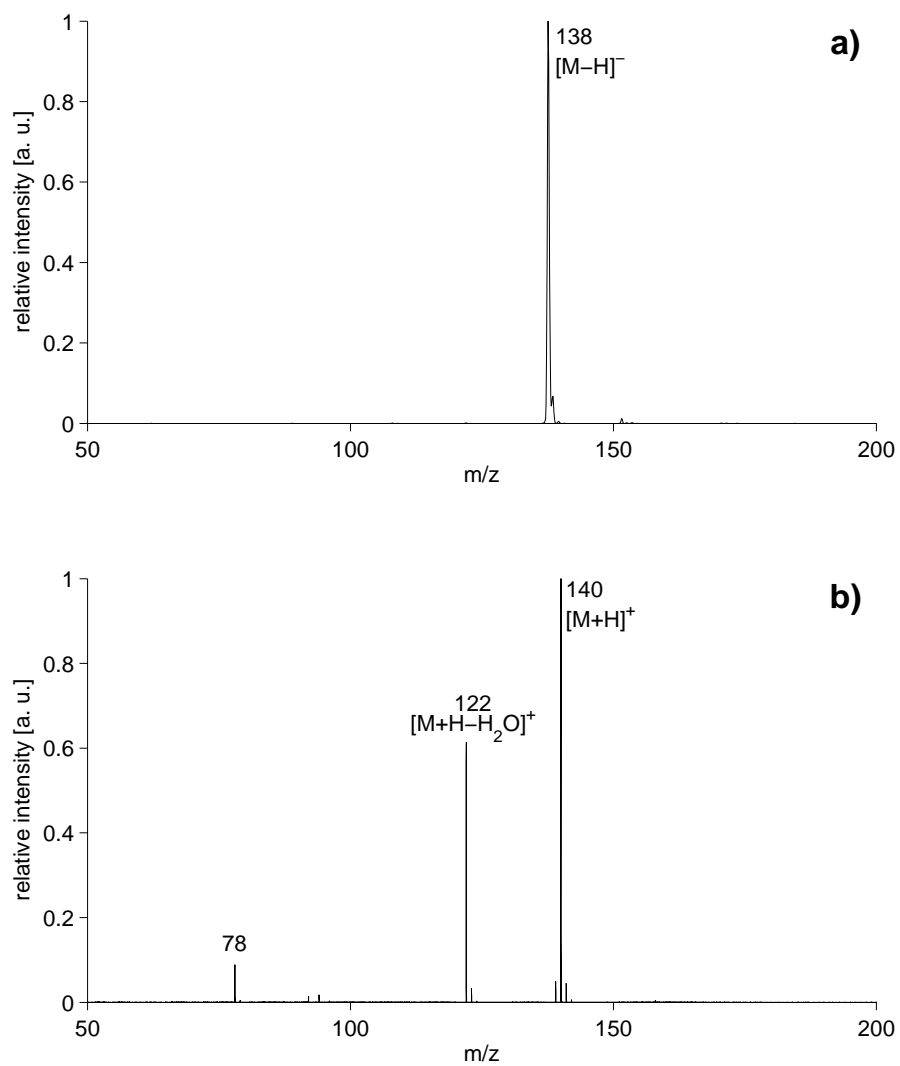


Figure 7.7: Mass spectra of 2-nitrophenol recorded simultaneously with a) cAPECI ion trap (negative ion mode) and b) PTR-TOF-MS (positive ion mode).

7 Applications

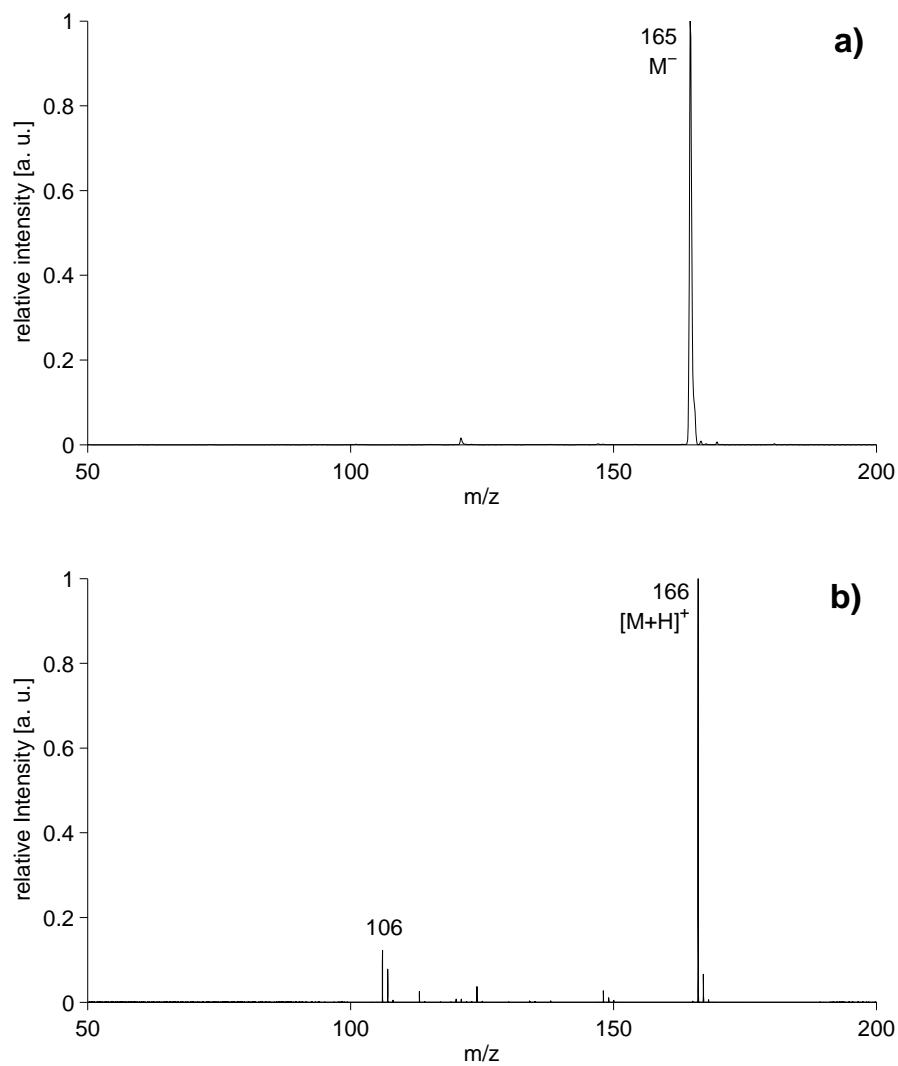


Figure 7.8: Mass spectra of 2-nitro-isopropylbenzene recorded simultaneously with a) cAPECI-ion trap (negative ion mode) and b) PTR-TOF-MS (positive ion mode).

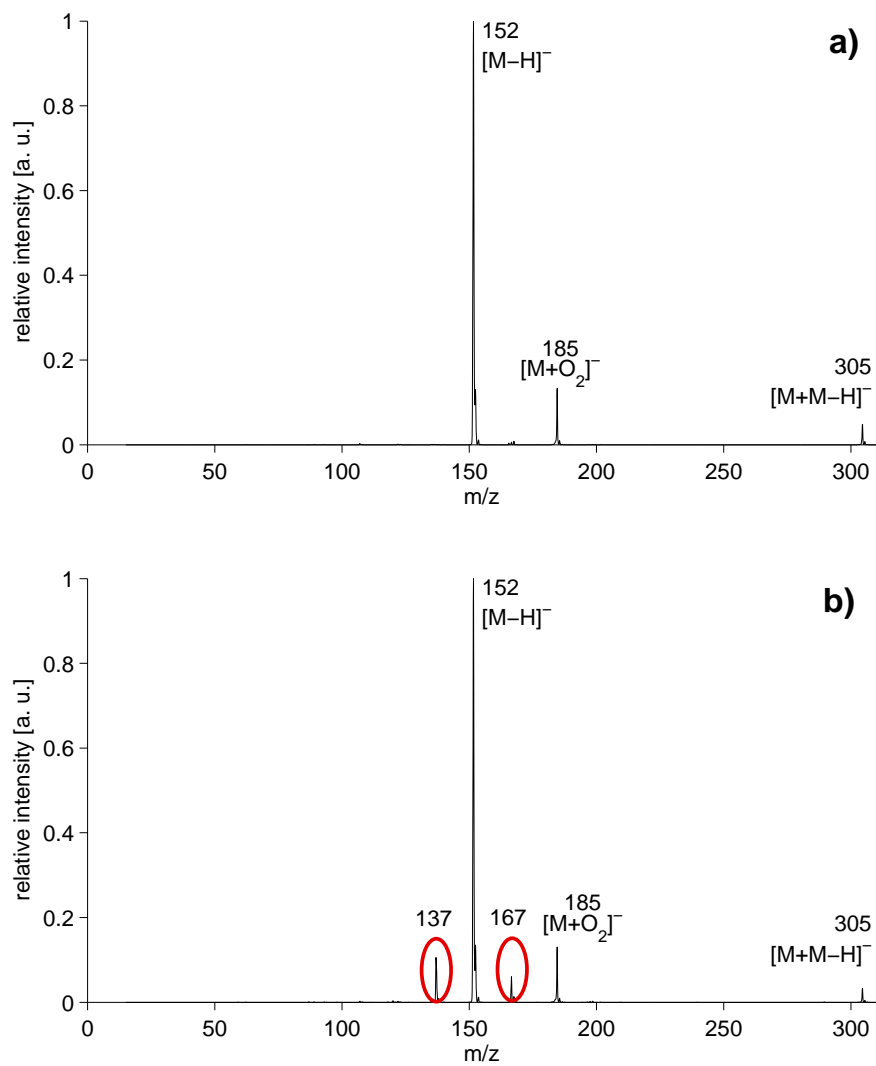


Figure 7.9: a) cAPECI mass spectrum of 3-methyl-2-nitrophenol prior to the photo-oxidation. b) cAPECI mass spectrum of the same analyte with the UV lamps switched on.

7 Applications

Before the UV/VIS lamps (emission from $\lambda = 290$ to 460 nm) are switched on, the main signal in the mass spectrum generated with cAPECI is the $[M-H]^-$ at m/z 152. Due to the reduced voltages applied to the ion optics reducing CID processes there are also signals corresponding to $[M+O_2]^-$ ion at m/z 185 and the dimer ion, $[M+M-H]^-$, at m/z 305 (see figure 7.9 a). When the photo-oxidation lamps are switched on, two additional signals appear in the cAPECI mass spectrum at m/z 137 and m/z 167, as shown in figure 7.9 b.

The extracted ion chromatograms of the analyte precursor, i.e., $[M-H]^-$ and photo-oxidation products were monitored and are shown in figure 7.10. Before the lamps are switched on, a constant signal of the deprotonated analyte is observed. When the photo-oxidation is initiated, the intensity of this ion increases initially, due to the heating of the glass tube by the UV/VIS lamps. Then, the signal decreases with time to around 65 %. The signals of the reaction products slowly increase. The signal at m/z 137 appears shortly after the lamps are switched on, while the other signal m/z 167 only appears after approximately 18 min. This suggests that the second ion is from a photo-oxidation product of the compound corresponding to the first signal at m/z 137. In addition to photolysis products from the analyte ion, products of the analyte decomposition induced by OH radicals may occur, as the photolysis of ortho-nitrophenols results in the formation of HONO, the photolysis of which produces hydroxyl radicals [226].

After the UV lights are switched off, the precursor ion signal immediately starts to increase, but does not reach its initial intensity even after one hour of waiting time. The reason for this effect remains unclear, particularly since the *extracted ion chromatogram* (EIC) of the analyte ion recorded with the PTR reaches the same intensity. The extracted ion chromatograms of the product signals do not decrease immediately after the lights are switched off, this occurs only after several minutes. This may be due to product molecules that stick to the glass walls or the Teflon tubing that connects the photoreactor with the mass spectrometers. An identical effect is observed with the PTR-MS [257].

In the analyte mass spectrum recorded with the PTR-MS without photo-oxidation the $[M+H-H_2O]^+$ signal has the highest intensity, followed by the $[M+H]^+$ signal of the analyte with 47 % intensity. Furthermore, a signal at m/z 92 with approximately 20 % intensity is present, which is not assignable to a specific ion. Starting the photo-oxidation process results in the occurrence of two additional signals. These are recorded at m/z 138.0531 and m/z 168.0286. Other signals also appear during the photo-oxidation phase in the PTR mass spectrum; an overview is given in table 7.3.

For the determination of the photo-oxidation products, the availability of the mass spectra from both cAPECI and PTR is advantageous as it gives valuable structural information. While PTR almost exclusively forms the $[M+H]^+$ ion, ionization with cAPECI leads to the M^- or $[M-H]^-$ ion depending on the presence of a hydroxyl group. The product molecule does contain a hydroxyl group when the signals in PTR and cAPECI mass spectrum have a nominal difference of 2. As both signals observed during the present study only have a difference of one, both products thus do not contain

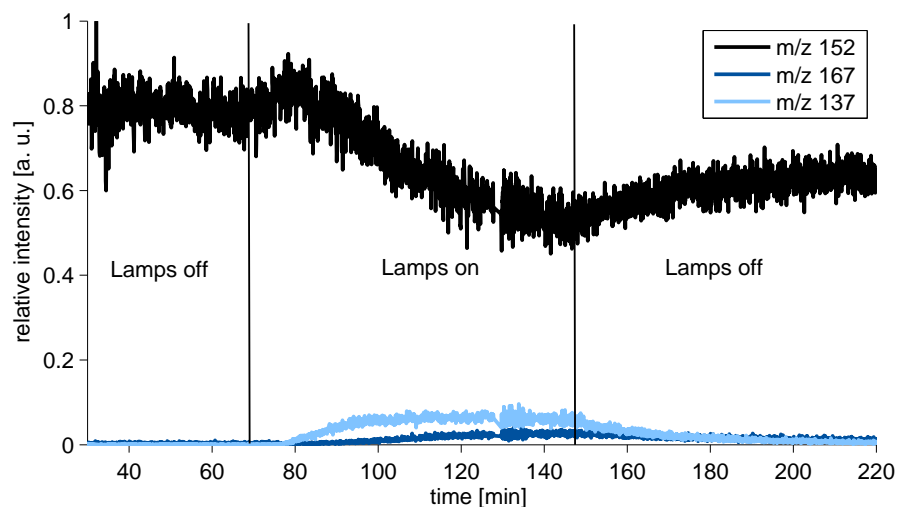


Figure 7.10: Extracted ion chromatograms for the analyte precursor (m/z 152) and the two reaction products recorded at m/z 137 and m/z 167.

an OH group. Additionally, the PTR-TOF-MS is a high resolution instrument with a resolution in the 1×10^4 range. The combination of the available information allows the structure determination of one product as shown in figure 7.12. The structure of the other product has not yet been determined. However, a molecular composition of $C_7H_5NO_4$ with a deviation of -3.0 ppm is proposed (see table 7.3). As this study was a test of the applicability of the ionization method, no effort was made to elucidate a reaction mechanism which relates the analyte ion with the product structure. The other photo-oxidation products observed in the PTR spectrum are also not assigned to a specific molecular structure. The signals at m/z 120 and m/z 150 can be fragment ions of the ions with m/z 138 and m/z 168, respectively. The mass difference of 18

Table 7.3: Observed product ion signals with the PTR-MS for the photo-oxidation study.

m/z	Molecular formula	Relative mass accuracy [ppm]
113.0590	$C_6H_8O_2H^+$	-6.2
120.0451	$C_7H_5NOH^+$	5.8
138.0531	$C_7H_7NO_2H^+$	-13.8
150.0182	$C_7H_3NO_3H^+$	-2.7
168.0286	$C_7H_5NO_4H^+$	-3.0

7 Applications

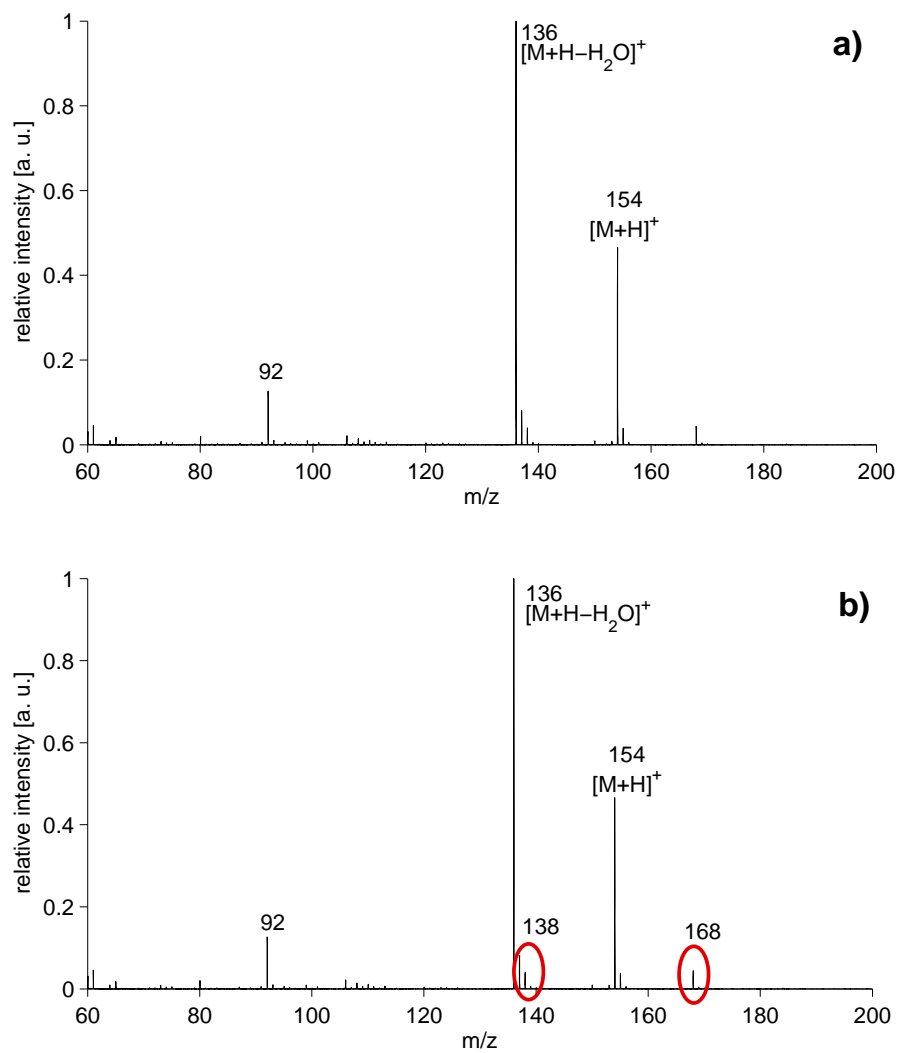


Figure 7.11: a) PTR mass spectrum of 3-methyl-2-nitrophenol prior to photo-oxidation. b) PTR mass spectrum of the same analyte when the UV lamps are switched on.

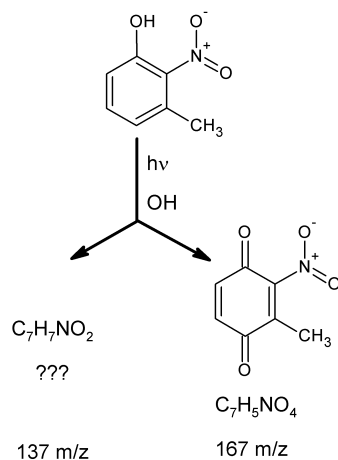


Figure 7.12: Proposed structure of the product ion in the photo-oxidation study. The structure of the second product is not identified.

and the parallel course of the signal intensities indicate the loss of a water molecule (see [257] for details).

7.3 Determination of Rate Constants

With the cAPECI ion source design 1 the determination of rate constants for the reaction of molecules with superoxide or other reagent ions is possible [302]. There are only a few reports in the literature on the rate constants for these reactions.

In this ion source, oxygen is in large excess over thermal electrons, which leads to a collisionally controlled reaction rate of the electron attachment. A typical value for the mixing ratio of thermal electrons generated by the photoelectric effect within the ion source is in the range of 100 pptV, which is therefore the upper limit for the mixing ratio of superoxide. In most cases, the analyte mixing ratio is larger by several orders of magnitude (ppbV range). Thus, it is safe to assume a pseudo-first order reaction with respect to O_2^- . The change of the mixing ratio of superoxide cannot be monitored directly with the mass spectrometer, but the change of the mixing ratio of the products, which is also pseudo-first order with respect to the analyte.

The major issue with this approach is that there is no defined position where the two reactants are mixed, which means that there is no clearly defined reaction time. However, the ion source is divided into two distinct regions, which are depicted in figure 7.13. In region A photo electrons are generated uniformly and are directly transformed to O_2^- . Reaction between the superoxide and the analyte is already occurring in this region. In region B, which is an inlet capillary segment to connect the ion source with the mass spectrometer, no ions are produced and only reaction with the

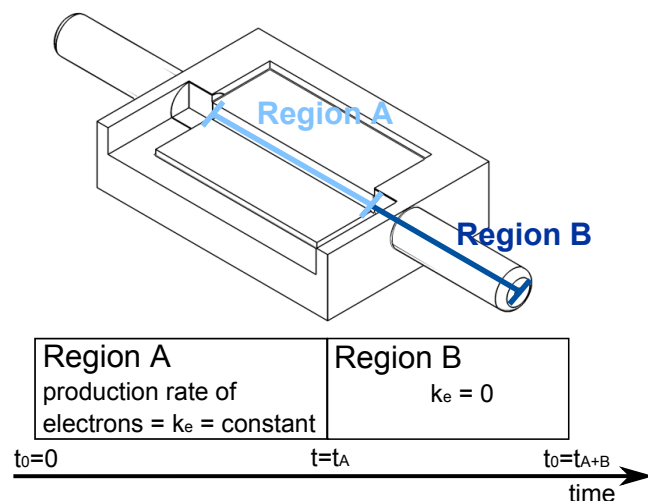


Figure 7.13: Schematic of the cAPECI ion source design 1. In region A ions are uniformly generated by the photoelectric effect. In region B no ions are formed. In both regions the reaction of analyte molecules with superoxide occurs.

analyte takes place. The calculated residence time of molecules inside both regions is roughly the same, with $t_A \approx 480 \mu\text{s}$ in region A and $t_B \approx 490 \mu\text{s}$ in region B. After passage through the inlet capillary the ions reach the first vacuum stage and then later the ion optics leading to the mass analyzer. The number of collisions and the concentration of the neutral reactant decreases drastically when the pressure is reduced, resulting in strongly decreased reaction rates. Thus, these regions are not included in the kinetic analysis.

The simultaneous generation of superoxide and the reaction with the analyte inside the ion source (region A) renders a formal description difficult. Thermal electrons are uniformly generated in this region, resulting in a linear increase in superoxide ions along the way through this region. However, as soon as superoxide ions are formed, the reaction with the analyte starts, resulting in an exponential decrease of the superoxide concentration along the linearly increasing concentration profile. These two processes must be taken into account in a formal kinetic description of this region.

Region A For the kinetic description of region A the following assumptions are made: The gas streams are assumed to be ideally mixed over the entire cross section of the capillary channel. As mentioned before in section 1.2, the gas flow in the inlet capillaries used here are considered as fully developed turbulent, ensuring a fast and

7.3 Determination of Rate Constants

complete mixing inside the capillary channel. Furthermore, only superoxide and not superoxide water clusters may react with the analyte. Even though there is a very high probability that this assumption holds true, it needs to be verified in future experiments.

The photoelectric effect generating thermal electrons in region A is regarded as a zero-order reaction.

$$\frac{d[e^-]}{dt} = k_e \quad (7.1)$$

The rate constant of this reaction, k_e , depends on the irradiated surface area, the quantum yield of the electron generation and the photon flux, which all remain constant during the course of the reaction. As stated previously, oxygen is in large excess compared to the thermal electrons. The electron capture reaction of oxygen is a third order reaction, as a third body is necessary to carry away excess energy. Oxygen as third body is much more efficient than nitrogen, the rate constant with O_2 as third body is two orders of magnitude larger than for N_2 (see equations R 3.1 and R 3.2 in section 3.2). The rate law for this reaction is

$$\frac{d[O_2^-]}{dt} = k \cdot [e^-] \cdot [O_2] \cdot [O_2] \quad (7.2)$$

The right hand side of equation 7.2 is equal to the pseudo-zero order rate constant $k_{O_2^-}$ for the formation of O_2^- :

$$k_{O_2^-} = k \cdot [e^-] \cdot [O_2] \cdot [O_2] \quad (7.3)$$

$$\frac{d[O_2^-]}{dt} = k_{O_2^-} \quad (7.4)$$

Integration yields:

$$[O_2^-] = k_{O_2^-} \cdot t \quad (7.5)$$

The consumption of O_2^- through reaction with the analyte is described by



where M denotes the analyte, P the ionic products and X other neutral products, e.g., HO_2 . The rate constant of this reaction is k_2 . As stated in chapter 4, the reaction of superoxide yields an adduct ion for analytes exhibiting a high gas-phase acidity. However, in the mass spectrum only the $[M-H]^-$ is observed due to CID processes in the ion optics. It is assumed that the efficiency of the CID processes occurs reproducibly and does not change with the number of precursor ions present.

Based on reaction R 7.1 the rate law for the generation of product ions is

$$\frac{d[P]}{dt} = k_2 \cdot [O_2^-] \cdot [M] \quad (7.6)$$

7 Applications

The large excess of the analyte concentration compared to the concentration of superoxide leads to a pseudo-first order production rate.

$$\frac{d[P]}{dt} = k' \cdot [O_2^-] \text{ with } k' = k_2 \cdot [M] \quad (7.7)$$

For analytes with a negative electron affinity reaction R 7.1 is termolecular, where a third body (TB) is necessary for the reaction to proceed. In this case the reaction is in the high pressure limit and the concentration of the third body is included in the rate constant.

$$k' = k_2 \cdot [M] \cdot [TB] \quad (7.8)$$

Substituting equation 7.5 into equation 7.7 yields

$$\frac{d[P]}{dt} = k' \cdot k_{O_2^-} \cdot t \quad (7.9)$$

Integration of this equation with $t = 0$ as the lower and t_A as the upper limit leads to

$$[P]_{t_A} = k' \cdot \frac{1}{2} \cdot k_{O_2^-} \cdot t_A^2 \quad (7.10)$$

Region B In the second region only the reaction of superoxide with the analyte takes place. The rate law is the same as given in equation 7.7, except that the concentration of superoxide cannot be replaced by equation 7.5 describing its formation.

Integration of this equation leads to

$$[P]_t = [O_2^-]_{t_A} - [O_2^-]_{t_A} \cdot e^{(-k' \cdot t)} \quad (7.11)$$

After region B the concentration of the product is

$$[P]_{t_B} = [O_2^-]_{t_A} \cdot \left(1 - e^{(-k' \cdot t_B)}\right) \quad (7.12)$$

Combination of both regions The description of the overall product concentration is determined by addition of equations 7.10 and 7.12.

$$[P]_{t_{AB}} = [P]_{t_A} + [P]_{t_B} \quad (7.13)$$

giving:

$$[P]_{t_{AB}} = \left(k' \cdot \frac{1}{2} \cdot k_{O_2^-} \cdot t_A^2\right) - \left[[O_2^-]_{t_A} \cdot \left(1 - e^{(-k' \cdot t_B)}\right)\right] \quad (7.14)$$

The concentration of superoxide at time t_A is given by the difference between the total concentration of superoxide produced after t_A and the concentration of the products generated.

$$[O_2^-]_{t_A} = [O_2^-]_t - [P]_{t_A} \quad (7.15)$$

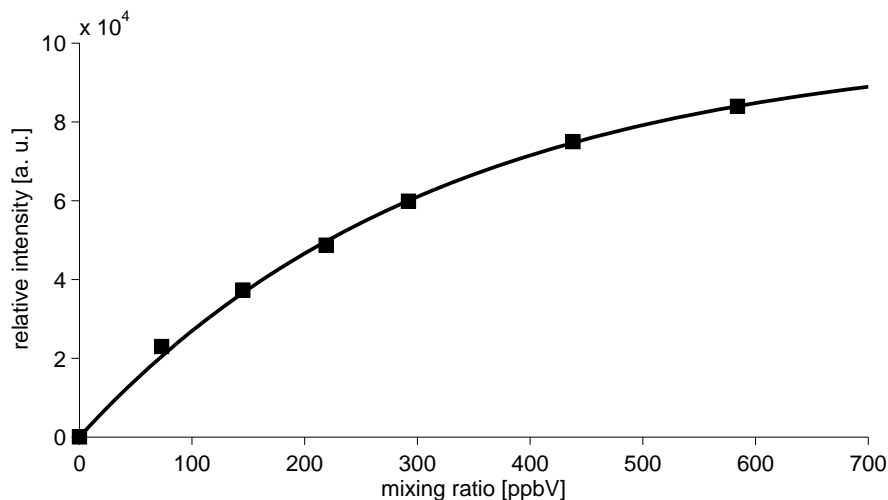


Figure 7.14: Dependence of the signal intensity of the $[M-H]^-$ on the mixing ratio of 3-methyl-2-nitrophenol. The curve was fitted using equation 7.20.

With 7.5 and 7.10 follows

$$[O_2^-]_{t_A} = k_{O_2^-} \cdot t_A - \frac{1}{2} \cdot k' \cdot k_{O_2^-} \cdot t_A^2 \quad (7.16)$$

Insertion into equation 7.14 leads to

$$[P]_{t_{AB}} = \left(k' \cdot \frac{1}{2} k_{O_2^-} \cdot t_A^2 \right) - \left(k_{O_2^-} \cdot t_A - k' \cdot \frac{1}{2} k_{O_2^-} \cdot t_A^2 \right) \cdot \left[1 - e^{(-k' \cdot t_B)} \right] \quad (7.17)$$

which simplifies to

$$[P]_{t_{AB}} = k_{O_2^-} \cdot t_A \cdot \left[1 - \left(1 - \frac{1}{2} \cdot k' \cdot t_A \right) \cdot e^{(-k' \cdot t_B)} \right] \quad (7.18)$$

Replacing k' with the expression in equation 7.7 yields finally

$$[P]_{t_{AB}} = k_{O_2^-} \cdot t_A \cdot \left[1 - \left(1 - k_2 \cdot [M]_0 \cdot \frac{1}{2} \cdot t_A \right) \cdot e^{(-k_2 \cdot [M]_0 \cdot t_B)} \right] \quad (7.19)$$

The transfer times, t_A and t_B and the initial concentration of the analyte are known. The concentration of the product cannot be determined directly but is directly proportional to the signal intensity of M^- or $[M-H]^-$ obtained from the mass spectra. Thus, the rate constant of the reaction between superoxide and the analyte, k_2 , is readily determined. Furthermore, the pseudo-zero order rate constant for the electron capture reaction of oxygen is calculated.

7 Applications

Example An example for this procedure is given in the following. 3-methyl-2-nitrophenol is chosen as analyte and the $[M-H]^-$ signal is considered as reaction product. Figure 7.14 shows the signal intensity of the $[M-H]^-$ ion in dependence on the mixing ratio of the analyte. The best fit to the data in figure 7.14 is obtained with equation 7.20 with a correlation coefficient of $R^2 = 0.9986$.

$$[P] = 4.77 \cdot 10^{-4} \cdot 1.910 \cdot 10^8 \cdot \left[1 - \left(1 - \frac{1}{2} \cdot 4.77 \cdot 10^{-4} \cdot 4.789 \cdot [M]_0 \right) \cdot e^{(-4.87 \cdot 10^{-4} \cdot 4.789 \cdot [M]_0)} \right] \quad (7.20)$$

The rather strange form of equation 6.3 is chosen to simplify the comparison with equation 7.19. An overall pressure of 610 mbar is assumed for both regions (see figure 1.2 in section 1.2) to determine the rate constants, yielding $k_{O_2^-} = 1.7 \times 10^8 \pm 0.5 \times 10^8 \text{ molecule cm}^{-3} \text{ s}^{-1}$ and $k_2 = 3.2 \times 10^{-10} \pm 1 \times 10^{-10} \text{ cm}^3 \text{ molecule}^{-1} \text{ s}^{-1}$, respectively.

Kinetic Simulation Monte Carlo simulations were carried out to determine the concentration profile in the two regions of the ion source. For this purpose, the recently developed Reaction Simulation extension for the charged particle solver Simion was used [26, 65, 260]. The statistical simulation considers the molecules residing inside a volume of 0.01 cm^3 . A total number of 4000 time steps, with a maximum time step duration of $8 \times 10^{-7} \text{ s}$, were used for the simulation and 5×10^9 analyte molecules present inside the simulation volume were chosen. The reaction times inside each region were set to $560 \mu\text{s}$ for region A and $420 \mu\text{s}$ for region B.

Two different scenarios were tested, differing in the rate constant used for the reaction of superoxide with the analyte. For the electron capture reaction of oxygen a rate constant of $k_{O_2^-} = 1 \times 10^8 \text{ molecule cm}^{-3} \text{ s}^{-1}$, estimated from the third order literature value [102] was assumed. The rate constant for the reaction of the analyte with superoxide was set to the collision limit, which relates to $k_2 = 1 \times 10^{-9} \text{ cm}^3 \text{ molecule}^{-1} \text{ s}^{-1}$ (figure 7.15 a). A second simulation used a slightly lower rate constant for k_2 of $1 \times 10^{-10} \text{ cm}^3 \text{ molecule}^{-1} \text{ s}^{-1}$ (figure 7.15 b). Inlet capillaries are used to reduce the pressure from atmospheric pressure inside the ion source to some millibars inside the first vacuum stage. The pressure inside the inlet capillary and thus inside the capillary ion source, steadily decreases, resulting in a constant decrease in the number density during the course of reaction. The average pressures in the two regions are 680 mbar and 450 mbar, respectively. Pressures of 680 mbar in region A and 477 mbar in region B were assumed for the simulation.

The collision controlled reaction simulation (figure 7.15 a) shows for region A a steady increase of the O_2^- mixing ratio during the passage through the ion source. Shortly after the superoxide ions are generated, the formation of product ions starts. At the end of region A, the number of molecules of the product has increased to approximately 83 % of the number of superoxide ions. The discontinuity in the concentration

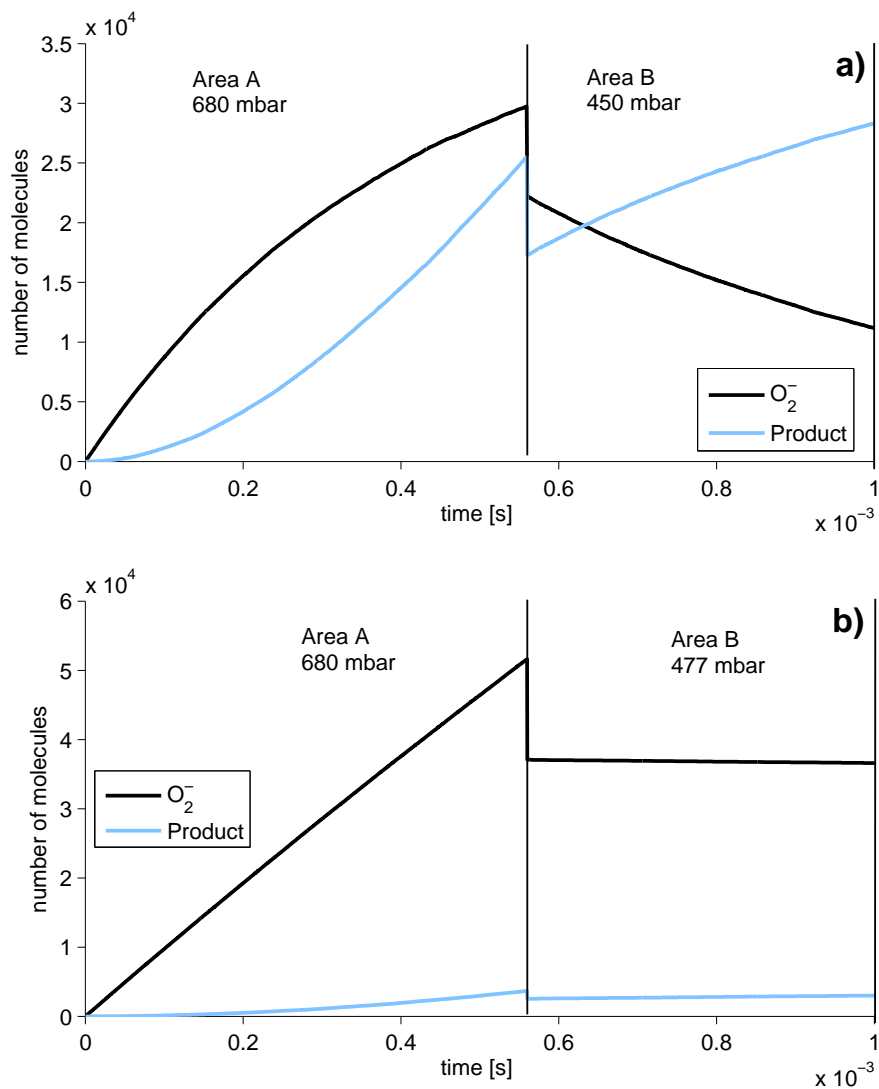


Figure 7.15: Monte Carlo simulation showing the concentration profiles of superoxide and the reaction product, with a) collisionally controlled rate constants ($k_{O_2^-} = 1 \times 10^8 \text{ molecule cm}^{-3} \text{ s}^{-1}$ and $k_2 = 1 \times 10^{-9} \text{ cm}^3 \text{ molecule}^{-1} \text{ s}^{-1}$) and b) rate constants of $k_{O_2^-} = 1 \times 10^8 \text{ molecule cm}^{-3} \text{ s}^{-1}$ and $k_2 = 1 \times 10^{-10} \text{ cm}^3 \text{ molecule}^{-1} \text{ s}^{-1}$.

7 Applications

traces at the transition from region A to region B is a simulation artifact, as a fixed pressure is assumed for both regions instead of a steady pressure decrease along the ion source. In region B no more superoxide is formed, thus the concentration of O_2^- decreases since the reaction with the analyte proceeds. The number of molecules of the product increases correspondingly. When the reaction rate between analyte and superoxide is assumed to be lower ($k_2 = 1 \times 10^{-10} \text{ cm}^3 \text{ molecule}^{-1} \text{ s}^{-1}$, figure 7.15 b)) the shape of the concentration profiles remain similar. However, due to the slower reaction between analyte and superoxide, the number of superoxide ions rises to a much higher value compared with the collisionally controlled case. At the same time, the concentration of the product ions increases only to a small fraction of the superoxide concentration.

A further decrease of the rate constant for the reaction between O_2^- and analyte would lead to a reaction too slow to occur significantly during the limited reaction time inside the ion source. Thus, with this method only relatively fast ion-molecule reactions ($1 \times 10^{-8} \geq k_2 \geq 1 \times 10^{-11} \text{ cm}^3 \text{ molecule}^{-1} \text{ s}^{-1}$) are measurable. It is noted though that most ion-molecule reactions proceed at or even above the collision limit or do not occur at all [50].

7.4 Desorption APECI

Desorption from surfaces is an important field especially for the detection of explosive compounds by wipe tests. While the long term goal is the development of a laser desorption stage in front of a capillary APECI source, two different ways to desorb analytes from surfaces are introduced in the following. The first version uses a gas stream of synthetic air that is directed onto the target. The gas stream was not heated for the measurements described. Heating the gas stream would lead to a larger amount of analyte desorption from the target and will be investigated in future experiments. A volume flow slightly higher than the volume flow that passes through the inlet capillary gave the highest analyte intensities and the cleanest mass spectra. The positioning of the gas stream on the target is not very important for the sensitivity, as long as the gas stream hits the target near the capillary duct. A narrower gas stream would improve the spatial resolution of the desorption process, but then the accuracy of the positioning of the gas stream would have to be controlled precisely.

The mass spectra of two exemplary compounds are shown in figure 7.16. Picric acid was desorbed from human skin, which was held in front of the capillary duct. Tetrachloro-p-benzoquinone was desorbed from a copper plate. Both mass spectra show only one signal, corresponding to the $[M-H]^-$ ion in the case of picric acid and M^- for tetrachloro-p-benzoquinone. Tetrachloro-p-benzoquinone contains four chlorine atoms and the correct chlorine isotope pattern is observed.

The second approach is more similar to “ambient” ionization methods, where a reagent ion gas stream is directed on a target to desorb and ionize the analyte quasi si-

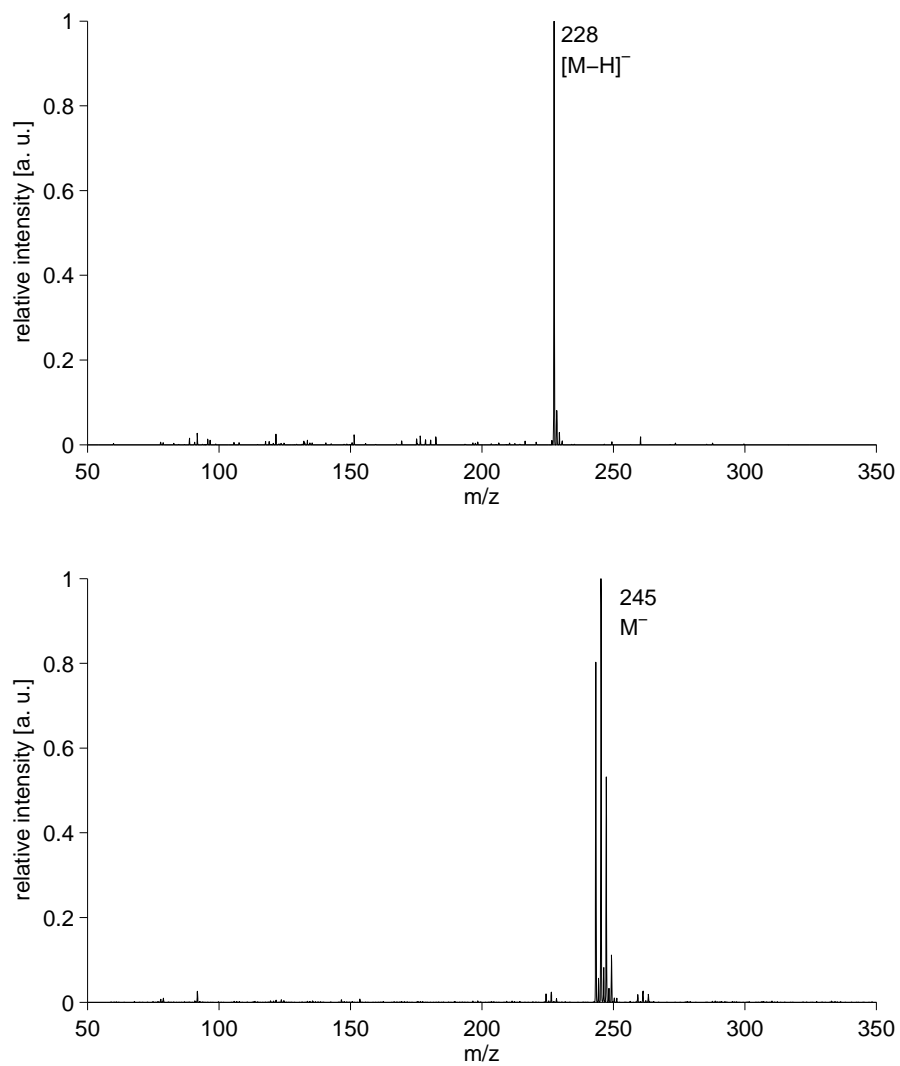


Figure 7.16: Mass spectra of the desorption of picric acid from a finger (upper panel) and tetrachloro-p-benzoquinone from a metal target (lower panel) with a gas stream of synthetic air.

7 Applications

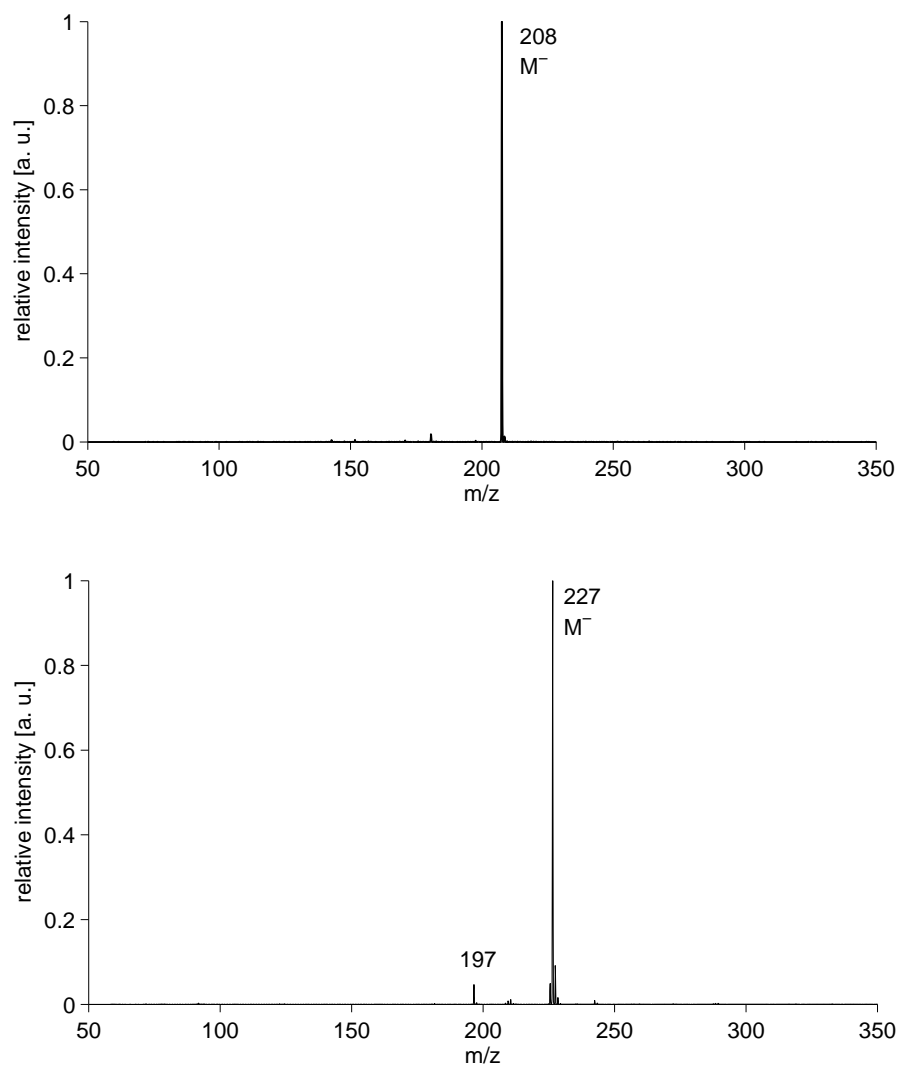


Figure 7.17: DAPECI measurements of anthraquinone (upper panel) and 1,3,5-trinitrotoluene (lower panel) in ambient air.

multaneously. For desorption APECI, primary ions were generated inside an anodized aluminum tube and a synthetic air gas stream containing the reagent ions was directed onto the target. With this setup the adjustment of the positioning of the reagent ion gas stream had a large impact on the sensitivity. The mass spectra shown in figure 7.17 were recorded with an optimized angle and distance from the capillary inlet (cf. section 3.11). The mass spectrum of anthraquinone shows one signal corresponding to the M^- ion. The measurement of 1,3,5-trinitrotoluene in ambient air also led to the M^- ion. An additional signal at m/z 197 was recorded, which is possibly a fragment ion of trinitrotoluene. When 1,3,5-trinitrotoluene was desorbed with a neutral gas stream and ionized within the inlet capillary this additional signal was hardly detected. For both measurements the metallic target was slightly heated.

With this desorption method the analyte concentration could not be accurately quantified. For trinitrotoluene a standard solution of 1 mg mL^{-1} in acetonitrile was used. One drop of this solution was applied to the target, which had a surface area of approximately 1 cm^2 . To measure picric acid on human skin, the vessel containing the compound was simply touched before analysis.

7.5 Summary and Outlook

Different applications of the ionization method developed during this work were successfully implemented. An important application is the coupling of a gas chromatograph with cAPECI. A custom transfer line operated around 300°C and a heated ion source (approximately 100°C) allowed retaining the separation efficiency of the neutral analyte evolving from the GC. The temperature of the transfer line has naturally a large impact on the sensitivity of the setup, in particular for thermally labile compounds. All three setups used here show comparable sensitivities, yielding a limit of detection for 2,4,6-trinitrotoluene of 2 nmol L^{-1} . The sensitivity must be improved significantly in further setups in order to compete with commonly used GC-MS setups. However, the coupling of GC with a cAPECI ion source does not seem to have many benefits due to the selective and sensitive ionization obtained when samples were directly introduced without upstream separation. The GC coupling is only advantageous when quantification is required.

During this study, it has been demonstrated that cAPECI can be applied for atmospheric chemistry investigations. PTR outperforms cAPECI in the accessible range of analytes, which is much broader for PTR. However, when analytes with high electron affinity or gas-phase basicity are of interest, cAPECI is the method of choice due to its selectivity. The mass spectra obtained with cAPECI show less complexity compared to the PTR spectra, especially for hydroxyl-containing compounds. These often show a fragment ion when measured with PTR, as water dissociates easily from the $[M+H]^+$ ion. Furthermore, many more signals are observed in PTR mass spectra, due to the wide range of ionizable molecules. This advantage is particularly important in the

7 Applications

field of product studies, as for example, photo-oxidation studies, where the product signals need to be clearly identifiable. With cAPECI only some analyte classes can be ionized, which means that some products may be missed. The best choice for those studies would be a combination of both PTR and cAPECI, which would give valuable structural information regarding the product molecules.

The limit of detection of the PTR instrument was less than 250 pptV, which is much better than cAPECI with less than 1 ppbV. However, the sampling period of the PTR-MS was 30 s while that of the ion trap with the cAPECI source was less than 1 s. The sensitivity of cAPECI could be easily improved by increasing the integration time using alternative mass spectrometers. It should also be noted that this measurement was not carried out with the most sensitive ion source developed during this work. In future, the measurement of the LOD should be repeated with a more recent ion source and extended to more analytes. The applicability of cAPECI needs to be demonstrated by performing other product studies with varying conditions, e.g., other radicals leading to decomposition of the analyte. When the applicability of the ionization method has been satisfactorily proven under laboratory conditions, its use in field studies should be examined.

It has been further demonstrated that the determination of rate constants of reactions between reagent ions and analyte molecules with the cAPECI source design 1 is possible. Very few rate constants between these types of molecules are available in the literature, which means that this method is a valuable contribution to this field. However, only comparably fast reactions can be examined with this setup. The method has the disadvantage that the reaction time cannot be precisely determined as the primary ions are generated in a larger region where the reaction partner, i.e., the analyte, is already present. In an improved version of this setup, the UV lamp should be mounted such that a specific point of ion generation or the analyte should be added downstream of the primary ion source. With such a setup, the determination of rate constants for a large number of analytes will be possible.

Both briefly investigated desorption methods proved to be quite effective. The highest sensitivity and the mass spectra with the lowest background signals were obtained when the target is slightly heated, the analyte is desorbed with a neutral gas stream and ionization takes place inside the capillary ion source. In all the measurements the analyte showed only one signal in the mass spectrum, corresponding to M^- or $[M-H]^-$ ions. Compounds that contain chlorine ions were also accessible without fragmentation.

Even though the sensitivity of both setups seems to be sufficient, a quantification of the analyte concentrations would be a valuable asset. Furthermore, the spatial resolution was very poor, an area of less than 0.5 cm^2 could not be spatially resolved. Thus, a future setup should try to incorporate both aspects. The spatial resolution could possibly be increased by decreasing the gas stream diameter. Laser desorption

7.5 Summary and Outlook

followed by ionization within the inlet capillary would further increase the spatial resolution and should improve the sensitivity. Determination of a suitable wavelength and laser power density will be the focus of future investigations.

8 Summary and Outlook

The aim of this work was the development of a novel ionization method for the negative ion mode and the design of an ion source providing short transfer times, leading to a kinetically controlled ion distribution recorded in the mass spectrometer. The generation of negative ions is advantageous for several compound classes, e.g., nitro-group containing species, oxygenated PAHs or aromatic phenols, as they are not easily measurable with positive ionization. Most ionization methods used in the negative ion mode yield complex mass spectra with additional ions due to ion transformation and fragmentation processes.

The developed ionization method is based on the photoelectric effect and thus produces solely negative ions. Nearly all work functions of metals reported in the literature are obtained under vacuum conditions. Thus, the photoelectric effect was first investigated at atmospheric pressure under various conditions. While the work functions at higher pressure did not differ significantly from those determined under vacuum, the surface conditions of the metals, e.g., oxidation, water or solvent layers on the surface, led to drastic changes in the photoelectron yield.

Generation of negative ions is less common compared with ionization in the positive ion mode. However, even the ionization mechanism for positive chemical ionization, which is the common ionization pathway for both methods, has only been elucidated in depth recently. The ionization mechanism for chemical ionization in the negative ion mode was examined during this study. Photoelectrons are captured immediately by oxygen when (synthetic) air is used as bulk gas, forming superoxide which reacts with analytes by two possible pathways: Analytes with high electron affinity react by charge transfer with O_2^- , yielding the M^- ion of the analyte. This ion can potential cluster with neutral water molecules. The reaction pathway is more complex for analytes with acidic protons. An adduct consisting of the analyte and superoxide forms, which dissociates to M^- or $[M-H]^-$ when additional energy is provided. The M^- clusters with neutral oxygen, which is in large excess, so that M^- is hardly observed in the mass spectrum. When the analyte mixing ratio is high, dimer or even trimer ions as oxygen adducts potentially form. As these adduct ions are less stable than the monomer-adduct ion, the $[M+M-H]^-$ ion is often recorded in the mass spectrum even under nearly CID free conditions. For elevated water mixing ratios, superoxide forms larger water clusters which have a smaller gas-phase basicity and higher electron affinity than pure superoxide. Thus, an increase of the water mixing ratio inside the

ion source leads to a decreasing ionization efficiency. The reaction pathways may possibly change when the reagent ion is not superoxide. However, kinetic simulations showed that under the conditions present in the novel ion source superoxide is the only relevant reagent ion, as the mixing ratio of generated ozone or hydroxyl radicals is too low.

Short transfer times from the ion generation region to the high vacuum region in the mass spectrometer are readily achieved when ionization takes place inside the inlet capillary. However, modifications of the glass inlet capillary used in commercial mass spectrometers of e.g., Bruker Daltonik, inevitably lead to changes in the ion-transmission characteristics. The ion transmissions of capillaries composed of different materials were investigated under various conditions. When ion streams consisting of both polarities pass through the inlet capillary hardly any charging effects occur, independent of the type of modification applied to the capillary. Unipolar ion gas streams are more readily affected by charging effects. These may occur when materials with different conductivities are in contact. Decreasing signal intensities with time were observed, especially when silica was part of the inlet capillary. Additionally, a signal peak at the beginning of each measurement was observed, even when intact glass capillaries were used. The magnitude of the initial signal peaks varied for different materials and for different amounts of ions that passed through the capillary before commencement of the measurement. The following potential explanation for these effects is offered: It takes different time periods for reaching equilibrium between the charges entering the water layer of the capillary wall and the ions that are discharged inside this layer. When the potential gradient between capillary material and the metallic end cap becomes sufficiently large ions are deflected onto the end cap. When equilibrium is reached, a constant number of ions enters the capillary and passes through it, resulting in a constant ion current with time. The different behavior of silica compared to other materials is probably due to the very long time that is necessary until equilibrium is reached. In addition the influences of the water mixing ratio, the voltages applied to the capillary and the temperature on the ion transmission characteristics were examined. Even though no conclusive results were obtained valuable insight into charging effects and ion transmission characteristics of modified inlet capillaries has been obtained.

With the above knowledge on the photoelectric effect and the ion transmission of inlet capillaries, different ion sources using the photoelectric effect for ionization were designed. A low pressure mercury lamp, emitting light with wavelengths of 254 and 185 nm, proved to be advantageous as light source. The photon density was sufficiently high and the photon emission was constant with time. However, it was shown that only the emission at 185 nm is responsible for the measured ion current. The first ion source had comparably high transfer times as ionization took place in front of the inlet capillary. However, this source demonstrated that ionization based on

8 Summary and Outlook

the photoelectric effect is feasible. Promising results were obtained, e.g., mass spectra with a low background signal level. For the second ion source the excitation region was shifted into the inlet capillary. An inlet capillary made of silica, which was partially silver plated on the inside to provide a photoemissive material, replaced the glass capillary. Mass spectra obtained with this setup showed negligible ion-transformation processes of the analyte ions. However, charging effects occurred with this ion source and the silver surface was not homogenous, resulting in hardly reproducible ion currents and a lack of long term stability which renders this source unsuitable for analytical purposes.

The third ion source provided a homogenous, exchangeable photoemissive material. It replaced the inlet capillary of the mass spectrometer maintaining the short transfer times. With this ion source one signal per analyte was observed in most cases. The signal-to-noise ratios of the signals were high, resulting in low limits of detection, e.g., less than 250 pptV 3-methyl-2-nitrophenol during an acquisition time of less than one second. The performance of different metals was investigated. Anodized aluminum showed the best results with respect to photoelectron yield and stability of the surface conditions. However, the lack of long term stability due to charging effects is a major drawback for the applicability of the source.

The last ion source design combined all the desired properties for ionization via the photoelectric effect. To minimize charging effects the glass inlet capillary was not modified and ionization took place in front of it. However, the transfer time of the ions still remained short as the reagent ions and the analyte gas stream are mixed in a region where the inner tubing diameter is already reduced to 0.6 mm, which corresponds to the inner diameter of the capillary channel. Ion transformation processes are again negligible in the obtained mass spectra.

This newly developed ionization method is termed *capillary Atmospheric Pressure Electron Capture Ionization, cAPECI*.

Several applications for the novel method were investigated. These were i) hyphenation with GC, ii) the determination of rate constants of analyte ions with superoxide, iii) the comparison with PTR-MS in a photo-oxidation study and iv) the desorption of analytes from targets.

The cAPECI-GC hyphenation uses a heated GC transfer line and an ion source that is similar to the latest designed ion source version. With this setup sufficient separation of different samples was obtained. The LOD of 1,3,5-trinitrotoluene was determined to be 2 fmol on column. However, due to the high selectivity of the method separation of samples is not necessary. Upstream separation with GC is advantageous only when quantification of analytes is required.

Very few rate constants of the reaction of analytes with superoxide have been reported in the literature. With the developed ion source such determinations become feasible for reactions that are comparably fast, i.e., near the collisional limit. To demonstrate the method a rate constant of $3.2 \times 10^{-10} \text{ cm}^3 \text{ molecule}^{-1} \text{ s}^{-1}$ for the reaction of

3-methyl-2-nitrophenol with superoxide is determined.

Sensitive detection of aromatic phenols and nitro-aromatic compounds is often required in the many areas of atmospheric chemistry. Thus, the newly developed ionization method was compared with PTR-MS, a widely used technique in this field, and a photo-oxidation study was carried out. PTR is much more less selective than cAPECI and for hydroxyl containing compounds fragmentation is observed for most analytes. However, in terms of sensitivity PTR outperforms cAPECI. In the photo-oxidation study two product ions were observed in the cAPECI mass spectrum. Together with the information obtained by the high resolution PTR-MS, a structure for one of the products has been proposed. It has been shown that ideally both methods should be used simultaneously for such studies.

Desorption of analytes from targets is an important application, especially for nitro-containing explosives. Two different ways were used to desorb neutral analytes from different targets. Both methods gave mass spectra with low background signal levels.

In summary, a sensitive and selective ionization method has been developed, which yields mass spectra that are easily interpretable, due to minimized ion transformation and fragmentation processes. An ion source that provides a constant ion current with time has been developed. An ionization in the negative ion mode was investigated and a reaction mechanism has been proposed. Examination of the ion transmission characteristics of inlet capillaries gave valuable insights into ion behavior in the capillaries and helped with the development of a stable ion source. Furthermore, different applications of the method were successfully demonstrated.

The field of ion transmission through capillaries needs further investigation and the applicability of the ion source in other fields should be demonstrated. The limit of detection obtained with this ion source or for GC coupling needs to be improved, by improving the number of photoelectrons generated and by use of a mass spectrometer that is capable of longer acquisition times. For the desorption of analytes from targets a suitable laser radiation source would help to improve the desorption efficiency and the spatial resolution.

Abbreviations

ΔG_{acid}	Gas-phase basicity
$\Delta_R G$	Gibbs free energy of a reaction
λ	Wavelength
ν	Frequency of light
Φ	Work function
m/z	Mass-to-charge ratio
2PPE	Two Photon Photoelectric Effect
3M2NP	3-methyl-2-nitrophenol
$[\text{M}+\text{H}]^+$	Protonated molecule
$[\text{M}-\text{H}]^-$	Deprotonated molecule
APCI	Atmospheric Pressure Chemical Ionization
API	Atmospheric Pressure Ionization
APLI	Atmospheric Pressure Laser Ionization
APPI	Atmospheric Pressure Photoionization
B3LYP	Becke-3-Parameter-Lee-Yang-Parr
BBO	Beta-Bariumborat
caPECI	capillary Atmospheric Pressure Electron Capture Ionization
caPPI	capillary Atmospheric Pressure Photoionization
CI	Chemical Ionization
CID	Collision Induced Dissociation
D/μ	Diffusion coefficient normalized to the ion mobility
DA-APPI	Dopant Assisted Atmospheric Pressure Photoionization
DAPECI	Desorption Atmospheric Pressure Electron Capture Ionization
DART	Direct Analysis in Real Time
DC	Direct Current
DFT	Density Functional Theory
DPSS	Diode Pumped Solid State
E	Electrical field strength
E_{electron}	Kinetic energy of an electron
E_{kin}	Kinetic energy
E/N	Reduced field strength
EA	Electron Affinity
ECD	Electron Capture Detector
EI	Electron Ionization
EIC	Extracted Ion Chromatogram

ESI	Electrospray Ionization
estd.	Estimated
eV	Electron Volts
FID	Flame Ionization Detector
FT-ICR	Fourier Transform Ion Cyclotron Resonance
FTIR	Fourier Transform Infrared Spectrometer
GC	Gas Chromatograph
h	Planck constant
HMX	High Molecular Weight RDX; 1,3,5,7-tetranitro-1,3,5,7-tetrazoctan
ID	Inner Diameter
IMS	Ion Mobility Spectrometry
IR	Infrared
LC	Liquid Chromatography
LED	Light Emitting Diode
LFIS	Laminar Flow Ion Source
LOD	Limit of Detection
M ⁺	Molecular radical cation
M ⁻	Molecular radical nion
MALDI	Matrix Assisted Laser Desorption/Ionization
MS	Mass Spectrometry
N	Molecular number density
N _A	Avogadros constant
Nd:YAG	Neodymium-doped Yttrium Aluminum Garnet
OPAH	Oxygenated Polycyclic Aromatic Hydrocarbons
OPO	Optical Parametrical Oszillator
PAH	Polycyclic Aromatic Hydrocarbons
PID	Proportional Integral Derivative
ppbV	Parts per billion by volume
ppmV	Parts per million by volume
pptV	Parts per trillion by volume
PTR	Proton Transfer Reaction
PVC	Polyvinyl Chloride
PVD	Physical Vapor Deposition
QIT	Quadrupole Ion Trap
R	Gas constant
RDX	Royal Demolition Explosive; 1,3,5-trinitro-1,3,5-triazacyclohexane
Ref.	References
RF	Radio Frequency
RS	Reaction Simulation
RT	Room Temperature
SDS	Statistical Diffusion Simulation
SHG	Second Harmonic Generation
TB	Third body reaction partner

8 Summary and Outlook

Td	Townsend
TIC	Total Ion Current
TOF	Time of Flight
UV	Ultraviolet
VUV	Vacuum Ultra Violet

List of Tables

3.1	Rate constants for neutral radical and electron capture reactions.	25
3.2	Adjusted gas flows and resulting oxygen mixing ratios.	41
3.3	Temperature programs for GC-cAPECI experiments.	54
6.1	Work functions of different metals at atmospheric pressure, measured in synthetic air (accuracy ± 0.05 eV).	124
6.2	Signal intensities at 266 nm for silver and aluminum for water and toluene on the metal surface.	129
6.3	Dependence of the signal intensity on the wavelength, the laser power density and the pathway of the laser beam.	132
6.4	Comparison of the different metals used as photoemissive materials in the cAPECI source design 1.	146
7.1	Assignment of the GC peaks in figure 7.1 and the corresponding chromatographic properties.	158
7.2	Assignment of the GC peaks in figure 7.4 and the corresponding chromatographic properties.	162
7.3	Observed product ion signals with the PTR-MS for the photo-oxidation study.	169

List of Figures

1.1	Comparison of the measured and calculated flow through an inlet capillary.	6
1.2	Calculated static pressure and velocity gradients along a capillary.	7
3.1	Schematic view of the ion transmission measurement setup.	27
3.2	Scheme of the ion transmission measurement setup.	28
3.3	Inlet capillaries made of different materials.	30
3.4	Schematic of the modular assembly of an inlet capillary.	31
3.5	Geometry used for the Comsol simulations of the entrance and outlet of an inlet capillary.	33
3.6	Analytical functions used to describe the potential on the capillary wall.	34
3.7	Schematic of the measurement setup to determine work functions at atmospheric pressure.	35
3.8	Schematic view of the custom designed inlet stage of the TOFWerk HTOF [7].	37
3.9	Schematic showing the two ionization positions; 5 ms position inside the LFIS and 1 ms position inside the inlet capillary.	40
3.10	Emission spectrum of the mercury Pen-Ray lamp.	42
3.11	Setup of the measurements with the LFIS.	44
3.12	Photograph of the silica inlet capillary.	45
3.13	Schematic view of the branched capillary.	46
3.14	Capillary ion source design 1 for cAPECI.	48
3.15	Insert of the cAPECI source design 1.	49
3.16	Aluminum insert with tungsten electrode as photoemissive material. . .	50
3.17	Picture of the aluminum target with a 2.5-fold increased capillary channel length.	50
3.18	Schematic setup and picture of the cAPECI source design 2.	51
3.19	Schematic setup of the cAPECI source design 2 with a longer transfer time.	52
3.20	Schematic setup of the cAPECI-GC coupling with custom built GC-transfer line and heated cAPECI source.	53
3.21	Schematic view of the PTR ion source and drift tube.	55
3.22	Schematic view of the experimental setups for the atmospheric chemistry experiments.	57
3.23	Schematic view of the desorption APECI source.	58

4.1	Calculated and measured proton bound water cluster distribution. . . .	60
4.2	Superoxide cluster distribution for different water mixing ratios.	63
4.3	Dependence of the normalized signal intensity on the water mixing ratio.	64
4.4	Extracted ion chromatogram for different water mixing ratios.	65
4.5	Influence of different water mixing ratios on the mass spectrum.	66
4.6	Calculated concentration profiles of O ₃ and OH.	67
4.7	Mass spectra of p-benzoquinone for different CID conditions.	68
4.8	Mass spectrum of p-benzoquinone when 0.2 % water is present in the ion source.	70
4.9	Mass spectrum of p-benzoquinone measured in ambient air.	71
4.10	Mass spectrum of 3-methyl-2-nitrophenol under CID free conditions.	72
4.11	Mass spectra of 3-methyl-2-nitrophenol for different extents of CID.	74
4.12	Mass spectrum of 3-methyl-2-nitrophenol recorded with the ion trap mass spectrometer.	75
4.13	Mass spectrum of 3-methyl-2-nitrophenol in laboratory air.	76
4.14	Mass spectra of 2,4-dinitrotoluene with different reaction times.	78
4.15	Measured signal intensities in dependence of the oxygen mixing ratio.	79
4.16	Calculated dependence of the signal intensities on the oxygen mixing ratio.	81
4.17	Mass spectrum of 2,4-dinitrotoluene when SF ₆ and oxygen are present.	82
5.1	Numerical simulation of the influence of a potential gradient on the ion motion at the entrance of an inlet capillary	88
5.2	Numerical simulation of the influence of a potential gradient on the ion motion at the outlet of an inlet capillary	89
5.3	Long term behavior of the lead oxide coated lead silicate glass capillary and the lead silicate glass capillary.	90
5.4	Continuous signal intensity-time profile for the blank out experiment shown in figure 5.3.	91
5.5	Close up view of the normalized initial signal peak with a standard glass capillary after different blank out times of the laser light.	92
5.6	Dependence of the integrated peak area of the initial signal peak on the laser blank out time period.	94
5.7	Determination of the pseudo-first order rate constant for different starting concentrations.	94
5.8	Determination of the second order rate constant by the pseudo-first order rate constants and the starting concentrations.	95
5.9	Buckled inlet capillary with a metal capillary piece between two glass capillary segments.	96
5.10	Ion transmission signal with time for different combinations of capillary segments compared to a standard glass capillary.	97

List of Figures

5.11 Normalized transmission curves with initial signal peak after different blank out times of the laser light with a metal capillary section between two glass capillary segments. 98

5.12 Normalized ion transmission-time profiles for different silica/metal capillary segments between two glass capillary segments. 100

5.13 Randomly occurring signal drop outs with an inlet capillary that consisted of a silica segment between two glass capillaries. 100

5.14 Intentionally caused signal drop outs. 101

5.15 Signal drop outs that occurred randomly with a TOF mass spectrometer equipped with a common glass capillary and APLI as ionization method. 102

5.16 Signal intensity-time profile of the cAPECI source design 1 recorded with the quadrupolar ion trap. 103

5.17 Ion transmission signals for laser ionization in front of the cAPECI source design 1 for different repetition rates. 104

5.18 Ion currents in dependence on the number of ions that passed through the capillary prior to the measurement caused by different repetition rates of the laser. 105

5.19 Dependence of cAPECI ion currents on the pretreatment of the inlet capillary by variation of the laser repetition rate. 106

5.20 Ion transmission intensity-time profiles for APLI, cAPECI and the simultaneous combination of both methods. 107

5.21 Dependence of the relative intensity of the laser signal and the signal of both laser and photoelectron generation on the repetition rate of the laser. 108

5.22 Dependence of the amplification of the negative cAPECI signal on the repetition rate of the laser for the generation of positive ions. 109

5.23 Dependence of the amplification of the positive ion signal by negative ion generation with cAPECI on the laser repetition rate. 109

5.24 Photoelectron transmission signal for different temperatures of the cAPECI source design 1. 111

5.25 Transmission signal of ions generated with APLI for different temperatures of the cAPECI source design 1. 111

5.26 Ion transmission-time profile in dependence of the humidity of the gas. 113

5.27 Negative TIC of a common glass capillary in dependence of the applied voltage to a metallic adaptor. 114

5.28 Dependence of the applied voltage to the total ion current. 115

5.29 Dependence of the ion current through an inlet capillary containing a silica segment on the applied voltage. 116

5.30 Dependence of the applied voltage to the negative ion current. 117

6.1 Overview about the ion sources developed during this work. 123

6.2 Photoelectron signal shapes under different pressures. 125

6.3 Photoelectron signals under different helium pressures. 127

6.4 Photocurrent signal shapes for different acceleration voltages. 128

6.5	Dependence of the measured work function threshold on the laser power density for copper and gold.	130
6.6	Dependence of the integrated peak area on the laser power density for two wavelengths.	133
6.7	Measured ozone mixing ratio in dependence of the oxygen mixing ratio inside the cAPECI source design 2.	135
6.8	Intensity of the 185 nm emission line of the Pen-Ray-UV lamp with time.	137
6.9	Emission intensity-time profile of the 185 nm line when the lamp is switched off for 80 min and 160 min.	138
6.10	Emission intensity-time profile when the power supply to the photo multiplier of the VUV spectrometer was switched off for different time periods.	138
6.11	Emission intensity of the 365 nm line with time, recorded with a photodiode.	139
6.12	Mass spectrum of 2-nitrophenol in synthetic air with ionization by photoelectron generation inside the laminar flow ion source.	140
6.13	Mass spectrum of 2-nitrophenol in synthetic air when ionization takes place upstream inside the LFIS.	141
6.14	Mass spectrum of sulfur hexafluoride in nitrogen obtained with photoelectron generation from a copper coated silica window.	142
6.15	Mass spectrum of sulfur hexafluoride in synthetic air obtained with ionization within the partially silver-plated silica capillary.	143
6.16	Measured ion current along the silica capillary axis.	144
6.17	Decreasing signal intensity with time for ionization within the partially silver-plated silica capillary.	145
6.18	Comparison of mass spectra obtained with different capillary channel length.	148
6.19	Total ion current for a first measurement of a day.	149
6.20	Temporal evolution of the signal intensity for a measurement with constant conditions with the cAPECI design 2.	151
6.21	Mass spectrum of 3-methyl-2-nitrophenol obtained with the cAPECI source design 2 measured in synthetic air.	151
6.22	Mass spectrum of 3-methyl-2-nitrophenol obtained with a cAPECI source design 2 with a longer reaction time.	152
6.23	Influence of a decreased oxygen mixing ratio on the mass spectrum of the cAPECI source design 2.	153
6.24	Dependence of the observed signal intensities obtained with the cAPECI source design 2, on the oxygen mixing ratio.	153
7.1	GC-cAPECI-MS chromatogram of a mixture of six compounds dissolved in hexane.	157
7.2	Mass spectrum of the same mixture as in figure 7.1, but without chromatographic separation.	159

List of Figures

7.3	Determination of the linear range of the GC-cAPECI-MS setup version 1 for 2-nitrophenol.	160
7.4	GC-cAPECI-MS chromatogram of a certified nitro-aromatic explosives mix of seven compounds.	160
7.5	Determination of the linear range of 2,4,6-trinitrotoluene detection with the second GC-cAPECI-MS setup.	161
7.6	Signal peaks of 2-nitrophenol for two different temperatures of the GC transfer line.	163
7.7	Mass spectra of 2-nitrophenol recorded simultaneously with a) cAPECI ion trap (negative ion mode) and b) PTR-TOF-MS (positive ion mode).	165
7.8	Mass spectra of 2-nitro-isopropylbenzene recorded simultaneously with a) cAPECI-ion trap (negative ion mode) and b) PTR-TOF-MS (positive ion mode).	166
7.9	cAPECI mass spectra before and after the photo-oxidation study started.	167
7.10	Extracted ion chromatograms for cAPECI for the analyte precursor and the two reaction products.	169
7.11	PTR mass spectra prior to and after the photo-oxidation study was started.	170
7.12	Proposed structure of the product ion in the photo-oxidation study.	171
7.13	Schematic of the cAPECI ion source design 1 for the kinetic experiments.	172
7.14	Dependence of the signal intensity on the analyte mixing ratio.	175
7.15	Monte Carlo simulation of the concentration profiles of superoxide and the reaction product.	177
7.16	Desorption mass spectra with cAPECI.	179
7.17	DAPECI measurements of anthraquinone (upper panel) and 1,3,5-trinitrotoluene (lower panel) in ambient air.	180

References

- [1] S. A. McLuckey and M. Mentinova. Ion/neutral, ion/electron, ion/photon, and ion/ion interactions in tandem mass spectrometry: do we need them all? Are they enough? *Journal of the American Society for Mass Spectrometry*, 22(1):3–12, 2011.
- [2] P. B. Armentrout, editor. *Encyclopedia of Mass Spectrometry Volume 1 Theory and Ion Chemistry*. Elsevier, Oxford, Great Britain, 1st ed., 2006.
- [3] H. Kersten, V. Funcke, M. Lorenz, K. J. Brockmann, T. Benter, and R. O'Brien. Evidence of Neutral Radical Induced Analyte Ion Transformations in APPI and Near-VUV APLI. *Journal of the American Society for Mass Spectrometry*, 20(10):1868–1880, 2009.
- [4] P. B. Armentrout. Collision-induced Dissociation. In P. B. Armentrout, editor, *Encyclopedia of Mass Spectrometry Volume 1*, pp. 426–434. Elsevier, Oxford, Great Britain, 1st ed., 2006.
- [5] J. M. Wells and S. A. McLuckey. Methodology. In M. L. Gross and R. M. Caprioli, editors, *Encyclopedia of Mass Spectrometry Volume 12*, pp. 441–451. Elsevier, Oxford, Great Britain, 1st ed., 2006.
- [6] L. Sleno and D. A. Volmer. Ion activation methods for tandem mass spectrometry. *Journal of Mass Spectrometry*, 39(10):1091–112, 2004.
- [7] V. Derpmann, S. Albrecht, and T. Benter. The role of ion-bound cluster formation in negative ion mass spectrometry. *Rapid Communications in Mass Spectrometry*, 26(17):1923–1933, 2012.
- [8] Z. Karpas, G. A. Eiceman, R. G. Ewing, and C. S. Harden. Collision induced dissociation studies of protonated alcohol and alcohol–water clusters by atmospheric pressure ionization tandem mass spectrometry.: Part 2. Ethanol, propanol and butanol. *International Journal of Mass Spectrometry and Ion Processes*, 133(1):47–58, 1994.
- [9] J. Yinon, D. Fraise, and I. J. Dagley. Electron impact, chemical ionization and negative chemical ionization mass spectra, and mass-analysed ion kinetic energy spectrometry–collision-induced dissociation fragmentation pathways of some deuterated 2,4,6-trinitrotoluene (TNT) derivatives. *Organic Mass Spectrometry*, 26(10):867–874, 1991.
- [10] Y. Song and R. G. Cooks. Atmospheric pressure ion/molecule reactions for the selective detection of nitroaromatic explosives using acetonitrile and air as reagents. *Rapid Communications in Mass Spectrometry*, 20(20):3130–3138, 2006.
- [11] R. B. Cody, R. C. Burnier, and B. S. Freiser. Collision-Induced Dissociation with Fourier Transform Mass Spectrometry. *Analytical Chemistry*, 54(24):96–101, 1982.

References

- [12] P. Kebarle. Ion-Molecule Equilibria at High Pressure. In P. B. Armentrout, editor, *Encyclopedia of Mass Spectrometry Volume 1*, pp. 319–337. Elsevier, Oxford, Great Britain, 1 ed., 2006.
- [13] E. W. McDaniel, V. Cermak, A. Dalgarno, E. E. Ferguson, and L. Friedman. *Ion Molecule Reactions*. Wiley-Interscience, Michigan, 1970.
- [14] T. R. Covey, B. A. Thomson, and B. B. Schneider. Atmospheric pressure ion sources. *Mass Spectrometry Reviews*, 28(6):870–897, 2009.
- [15] S. K. Panda, K.-J. Brockmann, T. Benter, and W. Schrader. Atmospheric pressure laser ionization (APLI) coupled with Fourier transform ion cyclotron resonance mass spectrometry applied to petroleum samples analysis: comparison with electrospray ionization and atmospheric pressure photoionization methods. *Rapid Communications in Mass Spectrometry*, 25(16):2317–26, 2011.
- [16] P. P. Wickramanayake, G. J. Gardner, K. W. Michael Siu, and S. S. Berman. Ion/molecule reaction between sulphur hexafluoride negative ion and water under atmospheric pressure ionization mass spectrometric conditions. *International Journal of Mass Spectrometry and Ion Processes*, 69(1):39–43, 1986.
- [17] N. G. Adams, L. M. Babcock, and C. D. Molek. Ion-Ion Recombination. In P. B. Armentrout, editor, *Encyclopedia of Mass Spectrometry Volume 1*, pp. 555–562. Elsevier, Oxford, Great Britain, 1st ed., 2006.
- [18] N. G. Adams, L. M. Babcock, and J. L. McLain. Electron-Ion Recombination. In P. B. Armentrout, editor, *Encyclopedia of Mass Spectrometry Volume 1*, pp. 542–555. Elsevier, Oxford, Great Britain, 1st ed., 2006.
- [19] P. Begley, R. Corbin, B. E. Foulger, and P. G. Simmonds. Photoemissive ionisation source for ion mobility detectors. *Journal of Chromatography A*, 588(1-2):239–249, 1991.
- [20] A. P. Bruins. Mass spectrometry with ion sources operating at atmospheric pressure. *Mass Spectrometry Reviews*, 10(1):53–77, 1991.
- [21] M. Meot-Ner. The Ionic Hydrogen Bond: Clusters and Ion Solvation. In P. B. Armentrout, editor, *Encyclopedia of Mass Spectrometry Volume 1*, pp. 687–702. Elsevier, Oxford, Great Britain, 1st ed., 2006.
- [22] E. de Hoffmann and V. Stroobant. *Mass Spectrometry Principles and Applications*. John Wiley & Sons, Ltd, Hoboken, NJ, USA, 3rd ed., 2007.
- [23] T. Poehler, R. Kunte, H. Hoenen, P. Jeschke, W. Wissdorf, K. J. Brockmann, and T. Benter. Numerical simulation and experimental validation of the three-dimensional flow field and relative analyte concentration distribution in an atmospheric pressure ion source. *Journal of the American Society for Mass Spectrometry*, 22(11):2061–9, 2011.
- [24] W. M. A. Nissen. *Liquid Chromatography-Mass Spectrometry*. Marcel Dekker, Inc., New York, NY, USA, 2nd ed., 1999.
- [25] A. P. Bruins and D. K. Cook. Electrospray Ionization: Principles and Instrumentation. In M. L. Gross and R. M. Caprioli, editors, *Encyclopedia of Mass Spectrometry Volume 6*, pp. 415–422. Elsevier, Oxford, Great Britain, 2007.
- [26] W. Wissdorf. *Simulation of ion dynamics in atmospheric pressure ionization sources*. Ph.D. thesis, University of Wuppertal, Germany, 2014.

References

- [27] I. Barnes, H. Kersten, W. Wissdorf, T. Pöhler, H. Hönen, S. Klee, K. J. Brockmann, and T. Benter. Novel Laminar Flow Ion Source for LC- and GC-API MS. In *Proceedings of the 58th ASMS Conference on Mass Spectrometry and Allied Topics*. Salt Lake City, UT, USA, 2010.
- [28] F. G. Kitson, B. S. Larsen, and C. N. McEwen. *Gas Chromatography and Mass Spectrometry A Practical Guide*. Academic Press, San Diego, CA, USA, 1996.
- [29] Y. Brachthaeuser, S. Klee, D. Klink, M. Thinius, K. Brockmann, and T. Benter. GC-MS Performance of a Novel Capillary Atmospheric Pressure Chemical Ionization (cAPCI) Source. In *Proceedings of the 61th ASMS Conference on Mass Spectrometry and Allied Topics*. Minneapolis, MN, USA, 2013.
- [30] W. Lindinger, A. Hansel, and A. Jordan. On-line monitoring of volatile organic compounds at pptv levels by means of proton-transfer-reaction mass spectrometry (PTR-MS) medical applications, food control and environmental research. *International Journal of Mass Spectrometry and Ion Processes*, 173(3):191–241, 1998.
- [31] M. Graus, M. Müller, and A. Hansel. High resolution PTR-TOF: Quantification and formula confirmation of VOC in real time. *Journal of The American Society for Mass Spectrometry*, 21(6):1037–1044, 2010.
- [32] S. Jürschik, P. Sulzer, F. Petersson, C. Mayhew, A. Jordan, B. Agarwal, S. Haidacher, H. Seehauser, K. Becker, and T. Märk. Proton transfer reaction mass spectrometry for the sensitive and rapid real-time detection of solid high explosives in air and water. *Analytical and Bioanalytical Chemistry*, 398(7):2813–2820, 2010.
- [33] R. Brdicka. *Grundlagen der physikalischen Chemie*. VEB Deutscher Verlag der Wissenschaften, Berlin, Germany, 15th ed., 1982.
- [34] H. Kambara and I. Kanomata. Determination of impurities in gases by atmospheric pressure ionization mass spectrometry. *Analytical Chemistry*, 49(2):270–275, 1977.
- [35] A. Uphoff and J. Grottemeyer. TOF and RTOF. In P. B. Armentrout, editor, *The Encyclopedia of Mass Spectrometry Volume 1*, pp. 121–130. Elsevier, Oxford, Great Britain, 1st ed., 2006.
- [36] A. G. Marshall. Fourier Transform Ion Cyclotron Resonance. In P. B. Armentrout, editor, *The Encyclopedia of Mass Spectrometry Volume 1*, pp. 131–143. Elsevier, Oxford, Great Britain, 1st ed., 2006.
- [37] R. E. March. Ion traps. In P. B. Armentrout, editor, *Encyclopedia of Mass Spectrometry Volume 1*, pp. 144–157. Elsevier, Oxford, Great Britain, 1st ed., 2006.
- [38] H. Kersten. *Development of an Atmospheric Pressure Ionization source for in situ monitoring of degradation products of atmospherically relevant volatile organic compounds*. Ph.D. thesis, University of Wuppertal, Germany, Wuppertal, 2011.
- [39] H. Rohrs, M. L. Gross, and M. Moini. Atmospheric Pressure Chemical Ionization: Principles, Instrumentation and Application. In M. L. Gross and R. M. Caprioli, editors, *Encyclopedia of Mass Spectrometry Volume 6*, pp. 344–354. Elsevier, Oxford, Great Britain, 1st ed., 2007.
- [40] A. Raffaelli and A. Saba. Atmospheric Pressure Photoionization: Basic Principles. In M. L. Gross and R. M. Caprioli, editors, *The Encyclopedia of Mass Spectrometry Volume 6 Ionization Methods*, pp. 219–223. Elsevier, Oxford, Great Britain, 1st ed., 2007.

References

- [41] T. J. Kauppila and R. Kostiainen. Dopant Assisted Atmospheric Pressure Photoionization. In M. L. Gross and R. M. Caprioli, editors, *The Encyclopedia of Mass Spectrometry Volume 6 Ionization Methods*, pp. 223–229. Elsevier, Oxford, Great Britain, 1st ed., 2007.
- [42] T. J. Kauppila. *Atmospheric pressure photoionization mass spectrometry*. Ph.D. thesis, University of Helsinki, Helsinki, Finland, 2004.
- [43] I. Orlandini and U. Riedel. Chemical kinetics of NO removal by pulsed corona discharges. *Journal of Physics D: Applied Physics*, 33(19):2467–2474, 2000.
- [44] M. Sabo, J. Páleník, M. Kučera, H. Han, H. Wang, Y. Chu, and v. Matejčík. Atmospheric Pressure Corona Discharge Ionisation and Ion Mobility Spectrometry/Mass Spectrometry study of the negative corona discharge in high purity oxygen and oxygen/nitrogen mixtures. *International Journal of Mass Spectrometry*, 293(1-3):23–27, 2010.
- [45] K. Sekimoto, M. Sakai, and M. Takayama. Specific Interaction Between Negative Atmospheric Ions and Organic Compounds in Atmospheric Pressure Corona Discharge Ionization Mass Spectrometry. *Journal of The American Society for Mass Spectrometry*, 23(6):1109–1119, 2012.
- [46] M. Lorenz, W. Wissdorf, S. Klee, H. Kersten, K. J. Brockmann, and T. Benter. Ion Transport Processes in API Sources: Temporally and Spatially Resolved APLI Measurements. In *Proceedings of the 57th ASMS Conference on Mass Spectrometry and Allied Topics*. Philadelphia, PA, USA, 2009.
- [47] M. Lorenz. *Räumlich und zeitlich aufgelöste Photoionisierung als Werkzeug zur Charakterisierung von Atmosphärendruckionenquellen in der Massenspektrometrie*. Ph.D. thesis, University of Wuppertal, Wuppertal, Germany, 2010.
- [48] G. Gioumousis and D. P. Stevenson. Reactions of Gaseous Molecule Ions with Gaseous Molecules. V. Theory. *The Journal of Chemical Physics*, 29(2):294, 1958.
- [49] B. R. Eichelberger, T. P. Snow, and V. M. Bierbaum. Collision rate constants for polarizable ions. *Journal of the American Society for Mass Spectrometry*, 14(5):501–5, 2003.
- [50] V. G. Anicich. *An Index of the Literature for Bimolecular Gas Phase Cation-Molecule Reaction Kinetics*. JPL Publication, Pasadena, California, 2003.
- [51] V. Le Page, Y. Keheyian, T. P. Snow, and V. M. Bierbaum. Gas phase chemistry of pyrene and related cations with molecules and atoms of interstellar interest. *International Journal of Mass Spectrometry*, 185-187:949–959, 1999.
- [52] D. I. Carroll, I. Dzidic, E. C. Horning, and R. N. Stillwell. Atmospheric Pressure Ionization Mass Spectrometry. *Applied Spectroscopy Reviews*, 17(3):337–406, 1981.
- [53] N. H. Mahle, R. G. Cooks, and R. W. Korzeniowski. Hydroxylation of Aromatic Hydrocarbons in Mass Spectrometer Ion Sources under Atmospheric Pressure Ionization and Chemical Ionization Conditions. *Analytical Chemistry*, 2275(17):2272–2275, 1983.
- [54] D. B. Robb and M. W. Blades. Effects of Solvent Flow, Dopant Flow, and Lamp Current on Dopant-Assisted Atmospheric Pressure Photoionization (DA-APPI) for LC-MS. Ionization via Proton Transfer. *Journal of the American Society for Mass Spectrometry*, 16(8):1275–1290, 2005.

References

- [55] T. J. Kauppila, T. Kuuranne, E. C. Meurer, M. N. Eberlin, T. Kotiaho, and R. Kostianen. Atmospheric pressure photoionization mass spectrometry. Ionization mechanism and the effect of solvent on the ionization of naphthalenes. *Analytical chemistry*, 74(21):5470–9, 2002.
- [56] S. Klee, S. Albrecht, V. Derpmann, H. Kersten, and T. Benter. Generation of ion-bound solvent clusters as reactant ions in dopant-assisted APPI and APLI. *Analytical and Bioanalytical chemistry*, 405(22):6933–51, 2013.
- [57] P. Kebarle, S. K. Searles, A. Zolla, J. Scarborough, and M. Arshadi. Solvation of the hydrogen ion by water molecules in the gas phase. Heats and entropies of solvation of individual reactions. $H+(H_2O)_{n-1} + H_2O \rightarrow H+(H_2O)_n$. *Journal of the American Chemical Society*, 89(25):6393–6399, 1967.
- [58] A. Good, D. A. Durden, and P. Kebarle. Ion–Molecule Reactions in Pure Nitrogen and Nitrogen Containing Traces of Water at Total Pressures 0.5–4 torr. Kinetics of Clustering Reactions Forming $H+(H_2O)_n$. *The Journal of Chemical Physics*, 52(1):212–221, 1970.
- [59] J. Sunner, G. Nicol, and P. Kebarle. Factors determining relative sensitivity of analytes in positive mode atmospheric pressure ionization mass spectrometry. *Analytical Chemistry*, 60(13):1300–1307, 1988.
- [60] D. R. Zook and E. P. Grimsrud. Measurement of ion clustering equilibria of proton hydrates by atmospheric pressure ionization mass spectrometry. *The Journal of Physical Chemistry*, 92(22):6374–6379, 1988.
- [61] J. Q. Searcy. Clustering of water on hydrated protons in a supersonic free jet expansion. *The Journal of Chemical Physics*, 61(12):4114, 1974.
- [62] H. Furuya, S. Fujimaki, S. Kambara, S. Suzuki, Y. Hashimoto, S. Okazaki, A. Wada, I. B. Beech, J. Sunner, and K. Hiraoka. Ion/molecule reactions in the orifice-skimmer region of an atmospheric pressure Penning ionization mass spectrometer. *Rapid Communications in Mass Spectrometry*, 19(17):2433–2442, 2005.
- [63] H. Kambara and I. Kanomata. Collision-induced dissociation of water cluster ions at high pressure. *International Journal of Mass Spectrometry and Ion Physics*, 25(2):129–136, 1977.
- [64] P. H. Dawson. The collision-induced dissociation of protonated water clusters studied using a triple quadrupole. *International Journal of Mass Spectrometry and Ion Physics*, 43(2-3):195–209, 1982.
- [65] W. Wissdorf, L. Seifert, V. Derpmann, S. Klee, W. Vautz, and T. Benter. Monte Carlo simulation of ion trajectories of reacting chemical systems: mobility of small water clusters in ion mobility spectrometry. *Journal of the American Society for Mass Spectrometry*, 24(4):632–41, 2013.
- [66] D. I. Carroll, I. Dzidic, R. N. Stillwell, and E. C. Horning. Identification of positive reactant ions observed for nitrogen carrier gas in plasma chromatograph mobility studies. *Analytical Chemistry*, 47(12):1956–1959, 1975.
- [67] F. W. Karasek, S. H. Kim, and H. H. Hill. Mass identified mobility spectra of p-nitrophenol and reactant ions in plasma chromatography. *Analytical Chemistry*, 48(8):1133–1137, 1976.

References

- [68] M. A. Bairn, R. L. Eatherton, and H. H. Hill. Ion Mobility Detector for Gas Chromatography with a Direct Photoionization Source. *Analytical Chemistry*, 55:1761–1766, 1983.
- [69] G. Scoles, D. Bassi, U. Buck, and D. C. Laine, editors. *Atomic and molecular beam methods Volume 1*. Oxford University Press, New York, NY, USA, 1988.
- [70] T. Imasaka, D. S. Moore, and T. Vo-Dinh. Critical assessment: Use of supersonic jet spectrometry for complex mixture analysis (IUPAC Technical Report). *Pure and Applied Chemistry*, 75(7):975–998, 2003.
- [71] S. König and H. M. Fales. Formation and decomposition of water clusters as observed in a triple quadrupole mass spectrometer. *Journal of the American Society for Mass Spectrometry*, 9(8):814–822, 1998.
- [72] X. Yang and A. W. Castleman. Large protonated water clusters $H+(H_2O)_n$ ($n > 60$): the production and reactivity of clathrate-like structures under thermal conditions. *Journal of the American Chemical Society*, 111(17):6845–6846, 1989.
- [73] K. J. Brockmann, W. Wissdorf, L. Hyzak, H. Kersten, D. Mueller, Y. Brachthaeuser, and T. Benter. Fundamental characterization of Ion Transfer Capillaries used in Atmospheric Pressure Ionization Sourced. In *Proceedings of the 58th ASMS Conference on Mass Spectrometry and Allied Topics*. Salt Lake City, UT, USA, 2010.
- [74] H. Kersten, V. Derpmann, I. Barnes, K. Brockmann, R. O'Brien, and T. Benter. A Novel APPI-MS Setup for In Situ Degradation Product Studies of Atmospherically Relevant Compounds: Capillary Atmospheric Pressure Photo Ionization (cAPPI). *Journal of the American Society for Mass Spectrometry*, 22(11):2070–2081, 2011.
- [75] C. M. Whitehouse. Personal Communication, 2010.
- [76] B. Lin and J. Sunner. Ion transport by viscous gas flow through capillaries. *Journal of the American Society for Mass Spectrometry*, 5(10):873–885, 1994.
- [77] C. M. Whitehouse, R. N. Dreyer, M. Yamashita, and J. B. Fenn. Electrospray interface for liquid chromatographs and mass spectrometers. *Analytical Chemistry*, 57(3):675–679, 1985.
- [78] A. Michalke. Beitrag zur Rohrströmung kompressibler Fluide mit Reibung und Wärmeübergang. *Archive of Applied Mechanics*, 57(5):377–392, 1987.
- [79] H. Zobl. *Strömung durch Rohre und Ventile*. Springer, Wien, New York, 2nd ed., 1982.
- [80] M. Wutz, H. Adam, and W. Walcher, editors. *Theorie und Praxis der Vakuumtechnik*. Friedr. Vieweg und Sohn, Braunschweig/Wiesbaden, Germany, 4th ed., 1988.
- [81] D. Mueller. *Untersuchung zur Ionentransmission bei cAPECI -capillary Atmospheric Pressure Electron Capture Ionization-*. Master-Thesis, University of Wuppertal, Wuppertal, Germany, 2013.
- [82] V. Derpmann, D. Mueller, I. Bejan, H. Sonderfeld, S. Wilberscheid, R. Koppmann, K. J. Brockmann, and T. Benter. Capillary atmospheric pressure electron capture ionization (cAPECI): a highly efficient ionization method for nitroaromatic compounds. *Journal of the American Society for Mass Spectrometry*, 25(3):329–42, 2014.
- [83] L. Clancy. *Aerodynamics*. John Wiley & Sons, Inc., Hoboken, NJ, USA, 1975.

- [84] D. Mueller, V. Derpmann, and T. Benter. Charging Effects in Ion Transfer Capillaries: an In-Depth Study. In *Proceedings of the 61th ASMS Conference on Mass Spectrometry and Allied Topics*. Minneapolis, MN, USA, 2013.
- [85] S. Klopotoski, Y. Brachthaeuser, D. Mueller, H. Kersten, W. Wissdorf, K. Brockmann, and T. Benter. Characterization of API-MS Inlet Capillary Flow: Examination of Transfer Times and Choked Flow Conditions. In *Proceedings of the 60th ASMS Conference on Mass Spectrometry and Allied Topics*. Vancouver, BC, Kanada, 2012.
- [86] S. Klee, M. Thinius, V. Derpmann, W. Wissdorf, S. Klopotoski, K. Brockmann, and T. Benter. A Novel Corona Discharge Source with Liquid Point Electrodes. In *Proceedings of the 61th ASMS Conference on Mass Spectrometry and Allied Topics*. Minneapolis, MN, USA, 2013.
- [87] T. Benter, S. Klee, V. Derpmann, H. Kersten, W. Wissdorf, D. Mueller, Y. Brachthaeuser, S. Klopotoski, and K.-J. Brockmann. Progress in the development of capillary Atmospheric Pressure Ionization Methods (cAPI). In *Proceedings of the 61st ASMS Conference on Mass Spectrometry and Allied Topics*. Minneapolis, MN, USA, 2013.
- [88] L. Thiesan, D. Hannum, D. W. Murray, and J. E. Parmeter. Survey of Commercially Available Explosives Detection Technologies and Equipment 2004. Technical report, NIJ Grant Report, 2005.
- [89] L. Song, A. D. Wellman, H. Yao, and J. E. Bartmess. Negative Ion-Atmospheric Pressure Photoionization: Electron Capture, Dissociative Electron Capture, Proton Transfer, and Anion Attachment. *Journal of the American Society for Mass Spectrometry*, 18(10):1789–1798, 2007.
- [90] J. E. Bartmess. Electron Affinities. In M. L. Gross and R. M. Caprioli, editors, *Encyclopedia of Mass Spectrometry Volume 6*, pp. 27–34. Elsevier, Oxford, Great Britain, 1st ed., 2007.
- [91] G. E. Caledonia, A. Everett, A. Corporation, B. Diatomics, L. Molecules, D. Attachment, and B. Triatomic. A Survey of the Gas-Phase Negative Ion Kinetics of Inorganic Molecules. Electron Attachment Reactions. *Chemical Reviews*, 75(3):333–351, 1975.
- [92] T. Jaffke, M. Meinke, R. Hashemi, L. G. Christophorou, and E. Illenberger. Dissociative electron attachment to singlet oxygen. *Chemical Physics Letters*, 193(1-3):62–68, 1992.
- [93] E. C. M. Chen, L.-R. Shuie, E. Desai D'sa, C. F. Batten, W. E. Wentworth, and E. D. D'sa. The negative ion states of sulfur hexafluoride. *The Journal of Chemical Physics*, 88(8):4711–4719, 1988.
- [94] A. Chutjian, A. Garscadden, and J. M. Wadehra. Electron attachment to molecules at low electron energies. *Physics Reports*, 264(6):393–470, 1996.
- [95] L. G. Christophorou. Free electrons: fundamental interactions, applications and data needs. *Nukleonika*, 48:67–74, 2003.
- [96] R. V. Khatymov, M. V. Muftakhov, and V. A. Mazunov. Phenol, chlorobenzene and chlorophenol isomers: resonant states and dissociative electron attachment. *Rapid Communications in Mass Spectrometry*, 17(20):2327–2336, 2003.
- [97] R. N. Compton, L. G. Christophorou, G. S. Hurst, and P. W. Reinhardt. Dissociative Electron Capture by Benzene Derivatives. *The Journal of Chemical Physics*, 45(2):536–547, 1966.

References

- [98] P. Cicman, M. Francis, J. D. Skalny, S. Matejcek, and T. D. Maerk. The Rate Constant for Dissociative Electron Attachment to Ozone Revisited. *Czechoslovak Journal of Physics*, 53(3):181–190, 2003.
- [99] G. Senn, J. D. Skalny, A. Stamatovic, N. J. Mason, P. Scheier, and T. D. Maerk. Low Energy Dissociative Electron Attachment to Ozone. *Physical Review Letters*, 82(25):5028, 1999.
- [100] L. G. Christophorou and J. K. Olthoff. Electron attachment cross sections and negative ion states of SF₆. *International Journal of Mass Spectrometry*, 205(1-3):27–41, 2001.
- [101] D. Lide, editor. *CRC Handbook of Chemistry and Physics*. CRC Press, Boca Raton, FL, USA, 88th ed., 2007.
- [102] H. Shimamori and R. W. Fessenden. Thermal electron attachment to oxygen and van der Waals molecules containing oxygen. *The Journal of Chemical Physics*, 74(1):453, 1981.
- [103] I. Dzidic, D. I. Carroll, R. N. Stillwell, and E. C. Horning. Gas phase reactions. Ionization by proton transfer to superoxide anions. *Journal of the American Chemical Society*, 96(16):5258–5259, 1974.
- [104] M. J. F. Asselin and J. J. R. Paré. Atmospheric pressure chemical ionization negative mass spectra of the dinitrotoluene isomers. *Organic Mass Spectrometry*, 16(6):275–278, 1981.
- [105] C. J. Proctor and J. F. J. Todd. Atmospheric pressure ionization mass spectrometry. *Organic Mass Spectrometry*, 18(12):509–516, 1983.
- [106] T. J. Kauppila, T. Kotiaho, R. Kostianen, and A. P. Bruins. Negative ion-atmospheric pressure photoionization-mass spectrometry. *Journal of the American Society for Mass Spectrometry*, 15(2):203–211, 2004.
- [107] A. Riu, D. Zalko, and L. Debrauwer. Study of polybrominated diphenyl ethers using both positive and negative atmospheric pressure photoionization and tandem mass spectrometry. *Rapid Communications in Mass Spectrometry*, 20(14):2133–42, 2006.
- [108] L. Debrauwer, A. Riu, M. Jouahri, E. Rathahao, I. Jouanin, J.-P. Antignac, R. Cariou, B. Le Bizec, and D. Zalko. Probing new approaches using atmospheric pressure photo ionization for the analysis of brominated flame retardants and their related degradation products by liquid chromatography–mass spectrometry. *Journal of Chromatography A*, 1082(1):98–109, 2005.
- [109] Y.-J. Jhong and W.-H. Ding. Method optimization for quantitation of decabromodiphenyl ether in sediments and earthworms using liquid chromatography/atmospheric pressure photoionization tandem mass spectrometry. *Rapid Communications in Mass Spectrometry*, 21(24):4158–61, 2007.
- [110] K. A. Daum, D. A. Atkinson, and R. G. Ewing. Formation of halide reactant ions and effects of excess reagent chemical on the ionization of TNT in ion mobility spectrometry. *Talanta*, 55(3):491–500, 2001.
- [111] A. Lawrence, P. Neudorfl, and J. A. Stone. The formation of chloride adducts in the detection of dinitro-compounds by ion mobility spectrometry. *International Journal of Mass Spectrometry*, 209:185–195, 2001.
- [112] A. A. Viggiano, F. Dale, and J. F. Paulson. Proton transfer reactions of H⁺(H₂O)_{n=2–11} with methanol, ammonia, pyridine, acetonitrile, and acetone. *The Journal of Chemical Physics*, 88(4):2469, 1988.

References

- [113] A. J. Midey, S. Williams, S. T. Arnold, and A. A. Viggiano. Reactions of $\text{H}_3\text{O}^+ + (\text{H}_2\text{O})_0,1$ with Alkylbenzenes from 298 to 1200 K. *The Journal of Physical Chemistry A*, 106(48):11726–11738, 2002.
- [114] N. G. Adams. Flowing Afterglow Studies of Formation and Reactions of Cluster Ions of O_2^- , O_2^+ , and O^- . *The Journal of Chemical Physics*, 52(6):3133, 1970.
- [115] C.-W. Liang, Y. T. Lee, C.-H. Chen, and Y.-S. Wang. Ionizing nonvolatile samples using laser desorption-proton-transfer reaction with cluster reagent ions. *International Journal of Mass Spectrometry*, 291(1-2):61–66, 2010.
- [116] C. N. McEwen and B. S. Larsen. Ionization Mechanisms Related to Negative Ion APPI, APCI, and DART. *Journal of The American Society for Mass Spectrometry*, 20(8):1518–1521, 2009.
- [117] E. C. Horning, D. I. Carroll, I. Dzidic, S. N. Lin, R. N. Stillwell, and J. P. Thenot. Atmospheric pressure ionization mass spectrometry: Studies of negative ion formation for detection and quantification purposes. *Journal of Chromatography A*, 142:481–495, 1977.
- [118] G. E. Spangler and C. I. Collins. Reactant ions in negative ion plasma chromatography. *Analytical Chemistry*, 47(3):393–402, 1975.
- [119] L. C. Short, R. G. Ewing, and C. J. Barinaga. Photoemission ambient pressure ionization (PAPI) with an ultraviolet light emitting diode and detection of organic compounds. *Rapid Communications in Mass Spectrometry*, 25(19):2888–2896, 2011.
- [120] P. Watts. Studies on gas-phase negative ion/molecule reactions of relevance to ion mobility spectrometry: kinetic modelling of the reactions occurring in "clean" air. *International Journal of Mass Spectrometry and Ion Processes*, 121(1-2):141–158, 1992.
- [121] J. A. Syage, K. A. Hanold, M. D. Evans, and Y. Liu. Atmospheric pressure photoionizer for mass spectrometry. (US6630664 B1).
- [122] J. A. Syage, K. A. Hanold, T. C. Lynn, J. A. Horner, and R. A. Thakur. Atmospheric pressure photoionization: II. Dual source ionization. *Journal of Chromatography A*, 1050(2):137–149, 2004.
- [123] G. Singh, A. Gutierrez, K. Xu, I. A. Blair, D. B. Robb, T. R. Covey, A. P. Bruins, R. A. Zubarev, D. M. Horn, E. K. Fridriksson, N. L. Kelleher, N. A. Kruger, M. A. Lewis, B. K. Carpenter, and F. W. McLafferty. Atmospheric Pressure Photoionization: An Ionization Method for Liquid Chromatography-Mass Spectrometry. *Analytical Chemistry*, 72(15):3653–3659, 2000.
- [124] D. B. Robb and A. P. Bruins. Atmospheric pressure photoionization (APPI): A new ionization method for liquid chromatography. (WO20010336).
- [125] A. Raffaelli and A. Saba. Atmospheric pressure photoionization mass spectrometry. *Mass Spectrometry Reviews*, 22(5):318–331, 2003.
- [126] T. Benter. Atmospheric Pressure Laser Ionization. In M. L. Gross and R. M. Caprioli, editors, *Encyclopedia of Mass Spectrometry Volume 6*, pp. 251–258. Elsevier, Oxford, Great Britain, 1st ed., 2007.

References

- [127] B.-M. Cheng, M. Bahou, W.-C. Chen, C.-h. Yui, Y.-P. Lee, and L. C. Lee. Experimental and theoretical studies on vacuum ultraviolet absorption cross sections and photodissociation of CH₃OH, CH₃OD, CDOH, and CD₃OD. *The Journal of Chemical Physics*, 117(4):1633, 2002.
- [128] K. Kanda, T. Nagata, and T. Ibuki. Photodissociation of some simple nitriles in the extreme vacuum ultraviolet region. *Chemical Physics*, 243(1-2):89–96, 1999.
- [129] Y. Hatano. Interaction of photons with molecules – cross-sections for photoabsorption, photoionization, and photodissociation. *Radiation and Environmental Biophysics*, 38(4):239–247, 1999.
- [130] J. A. Nuth and S. Glicker. The vacuum ultraviolet spectra of HCN, C₂N₂, and CH₃CN. *Journal of Quantitative Spectroscopy and Radiative Transfer*, 28(3):223–231, 1982.
- [131] K. Watanabe, M. Zelikoff, and C. Y. Edward. Absorption coefficients of several atmospheric gases. Technical report, AFCRC Technical Report No. 52-53, 1953.
- [132] B. R. Russell, L. O. Edwards, and J. W. Raymond. Vacuum ultraviolet absorption spectra of the chloromethanes. *Journal of the American Chemical Society*, 95(7):2129–2133, 1973.
- [133] D. B. Robb and M. W. Blades. State-of-the-art in atmospheric pressure photoionization for LC/MS. *Analytica Chimica Acta*, 627(1):34–49, 2008.
- [134] S. Klee, V. Derpmann, W. Wißdorf, S. Klopotoski, H. Kersten, K. J. Brockmann, T. Benter, S. Albrecht, A. P. Bruins, F. Dousty, T. J. Kauppila, R. Kostianen, R. O'Brien, D. B. Robb, and J. A. Syage. Are clusters important in understanding the mechanisms in atmospheric pressure ionization? Part 1: reagent ion generation and chemical control of ion populations. *Journal of the American Society for Mass Spectrometry*, 25(8):1310–21, 2014.
- [135] S. Cheng, J. Dou, W. Wang, C. Chen, L. Hua, Q. Zhou, K. Hou, J. Li, and H. Li. Dopant-assisted Negative Photoionization Ion Mobility Spectrometry for Sensitive Detection of Explosives. *Analytical Chemistry*, 85(1):319–326, 2013.
- [136] F. Dousty, R. T. O'Brien, R. Gahler, H. Kersten, and T. Benter. Carbon disulfide as a dopant in photon-induced chemical ionization mass spectrometry. *Rapid Communications in Mass Spectrometry*, 27(17):1969–76, 2013.
- [137] Y. Cai, O. McConnell, and A. C. Bach. Suitability of tetrahydrofuran as a dopant and the comparison to other existing dopants in dopant-assisted atmospheric pressure photoionization mass spectrometry in support of drug discovery. *Rapid Communications in Mass Spectrometry*, 23(15):2283–91, 2009.
- [138] G. A. Eiceman and Z. Karpas. *Ion mobility spectrometry*. CRC Press, Inc., Boca Raton, FL, USA, 1st ed., 1994.
- [139] I. Dzidic, D. I. Carroll, R. N. Stillwell, E. C. Horning, and K. D. Haegele. Atmospheric pressure ionization mass spectrometry. Corona discharge ion source for use in a liquid chromatograph-mass spectrometer-computer analytical system. *Analytical Chemistry*, 47(14):2369–2373, 1975.
- [140] H. Borsdorf and G. A. Eiceman. *Ion Mobility Spectrometry: Principles and Applications*. *Applied Spectroscopy Reviews*, 41(4):323–375, 2006.

- [141] D. Halliday, R. Resnick, J. Walker, and S. W. Koch. *Halliday Physik*. WILEY-VCH Verlag GmbH, Weinheim, Germany, 2nd ed., 2009.
- [142] H. Hertz. Ueber einen Einfluss des ultravioletten Lichtes auf die elektrische Entladung. *Annalen der Physik und Chemie*, 267(8):983–1000, 1887.
- [143] P. Lenard. Ueber die lichtelektrische Wirkung. *Annalen der Physik*, 313(5):149–198, 1902.
- [144] L. B. Linford. Recent Developments in the Study of the External Photoelectric Effect. *Reviews of Modern Physics*, 5(1):34, 1933.
- [145] A. Einstein. Über einen die Erzeugung und Verwandlung des Lichtes betreffenden heuristischen Gesichtspunkt. *Annalen der Physik*, 322(6):132–148, 1905.
- [146] A. Einstein. Fundamental Ideas and Problems of the Theory of Relativity. In C. G. Santesson, editor, *Les Prix Nobel*. Nobel Foundation, Stockholm, 1921-19 ed., 1923.
- [147] N. W. Ashcroft and N. D. Mermin. *Festkörperphysik*. Oldenbourg Wissenschaftsverlag GmbH, München, Germany, 2nd ed., 2005.
- [148] M. Planck. Ueber das Gesetz der Energieverteilung im Normalspectrum. *Annalen der Physik*, 309(3):553–563, 1901.
- [149] P. G. Simmonds. Electron-capture detector with a photoemissive electron source. *Journal of Chromatography A*, 399:149–164, 1987.
- [150] J. C. Traeger and R. G. McLoughlin. Threshold photoionization and dissociation of toluene and cycloheptatriene. *Journal of the American Chemical Society*, 99(22):7351–7352, 1977.
- [151] J. E. Demuth and T. N. Rhodin. Chemisorption on (001), (110) and (111) nickel surfaces: A correlated study using LEED spectra, Auger spectra and work function change measurements. *Surface Science*, 45(1):249–307, 1974.
- [152] R. Michel, J. Gastaldi, C. Allasia, C. Jourdan, and J. Derrien. Initial interaction of oxygen with aluminium single crystal faces: A LEED, AES and work function study. *Surface Science*, 95(1):309–320, 1980.
- [153] T. T. M. Vladimirov, G. G. T. T. Magkoev, and G. G. Vladimirov. Aluminium oxide ultrathin-film growth on the Mo(110) surface: a work-function study. *Journal of Physics: Condensed Matter*, 13(28):L655, 2001.
- [154] G. Strasser, G. Rosina, E. Bertel, and P. P. Netzer. Surface oxidation of cerium and lanthanum. *Surface Science*, 152-153:765–775, 1985.
- [155] E. E. Huber Jr and C. T. Kirk Jr. Work function changes due to the chemisorption of water and oxygen on aluminum. *Surface Science*, 5(4):447–465, 1966.
- [156] J. Mueller. The effects of oxygen on the work function of metal films. *Surface Science*, 69(2):708–711, 1977.
- [157] B. Goldstein and D. J. Szostak. Characterization of clean and oxidized (100)LaB₆. *Surface Science*, 74(2):461–478, 1978.
- [158] C. M. Zimmer, J. Schubert, S. Hamann, U. Kunze, and T. Doll. Nanoscale photoelectron ionisation detector based on lanthanum hexaboride. *Physica Status Solidi (a)*, 208(6):1241–1245, 2011.

References

- [159] P. G. May, R. R. Petkie, J. M. E. Harper, and D. S. Yee. Photoemission from thin-film lanthanum hexaboride. *Applied Physics Letters*, 57:1584–1585, 1990.
- [160] C. M. Quinn and M. W. Roberts. Chemisorption of oxygen and subsequent processes on metal films : work function measurements. *Transactions of the Faraday Society*, 60:899–912, 1964.
- [161] V. E. Frankevich, J. Zhang, S. D. Friess, M. Dashtiev, and R. Zenobi. Role of Electrons in Laser Desorption/Ionization Mass Spectrometry. *Analytical Chemistry*, 75(22):6063–6067, 2003.
- [162] K. Inumaru, Y. Okubo, T. Fujii, and S. Yamanaka. Effects of organic vapour adsorption on the photoelectron emission from Au thin films in atmospheric air. *Physical Chemistry Chemical Physics*, 2(16):3681–3685, 2000.
- [163] H. Monjushiro. Ultraviolet Measured Photoelectron in Air Yield Spectra of Thin Gold Films. *Analytical Sciences*, 7, 1991.
- [164] H. Kirihaata. Externally quenched air counter for low-energy electron emission measurements. *Review of Scientific Instruments*, 52(1):68, 1981.
- [165] G. Brodén. UV-photoemission measurements on erbium and samarium. *Zeitschrift für Physik B Condensed Matter*, 15(3):171–190, 1972.
- [166] U. Müller, A. Schmidt-Ott, and H. Burtscher. Photoelectric quantum yield of free silver particles near threshold. *Zeitschrift für Physik B Condensed Matter*, 73(1):103–106, 1988.
- [167] B. Schleicher, H. Burtscher, and H. C. Siegmann. Photoelectric quantum yield of nanometer metal particles. *Applied Physics Letters*, 63(9):1191, 1993.
- [168] R. L. Smith. Two-Photon Photoelectric Effect. *Physical Review*, 128(5):2225, 1962.
- [169] M. Sipilä, A. A. Lushnikov, L. Khriachtchev, M. Kulmala, H. Tervahattu, and M. Räsänen. Experimental observation of two-photon photoelectric effect from silver aerosol nanoparticles. *New Journal of Physics*, 9(10):368–368, 2007.
- [170] M. Teich, J. Schroeder, and G. Wolga. Double-Quantum Photoelectric Emission from Sodium Metal. *Physical Review Letters*, 13(21):611–614, 1964.
- [171] J. Lehmann, M. Merschdorf, W. Pfeiffer, a. Thon, S. Voll, and G. Gerber. Silver nanoparticles on graphite studied by femtosecond time-resolved multiphoton photoemission. *The Journal of Chemical Physics*, 112(12):5428, 2000.
- [172] P. Bloch. Preliminary Investigation of the Two-Photon Photoelectric Effect. *Journal of Applied Physics*, 35(7):2052, 1964.
- [173] M. Göppert-Mayer. Über die Wahrscheinlichkeit des Zusammenwirkens zweier Lichtquanten in einem Elementarakt. *Die Naturwissenschaften*, 17(48):932–932, 1929.
- [174] S. Dushman. Thermionic Emission. *Reviews of Modern Physics*, 2(4):381, 1930.
- [175] H. Ibach and H. Lüth. *Solid-State Physics*. Springer Berlin / Heidelberg, Berlin, Germany, 7th ed., 2009.
- [176] S. Hüfner. *Photoelectron spectroscopy: principles and application*. Springer Berlin / Heidelberg, Berlin, Germany, 3rd ed., 2003.

- [177] N. Lang and W. Kohn. Theory of Metal Surfaces: Work Function. *Physical Review B*, 3(4):1215–1223, 1971.
- [178] M. Le Bellac. *Quantum Physics*. Cambridge University Press, Cambridge, UK, 2006.
- [179] J. G. Boyle, L. D. Pfefferle, E. E. Gulcicek, and S. D. Colson. Laser driven electron ionization for a VUV photoionization time-of-flight mass spectrometer. *Review of Scientific Instruments*, 62(2):323–333, 1991.
- [180] S. M. Colby and J. P. Reilly. Photoemission electron impact ionization in time-of-flight mass spectrometry: an examination of experimental consequences. *International Journal of Mass Spectrometry and Ion Processes*, 131:125–138, 1994.
- [181] D. C. Schriemer and L. Li. Laser-induced surface ionization in a time-of-flight mass spectrometer. *Review of Scientific Instruments*, 66(1):55, 1995.
- [182] B. W. LaFranchi and G. A. Petrucci. Photoelectron resonance capture ionization (PERCI): a novel technique for the soft-ionization of organic compounds. *Journal of the American Society for Mass Spectrometry*, 15(3):424–30, 2004.
- [183] U. Boesl and W. J. Knott. Negative ions, mass selection, and photoelectrons. *Mass Spectrometry Reviews*, 17(4):275–305, 1998.
- [184] F. Moritz, M. Dey, K. Zipperer, S. Prinke, and J. Grotemeyer. Laser-induced electron impact ionization in a reflectron time-of-flight mass spectrometer. *Organic Mass Spectrometry*, 28(12):1467–1475, 1993.
- [185] G. Gamez, L. Zhu, T. A. Schmitz, and R. Zenobi. Photoelectron Emission as an Alternative Electron Impact Ionization Source for Ion Trap Mass Spectrometry. *Analytical Chemistry*, 80(17):6791–6795, 2008.
- [186] J. Zahardis, B. W. LaFranchi, and G. A. Petrucci. Photoelectron resonance capture ionization mass spectrometry of fatty acids in olive oil. *European Journal of Lipid Science and Technology*, 108(11):925–935, 2006.
- [187] F. Hong. *Photoemission applied to Ion Mobility Spectrometry to detect explosives at ambient pressure and room temperature*. Ph.D. thesis, Dakota State University, Madison (SD), USA, 2004.
- [188] C. J. Walls, O. F. Swenson, and G. D. Gillispie. *Real-time monitoring of chlorinated aliphatic compounds in air using ion mobility spectrometry with photoemissive electron sources*, volume 3534. SPIE, 1999.
- [189] G. A. Eiceman, E. V. Krylov, N. S. Krylova, E. G. Nazarov, and R. A. Miller. Separation of Ions from Explosives in Differential Mobility Spectrometry by Vapor-Modified Drift Gas. *Analytical Chemistry*, 76(17):4937–4944, 2004.
- [190] Y. Gosho and A. Harada. A new technique for measuring negative ion mobilities at atmospheric pressure. *Journal of Physics D: Applied Physics*, 16(7):1159–1166, 1983.
- [191] C. Chen, C. Dong, Y. Du, S. Cheng, F. Han, L. Li, W. Wang, K. Hou, and H. Li. Bipolar Ionization Source for Ion Mobility Spectrometry Based on Vacuum Ultraviolet Radiation Induced Photoemission and Photoionization. *Analytical Chemistry*, 82(10):4151–4157, 2010.

References

- [192] A. Hansel, A. Jordan, R. Holzinger, P. Prazeller, W. Vogel, and W. Lindinger. Proton transfer reaction mass spectrometry: on-line trace gas analysis at the ppb level. *International Journal of Mass Spectrometry and Ion Processes*, 149-150:609–619, 1995.
- [193] C. Warneke, C. van der Veen, S. Luxembourg, J. A. de Gouw, and A. Kok. Measurements of benzene and toluene in ambient air using proton-transfer-reaction mass spectrometry: calibration, humidity dependence, and field intercomparison. *International Journal of Mass Spectrometry*, 207(3):167–182, 2001.
- [194] C. A. Mayhew, P. Sulzer, F. Petersson, S. Haidacher, A. Jordan, L. Märk, P. Watts, and T. D. Märk. Applications of proton transfer reaction time-of-flight mass spectrometry for the sensitive and rapid real-time detection of solid high explosives. *International Journal of Mass Spectrometry*, 289(1):58–63, 2010.
- [195] T. Wróblewski, L. Ziemczonek, and G. Karwasz. Proton transfer reactions for ionized water clusters. *Czechoslovak Journal of Physics*, 54:C747–C752, 2004.
- [196] M. Constapel, M. Schellenträger, O. J. Schmitz, S. Gäb, K. J. Brockmann, R. Giese, and T. Benter. Atmospheric-pressure laser ionization: a novel ionization method for liquid chromatography/mass spectrometry. *Rapid Communications in Mass Spectrometry*, 19(3):326–36, 2005.
- [197] D. Zakett, J. D. Ciupek, and R. G. Cooks. Determination of polycyclic aromatic hydrocarbons in solvent-refined coal by negative chemical ionization-charge inversion mass spectrometry/mass spectrometry. *Analytical Chemistry*, 53(4):723–726, 1981.
- [198] G. K.-C. Low, G. E. Batley, R. O. Lidgard, and A. M. Duffield. Determination of polycyclic aromatic hydrocarbons in coal fly ash using gas chromatography/negative ion chemical ionization mass spectrometry. *Biological Mass Spectrometry*, 13(2):95–104, 1986.
- [199] S. Tobita, M. Meinke, E. Illenberger, L. G. Christophorou, H. Baumgtirtel, and S. Leach. Polycyclic aromatic hydrocarbons : negative ion formation following low energy (0- 15 eV) electron impact. *Chemical Physics*, 161(3):501–508, 1992.
- [200] M. Niederer. Determination of polycyclic aromatic hydrocarbons and substitutes (nitro-, Oxy-PAHs) in urban soil and airborne particulate by GC-MS and NCI-MS/MS. *Environmental Science and Pollution Research International*, 5(4):209–16, 1998.
- [201] M. Nishioka, C. C. Howard, D. A. Contos, L. M. Bail, and J. Lewtas. Detection of Hydroxylated Nitro Aromatic and Hydroxylated Nitro Polycyclic Aromatic Compounds in an Ambient Air Particulate Extract Using. *Environmental Science & Technology*, 22:908–915, 1988.
- [202] D. Z. Bezabeh, T. M. Allen, E. M. McCauley, P. B. Kelly, and A. D. Jones. Negative ion laser desorption ionization time-of-flight mass spectrometry of nitrated polycyclic aromatic hydrocarbons. *Journal of the American Society for Mass Spectrometry*, 8(6):630–636, 1997.
- [203] T. Ramdahl and K. Urdal. Determination of nitrated polycyclic aromatic hydrocarbons by fused silica capillary gas chromatography/negative ion chemical ionization mass spectrometry. *Analytical Chemistry*, 54(13):2256–2260, 1982.
- [204] D. Z. Bezabeh, H. A. Bamford, M. M. Schantz, and S. A. Wise. Determination of nitrated polycyclic aromatic hydrocarbons in diesel particulate-related standard reference materials by using gas chromatography/mass spectrometry with negative ion chemical ionization. *Analytical and Bioanalytical Chemistry*, 375(3):381–8, 2003.

- [205] B. L. Valle-Hernández, V. Mugica-Alvarez, E. Salinas-Talavera, O. Amador-Muñoz, M. A. Murillo-Tovar, R. Villalobos-Pietrini, and A. De Vizcaya-Ruíz. Temporal variation of nitropolycyclic aromatic hydrocarbons in PM10 and PM2.5 collected in Northern Mexico City. *The Science of the Total Environment*, 408(22):5429–38, 2010.
- [206] Z. Takats, I. Cotte-Rodriguez, N. Talaty, H. Chen, and R. G. Cooks. Direct, trace level detection of explosives on ambient surfaces by desorption electrospray ionization mass spectrometry. *Chemical Communications*, (15):1950–1952, 2005.
- [207] R. G. Ewing and C. J. Miller. Detection of volatile vapors emitted from explosives with a handheld ion mobility spectrometer. *Field Analytical Chemistry & Technology*, 5(5):215–221, 2001.
- [208] M. Tam and H. H. Hill. Secondary Electrospray Ionization-Ion Mobility Spectrometry for Explosive Vapor Detection. *Analytical Chemistry*, 76(10):2741–2747, 2004.
- [209] I. A. Buryakov. Express analysis of explosives, chemical warfare agents and drugs with multicapillary column gas chromatography and ion mobility increment spectrometry. *Journal of Chromatography B*, 800(1-2):75–82, 2004.
- [210] R. Atkinson, S. M. Aschmann, and J. Arey. Reactions of hydroxyl and nitrogen trioxide radicals with phenol, cresols, and 2-nitrophenol at 296 ± 2 K. *Environmental Science & Technology*, 26(7):1397–1403, 1992.
- [211] R. I. Olariu, B. Klotz, I. Barnes, K. H. Becker, and R. Mocanu. FT-IR study of the ring-retaining products from the reaction of OH radicals with phenol, o-, m-, and p-cresol. *Atmospheric Environment*, 36(22):3685–3697, 2002.
- [212] D. Grosjean. Atmospheric reactions of ortho cresol: Gas phase and aerosol products. *Atmospheric Environment*, 18(8):1641–1652, 1984.
- [213] E. Bolzacchini, M. Bruschi, J. Hjorth, S. Meinardi, M. Orlandi, B. Rindone, and E. Rosenbohm. Gas-Phase Reaction of Phenol with NO₃. *Environmental Science & Technology*, 35(9):1791–1797, 2001.
- [214] B. J. Finnlaysen-Pitts and J. N. Pitts Jr. *Chemistry of the upper and lower atmosphere*. Academic Press, San Diego, CA, USA, 6th ed., 1999.
- [215] J. G. Dillard. Negative ion mass spectrometry. *Chemical Reviews*, 73(6):589–643, 1973.
- [216] J. G. Calvert, R. Atkinson, K. H. Becker, R. M. Kamens, J. H. Seinfeld, T. J. Wallington, and G. Yarwoods. *The mechanisms of atmospheric oxidation of aromatic hydrocarbons*. Oxford University Press, New York, NY, USA, 2002.
- [217] J. H. Seinfeld and S. N. Pandis. *Atmospheric Chemistry and Physics -From Air Pollution to Climate Change*. Wiley-Interscience, New York, NY, USA, 1998.
- [218] G. Rippen, E. Zietz, R. Frank, T. Knacker, and W. Klöpffer. Do airborne nitrophenols contribute to forest decline? *Environmental Technology Letters*, 8(1-12):475–482, 1987.
- [219] A. Kawai, S. Goto, Y. Matsumoto, and H. Matsushita. Mutagenicity of aliphatic and aromatic nitro compounds. Industrial materials and related compounds. *Japanese Journal of Industrial Health*, 29:34–54, 1987.
- [220] V. Purohit and A. K. Basu. Mutagenicity of Nitroaromatic Compounds. *Chemical Research in Toxicology*, 13(8):673–692, 2000.

References

- [221] M. A. J. Harrison, S. Barra, D. Borghesi, D. Vione, C. Arsene, and R. I. Olariu. Nitrated phenols in the atmosphere: a review. *Atmospheric Environment*, 39(2):231–248, 2005.
- [222] J. Lüttke, V. Scheer, K. Levsen, G. Wünsch, J. Neil Cape, K. J. Hargreaves, R. L. Storeton-West, K. Acker, W. Wieprecht, and B. Jones. Occurrence and formation of nitrated phenols in and out of cloud. *Atmospheric Environment*, 31(16):2637–2648, 1997.
- [223] K. Kawamura and I. R. Kaplan. Biogenic and anthropogenic organic compounds in rain and snow samples collected in southern california. *Atmospheric Environment*, 20(1):115–124, 1986.
- [224] J. Podehradsk, Z. Voznakova, J. Podehradska, and M. Kohlickova. Determination of nitrophenols in soil. *Chemosphere*, 33(2):285–291, 1996.
- [225] D. Grosjean. Ambient levels of formaldehyde, acetaldehyde and formic acid in southern California: results of a one-year baseline study. *Environmental Science & Technology*, 25(4):710–715, 1991.
- [226] I. Bejan, Y. Abd-el Aal, I. Barnes, T. Benter, B. Bohn, P. Wiesen, and J. Kleffmann. The photolysis of ortho-nitrophenols: a new gas phase source of HONO. *Physical Chemistry Chemical Physics*, 8(17):2028–35, 2006.
- [227] S. Jagiella and F. Zabel. Reaction of phenylperoxy radicals with NO₂ at 298 K. *Physical Chemistry Chemical Physics*, 9(36):5036–5051, 2007.
- [228] M. J. Frisch, G. W. Trucks, H. B. Schlegel, G. E. Scuseria, M. A. Rob, J. R. Cheeseman, J. A. M. Jr., T. Vreven, K. N. Kudin, J. C. Burant, J. M. Millam, S. S. Iyengar, J. Tomasi, V. Barone, B. Mennucci, M. Cossi, G. Scalmani, N. Rega, G. A. Petersson, H. Nakatsuji, M. Hada, M. Ehara, K. Toyota, R. Fukuda, J. Hasegawa, M. Ishida, T. Nakajima, Y. Honda, O. Kitao, H. Nakai, M. Klene, X. Li, J. E. Knox, H. P. Hratchian, J. B. Cross, V. Bakken, C. Adamo, J. Jaramillo, R. Gomperts, R. E. Stratmann, O. Yazyev, A. J. Austin, R. Cammi, C. Pomelli, J. W. Ochterski, P. Y. Ayala, K. Morokuma, G. A. Voth, P. Salvador, J. J. Dannenberg, V. G. Zakrzewski, S. Dapprich, A. D. Daniels, M. C. Strain, O. Farkas, D. K. Malick, A. D. Rabuck, K. Raghavachari, J. B. Foresman, J. V. Ortiz, Q. Cui, A. G. Baboul, S. Clifford, J. Cioslowski, B. B. Stefanov, G. Liu, A. Liashenko, P. Piskorz, I. Komaromi, R. L. Martin, D. J. Fox, T. Keith, M. A. Al-Laham, C. Y. Peng, A. Nanayakkara, M. Challacombe, P. M. W. Gill, B. Johnson, W. Chen, M. W. Wong, C. Gonzalez, and J. A. Pople. Gaussian 03W, Gaussian, Inc., Wallingford, CT, 2003.
- [229] M. J. Frisch, G. W. Trucks, H. B. Schlegel, G. E. Scuseria, M. A. Robb, J. R. Cheeseman, G. Scalmani, V. Barone, B. Mennucci, G. A. Petersson, H. Nakatsuji, M. Caricato, X. Li, H. P. Hratchian, A. F. Izmaylov, J. Bloino, G. Zheng, J. L. Sonnenberg, M. Hada, M. Ehara, K. Toyota, R. Fukuda, J. Hasegawa, M. Ishida, T. Nakajima, Y. Honda, O. Kitao, H. Nakai, T. Vreven, J. A. J. Montgomery, J. E. Peralta, F. Ogliaro, M. Bearpark, J. J. Heyd, E. Brothers, K. N. Kudin, V. N. Staroverov, R. Kobayashi, J. Normand, K. Raghavachari, A. Rendell, J. C. Burant, S. S. Iyengar, J. Tomasi, M. Cossi, N. Rega, J. M. Millam, M. Klene, J. E. Knox, J. B. Cross, V. Bakken, C. Adamo, J. Jaramillo, R. Gomperts, R. E. Stratmann, O. Yazyev, A. J. Austin, R. Cammi, C. Pomelli, J. W. Ochterski, R. L. Martin, K. Morokuma, V. G. Zakrzewski, G. A. Voth, P. Salvador, J. J. Dannenberg, S. Dapprich, A. D. Daniels, O. Farkas, J. B. Foresman, J. V. Ortiz, J. Cioslowski, and D. J. Fox. Gaussian 09, Revision D.01, Gaussian, Inc., Wallingford, CT, 2009.
- [230] R. Dennington, T. Keith, and J. Millam. GaussView Version 4.1, Semichem, Inc., Shawnee Mission, KS, USA, 2007.

References

- [231] S. R. Langhoff. Theoretical Infrared Spectra for Polycyclic Aromatic Hydrocarbon Neutrals, Cations, and Anions. *The Journal of Physical Chemistry*, 100(8):2819–2841, 1996.
- [232] C. F. Rodriguez, T. Shoeib, I. K. Chu, K. W. M. Siu, and A. C. Hopkinson. Comparison between Protonation, Lithiation, and Argentionation of 5-Oxazolones: A Study of a Key Intermediate in Gas-Phase Peptide Sequencing. *The Journal of Physical Chemistry A*, 104(22):5335–5342, 2000.
- [233] P. J. Stephens, F. J. Devlin, C. F. Chabalowski, and M. J. Frisch. Ab Initio Calculation of Vibrational Absorption and Circular Dichroism Spectra Using Density Functional Force Fields. *The Journal of Physical Chemistry*, 98(45):11623–11627, 1994.
- [234] M. Jelezniak and I. Jelezniak. CHEMKED: Chemical Kinetics of Gas Phase Reactions. <http://www.chemked.com/> (last accessed: 4.2014), 2007.
- [235] Bruker Daltonik GmbH. HCTultra User Manual Version 1.2.1, 2006.
- [236] Bruker Daltonik GmbH. Esquire Control Service Version 6.1.
- [237] Bruker Daltonik GmbH. Data Analysis Version 3.4.
- [238] M. Ackermann. UV-solar radiation related to mesospheric processes. In G. Fiocco, editor, *Mesospheric Models and Related Experiments*, pp. 149–159. D. Reidel Publishing Company, Dordrecht, 1971.
- [239] J. A. Manion, R. E. Huie, R. D. Levin, D. R. B. Jr., V. L. Orkin, W. Tsang, W. S. McGivern, J. W. Hudgens, V. D. Knyazev, D. B. Atkinson, E. Chai, A. M. Tereza, C.-Y. Lin, T. C. Allison, W. G. Mallard, F. Westley, J. T. Herron, R. F. Hampson, and D. H. Frizzell. NIST Chemical Kinetics Database, NIST Standard Reference Database 17, Version 7.0 (Web Version), Release 1.4.3, Data version 2008.12, National Institute of Standards and Technology, Gaithersburg, Maryland, 20899-8320, Web address: <http://kinetics.nist.gov/>.
- [240] R. Mota, R. Parafita, A. Giuliani, M. J. Hubin-Franskin, J. M. C. Lourenço, G. Garcia, S. V. Hoffmann, N. J. Mason, P. A. Ribeiro, M. Raposo, and P. Limão Vieira. Water VUV electronic state spectroscopy by synchrotron radiation. *Chemical Physics Letters*, 416(1-3):152–159, 2005.
- [241] H. Keller-Rudek and G. K. Moortga. MPI-Mainz-UV-VIS Spectral Atlas of Gaseous Molecules. www.atmosphere.mpg.de/spectral-atlas-mainz (last accessed: 4.2013).
- [242] J. Franzen. Method and device for transport of ions in gas through a capillary. (US5736740A).
- [243] Scientific Instrument Services Inc. SIMION Version 8.1.1. *Ringoes, NJ, USA*, (Available at: <http://simion.com> (last accessed: 6.2013)).
- [244] A. D. Appelhans and D. A. Dahl. SIMION ion optics simulations at atmospheric pressure. *International Journal of Mass Spectrometry*, 244(1):1–14, 2005.
- [245] Comsol AB. Comsol Multiphysics ver. 4.4. *Stockholm, Sweden*, <http://www.comsol.de>, 2013.
- [246] W. Wissdorf, L. Pohler, S. Klee, D. Müller, and T. Benter. Simulation of ion motion at atmospheric pressure: particle tracing versus electrokinetic flow. *Journal of the American Society for Mass Spectrometry*, 23(2):397–406, 2012.

References

- [247] S. Albrecht, S. Klopotoski, V. Derpmann, S. Klee, K. J. Brockmann, F. Stroh, and T. Benter. Studies of the mechanism of the cluster formation in a thermally sampling atmospheric pressure ionization mass spectrometer. *The Review of Scientific Instruments*, 85(1):1–10, 2014.
- [248] H. Kersten, W. Wissdorf, K. J. Brockmann, T. Benter, and R. O'Brien. VUV Photoionization within Transfer Capillaries of Atmospheric Pressure Ionization Sources. In *Proceedings of the 58th ASMS Conference on Mass Spectrometry and Allied Topics*. Salt Lake City, UT, USA, 2010.
- [249] H. G. Becker, W. Berger, G. Domschke, E. Fanghänel, J. Faust, M. Fischer, F. Gentz, K. Gewalt, R. Gluch, R. Mayer, K. Müller, D. Pavel, H. Schmidt, K. Schollberg, K. Schwetlick, E. Seiler, G. Zeppenfeld, R. Beckert, W. D. Habicher, and P. Metz. *Organikum*. WILEY-VCH Verlag GmbH, Weinheim, Germany, 21st ed., 2001.
- [250] UVP LLC. Pen-Ray Mercury Lamps - Specifications. <http://uvp.com/mercury.html> (last accessed: 7.2011).
- [251] H. Kersten, M. Dlugosch, K. Kroll, K. J. Brockmann, T. Benter, and R. O'Brien. Progress in VUV measurements of a spark discharge lamp used for capillary Atmospheric Pressure Photoionization (cAPPI). In *Proceedings of the 60th ASMS Conference on Mass Spectrometry and Allied Topics*. Vancouver, BC, Kanada, 2012.
- [252] Huntingdon Fusion Techniques. <http://www.huntingdonfusion.com/de/produkte/wolfram-elektroden-und-schleifmaschinen/multi-strike-wolfram-elektroden.html> (last accessed: 8.2012).
- [253] R. Ishii, K. Matsumura, A. Sakai, and T. Sakata. Work function of binary alloys. *Applied Surface Science*, 169-170:658–661, 2001.
- [254] N. Kiwa, Y. Gotoh, H. Tsuji, and J. Ishikawa. Relationship between composition and work function of gold-samarium alloy thin films. *Vacuum*, 66(3-4):517–521, 2002.
- [255] R. Schiewek. *Entwicklung einer Multi-Purpose Ionenquelle für die AP-MS sowie Design und Anwendung von APLI-Ionisationslabeln*. Ph.D. thesis, University of Wuppertal, Wuppertal, Germany, 2008.
- [256] D. Klink. *Optimierung der Laserionisation bei Atmosphärendruck und Aufbau einer SFC-APLI-Kopplung*. Ph.D. thesis, University of Wuppertal, Wuppertal, Germany, 2013.
- [257] H. Sonderfeld. *Charakterisierung und Einsatz eines PTR-ToF-MS zur Messung von flüchtigen organischen Verbindungen*. Ph.D. thesis, University of Wuppertal, Germany, 2014.
- [258] I. Barnes, K. H. Becker, and N. Mihalopoulos. An FTIR product study of the photooxidation of dimethyl disulfide. *Journal of Atmospheric Chemistry*, 18(3):267–289, 1994.
- [259] A. Hansel, A. Jordan, C. Warneke, R. Holzinger, A. Wisthaler, and W. Lindinger. Proton-transfer-reaction mass spectrometry (PTR-MS): on-line monitoring of volatile organic compounds at volume mixing ratios of a few pptv. *Plasma Sources Science and Technology*, 8(2):332–336, 1999.
- [260] W. Wissdorf. Chemical Reaction Simulation (RS) extension to SIMION. <http://rs.ipams.uni-wuppertal.de/> (last accessed: 3.2014).

References

- [261] I. Barnes, V. Derpmann, S. Albrecht, and T. Benter. On the Ionization Mechanism in Negative Ion Atmospheric Pressure Mass Spectrometry and the Role of Cluster Formation. In *Proceedings of the 60th ASMS Conference on Mass Spectrometry and Allied Topics*. Vancouver, BC, Kanada, 2012.
- [262] Y. K. Lau, S. Ikuta, and P. Kebarle. Thermodynamics and kinetics of the gas-phase reactions $\text{H}_3\text{O}^+(\text{H}_2\text{O})_{n-1} + \text{water} = \text{H}_3\text{O}^+(\text{H}_2\text{O})_n$. *Journal of the American Chemical Society*, 104(6):1462–1469, 1982.
- [263] K. Itoh, M. Nishikawa, and R. Holroyd. Electron attachment to toluene in n-hexane and 2,2-dimethylbutane at high pressure. *The Journal of Physical Chemistry*, 97(2):503–507, 1993.
- [264] H. M. Rosenstock, K. Draxl, B. W. Steiner, and J. T. Herron. Ion Energetics Data. In P. J. Linstrom and W. G. Mallard, editors, *Gaithersburg MD, <http://webbook.nist.gov>, (April 15, 2012)*. National Institute of Standards and Technology, NIST Chemistry WebBook, NIST Standard Reference Database Number 69.
- [265] M. Arshadi and P. Kebarle. Hydration of OH^- and O_2^- in the gas phase. Comparative solvation of OH^- by water and the hydrogen halides. Effects of acidity. *The Journal of Physical Chemistry*, 74(7):1483–1485, 1970.
- [266] H. M. Lee and K. S. Kim. Ab initio study of superoxide anion-water clusters. *Molecular Physics*, 100(6):875–879, 2002.
- [267] K. A. Daum, D. A. Atkinson, and R. G. Ewing. The role of oxygen in the formation of TNT product ions in ion mobility spectrometry. *International Journal of Mass Spectrometry*, 214(2):257–267, 2002.
- [268] D. B. Robb, M. W. Blades, S.-S. Cai, J. A. Syage, C. Mullen, A. Irwin, B. V. Pond, D. L. Huestis, M. J. Coggiola, and H. Oser. Detection of Explosives and Explosives-Related Compounds by Single Photon Laser Ionization Time-of-Flight Mass Spectrometry. *Analytical Chemistry*, 78(11):3807–3814, 2006.
- [269] G. R. Asbury, J. Klasmeier, and H. H. Hill Jr. Analysis of explosives using electrospray ionization/ion mobility spectrometry (ESI/IMS). *Talanta*, 50(6):1291–1298, 2000.
- [270] K. Tönnies, R. Schmid, C. Weickhardt, J. Reif, and J. Grotemeyer. Multiphoton ionization of nitrotoluenes by means of ultrashort laser pulses. *International Journal of Mass Spectrometry*, 206(3):245–250, 2001.
- [271] G. K. Jarvis, R. A. Kennedy, and C. A. Mayhew. Investigations of low energy electron attachment to ground state group 6B hexafluorides (SF_6 , SeF_6 , and TeF_6) using an electron-swarm mass spectrometric technique. *International Journal of Mass Spectrometry*, 205(1-3):253–270, 2001.
- [272] K. J. Laidler and J. H. Meiser. *Physical Chemistry*. The Benjamin/Cummings Publishing Company, Inc., Menlo Park, CA, 1982.
- [273] M. Kochsiek. Measurement of Water Adsorption Layers on Metal Surfaces. *Metrologia*, 18(3):153–159, 1982.
- [274] M. Tschapek, R. Santamaria, and I. Natale. The surface conductance of quartz as a function of its hydration. *Electrochimica Acta*, 14(9):889–895, 1969.

References

- [275] S. Kurosaki, S. Saito, and G. Sato. Transformation of Adsorbed Water on Solid Surfaces and its Dielectric Losses and Conductivities. *The Journal of Chemical Physics*, 23(10):1846, 1955.
- [276] R. I. Razouk and A. S. Salem. The Adsorption of Water Vapor on Glass Surfaces. *The Journal of Physical and Colloid Chemistry*, 52(7):1208–1227, 1948.
- [277] D. Mueller. *Gasfluss- und Ionentransmissionsmessungen an Massenspektrometereinlasskapillaren*. Bachelor-Thesis, University of Wuppertal, Wuppertal, Germany, 2010.
- [278] M. Lorenz, S. Klee, R. Moennikes, A. L. M. Suárez, K. J. Brockmann, O. J. Schmitz, S. Gaeb, and T. Benter. Atmospheric Pressure Laser Ionization (APLI): Investigations on Ion Transport in Atmospheric Pressure Ion Sources. In *Proceedings of the 56th ASMS Conference on Mass Spectrometry and Allied Topics*. Denver, CO, USA, 2008.
- [279] P. L. Houston. *Chemical Kinetics and Reaction Dynamics*. Dover Publications Inc, Mineola, NY, 2006.
- [280] A. Eberhagen. Die Änderung der Austrittsarbeit von Metallen durch eine Gasadsorption. *Fortschritte der Physik*, 8(5-6):245–294, 1960.
- [281] J. L. Pack, R. E. Voshall, a. V. Phelps, and L. E. Kline. Longitudinal electron diffusion coefficients in gases: Noble gases. *Journal of Applied Physics*, 71(11):5363, 1992.
- [282] V. De Renzi, R. Rousseau, D. Marchetto, R. Biagi, S. Scandolo, and U. del Pennino. Metal Work-Function Changes Induced by Organic Adsorbates: A Combined Experimental and Theoretical Study. *Physical Review Letters*, 95(4):46804, 2005.
- [283] J. Du, L. Huang, and L. Zhu. Absorption cross sections of surface-adsorbed H₂O in the 295-370 nm region and heterogeneous nucleation of H₂O on fused silica surfaces. *The Journal of Physical Chemistry A*, 117(36):8907–14, 2013.
- [284] C. Tomas, E. Vinet, and J. P. Girardeau-Montaut. Simultaneous measurements of second-harmonic generation and two-photon photoelectric emission from Au. *Applied Physics A: Materials Science & Processing*, 68(3):315–320, 1999.
- [285] A. T. Georges. Coherent and incoherent multiple-harmonic generation from metal surfaces. *Physical Review A*, 54(3):2412, 1996.
- [286] J. E. Sipe, V. C. Y. So, M. Fukui, and G. I. Stegeman. Analysis of second-harmonic generation at metal surfaces. *Physical Review B*, 21(10):4389, 1980.
- [287] F. Ehlötzky and S. Varro. The multiphoton photo-effect and harmonic generation at metal surfaces. *Journal of Physics D: Applied Physics*, 30(22):3071, 1997.
- [288] A. Kadyshevitch and R. Naaman. Photoelectron Transmission through Organized Organic Thin Films. *Physical Review Letters*, 74(17):3443–3446, 1995.
- [289] W. Schmickler. Tunneling of electrons through thin layers of water. *Surface Science*, 335:416–421, 1995.
- [290] J. Chen, J. C. Wenger, and D. S. Venables. Near-ultraviolet absorption cross sections of nitrophenols and their potential influence on tropospheric oxidation capacity. *The Journal of Physical Chemistry A*, 115(44):12235–42, 2011.
- [291] M. Ackerman, F. Biaume, and M. Nicolet. Absorption in the spectral range of the Schumann–Runge bands. *Canadian Journal of Chemistry*, 47(10):1834–1840, 1969.

- [292] V. Pishchik, L. A. Lytvynov, and E. R. Dobrovinskaya. *Sapphire: Material, Manufacturing, Applications*. Springer US, Boston, MA, 2009.
- [293] H. Kaiser and H. Specker. Bewertung und Vergleich von Analysenverfahren. *Fresenius Journal of Analytical Chemistry*, 149:46–66, 1956.
- [294] M. Bader, T. Göen, J. Müller, and J. Angerer. Analysis of nitroaromatic compounds in urine by gas chromatography-mass spectrometry for the biological monitoring of explosives. *Journal of Chromatography B, Biomedical Sciences and Applications*, 710(1-2):91–9, 1998.
- [295] S.-A. Barshick and W. H. Griest. Trace Analysis of Explosives in Seawater Using Solid-Phase Microextraction and Gas Chromatography/Ion Trap Mass Spectrometry. *Analytical Chemistry*, 70(14):3015–3020, 1998.
- [296] D. S. Moore. Instrumentation for trace detection of high explosives. *Review of Scientific Instruments*, 75(8):2499–2512, 2004.
- [297] S. P. Sharma and S. C. Lahiri. Characterization and Identification of Explosives and Explosive Residues Using GC-MS, an FTIR Microscope, and HPTLC. *Journal of Energetic Materials*, 23(4):239–264, 2005.
- [298] J. M. Perr, K. G. Furton, and J. R. Almirall. Gas chromatography positive chemical ionization and tandem mass spectrometry for the analysis of organic high explosives. *Talanta*, 67(2):430–6, 2005.
- [299] C. Lenchitz and R. W. Velicky. Vapor pressure and heat of sublimation of three nitro-toluenes. *Journal of Chemical & Engineering Data*, 15(3):401–403, 1970.
- [300] V. Derpmann, H. Sonderfeld, I. Bejan, H. Kersten, J. Kleffmann, R. Koppmann, and T. Benter. Highly Efficient Ionization of Nitro-aromatic Compounds using Photoelectron Induced Atmospheric Pressure Ionization (PAPI). In *Proceedings of the 59th ASMS Conference on Mass Spectrometry and Allied Topics*. Denver, CO, USA, 2011.
- [301] V. Derpmann, I. Bejan, H. Kersten, K. J. Brockmann, I. Barnes, J. Kleffmann, and T. Benter. An Ionization Method Based on Photoelectron Induced Thermal Electron Generation: capillary Atmospheric Pressure Electron Capture Ionization (cAPECI). In *NATO Workshop: Disposal of Dangerous Chemicals in Urban Areas and Mega Cities*. Danzig, Poland, 2011.
- [302] V. Derpmann, W. Wissdorf, D. Mueller, and T. Benter. Development of a New Ion Source for Capillary Atmospheric Pressure Electron Capture Ionization (cAPECI). In *Proceedings of the 60th ASMS Conference on Mass Spectrometry and Allied Topics*. Vancouver, BC, Canada, 2012.